Structured population models for macrophage heterogeneity in early atherosclerosis



Keith Li Chambers

Balliol College

University of Oxford

A thesis submitted for the degree of

DPhil in Mathematics

Michaelmas 2024

Acknowledgements

This thesis would not exist without the support of my supervisor, Professor Helen Byrne, and external co-supervisor, Professor Mary Myerscough. Helen and Mary, thank you both so much for taking a chance on me and for your sustained encouragement throughout the past four years. Your patience, care, discipline, imagination and dedication to pragmatic advice will continue to be a source of inspiration in the coming years.

I would also like to extend my gratitude to Dr Michael Watson. Mike, your authenticity, conscientiousness and unwavering support kept me sane during the Sydney lockdown and continue to motivate me to do diligent work. Thank you for being so generous with your time and advice.

Further, I would like to thank Professor David Greaves and members of his lab from 2020-2024, including: Laura Chaffey, Vincent Luscombe, Annabell Roberti, Agata Rumianek and Gareth Purvis. David and team, you have taught me so much about what it means to be a good scientist. The time spent discussing science in meetings and wrestling with phagocytosis data were invaluable lessons towards keeping my work grounded and testable.

I am also thankful to the members of the WCMB for always making the department a welcoming and lively place. This includes Professor Philip Maini, for being as caring and nurturing as he is insightful, and my officemates from 2020-2024: George Atkinson, Robert McDonald and Nathan Schofield, for their friendship, support and for many stimulating conversations over the years.

My deepest gratitude goes to the resident Aussies: Dr Jessica Crawshaw and Dr Alex Browning. Jess, your friendship, sincerity and relentless optimism always brightens my day. Thanks for always being there when I need it. Alex, thank you for all the support and for being so open with advice. Looking forward to more spontaneous, and slightly unhinged, trips into the countryside.

I would also like to thank various friends from college that I have leaned on over the years, including: Kristijana, Hillary, Elyse, Titiksha, Tafadzwa, Anupriya, Gunseli, Itai, Neel, Akari, Ana, Zoe and Konrad. Thank you all for your support, the conversations, the spontaneous food trips, the climbing at Brookes, and the commiseration sessions throughout the years.

Finally, I am deeply thankful for the close friends and family I have in Sydney. To my friends Edgar, Hosea, Jesenia and Sud, thank you so much for keeping in touch from across the world, for all the support and for the honest dialogue over the past few years. You're always welcome at my place when you're around. To my sister, Jennifer, and brother-in-law, Jordan, thank you for the support, friendship and for letting me work at yours during the final crunch. To Mum and Dad, thank you for always making me feel like I have a safe home to return to in difficult times.

Abstract

Atherosclerosis is a chronic inflammatory condition of the artery wall and a leading cause of death. A particular danger is the asymptomatic nature of its early stages of development. These early stages are characterised by lipid accumulation within immune cells called monocyte-derived macrophages (MDMs). MDMs ingest extracellular lipids, sourced by low-density lipoprotein particles (LDL), and offload them onto high-density lipoprotein (HDL) particles for clearance. These interactions, together with other microenvironmental factors, generate heterogeneity in the lipid content, phenotype and spatial position of the MDMs. Understanding this heterogeneity is key to predicting which early lesions will resolve and which will persist to become life-threatening. In this thesis, we use mathematical modelling to explore how MDM heterogeneity arises and evolves in early atherosclerotic lesions.

The mathematical models we study are formulated using structured differential equations that focus on the different facets of MDM heterogeneity. In Chapter 4, we develop a new lipid-structured model in which the rate of lipid uptake by MDMs depends on their available capacity We extend this model to include phenotype resolution in Chapter 5, and spatial resolution in Chapter 6. MDM phenotype is viewed as a spectrum, ranging from inflammatory (M1) to resolving (M2) states. Spatial heterogeneity is included via a Cartesian variable that represents distance into the artery wall. In Chapter 7, we combine the models of Chapters 5 and 6 into a spatially-resolved, phenotype-lipid structured model.

The model analyses, which include numerical and asymptotic solutions, show that MDM heterogeneity arises in a manner dependent on blood LDL and HDL levels. When LDL lipid dominates HDL capacity in the blood, the distributions of MDM lipid content and phenotype eventually skew towards maximal capacity and inflammatory states, respectively. MDMs deeper in the lesion exhibit greater lipid loads and more inflammatory phenotypes. When instead HDL capacity dominates in the blood, mean MDM lipid content is lower and mean MDM phenotype is resolving. MDMs deeper in the lesion exhibit greater lipid loads, but a more resolving phenotype. These results provide a framework for future model validation using single-cell RNA sequencing data, and for the numerical investigation of lipoprotein-modulating and anti-inflammatory therapies for human atherosclerotic lesions.

Contents

1 Introduction **1**
1.1 Thesis outline 2

2 Atherosclerotic lesion formation **5**
2.1 Where do lesions form? 5
2.2 How do lesions form? 6
2.3 Development of early atherosclerosis 8

3 Mathematical models of atherosclerosis **17**
3.1 Mechanical models 17
3.2 Well-mixed ODE models 18
3.3 Spatially-resolved models 19
3.4 Structured population models 21

4 A new lipid-structured model **29**
4.1 Introduction 29
4.2 Model development 30
4.3 Results 37
4.4 Discussion 54

5 A phenotype-lipid structured model **59**
5.1 Introduction 59
5.2 Model development 60
5.3 Results 73
5.4 Discussion 89

6 A spatially-resolved lipid structured model **93**
6.1 Introduction 93
6.2 Model development 94
6.3 Results 108
6.4 Discussion 122

7 A spatially-resolved phenotype-lipid structured model **129**
7.1 Introduction 129
7.2 Model development 130
7.3 Results 144
7.4 Discussion 155

8 Discussion and conclusions **161**
8.1 Thesis summary 161
8.2 Model limitations and future work 164

Bibliography **173**

Chapter 1

Introduction

Atherosclerosis is a chronic inflammatory disease of the artery wall that causes approximately 50% of all deaths in Westernised society [1]. A particular danger is the asymptomatic development of its early stages [2]. These early stages are driven by interactions between fatty compounds called lipids, and a class of immune cells called monocyte-derived macrophages (MDMs). MDMs ingest extracellular lipids, sourced by the infiltration of low-density lipoprotein (LDL) particles, and offload them onto high-density lipoprotein (HDL) particles for clearance from the lesion. Over time, the sustained influx of lipid and the death of lipid-laden MDMs may cause the lesion to develop into an atherosclerotic plaque containing a large core of extracellular lipid [3]. Such plaques are vulnerable to rupture, upon which the lipid core is released into the bloodstream, promoting blood clot formation. In turn, blood clots trigger myocardial infarction or stroke when they block vessels in the heart and brain respectively. The mechanisms which drive early atherosclerosis and, consequently, set the stage for such clinical events, are active areas of research.

MDM heterogeneity is a major obstacle in our understanding of early atherosclerosis. Specifically, interactions with their microenvironment cause macrophages in atherosclerotic lesions to develop substantial heterogeneity in their lipid content, phenotype and spatial location. Early observations of cell-to-cell variation in lipid content led to the distinction of nascent macrophages from lipid-laden 'foam cells' in the biological literature; foam cells are a hallmark of atherosclerotic lesions [4]. This dichotomous classification is, however, a simplistic representation of lipid content heterogeneity given that lipid load changes incrementally in response to uptake and efflux events [5]. Similarly, macrophages in atherosclerotic lesions are seen to adopt both pro-inflammatory and resolving phenotypes, which led to the distinction between M1- and M2-like cells respectively [6]. However, macrophages are now understood to adopt a spectrum of phenotypes between the M1- and M2-polarised states [7]. These macrophage sub-types are non-uniformly distributed in space; M1-like cells dominate over M2-like cells in the shoulder regions of the lesion, and foam cells accumulate near the lipid core [8]. Such heterogeneity is a major obstacle in understanding disease progression; the variation in macrophage heterogeneity within lesions and how it is affected by blood LDL and HDL levels remain poorly

understood.

In this DPhil thesis, we use mathematical modelling to investigate how MDM heterogeneity arises and evolves in early atherosclerotic lesions.

1.1 Thesis outline

The thesis consists of two literature review chapters (Chapters 2 and 3), in which we survey the biological and mathematical modelling literature for atherosclerosis, and four research chapters (Chapters 4-7), in which we propose new differential equation models for early atherosclerosis. We derive a lipid-structured model in Chapter 4, a phenotype-lipid structured model in Chapter 5, a spatially resolved lipid-structured model in Chapter 6, and a spatially resolved phenotype-lipid structured model in Chapter 7. We provide further details below.

In **Chapter 4**, we formulate a model for early atherosclerosis in which the MDM population is structured according to lipid content. The key features of this model are that MDMs have a finite capacity for lipid and that their rate of lipid uptake depends on their available capacity. The model analyses, which include time-dependent numerical solutions and asymptotic analysis of the unique steady state solution, indicate that lesion composition is sensitive to the influx of LDL lipid relative to HDL capacity. The MDM lipid distribution evolves in a wave-like manner towards an equilibrium profile. The qualitative form of this equilibrium profile depends non-linearly on the LDL and HDL influxes; in general, lesions with an unhealthy LDL to HDL balance give rise to distributions with local maxima near the MDM lipid capacity, while distributions with healthy LDL to HDL balances may be monotone decreasing, quasi-uniform, or attain local maxima at low lipid loads.

In **Chapter 5**, we extend the model of Chapter 4 to account for changes in MDM phenotype. MDM phenotype is incorporated via an additional structure variable/index, representing the spectrum of values between M1 and M2 polarisation states. We use the model to investigate the distribution of MDM phenotype, its correlation with MDM lipid content, and relation to the densities of LDL and HDL in the blood. The model reduces to a simpler, closed subsystem whose analysis shows how lesion composition becomes more pathological as the blood density of LDL increases relative to HDL capacity. Steady state analysis indicates that the MDM phenotype distribution always attains a local maximum, while the lipid content distribution may be unimodal, adopt a quasi-uniform profile or decrease monotonically. We also use asymptotic analysis to derive a power law relationship between MDM phenotype and lipid content at steady-state. This relationship enables us to understand why, for example, lipid-laden MDMs have a more inflammatory phenotype than lipid-poor MDMs when blood LDL lipid density greatly exceeds HDL capacity.

In **Chapter 6**, we extend the lipid-structured model of Chapter 4 to account for spatial heterogeneity. Motivated by images of macrophages and lipids in human coronary arteries [9], we introduce a spatially non-uniform LDL retention capacity to capture the

early retention of LDL deep in the intima, and allow MDM lifespan and mobility to depend on lipid content. For simplicity, we assume MDMs undergo unbiased random motion. Our results indicate that if MDM mobility is highly sensitive to lipid content, and MDM lifespan is insensitive to lipid content, then our model qualitatively reproduces the densities reported in [9]. Allowing MDM lifespan to decrease with lipid content results in fewer lipid-laden MDMs in the lesion and a reduced mean MDM infiltration depth. Allowing MDM mobility to decrease with lipid content also reduces the MDM infiltration depth, but increases the proportion of lipid-laden MDMs. We find that MDM lipid content increases with depth in all simulations, regardless of how MDM mobility and lifespan depend on lipid content.

In **Chapter 7**, we combine the models from Chapters 5 and 6 to give a spatially-resolved, phenotype-lipid-structured model. In this setting, the MDM population is coupled to the densities of free LDL lipid, retained LDL lipid, apoptotic lipid, necrotic lipid, HDL efflux capacity, inflammatory mediators and resolving mediators. We use the model to investigate how MDM phenotype varies with spatial depth. Numerical simulations indicate that when LDL lipid dominates HDL capacity in the blood, MDM phenotype becomes more inflammatory with increasing spatial depth. This trend is consistent with observations that (inflammatory) M1-like macrophages are found near the necrotic core in mid-to-late stage lesions.

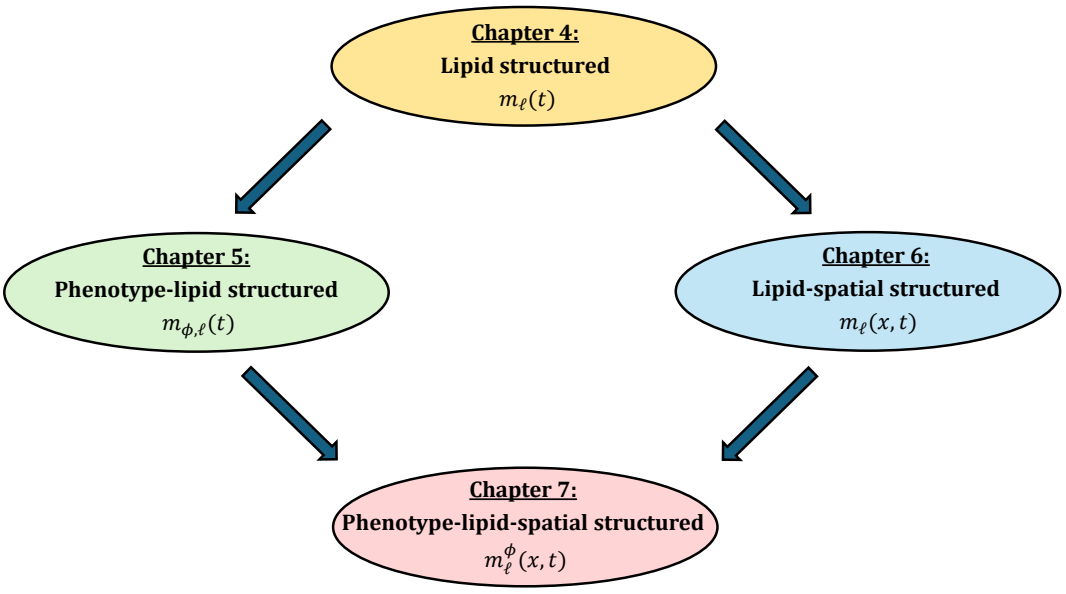


Figure 1.1: **Outline of the research conducted in this thesis.**

The thesis concludes in **Chapter 8**, where we summarise our findings and discuss directions for further investigation.

- The content of Chapter 4 was published in *Mathematical Biosciences* [10].
- The content of Chapter 5 was published in the *Bulletin of Mathematical Biology* [11].

- The content of Chapter 6 will be submitted to the *Journal of Theoretical Biology*, pending copyright clearance.

Chapter 2

Atherosclerotic lesion formation

In this chapter we review the biology associated with atherosclerotic lesion formation. In Sect. 2.1, we explain where atherosclerosis develops and describe the structure of the artery wall. Then, in Sect. 2.2, we describe the key stages of disease progression. Finally, in Sect. 2.3, we detail the components and processes involved in early atherosclerosis. We focus on the role of lipoproteins in the blood, of lipoprotein infiltration and retention in the artery wall, and of monocytes and monocyte-derived macrophages. At the same time, we highlight the processes that give rise to macrophage heterogeneity, which are of particular relevance in this thesis.

2.1 Where do lesions form?

Atherosclerosis can develop in the walls of major arteries throughout the body [12]. The arterial distribution of atherosclerotic lesions is not random, but, rather, localised to susceptible sites where there is disturbed blood flow and low wall shear stress [13, 14]. Such regions include the coronary and carotid artery bifurcations in humans, and the aortic root and arch in mice [15]. Disturbed flow at these sites drives adaptive changes in the artery wall which promote atherosclerosis.

The artery wall consists of a thin outer lining, called the *endothelium*, and three concentric layers: the *(tunica) intima*, *media* and *adventitia* [16]. A schematic is given in Fig. 2.1. The endothelium is a monolayer of endothelial cells that separates the *lumen*, where the blood flows, from the intima. The intima is the innermost layer and highly relevant to atherosclerosis. It is composed of collagen-rich extracellular matrix (ECM), and contains a sporadic distribution of smooth muscle cells (SMCs) [17, 18]. The intima is connected to the media by a fenestrated sheet called the *internal elastic lamina* (IEL). The media itself is dense in SMCs, which are embedded circumferentially in the medial ECM. Finally, the media is separated from the adventitia, the outermost layer, by the *external elastic lamina*. The adventitia is a loose connective tissue, dense in collagen and elastic fibres, that anchors the artery to nearby organs for stability.

Atherosclerosis-susceptible regions of the artery wall that are adjacent to disturbed blood flow are structurally distinct from regions adjacent to laminar flow. First, the intima

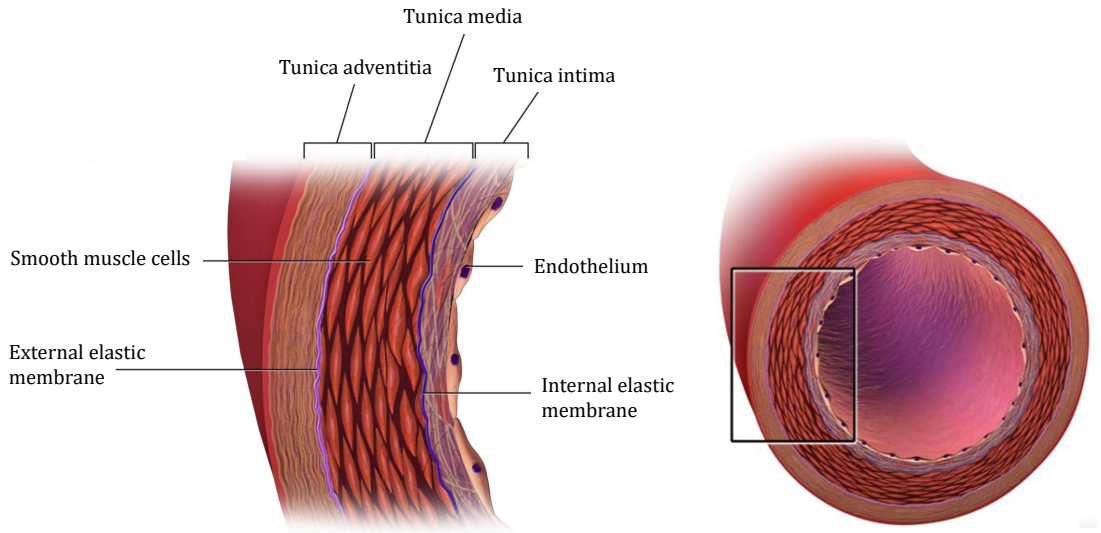


Figure 2.1: **Structure of the artery wall.** The lumen is separated from the artery wall via a thin monolayer of cells called the endothelium. The tunica intima is the deepest layer of the wall and is the region most relevant to atherosclerosis. The intima is connected via the internal elastic membrane to the tunica media, which, in-turn, is supported by the tunica adventitia. Images modified from [19].

in susceptible regions has an augmented capacity for low-density lipoprotein (LDL) retention [20]. LDL retention is a key initiating event in the development of atherosclerosis [21]. In mice, an increased LDL retention capacity has been causally linked to disturbed blood flow via changes to SMC phenotype; disturbed flow up-regulates SMC expression and post-translational modification of LDL-binding proteoglycans [20]. Susceptible regions of human arteries also exhibit increased proteoglycan densities in the intima, suggesting that similar mechanisms are at play [9]. Second, endothelial cells exposed to laminar flow typically elongate in the direction of flow, forming tight junctions between cells that minimise endothelial permeability [22]. By contrast, endothelial cells exposed to disturbed flow adopt non-uniform orientations, with larger junctions and increased permeability. The increased permeability increases the rate of LDL influx from the lumen into the intima, promoting LDL accumulation [23]. Experiments in mice indicate, however, that increased retention capacity rather than endothelial flux is the rate-limiting process for LDL accumulation in the intima [24]. Finally, human artery walls exposed to disturbed flow undergo a further adaptation called *diffuse intimal thickening* (DIT) [25]. DIT refers to an increase in the size of the intima caused by SMC infiltration from the media prior to atherosclerosis. Importantly, DIT is absent in small animals including mice, rats and rabbits [26].

2.2 How do lesions form?

Atherosclerotic lesions form due to the accumulation of lipids and cells in the intima. A summary of the development of atherosclerosis in humans is provided in Fig. 2.2. Several

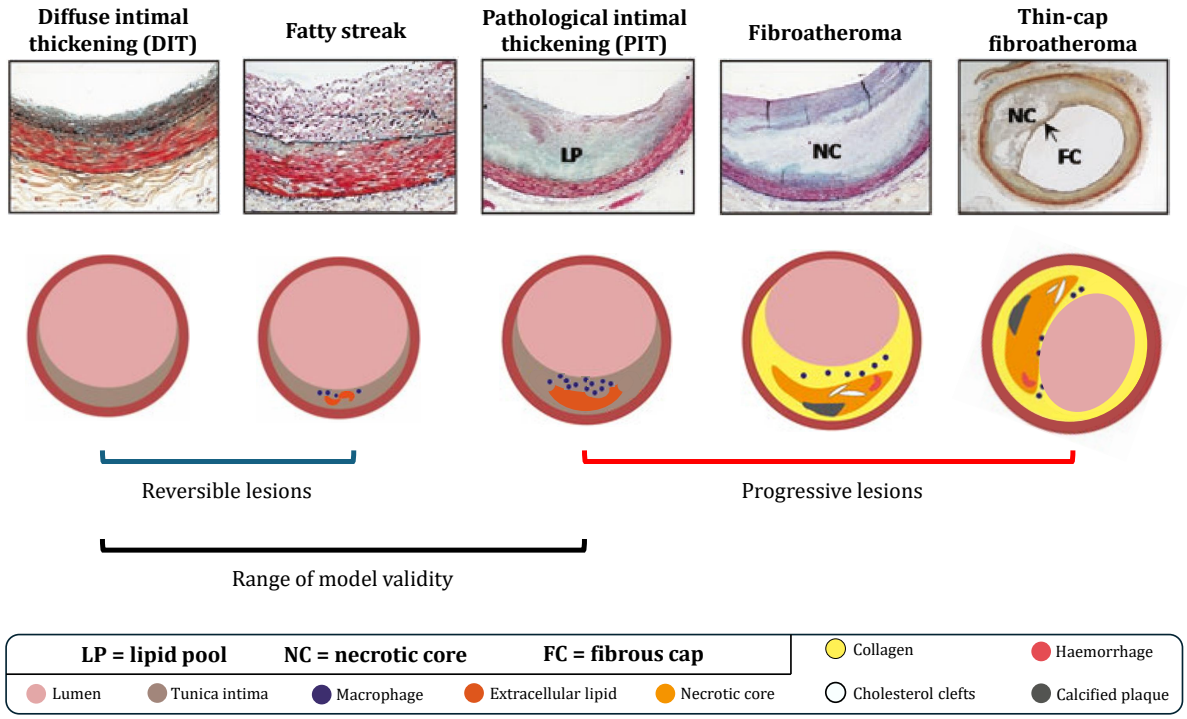


Figure 2.2: **Stages of human atherosclerosis.** Atherosclerosis-susceptible regions first undergo diffuse intimal thickening (DIT). DIT is followed by fatty streak onset, which is characterised by sparse quantities of lipid and macrophages. The lesion then undergoes pathological intimal thickening (PIT), when it develops a pool of extracellular lipids behind a population of macrophages. Late-stage lesions may be classified as fibroatheroma, and thin-cap fibroatheroma, which contain a fibrous cap near the lumen and a necrotic core deep in the intima. The models we develop in this thesis are valid until early PIT, when intimal thickening beyond DIT becomes substantial. Adapted, with permission, by combining Fig. 11.1 of [27] and Fig. 2 of [28].

classification schemes exist for human atherosclerosis. We refer to the Virmani-modified AHA classification in this thesis. As mentioned above, DIT is present prior to disease onset. The earliest lesions, called *fatty streaks*, consist primarily of lipid and MDMs, although both are present in low densities. The lesion does not protrude into the lumen, at this stage, and is reversible. The continued accumulation of lipid and MDMs may cause the lesion to progress to *pathological intimal thickening* (PIT). PIT, considered the first irreversible stage of development, is characterised by a pool of extracellular lipid behind the MDMs. PIT lesions also protrude slightly into the lumen, relative to non-atherosclerotic DIT. Since the mathematical models we develop in this thesis are defined on spatial domains of fixed size, we consider PIT to be the limit of their validity. As time progresses, the lesion may develop into a *fibroatheroma*. At this stage, SMCs begin to accumulate near the endothelium, where they form a fibrous cap. The cap protects the lesion from the blood flow as it protrudes further into the lumen. The intima develops a necrotic core due to the death of lipid-laden MDMs. Cholesterol clefts and haemorrhages may also form in the core. Late-stage fibroatheromas may grow large enough to constrict arterial blood flow. More commonly, however, the fibrous cap begins to thin. *Thin-cap fibroatheromas* are vulnerable to ruptures, which cause the necrotic core material to leak into the lumen where it may cause the blood to produce clots. Blood clots may lead to severe clinical outcomes, including myocardial infarction or stroke, depending on the location of the artery.

For the remainder of this chapter, we focus on early atherosclerosis. We emphasise the processes that give rise to MDM heterogeneity as the lesion develops from DIT, through fatty streak formation, towards PIT.

2.3 Development of early atherosclerosis

Early atherosclerosis is largely driven by interactions between lipoproteins and MDMs. In brief: lipoproteins enter and become trapped within the artery wall; lipoprotein retention triggers a local immune response that attracts monocytes to the lesion from the blood-stream; recruited monocytes rapidly differentiate into macrophages (i.e., MDMs) upon entry, which attempt to ingest the excess lipid in the intima and offload/transport it for clearance. We provide a more detailed picture below.

2.3.1 Lipoproteins in the blood

Lipoproteins are the primary vehicles for lipid transport in the body [29]. They are soluble particles with a central core of cholesteryl esters, cholesterol and triglycerides. The core is surrounded by a phospholipid outer shell which contains an embedded apolipoprotein [30]. Lipoproteins are classed by density: chylomicrons (< 0.95g/mL); very low density lipoproteins ($0.95 - 1.006$g/mL); intermediate density lipoproteins ($1.006 - 1.019$g/mL); low density lipoproteins (LDL) ($1.019 - 1.063$g/mL); and high density lipoproteins (HDL)

(1.063−1.210g/mL). These classes are inhomogeneous and represent a traditional discretisation of the particle density continuum [31]. Of particular relevance to atherosclerosis are LDL and HDL, which, colloquially, carry *bad* and *good* cholesterol, respectively.

Data from genetic and clinical studies consistently demonstrates that LDL plays a causal role in the development of atherosclerosis [34, 35]. International guidelines use blood LDL cholesterol (LDL-C) levels to assess the risk of atherosclerotic cardiovascular disease (ASCVD) [36, 37]. Since blood LDL-C levels depend on lifestyle factors, including diet and exercise [38], there is considerable variation amongst the general population. Typical LDL-C values range from 40-220 mg/dL, which covers over 98% of the 34415 subjects in a South Korean study [32] (see Fig. 2.3 (a)). Another study by Fernández-Friera *et al.* [33] showed that the prevalence of atherosclerosis increases with LDL-C in a population of 4184 subjects with mean age 45.1 years. The mean number of atherosclerotic sites increased from zero at $50 - 60$ mg/dL to greater than one at $150 - 160$ mg/dL. Motivated by these findings, we use total blood LDL lipid density as a key parameter in the mathematical models we develop. This metric accounts for LDL-C in addition to phospholipids on LDL particles, which typically constitute approximately 22% of the particles by mass [39].

Unlike LDL, HDL is considered protective in the context of atherosclerosis [41]. Early clinical studies established a strong inverse association between blood HDL cholesterol (HDL-C) levels and risk of ASCVD that is independent of LDL-C [42, 43]. The protective effect of HDL is typically attributed to its role in *reverse cholesterol transport* (RCT) [41]. Surprisingly, recent clinical trials which attempted to manipulate RCT by elevating HDL-C failed to demonstrate a reduction in ASCVD risk [44–46]. The crux of the issue is the inconsistent relationship between HDL-C and RCT [46]. The search for a consistent metric led to the emergence of HDL cholesterol efflux capacity (HDL cholesterol efflux capacity), which directly measures the ability for HDL particles to promote RCT [47–49]. In their seminal study [40], Rohatgi *et al.* showed that HDL cholesterol efflux capacity was consistently a better predictor of ASCVD than HDL-C in a population-based cohort of 2416 participants (see Fig. 2.4). HDL cholesterol efflux capacity is typically a dimensionless readout which serves as a proxy for the total amount of lipid that HDL particles can accept via RCT. In the mathematical models we develop, this dimensional HDL lipid capacity is a key parameter.

2.3.2 Lipoproteins in the wall

Lipoproteins enter the artery wall, from the lumen, via the endothelium [50]. They enter either by *transcytosis*, in which endothelial cells uptake and transport the lipoprotein across the endothelium, or by diffusion through junctions in regions of disturbed flow. Intimal lipoproteins are subject to numerous modifications that contribute to atherosclerosis. These include oxidation, acetylation, ethylation, methylation and glycation [51]. LDL oxidation has long been considered the main atherogenic modification due to its ability

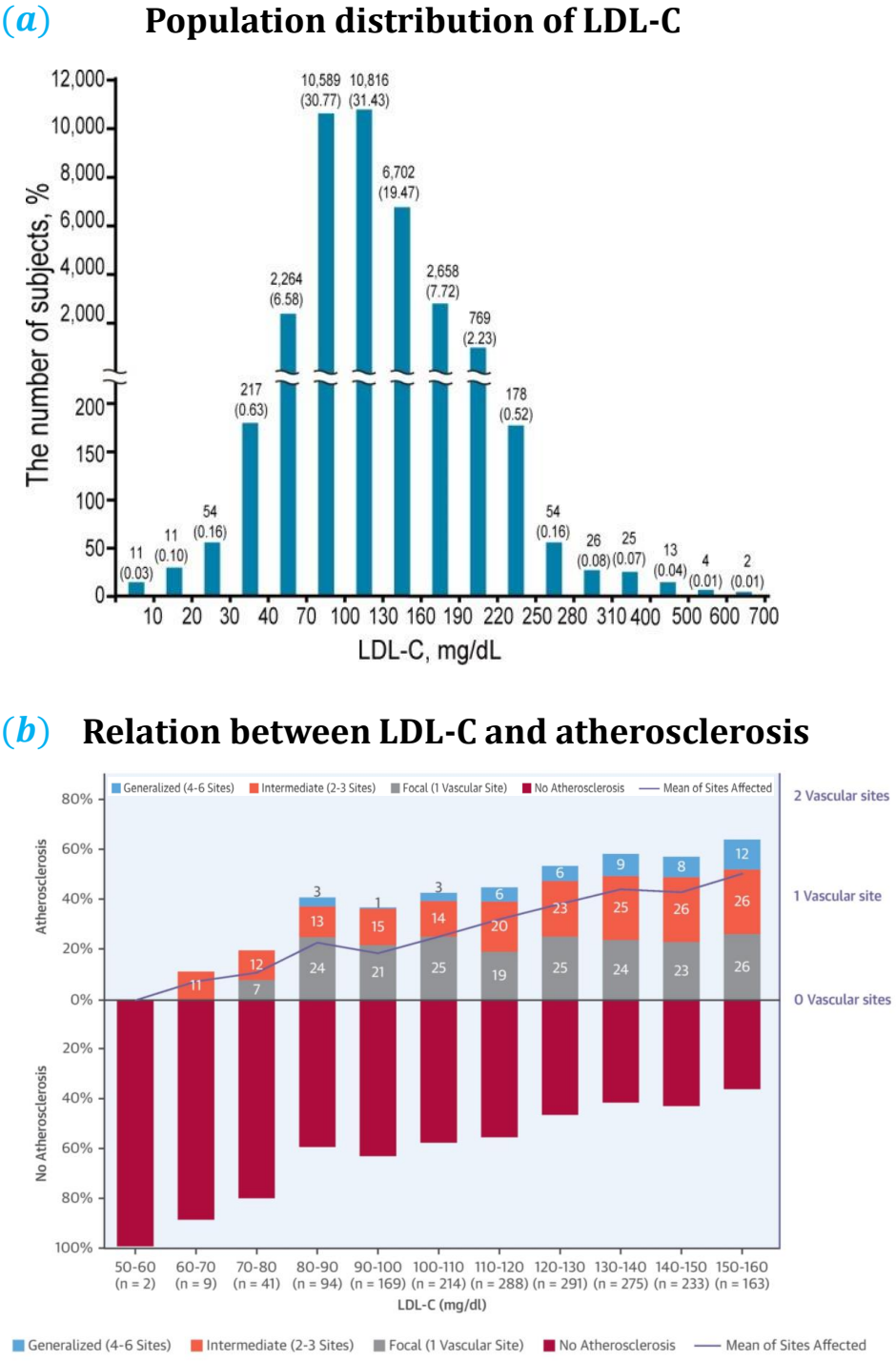


Figure 2.3: **Link between LDL cholesterol (LDL-C) in the population and risk of atherosclerosis.** Plot (a) shows the distribution of LDL cholesterol within a South Korean cohort of 34415 subjects, reproduced with open access from [32]. Plot (b) shows how the prevalence of atherosclerosis depends on LDL-C within a Spanish cohort of 4184 subjects with mean age 45.1, reproduced with open access from [33]. Note the approximately linear increase in the mean number of vascular sites affected by atherosclerosis with LDL-C.

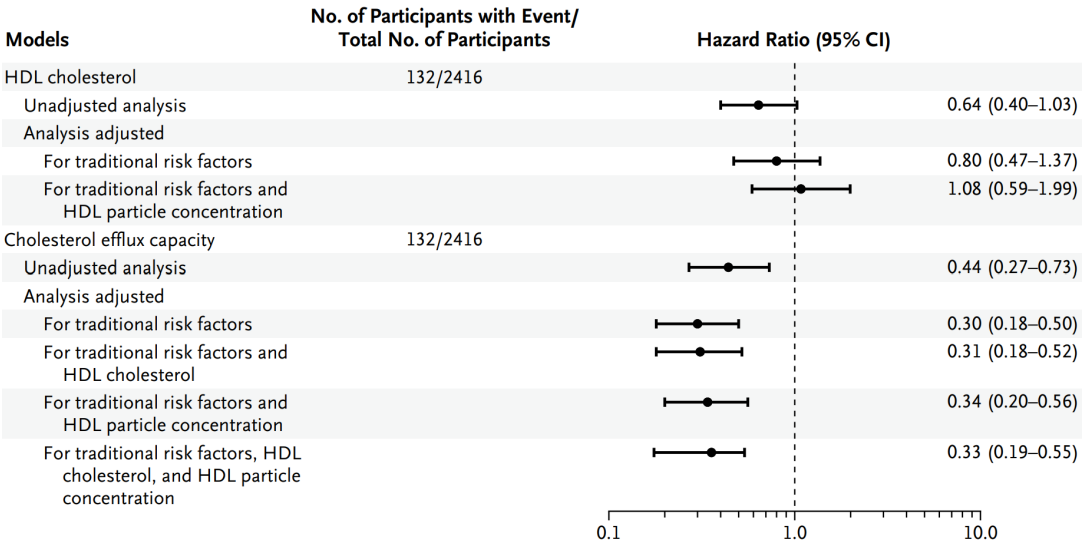


Figure 2.4: **HDL cholesterol efflux capacity is a more consistent predictor of atherosclerosis than HDL cholesterol (HDL-C).** Hazard ratios less than 1 indicate an association with risk of cardiovascular events. Traditional risk factors include older age, male sex, hypertension, diabetes, smoking and family history of ASCVD. Note how the association of cardiovascular events with HDL-C diminished after adjustment for risk factors and HDL particle concentration, while the association for HDL cholesterol efflux capacity is robust. Reproduced with permission from [40], Copyright Massachusetts Medical Society.

to induce SMC apoptosis and activation in both endothelial cells and macrophages [52]. However, a growing body of evidence supports the impact of another form of modification, namely retention and aggregation [53].

Intimal lipoproteins may bind to ECM proteoglycans [21]. LDL retention by ECM dominates retention of HDL due to the markedly lower binding affinity of apolipoprotein E on HDL to apolipoprotein B on LDL [54]. Importantly, ECM-bound LDL is trapped in the intima and, unlike free lipoproteins, cannot exit the intima by diffusing into the lumen, or through the IEL into the media [55]. ECM-retained LDL is also highly susceptible to modification [56]. In particular, LDL is prone to aggregate into ECM-bound lipid droplets that greatly enhance LDL uptake by macrophages [53, 57].

LDL retention is considered to be the key initial event in atherosclerosis [58, 59]. Although the exact signalling pathways remain unclear, interactions between retained LDL and tissue-resident cells (e.g., SMCs and endothelial cells) trigger an inflammatory response that recruits monocytes to the intima from the lumen [60].

2.3.3 Monocytes

Monocytes are a type of white blood cell involved in the innate immune response [61]. They are generated in the bone marrow and released into the circulation when they mature [62]. Monocytes are recruited to atherosclerotic lesions in response to chemokines, such as MCP-1, that are produced by the activated endothelium [63]. The attracted monocytes adhere to and roll across the endothelium in a process mediated by adhesion molecules,

including VCAM-1, before eventually migrating through endothelial junctions into the intima [64].

Once in the intima, monocytes may differentiate into either dendritic cells or macrophages [65]. The relative frequency of dendritic cell to macrophage differentiation *in vivo* is unknown, and depends on the relative amount of macrophage colony stimulating factor to granulocyte-macrophage colony simulating factor [66]. However, *in vitro* models tracking trans-endothelial migration suggest that approximately half of the infiltrating monocytes differentiate into dendritic cells and emigrate from the sub-endothelial space via the endothelium within two days. Monocytes that remain in the sub-endothelial matrix become macrophages [67].

2.3.4 Monocyte-derived macrophages (MDMs)

Monocyte-derive macrophages (MDMs) are typically the most numerous immune cell type in early atherosclerotic lesions [68]. Macrophages are long-lived cells (lifespan of months to years) that specialise in the uptake of extracellular debris, a process called *phagocytosis* [69]. They play a critical and multifaceted role in the development of atherosclerosis [70].

MDMs can play a protective role by ingesting extracellular lipid and removing it from the lesion [71]. Removal may occur via the RCT pathway in which MDMs offload lipid onto HDL particles that subsequently ferry the lipid from the lesion [72]. MDMs can also reduce lesion lipid content by directly emigrating from the intima. In doing so, they remove the lipid they have ingested and their endogenous lipid content from the lesion. Emigration can occur via the endothelium in a process called *reverse transendothelial migration* [73]. Emigration into the media may be possible in mice [73], but is unlikely to occur in early human lesions due to limited MDM infiltration depth [26]. Evidence from swine models indicates that emigration occurs in early lesions but with reduced rates at later stages [74, 75]. The signal pathways that govern MDM emigration remain poorly defined [73, 74].

MDMs can play a pathological role if they die in the intima. Although MDM death may take many forms, including ferroptosis, necroptosis and pyroptosis, the most established pathway linked to atherosclerosis is apoptosis followed by secondary necrosis [76]. Apoptosis is a programmed mode of cell death that is considered vital in normal cell turnover and immune function [77]. In atherosclerotic lesions, MDM apoptosis may be the endpoint of the cell's natural lifespan, or, in lipid-laden MDMs, the result of excess intracellular free cholesterol [78]. Uncleared apoptotic cells undergo secondary necrosis and spill their content into the extracellular space [79]. In this way, MDMs may contribute to necrotic core formation [80].

MDMs in atherosclerotic lesions are also highly heterogeneous and plastic [81]. The functional heterogeneity of lesion MDMs may be partly attributable to diversity in their

monocyte progenitors [82]. However, research on human monocyte subset-dependent differentiation to MDMs is conflicting and without clear consensus [83]. Functional heterogeneity of MDMs is known to be driven by interactions with the lesion microenvironment [7, 84]. In this thesis, we focus on heterogeneity in MDM lipid content, phenotype and spatial position. The microenvironmental interactions that influence these factors are detailed below.

2.3.4.1 Lipid uptake and efflux

Early observations of cell-to-cell variation in MDM lipid content led to the distinction between nascent macrophages and lipid-laden 'foam cells' [85, 86]. Foam cells are a hallmark of atherosclerotic lesions [4]. While this dichotomous classification is diagnostically useful, in practice MDMs exhibit a spectrum of lipid contents due to many lipid uptake and efflux events [74].

MDMs increase their lipid content by ingesting extracellular lipids. The mechanisms of ingestion depend on the particular form of lipid. First, MDMs uptake free-diffusing native and modified LDL via *fluid-phase pinocytosis* [87]. During pinocytosis, macrophages ingest extracellular fluid and any LDL contained in that fluid in a receptor-independent manner [88]. MDMs also ingest the aggregated LDL trapped in the intima via receptor-mediated mechanisms including *phagocytosis* and *patocytosis* [89]. Importantly, uptake of aggregated LDL is much more efficient than uptake of free-diffusing LDL (even when the latter is oxidised) [57, 90]. MDMs may also ingest lipid-rich cellular debris. This includes uptake of apoptotic bodies, a process called *efferocytosis*, and uptake of necrotic debris via phagocytosis. While efferocytosis of whole apoptotic bodies has been observed *in vitro*, studies *in vivo* often report piecemeal uptake by multiple cells [91]. Efferocytosis is also known to become defective in atherosclerotic lesions, although the precise mechanisms remain unclear [92]. Experimental studies nonetheless indicate that uptake of apoptotic debris is more efficient than uptake of necrotic debris [93]. Finally, experimental studies show that macrophages in environments with excess debris typically do not engulf material to the point of lysis. Rather, they adjust their rate of uptake in a manner commensurate with their available capacity, according to mechanical and biochemical negative feedback mechanisms [94].

MDMs decrease their lipid content via lipid efflux to HDL particles [95]. MDM lipid efflux is mediated by the ATP-binding cassette transporters ABCA1 and ABCG1 [96]. ABCA1 and ABCG1 transport phospholipids and cholesterol to lipid domains on the MDM surface, where they are offloaded onto HDL particles [97]. The expression of ABCA1/G1 is up-regulated by the activation of liver and retinoid X receptors, which, in turn is driven by accumulation of intracellular lipid [98].

2.3.4.2 Phenotypic modulation

Recent studies have demonstrated cell-to-cell variation in MDM phenotype. This has led to the distinction between inflammatory M1-like and resolving M2-like cells [7]. M1-like MDMs predominate in progressive lesions, while M2-like cells are enriched in regressing lesions [6]. This dichotomous classification is now considered overly simplistic, and MDMs are typically understood to reversibly adopt a spectrum of phenotypes between M1- and M2-polarised states according to the balance of (pro-)inflammatory and resolving mediators [7, 99].

MDMs modulate towards an M1-polarised state in response to inflammatory mediators. Production of inflammatory mediators is partly driven by interactions between MDMs and LDL. For example, MDM uptake of oxidised LDL results in secretion of TNF via a vimentin-NFκB pathway [100], and IL-1 via inflammasome activation [101]. Native LDL may also induce inflammatory mediator production in MDMs [102]. Secondary necrosis is another important source of inflammatory mediators [79]. The loss of cell membrane integrity during this process causes leakage of damage-associated molecular patterns (DAMPs) that activate MDMs [103]. Finally, M1-like MDMs can sustain inflammatory mediator production (even in the absence of stimulants) that can stimulate neighbour cells [104, 105].

MDMs modulate towards an M2-polarised state in response to resolving mediators. Production of resolving mediators is partly driven by MDM efferocytosis, which stimulates the emission of RvD1 and IL-10 among other products [106, 107]. MDM interactions with HDL also stimulate production of resolving mediators LXB_4 and RvE2 [108]. Although the mechanisms are incompletely understood, the anti-inflammatory effects of HDL on MDMs are at least partly mediated by lipid efflux [109]. Finally, M2-like MDMs can maintain resolving mediator production (even in the absence of stimulants) that can stimulate neighbour cells [104, 105].

2.3.4.3 Spatial movement

MDMs are also heterogeneous in terms of their location in the lesion. The mechanisms that govern MDM motion *in vivo* are incompletely understood [68]. Observations in early human lesions show that MDMs are initially sparsely distributed near the lumen upon fatty streak onset, and accumulate towards the middle of the intima during PIT [9]. Images of late PIT and fibroatheroma suggest that MDMs fail to infiltrate into the media and remain localised to the intima interior [110]. Consistent with these observations, bead-tracking studies in mice also indicate that MDMs have a limited depth of infiltration into the intima, and may become largely immobile in both progressing and regressing lesions [68]. Importantly, the role of lipid accumulation and phenotype in MDM positional dynamics is largely unexplored. Given that MDMs deeper in the intima are typically lipid-laden [110], and adopt an M1-like phenotype at later stages [111], MDM lipid content and phenotypic heterogeneity may play a key role in explaining the spatial

position of lesion MDMs.

Conclusions. In this chapter we have surveyed the biological literature on atherosclerosis. We presented an overview of where lesions form in arteries, the main stages of disease progression and a detailed summary of the roles of lipoproteins and monocyte-derived macrophages in early lesions. In the following chapter, we turn instead to the mathematical literature on atherosclerosis.

Chapter 3

Mathematical models of atherosclerosis

In this chapter we survey the current literature on the mathematical modelling of atherosclerosis. We review mechanical models in Sect. 3.1, before discussing well-mixed ODE models in Sect. 3.2 and spatially-resolved models in Sect. 3.3. Spatially-resolved formulations include reaction-diffusion-taxis PDE models, multiphase mixture PDE models and stochastic models. Finally, we survey the literature on structured population models in Sect. 3.4. Due to their relevance to this thesis, we first outline the broader literature concerning structured modelling before discussing their application to atherosclerosis.

3.1 Mechanical models

The earliest mathematical models related to atherosclerosis focus on blood flow in vulnerable arterial regions [112–114]. These studies treat blood as a non-Newtonian fluid, using modified forms of the Navier-Stokes equations to account for its shear rate-dependent viscosity. The arteries are considered rigid and the models are typically solved numerically with the finite element method (FEM). We highlight the work of Perktold *et al.* [112], which predicts the distributions of mechanical stress in human carotid artery bifurcations under pulsatile flow. These models predict the existence of zones of reversed flow near arterial bifurcations characterised by low flow velocity gradients, and, consequently, low wall shear stress. Misra *et al.* show that analytical progress on small-amplitude wave propagation in blood is also possible in straight geometries [113]. More recent blood flow models have considered realistic geometries derived from MRI images of carotid arteries [115, 116]. Their analysis indicates that longitudinal fibrous cap stresses may inform assessments of plaque vulnerability.

Several fluid mechanical models focus on the deposition of LDL in the artery wall [117–120]. These models couple blood flow to an advection-diffusion equation for LDL concentration. The work of Wada *et al.* [117], which considers only lumenal flow of LDL, predicts that regions of greater LDL concentration at the lumenal wall (i.e., the endothelium) generally co-localise with regions of low wall shear stress. Other studies

explicitly treat the sub-endothelial transport of LDL by modelling the artery wall as a porous medium [118–121]. These models consider porosity-dependent inhibition of LDL movement in the wall to account for collisions between LDL and tissue, but neglect LDL-proteoglycan binding. We highlight the work of Yang and Vafai, who identified wall thickness, curvature and lumen area as important factors for LDL accumulation in a numerical FEM study with pulsatile blood flow [119]. They further derived analytical solutions for a straight arterial geometry where the impact of pulsatile flow can be neglected [120].

More recent mechanical studies have focused on the response of the artery wall to atherosclerotic growth [122–124]. These models adopt a morphoelastic approach, decomposing the wall stress tensor into a growth component and an elastic component. The wall is treated as an incompressible and anisotropic hyperelastic solid. Fok first considers a radially symmetric response to intimal growth [122]. The study reproduces the lumen area-preserving compensatory enlargement observed in human coronary arteries, known as Glagov remodelling [125]. Fok and Gou subsequently treat asymmetric growth in a detailed FEM study [123]. Their model predicts that curvature oscillations in the endothelium are unstable and amplify with growth, and that stresses migrate from the endothelium to the media, so that the latter eventually bears maximum stress. Thon *et al.* attempt a multi-physics treatment in which a morphoelastic model of the artery wall is coupled to non-Newtonian blood flow [124]. However, their model only permits growth in the lumenal direction, which is inconsistent with Glagov remodelling.

In general, the detailed treatment of stresses in mechanical models is balanced by a simplistic treatment of cellular processes. An increasing appreciation of atherosclerosis as an inflammatory response has stimulated the development of many phenomenological models that account for interactions between intimal cell populations, in particular MDMs, signalling molecules and lipids.

3.2 Well-mixed ODE models

Ordinary differential equations (ODEs) are ubiquitous in mathematical biology due to their analytical tractability. They have been used to study numerous features of the early inflammatory response.

Several ODE models focus on MDM recruitment and subsequent lipid accumulation [126–129]. There are three main approaches which differ in their treatment of MDMs. The first, introduced by Ougrinovaskaia *et al.*, considers a three compartment model for the densities of LDL, MDM capacity for LDL, and internalised lipid content [126]. MDM capacity is sourced in response to LDL accumulation at a basal rate, representing direct interactions between endothelial cells and LDL, and an additional rate that increases with existing MDM capacity to account for MDM signalling. Using bifurcation analysis, they conclude that lesion instability is driven primarily via MDM signalling, rather than increased LDL influx. This model was later extended by Cohen *et al.* to account

for MDM emigration and lipid efflux to HDL [128]. Analysis of the more detailed phase plane indicates that efflux to HDL can stabilise the internalised lipid content in the lesion, but emigration is required to stabilise MDM capacity. While the explicit use of MDM capacity in the above models allows for a natural representation of LDL uptake, an obvious drawback is that it is difficult to extract information on cell densities in their formulation. A second approach, taken by Bulelzai *et al.*, avoids this issue by including separate compartments for MDMs and foam cells [127]. Through numerical simulations, they show that their model exhibits bistability between a physically realistic state, and a state of infinite growth if LDL intake is too high. Although cell densities are explicit in their model, the distinction between MDMs and foam cells is an arbitrary binarisation of the gradual lipid accumulation that occurs in real lesions. In a recent approach, Lui and Myerscough consider separate compartments for MDM density and lipid content [129]. Using separation of timescales, they show that necrotic lipid may slowly accumulate even when MDMs, apoptotic lipid and LDL lipid appear to have reached equilibrium. Their formulation is a simplification of the lipid-structured population models that we outline in Sect. 3.4.

An ODE model by Bezyaev *et al.* accounts for MDM phenotype [130]. The authors decompose the MDMs into compartments for M1 (inflammatory), M2 (resolving) and foam cells. While the framework is promising, their results are limited to a phase plane analysis for an idealised case where most species are zero. Moreover, in contrast to the biological literature [7, 83, 84], MDM phenotype is assumed to be fixed upon entry to the lesion and reflective of monocyte class.

We finally note that the majority of ODE models for atherosclerosis are qualitative, due to the scarcity of *in vivo* data. An exception is the study of Thon *et al.* [131]. In this work, the authors use the method of least squares to fit three sub-models to *in vitro* data. The experiments considered LDL modification and uptake, HDL protection against LDL modification, and intracellular cholesterol processing and RCT. Although an important step towards quantitative *in vivo* modelling, their uncertainty analysis is limited to a local sensitivity calculation. Since parameter values are also likely to vary considerably between *in vitro* and *in vivo*, it is unclear how relevant their estimates are for real lesions. More work is needed to derive parameter estimates that are relevant to atherosclerotic progression *in vivo*. Two structured ODE models based on *in vitro* data have also been proposed [132, 133]. We consider them in more detail in Sect. 3.4.

3.3 Spatially-resolved models

Spatially-resolved models of atherosclerosis may be broadly categorised into reaction-diffusion PDE models, multiphase mixture PDE models and agent-based/PDE hybrid models. We survey each of these model types below.

3.3.1 Reaction-diffusion-taxis PDE models

Reaction-diffusion-taxis PDE models are the most common type of mathematical model for atherosclerosis. They have focused on early stage processes, such as the interaction between lipids and MDMs [134–143], and mid-to-late stage processes like necrotic core formation [144, 145].

Reaction-diffusion-taxis models have been posed on a variety of domain geometries. Several models use a fixed one-dimensional domain which spans the endothelium to the internal elastic lamina [141, 142, 146]. Other models are defined on a fixed 2-dimensional domain, which may represent a cross-section of the artery perpendicular to the blood flow [144] or contain one axis along the direction of flow and another perpendicular to it (e.g., radial from the lumen centre) [134, 138]. Models posed on a growing 2-dimensional domain have also been proposed, with models by Hao and Friedman on a cross-sectional domain perpendicular to blood flow [139, 140], and a model by Calvez *et al.* with an axial coordinate [136]. For simplicity, these growing 2-dimensional models only consider the endothelium to be a free boundary. As a result, model lesions grow inwards and constrict the lumen at early stages, which is inconsistent with Glagov remodelling [125]. A model by Thon *et al.* considers a three-dimensional fixed domain using the FEM [143]. Their results indicate negligible variation in cell densities along the radial coordinate, presumably because they assume an intima-media thickness of 0.04mm, which is considerably smaller than estimates of human physiology [9].

Reaction-diffusion-taxis models also vary considerably in their treatment of MDM movement. Several studies assume that MDM motion is random and can be modelled using a diffusion term [134, 135, 138, 146]. Other studies assume that MDM motion may be biased in response to gradients of chemokines (i.e., chemotaxis) [137, 139, 140], or gradients of modified LDL (modLDL) [141, 142, 144]. We note that MDM taxis towards modLDL is speculative, but consistent with macrophages chasing live bacteria phagocytic targets [147]. In a separate study, Calvez *et al.* view the intima as a porous medium and assume that MDMs may be advected by sub-endothelial flow [136]. This effect is not analysed in detail, but is anticipated to transport MDMs along the axial direction in the intima.

Finally, we note that in reaction-diffusion-taxis models a binary distinction is made between lipid-poor "macrophages" and lipid-laden foam cells. As a result, loss of MDM mobility with lipid content is either ignored [139, 140] or incorporated in a simplistic manner by assuming that foam cells are immobile [141, 142]. Additionally, a binary distinction is made between (inflammatory) M1 and (resolving) M2 cells [140, 148]. In Chapters 6 and 7, we relax these assumptions by introducing a more nuanced treatment of MDM heterogeneity in spatially-resolved settings.

3.3.2 Multiphase mixture PDE models

A multiphase framework has also been used to develop spatially-resolved PDE models for atherosclerosis [149–152]. PDEs govern the time evolution of the volume fractions for each phase. These equations are derived by employing principles of mass conservation, momentum conservation and other phenomenological or constitutive relations. Although the multiphase framework provides a means to incorporate mechanical feedback, multiphase models of atherosclerosis have focused primarily on cell-ECM interactions [149, 150] and cell-lipid interactions [151, 152]. Hence, we survey them here instead of in Sect. 3.1.

Recent models by Ahmed *et al.* consider the role of MDMs in early lesions [151, 152]. Their three-phase model for MDMs, modLDL and dead cellular material, highlights the importance of efferocytosis in modulating the amount of dead material in the lesion. They incorporate a free boundary at the internal elastic lamina so that early lesion growth pushes into the media rather than the lumen, consistent with Glagov remodelling [125]. In their later seven-phase model they distinguish between an MDM phase, $m(x,t)$, and an intracellular lipid phase, $a(x,t)$ [152]. This distinction allows them to define an MDM lipid content fraction, $\overline{a} := a/(m+a)$, which they use to indirectly account for lipid-dependent MDM death and emigration rates.

Multiphase models have also been developed by Watson *et al.* to treat fibrous cap formation in mid-to-late stage lesions [149, 150]. Both models consider a matrix-producing smooth muscle cell phase, and use net mass-conservative source and sink terms so that fixed boundary conditions may be imposed.

3.3.3 Stochastic models

Stochastic models for atherosclerotic lesion formation are increasing in number. The literature includes agent-based modelling [153, 154], hybrid cellular automata/PDE models [155, 156], and a stochastic PDE model [148].

Of particular relevance is the study by Liu *et al.*, which accounts for MDM phenotype switching [148]. The authors make a binary M1/M2 distinction between MDM phenotypes and assume that switching may occur at each timestep with a probability that depends on the local concentration of oxidised LDL. Higher levels of oxidised LDL increase the likelihood of switching from M2 to M1 and decrease the probability of switching from M1 to M2. This approach captures the inflammatory effects of LDL but neglects the impact of necrosis, HDL and efferocytosis. We consider a more detailed treatment of MDM phenotype in Chapters 5 and 7, albeit in a deterministic setting.

3.4 Structured population models

Structured population models are a natural means to account for the time-evolution of heterogeneous populations. As the primary framework for the models we develop in Chap-

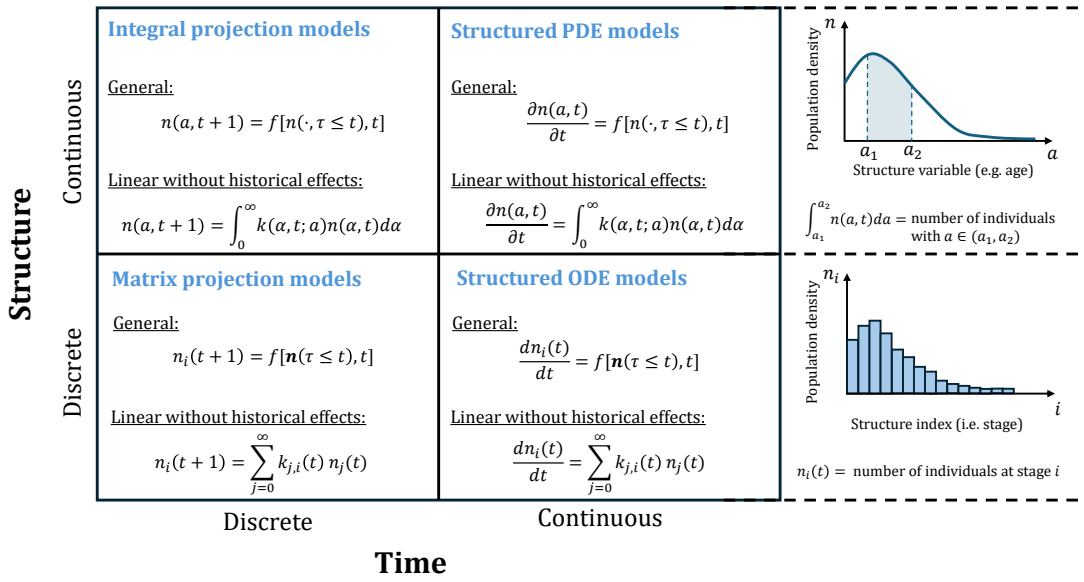


Figure 3.1: **Classification of structured population models.** Models with a continuous structure variable, a, are formulated in terms of a continuous population density, $n(a,t)$. They may update in discrete time, as for integral projection models, or continuous time, as for structured PDE models. Models with a discrete structure index, i, are cast in terms of a discrete density, $n_i(t)$. These may proceed in discrete timesteps, as for matrix projection models, or in continuous time, as in structured ODE models.

ters 4, 5, 6 and 7, we first survey the broader literature concerning structured modelling before discussing their application to atherosclerosis.

3.4.1 Discrete vs. continuous structures

Structured population models can be broadly categorised according to their treatment of structure and time. A summary is provided in Fig. 3.1.

Many structured models update in discrete timesteps (comprehensively reviewed in [157, 158]). These are called projection models. Early projection models, popularised by Leslie *et al.* in their 1945 seminal paper [159], typically use a discrete structure index to decompose the population into age classes. Although nonlinear [160] and delay [161] projection models have been considered, the vast majority of projection models are linear and depend on the current time only [157]. This allows the evolution of the state vector, $\mathbf{n} = (n_0, n_1, \dots)^T$, to be computed by repeated multiplication of a (possibly infinite) Leslie matrix, with components $k_{j,i}$ in the notation of Fig. 3.1. Several recent projection models consider a continuously structured population instead (reviewed in [158]). Such models are called integral projection models since the continuous analogue of the Leslie matrix, assuming linearity, is an integral operator. The integral kernel, $k(\alpha, t; a)$, captures the contribution of individuals with structure value α at time t to the production of individuals with structure value a at time $t+1$. Since we do not consider discrete time evolution in this thesis, we focus the remainder of this review on continuous time structured models.

Structured population models in continuous time are formulated in terms of differential equations. Discretely structured models are cast as ODE systems, and continuously structured models are written as PDEs. In the context of population ageing, discrete stage-structured models are considerably more popular than continuous age-structured models [162]. One structured ODE model relevant to atherosclerosis is provided by Cobbold *et al.*, who consider LDL oxidation in various *in vitro* settings [132]. In their most basic formulation, the authors partition LDL particles into 8 classes according to the number of non-oxidised vitamin E molecules on each LDL particle ($L_0(t), \ldots, L_6(t)$), and whether the LDL particle has been oxidised ($L_{\text{ox}}(t)$). LDL oxidation may only occur once all vitamin E molecules have been oxidised. The ODEs are given by:

$$\frac{dL_{\text{ox}}}{dt} = k_{\text{e}0} R L_0, \tag{3.1}$$

$$\frac{dL_i}{dt} = k_e R(L_{i+1} - L_i) - \delta_{i,0} k_{\text{e}0} R L_0, \qquad \text{for } i = 0, \ldots, 6, \tag{3.2}$$

$$\frac{dR}{dt} = p_r - k_e \sum_{i=1}^{6} L_i - k_{\text{e}0} R L_0, \tag{3.3}$$

where $L_7(t) \equiv 0$, $\delta_{i,0}$ is the Kronecker delta, and p_r is a source of oxidising free radicals, $R(t)$. The local coupling of L_i to the neighbour class L_{i+1} creates an advective flux that captures the gradual change as free radicals oxidise the vitamin E molecules and, finally, lipid core of the LDL particles. A structured ODE model has also been proposed by Ford *et al.* to study bead accumulation in macrophages via efferocytosis [133]. The authors propose the following ODEs:

$$\frac{d\phi_n}{dt} = \eta \sum_{n'=0}^{n} \phi^{\times}_{n'} \phi_{n-n'} - \eta \phi_n \sum_{n'=0}^{\infty} \phi^{\times}_{n'} - \beta \phi_n, \tag{3.4}$$

$$\frac{d\phi^{\times}_n}{dt} = \beta \phi_n - \eta \phi^{\times}_n \sum_{n'=0}^{\infty} \phi_{n'}, \tag{3.5}$$

where $\phi_n(t)$ and $\phi^{\times}_n(t)$ respectively represent the number of live and apoptotic macrophages carrying $n \geq 0$ beads at time $t \geq 0$. The constants β and η denote the rates of apoptosis and efferocytosis, respectively. By contrast to the LDL oxidation model [132], Eqs. (3.4) and (3.5) exhibit non-local dependence in the structure index, n, due to the treatment of efferocytosis as a whole-cell engulfment process of the form: $\phi_n + \phi^{\times}_{n'} \to \phi_{n+n'}$. This non-local dependence promotes more rapid formation of highly bead-laden cells.

The earliest continuous time structured model is the age-structured model proposed by Sharpe and Lotka in 1911 [163]. We note that structured PDE models are seldom written in the integral form presented in Fig. 3.1, which we introduce for comparison with integral projection models. Typically, the time-evolution of $n(a,t)$ is governed by a local dependence on a for which the kernel takes the form:

$$k(\alpha, t; a) := \delta'(\alpha - a) v(\alpha, t) - \delta(\alpha - a) \beta(\alpha, t), \qquad \text{for all } \alpha, a, t > 0, \tag{3.6}$$

where δ is the Dirac-delta distribution, and $v(\alpha, t)$ and $\beta(\alpha, t)$ are continuous functions. The kernel (3.6) yields the following advection-type PDE for $n(a, t)$:

$$\frac{\partial n}{\partial t} + \frac{\partial}{\partial a}\Big[v(a,t)n\Big] = -\beta(a,t)n, \qquad \text{for all } a, t > 0. \tag{3.7}$$

The velocity $v(a, t)$ represents the rate at which individuals change their structure value. It can represent the rate of continuous accretion in mass-structured models, growth in size-structured models [164] and lipid uptake/efflux in lipid-structured models [10, 165, 166]. For age-structured models we have $v(a, t) \equiv 1$, since ageing occurs at the rate of time evolution [163, 167, 168]. The term $\beta(a, t)$ represents the rate at which individuals of structure value a leave the system. Eq. (3.7) is typically coupled to a boundary condition of the form

$$v(0,t)n(0,t) = \mu(t), \tag{3.8}$$

which represents birth of individuals with age 0 at rate $\mu(t)$. We note that Eqs. (3.6)-(3.8) are not all-encompassing. For instance, non-local dependencies have been introduced to capture cell division in size and lipid-structured models [10, 164]. Diffusion in the structure variable is also used to model phenotype change due to random mutations in evolutionary models [169, 170]. Interestingly, structure diffusion also arises when taking a continuum limit of a discretely structured model [171].

3.4.2 Multi-structured and spatially-resolved models

Structured population models may be extended to account for multiple structures and spatial resolution. We discuss these extensions briefly below.

Several models partition the population using multiple structure variables (reviewed in [172]). The literature includes models with two continuous structure variables [173–175], a model with one continuous and one discrete structure [176], and a model with two discrete structures [177]. In these models, the continuous structures are treated using a mixture of local advection and non-local integral terms, while the discrete structures are treated using neighbour interactions. We contribute to this literature in Chapters 5 and 7, where we consider a dual-structured MDM population resolved in lipid content and phenotype. We convert from a discrete formulation to a continuum one for analytical tractability.

Structured population models may also be spatially resolved [178–183]. Spatial movement is generally treated as it is in reaction-diffusion-taxis models, by including terms that account for diffusion and directed motion. Movement may be independent of structure, as in [180], or coupled to the structure variable (e.g., Fiandaca *et al.* consider phenotype-dependent cell speeds [179]). We contribute to this literature in Chapters 6 and 7, in which we resolve the MDM population according to spatial distance from the endothelium, and assume that MDM mobility depends on lipid content.

3.4.3 Lipid-structured models in atherosclerosis

Several lipid-structured models were developed prior to this thesis to study lipid accumulation in atherosclerotic lesion macrophages [165, 166, 184, 185]. The earliest study, by Meunier and Muller, focuses on the existence and uniqueness of solutions to a nonlinear renewal system of the form (3.7)-(3.8) [184]. Their model accounts for LDL uptake, but neglects efferocytosis, necrotic uptake and efflux to HDL.

The remaining models are more biologically realistic and share a common integro-PDE-structured framework [165, 166, 185]. They are formulated in terms of a lipid-structured macrophage population, $m(a,t) \geq 0$, apoptotic cell population, $p(a,t) \geq 0$, and a variable for necrotic lipid content, $N(t) \geq 0$. The structure variable, $a \geq a_0$, represents cell lipid content and is assumed to take values above a minimal value, a_0, that represents macrophage endogenous lipid content. The original model by Ford *et al.* takes the form [165]:

$$\frac{\partial m}{\partial t} + \left(\frac{\lambda}{M} + \theta N\right)\frac{\partial m}{\partial a} = \eta \int_{a_0}^{a-a_0} m(a-a',t)p(a',t)da' - \eta P m - (\beta+\gamma)m, \tag{3.9}$$

$$\frac{\partial p}{\partial t} = \beta m - (\eta M + \nu)p, \tag{3.10}$$

$$\frac{dN}{dt} = \eta A_P - \theta M N, \tag{3.11}$$

with an associated boundary condition to account for macrophage recruitment:

$$\left(\frac{\lambda}{M} + \theta N\right)m(a_0,t) = \alpha \frac{A_M - a_0 M}{\Gamma + A_M - a_0 M}. \tag{3.12}$$

Here M and P denote the total density of live and apoptotic macrophages, respectively:

$$M(t) := \int_{a_0}^{\infty} m(a,t)\,da, \qquad P(t) := \int_{a_0}^{\infty} p(a,t)\,da, \tag{3.13}$$

while A_M and A_P denote the total lipid content in each respective population:

$$A_M(t) := \int_{a_0}^{\infty} am(a,t)\,da, \qquad A_P(t) := \int_{a_0}^{\infty} ap(a,t)\,da. \tag{3.14}$$

The model accounts for continuous changes to macrophage lipid content due to LDL uptake and HDL efflux (net rate $\propto \lambda$), and necrotic uptake at rate θ. Efferocytosis is treated via whole cell engulfment at rate η, which gives rise to the non-local convolution in Eq. (3.9). The model further accounts for apoptosis (rate β), emigration (rate γ) and secondary necrosis (rate ν). Using time-dependent numerical solutions and analytical solutions at steady state, Ford *et al.* demonstrate that the macrophage lipid distribution may be monotone decreasing or exhibit multiple local maxima, depending on parameter values. This model was later extended to account for macrophage proliferation, which introduces another non-local term [166], and lipid content-dependent rates of apoptosis, emigration and proliferation [185].

Although insightful, the lipid-structured models discussed above are based on assumptions that warrant further investigation. We detail these issues below:

- **The treatment of LDL uptake and efflux to HDL.** Based on a quasi-steady approximation of LDL and HDL particle densities in the intima, these processes are lumped together and assumed to modulate macrophage lipid content at a constant net rate λ. This makes it difficult to investigate the impact of blood LDL and HDL levels on lesion composition. For instance, the model yields non-physical solutions for $\lambda < 0$, when the rate of HDL efflux exceeds that of LDL uptake. Mathematically, this is because the lipid content advection velocity becomes negative, enabling macrophages to leave the domain through the boundary at $a = a_0$. We address this issue in Chapter 4, where we introduce a lipid content-dependent treatment of efflux and explicitly account for blood LDL and HDL content in Chapters 5-7.

- **The non-local treatment of efferocytosis via whole-cell engulfment.** Although whole cell efferocytosis can be seen *in vitro* [133], efferocytosis *in vivo* often occurs via piecemeal uptake by multiple cells [91, 186]. Moreover, treatment of whole-cell engulfment requires a structured treatment of the apoptotic cells in the lesion. Apoptotic debris is rarely seen *in vivo* due to the rapidity of efferocytosis and secondary necrosis [187, 188], suggesting that this level of detail may be unnecessary. We avoid this issue in our models by assuming that apoptotic and necrotic lipid are both taken up gradually via "nibbling".

- **The treatment of macrophage recruitment.** The above models assume that the MDM recruitment rate increases with the total amount of ingested lipid in the macrophage population, $A_M - a_0 M$ (see Eq. (3.12)); this quantity is used as a proxy for the inflammatory mediator density in the lesion. This formulation is at odds with *in vivo* observations that lipid-laden macrophages may be anti-inflammatory [189] or pro-inflammatory [190], depending on phenotype. We address this issue by explicitly considering mediator densities in our models, which may arise due to lipid retention alone (Chapters 4 and 6), or be influenced by MDM phenotype (Chapters 5 and 7).

- **The extent of the lipid content structure variable.** The lipid-structured models have been cast on an infinite lipid content domain, $a_0 \leq a < \infty$, with uptake rates that are independent of lipid content. This formulation is at odds with observations that macrophages have a finite capacity for lipid accumulation, and modulate their uptake rate in a manner commensurate with available capacity [94]. The models we develop in Chapters 4-7 directly account for this effect. To avoid issues of shock-discontinuities that arise when MDM lipid content velocity becomes negative, we use a discrete ODE structured approach in our models that naturally introduces a diffusive effect that regularises the MDM lipid distribution. To do so, we explicitly consider finite increments of lipid uptake, $\Delta a > 0$, which are assumed infinitesimally small in the PDE-structured models [165, 166, 185].

Conclusions. In this chapter we have surveyed the literature on mathematical models of atherosclerosis. The literature includes mechanical models, well-mixed ODE models, reaction-diffusion-taxis PDE models, multiphase mixture PDE models, stochastic models and structured population models. In the following chapters, we contribute to the literature on structured population models by developing a series of structured models for MDM populations in early atherosclerotic lesions. These models address the limitations of current lipid-structured models outlined above and consider the MDM population in various levels of biological detail.

Chapter 4

A new lipid-structured model

In this chapter, we develop a new lipid-structured model for MDMs in early atherosclerotic lesions. The model uses the principle of mass conservation to couple the dynamics of the lipid-structured MDM population to the densities of extracellular lipid and HDL capacity in the lesion. The model addresses our critique of existing lipid-structured models, detailed in Chapter 3, within a minimalist formulation that serves as the foundation for the more detailed modelling in Chapters 5-7.

4.1 Introduction

MDM lipid content is the product of lipid uptake and efflux events. MDMs increase their lipid load by clearing the extracellular environment of LDL particles (which become modified and susceptible to MDM ingestion upon entry [51]) and cellular debris. In particular, MDMs take up the lipid-rich contents of nearby dead MDMs. This includes lipid ingested by dead cells during their lifetime and also endogenous lipid contained in the membranes of cell corpses. MDMs reduce their lipid burden by offloading lipid onto high-density-lipoprotein (HDL) particles, which also enter the lesion from the bloodstream. The lipoproteins LDL and HDL (which carry 'bad' and 'good' cholesterol, respectively) therefore have opposing effects on MDM lipid content. The impact of blood LDL and HDL levels on overall lesion composition and the distribution of lipid within the MDM population are not completely understood.

The efficiency of lipid uptake and efflux by MDMs is modulated by intracellular signalling [94, 98]. We note first that macrophages have a finite capacity for lipid uptake [94]. More specifically, experimental observations indicate that macrophages surrounded by an abundance of phagocytic targets dynamically regulate their rate of uptake according to the available capacity. This behaviour is the result of physical limitations (e.g., finite cell size) and intracellular biochemical negative feedback signals. Similarly, the efficiency of lipid efflux is also mediated by intracellular signalling [98]. The accumulation of cholesterol is known to activate transcription factors (e.g., Lxrα, Lxrβ) that upregulate the expression of transporters (e.g., ABCA1) which mediate cholesterol efflux to HDL particles. Taken together, the observations above indicate that, on average, heavily lipid-laden

macrophages are less efficient at uptake but more efficient at efflux than macrophages with a lower lipid burden. Many studies also report that macrophage uptake of apoptotic cells (termed *efferocytosis*) becomes defective during atherosclerosis ([92, 191]). The extent to which this defective efferocytosis is attributable to the intrinsic down-regulation of uptake due to lipid loading is not known.

Motivated by the above biological observations, we investigate the following key questions in our analysis:

Q1. **How do the LDL and HDL influx rates impact the model lesion? Specifically:**

   a. How do they impact overall lesion composition?

   b. How do they impact the distribution of lipid in lesion MDMs?

Q2. **Can defective efferocytosis be plausibly attributed to uptake feedback in MDMs due to high lipid loads?**

The model developed in this chapter contributes to the growing body of models that account for gradual lipid accumulation in macrophages via structured population modelling [165, 166, 184, 185]. By contrast, the majority of existing models for atherosclerosis that account for MDM lipid uptake do so by introducing a binary distinction between lipid-poor macrophages and lipid-laden foam cells [127, 136, 141, 142, 192], or by introducing a population lipid capacity for MDMs without explicit formulation of cell densities [126, 128]. The model developed in this chapter is novel in that it accounts for lipid content-dependent rates of lipid uptake and efflux, explicitly tracks the amounts of extracellular lipid and HDL lipid capacity in the lesion, and is based on a discrete structuring of the MDM population. We nonetheless derive a continuum approximation of the discrete model to facilitate analysis of the MDM lipid distribution. This approximation replaces the dynamical equations of the MDM population with an advection-diffusion PDE subject to appropriate boundary conditions.

The remainder of the chapter is structured as follows. Sect. 4.2 describes the model development, including the derivation of an ODE subsystem, non-dimensionalisation and treatment of model parameters. Sect. 4.3 contains the results of our model analysis. We present time-dependent numerical solutions and a steady state analysis of the ODE subsystem and MDM lipid distribution. Finally, in Sect. 4.4, we discuss the results in relation to the above key questions. We also address the limitations of our model and its relation to Chapters 5-7.

4.2 Model development

In this section we present a lipid-structured model for MDM populations in early atherosclerotic lesions. We first outline our assumptions and formulate the model as a coupled system of ODEs. We then show that the model admits a closed subsystem that can be

solved and analysed independently of the full model. Finally we non-dimensionalise the model and outline our treatment of the dimensionless parameters.

4.2.1 Definitions and model statement

We assume for simplicity that macrophages take up and offload lipid in increments of mass Δa, and decompose the MDM population into a series of compartments according to lipid load. Specifically, we let $m_\ell(t) \geq 0$ be the number density of lesion MDMs with lipid content $a_0 + \ell\Delta a$ at time $t \geq 0$. Here a_0 is the mass of endogenous lipid that macrophages contain due to their membrane structure. The index ℓ runs over integer values $\ell = 0, 1, \ldots, \ell_{\max}$, where $\ell_{\max} > 0$ defines the macrophage lipid capacity. It follows that MDMs have a maximal lipid content, $a_0 + \kappa$, where $\kappa := \ell_{\max}\Delta a$ is the maximal capacity of ingested lipid. Finally, we denote by $L(t)$ the density of extracellular lipid, and by $H(t)$ the HDL lipid capacity.

We propose that the MDM population evolves according to the following ODEs:

$$\frac{dm_0}{dt} = \sigma_M \frac{L}{L_c + L} - k_L \ell_{\max} L m_0 + k_H H m_1 - (\beta + \gamma) m_0, \tag{4.1}$$

$$\begin{aligned}\frac{dm_\ell}{dt} &= k_L L\big[(\ell_{\max} - \ell + 1)m_{\ell-1} - (\ell_{\max} - \ell)m_\ell\big] + k_H H\big[(\ell+1)m_{\ell+1} - \ell m_\ell\big] \\ &\quad - (\beta + \gamma)m_\ell, \quad 1 \leq \ell \leq \ell_{\max} - 1,\end{aligned} \tag{4.2}$$

$$\frac{dm_{\ell_{\max}}}{dt} = k_L L m_{\ell_{\max}-1} - k_H \ell_{\max} H m_{\ell_{\max}} - (\beta + \gamma) m_{\ell_{\max}}. \tag{4.3}$$

Eqs. (4.1)-(4.3) account for lipid uptake and efflux via the Law of Mass Action. Lipid uptake is modelled via the reaction:

$$\mathrm{M}_\ell + \Delta a \xrightarrow{k_L(\ell_{\max} - \ell)} \mathrm{M}_{\ell+1}, \qquad \ell = 0, 1, \ldots, \ell_{\max} - 1. \tag{4.4}$$

Here we assume that the rate of lipid uptake decreases linearly with lipid content; it takes its maximal value $k_L\ell_{\max}$ when $\ell = 0$ and decreases to zero at $\ell = \ell_{\max}$ so that MDMs cannot exceed $\ell_{\max}$ units of ingested lipid. Our treatment of lipid uptake is consistent with current understanding that macrophages have a finite capacity for uptake, and that uptake is mediated by intracellular feedback that decreases the uptake rate in a manner commensurate with available capacity [94]. We assume that this decrease in uptake rate is linear for simplicity. Lipid efflux is modelled via the reaction

$$\mathrm{M}_\ell \xrightarrow{k_H \ell} \mathrm{M}_{\ell-1}, \qquad \ell = 1, 2, \ldots, \ell_{\max}, \tag{4.5}$$

so that the rate constant for efflux increases linearly from zero at $\ell = 0$ to its maximal value $k_H\ell_{\max}$ at $\ell = \ell_{\max}$. This formulation is consistent with experimental evidence that intracellular accumulation of lipid leads to the up-regulation of transporters (e.g., ABCA1) that mediate the efflux of lipid to HDL particles [98]. We assume that the increase in offloading rate with lipid load is linear for simplicity.

Eqs. (4.1)-(4.3) also account for MDM recruitment, cell death and emigration. We assume that the rate at which MDMs are recruited to the lesion from the bloodstream can

be described via a first-order Hill function in $L(t)$. The maximal recruitment rate is σ_M and half-maximal recruitment occurs at the value $L = L_c$. We assume that newly recruited MDMs carry only endogenous lipid (corresponding to $\ell = 0$). Therefore, the recruitment source term appears in Eq. (4.1) only. We further assume that MDMs undergo cell death at rate $\beta > 0$ and emigrate from the lesion at rate $\gamma > 0$.

We propose that the extracellular lipid dynamics are governed by

$$\frac{dL}{dt} = \sigma_L + \beta \sum_{\ell=0}^{\ell_{\max}} (a_0 + \ell \Delta a) m_\ell - k_L \Delta a \, L \sum_{\ell=0}^{\ell_{\max}} (\ell_{\max} - \ell) m_\ell - \delta_L L. \tag{4.6}$$

In Eq. (4.6) we assume that extracellular lipid is sourced from the bloodstream at rate σ_L, due to LDL particle influx. We assume further that the lipid content of dying MDMs is transferred to the extracellular space, giving rise to the second source term in Eq. (4.6). The third term accounts for lipid ingestion by MDMs, at a rate proportional to k_L (see reaction (4.4)). Finally, we assume that extracellular lipid is lost to non-MDM interactions (e.g., uptake by the self-renewing population of tissue-resident cells [68]) at a constant rate δ_L, which we assume to be small.

We model the HDL dynamics via the equation

$$\frac{dH}{dt} = \sigma_H - k_H \Delta a \, H \sum_{\ell=0}^{\ell_{\max}} \ell m_\ell - \delta_H H. \tag{4.7}$$

The ODE (4.7) assumes that HDL lipid capacity is sourced at rate σ_H, due to a constant influx of HDL particles from the bloodstream, and lost to MDM efflux at a rate proportional to k_H (according to the reaction (4.5)). The final term accounts for loss of HDL capacity to non-MDM interactions (e.g., lipid efflux by tissue-resident cells) at the constant rate δ_H, which we assume to be small.

We close Eqs. (4.1)-(4.3), (4.6) and (4.7) by imposing the following initial conditions:

$$m_\ell(0) = 0, \quad \ell = 0, 1, \ldots, \ell_{\max}, \qquad L(0) = 0, \qquad H(0) = 0. \tag{4.8}$$

Eqs. (4.8) assume that the lesion is initially devoid of MDMs, extracellular lipid and HDL lipid capacity. We provide a schematic representation of the model in Fig. 4.1.

4.2.2 An ODE subsystem

A closed ODE subsystem can be derived from Eqs. (4.1)-(4.8) by considering the total density of lesion MDMs, $M(t)$, and the total density of intracellular lipid, $L_M(t)$, where

$$M(t) := \sum_{\ell=0}^{\ell_{\max}} m_\ell(t), \qquad L_M(t) := \sum_{\ell=0}^{\ell_{\max}} (a_0 + \ell \Delta a) m_\ell(t). \tag{4.9}$$

Summing Eqs. (4.1)-(4.3), we find that $M(t)$ evolves according to the equation

$$\frac{dM}{dt} = \sigma_M \frac{L}{L_c + L} - (\beta + \gamma) M. \tag{4.10}$$

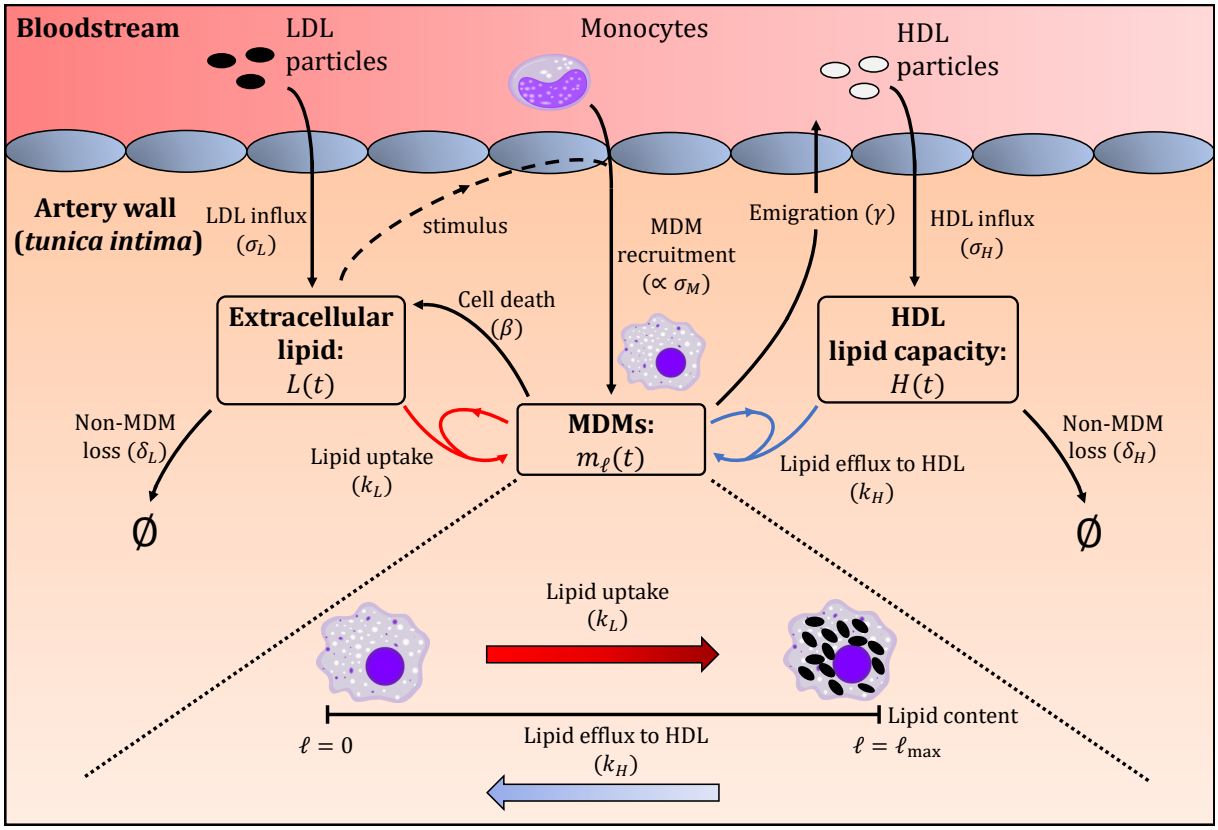


Figure 4.1: **Schematic representation of the model** (4.1)-(4.8)**.** We track extracellular lipid, $L(t)$, the lipid capacity of the HDL particles, $H(t)$, and the number of MDMs, $m_\ell(t)$, with lipid content $a_0 + \ell\Delta a$ ($\ell = 0, 1, \ldots, \ell_{\max}$). Note the opposing effect of LDL vs. HDL particle influx on MDM lipid content. LDL influx provides a source of extracellular lipid and promotes increases to MDM lipid load via lipid uptake. By contrast, the entry of HDL promotes decreases to MDM lipid content via lipid efflux.

Eq. (4.10) reflects our assumptions that lesion MDMs are sourced from the bloodstream at a rate which is an increasing, saturating function of the extracellular lipid load, $L(t)$, and removed via apoptosis and emigration at constant rates β and γ, respectively. By multiplying each of Eqs. (4.1)-(4.3) by $(a_0 + \ell\Delta a)$ for the corresponding index ℓ and then summing, it is straightforward to show that the dynamics of $L_M(t)$ are given by

$$\frac{dL_M}{dt} = a_0\sigma_M \frac{L}{L_c + L} + k_L L\big[(\kappa + a_0)M - L_M\big] - k_H H(L_M - a_0 M) - (\beta + \gamma)L_M. \tag{4.11}$$

Eq. (4.11) shows how intracellular lipid levels increase due to the influx of MDMs from the bloodstream and uptake of extracellular lipid. The rate of uptake across the MDM population is proportional to the quantity $(\kappa + a_0)M(t) - L_M(t)$, which represents the lipid capacity of the MDM population at time t. Intracellular lipid is removed by efflux to HDL, apoptosis and emigration. The rate of lipid efflux across the MDM population is proportional to $L_M(t) - a_0 M(t)$, which is the total amount of ingested lipid (i.e., non-endogenous lipid) in the MDM population.

Using definitions (4.9) we simplify Eqs. (4.6) and (4.7) to obtain

$$\frac{dL}{dt} = \sigma_L + \beta L_M - k_L L\big[(\kappa + a_0)M - L_M\big] - \delta_L L, \tag{4.12}$$

$$\frac{dH}{dt} = \sigma_H - k_H H(L_M - a_0 M) - \delta_H H. \tag{4.13}$$

We note that Eqs. (4.10)-(4.13) define a closed subsystem for M, L_M, L and H, which we solve subject to the following initial conditions:

$$M(0) = 0, \qquad L_M(0) = 0, \qquad L(0) = 0, \qquad H(0) = 0, \tag{4.14}$$

that are obtained from Eqs. (4.8).

4.2.3 Non-dimensionalisation

We recast the model in terms of the following dimensionless variables:

$$\begin{aligned} \tilde{t} &:= \beta t, \qquad & \tilde{m}_\ell(\tilde{t}) &:= \frac{\beta}{\sigma_M} m_\ell(t), \qquad & \tilde{M}(\tilde{t}) &:= \frac{\beta}{\sigma_M} M(t), \\ \tilde{L}(\tilde{t}) &:= \frac{\beta}{a_0\sigma_M} L(t), & \tilde{L}_M(\tilde{t}) &:= \frac{\beta}{a_0\sigma_M} L_M(t), & \tilde{H}(\tilde{t}) &:= \frac{\beta}{a_0\sigma_M} H(t). \end{aligned} \tag{4.15}$$

Under this rescaling, time is measured in units of average MDM lifespan, β^{-1}, and the MDM densities are normalised with respect to $\frac{\sigma_M}{\beta}$, the maximal density of MDMs supplied to the lesion per MDM lifespan. The lipid densities $L(t)$, $L_M(t)$ and the HDL lipid capacity, $H(t)$, are scaled with respect to $a_0\sigma_M/\beta$, which is the maximal density of endogenous lipid entering the lesion per MDM lifespan.

We also define a number of dimensionless parameters in Table 4.1. The first two parameters, $\ell_{\max}$ and κ, are ratios of the MDM lipid capacity to the uptake/efflux increment and endogenous lipid content, respectively. The remaining parameters pertain to

Table 4.1: Dimensionless parameters in Eqs. (4.16)-(4.21)

Parameter	Definition	Interpretation
$\ell_{\max}$	$\frac{\kappa}{\Delta a}$	MDM lipid capacity per unit uptake/efflux increment
$\tilde{\kappa}$	$\frac{\kappa}{a_0}$	MDM lipid capacity per unit endogenous lipid
$\tilde{\sigma}_L$	$\frac{1}{a_0\sigma_M}\sigma_L$	Influx of LDL lipid relative to max. influx of endogenous lipid
$\tilde{\sigma}_H$	$\frac{1}{a_0\sigma_M}\sigma_H$	Influx of HDL capacity relative to max. influx of endogenous lipid
$\tilde{k}_L$	$\frac{a_0\sigma_M}{\beta^2}k_L$	Dimensionless lipid uptake rate
$\tilde{k}_H$	$\frac{a_0\sigma_M}{\beta^2}k_H$	Dimensionless lipid efflux rate
$\tilde{\gamma}$	$\frac{1}{\beta}\gamma$	Dimensionless MDM egress rate
$\tilde{\delta}_L$	$\frac{1}{\beta}\delta_L$	Extracellular lipid loss to non-MDM interactions
$\tilde{\delta}_H$	$\frac{1}{\beta}\delta_H$	HDL lipid capacity loss to non-MDM interactions
$\tilde{L}_c$	$\frac{\beta}{a_0\sigma_M}L_c$	Value of $\tilde{L}$ for half-maximal MDM recruitment

the model kinetics: $\tilde{\sigma}_L$ and $\tilde{\sigma}_H$, determine the rates at which LDL lipid and HDL capacity enter the lesion, respectively; $\tilde{k}_L$ is the dimensionless uptake rate per unit extracellular lipid; $\tilde{k}_H$ is the dimensionless efflux rate per unit HDL capacity; $\tilde{\gamma}$ is the dimensionless emigration rate; $\tilde{\delta}_L$ is the dimensionless rate of extracellular lipid loss to non-MDM effects; $\tilde{\delta}_H$ determines the rate of HDL capacity loss to non-MDM effects; and $\tilde{L}_c$ is the value of $\tilde{L}(\tilde{t})$ at which MDM recruitment is half-maximal.

By applying the scaling (4.15) and the definitions of Table 4.1, and dropping the tildes for notational convenience, we obtain the following dimensionless ODEs for the MDM dynamics:

$$\frac{dm_0}{dt} = \frac{L}{L_c + L} - k_L\ell_{\max}Lm_0 + k_HHm_1 - (1+\gamma)m_0, \tag{4.16}$$

$$\begin{aligned}\frac{dm_\ell}{dt} &= k_LL\big[(\ell_{\max} - \ell + 1)m_{\ell-1} - (\ell_{\max} - \ell)m_\ell\big] + k_HH\big[(\ell+1)m_{\ell+1} - \ell m_\ell\big] \\ &\quad - (1+\gamma)m_\ell, \quad 1 \le \ell \le \ell_{\max} - 1,\end{aligned} \tag{4.17}$$

$$\frac{dm_{\ell_{\max}}}{dt} = k_LLm_{\ell_{\max}-1} - k_HH\ell_{\max}m_{\ell_{\max}} - (1+\gamma)m_{\ell_{\max}}, \tag{4.18}$$

and the following closed subsystem for M, L_M, L and H:

$$\frac{dM}{dt} = \frac{L}{L_c + L} - (1+\gamma)M, \tag{4.19}$$

$$\frac{dL_M}{dt} = \frac{L}{L_c + L} + k_LL\big[(\kappa+1)M - L_M\big] - k_H(L_M - M)H - (1+\gamma)L_M, \tag{4.20}$$

$$\frac{dL}{dt} = \sigma_L + L_M - k_LL\big[(\kappa+1)M - L_M\big] - \delta_LL, \tag{4.21}$$

$$\frac{dH}{dt} = \sigma_H - k_H(L_M - M)H - \delta_HH. \tag{4.22}$$

The initial conditions used to close Eqs. (4.16)-(4.22) are unchanged and stated here for completeness:

$$m_\ell(0) = 0, \quad \ell = 0, 1, \ldots, \ell_{\max}, \qquad M(0) = L_M(0) = L(0) = H(0) = 0. \tag{4.23}$$

In their dimensionless forms, $M(t)$ and $L_M(t)$ are related to the functions $m_\ell(t)$ via the summations

$$M(t) = \sum_{\ell=0}^{\ell_{\max}} m_\ell(t), \qquad L_M(t) = M(t) + \kappa \sum_{\ell=0}^{\ell_{\max}} \left(\frac{\ell}{\ell_{\max}}\right) m_\ell(t). \tag{4.24}$$

4.2.4 Model parameter estimation

In what follows, unless stated otherwise, we use the following dimensionless parameter values in our numerical simulations:

$$\tilde{\kappa} = 29, \quad \ell_{\max} = 100, \quad \tilde{k}_L = \tilde{k}_H = 1, \quad \tilde{\gamma} = 0.25, \quad \tilde{L}_c = 1, \quad \tilde{\delta}_L = \tilde{\delta}_H = 0.01. \tag{4.25}$$

The influx ratios $\tilde{\sigma}_L$ and σ_H are varied over a range of positive values. We briefly justify these order-of-magnitude estimates below.

The estimate for $\tilde{\kappa} = \kappa/a_0$ is based on the experimental results presented in [133]. Ford *et al.* measured the rate at which macrophages uptake endogenous lipid from apoptotic cells and found that, even when extracellular lipid was in abundance, macrophages did not attain a lipid load exceeding $\sim 30a_0$.

The average unit of lipid exchange, Δa, is likely to be much smaller than the macrophage capacity, κ. Indeed, the largest increment of lipid exchange is likely to be due to apoptotic cell uptake (efferocytosis) or necrotic cell uptake, processes which are often reported to occur via piecemeal uptake or via nibbling, respectively [91, 193]. Hence, a possible upper bound for Δa in early atherosclerotic lesions is the endogenous lipid content, i.e., $\Delta a \lesssim a_0$. In light of our estimate for κ, it follows that $\ell_{\max}^{-1} = \frac{\Delta a}{\kappa} \lesssim 0.03$.

The estimate for $\tilde{\gamma} = \gamma/\beta$ is based on a macrophage death rate of $\beta = 0.05$ h^{-1} and an emigration rate of $\gamma = 0.013$ h^{-1}. The stated death rate is the half-maximal value of the apoptosis rate reported in [131], where the authors fit an ODE model to *in vitro* data for macrophage lipid uptake. Thon *et al.* assume that the death rate increases with lipid content (by contrast, we assume a constant death rate). Since our model distinguishes between newly recruited and lipid-laden MDMs, we use the half-maximal rate rather than the maximal rate. The stated emigration rate is intermediate between the 12.6% transmigration rate reported in [194] and the 20h residence time reported in [195].

The remaining parameters are more difficult to estimate due to the current lack of quantitative *in vivo* data. In the absence of such data, we fix $\tilde{k}_L = \tilde{k}_H = 1$. These values ensure that MDM uptake and efflux are comparable and occur on the same timescale as the MDM lifespan. We also fix $\delta_L = \delta_H = 0.01$ so that loss of extracellular lipid and HDL lipid capacity to non-MDM interactions is small relative to MDM uptake and efflux. This assumption is consistent with observations that the number of tissue-resident cells in atherosclerotic lesions is dominated by the number of recruited MDMs [68]. Finally, we set $\tilde{L}_c = 1$ so MDM recruitment also occurs on the $t = \mathcal{O}(1)$ macrophage lifespan timescale. The LDL and HDL influx ratios, $\tilde{\sigma}_L$ and $\tilde{\sigma}_H$, are likely to vary significantly between individuals since blood cholesterol levels depend sensitively on lifestyle factors

such as diet [38]. Nonetheless, the estimates in [131] indicate that $\tilde{\sigma}_L$ and σ_H are likely to be $\mathcal{O}(1)$ quantities.

4.2.5 Numerical solutions

We use the *NDSolve* routine in Wolfram Mathematica to generate numerical solutions to Eqs. (4.16)-(4.23). By default, *NDSolve* uses an adaptive algorithm which reduces the computational timestep so that tolerances for absolute error (accuracy) and relative error (precision) are satisfied. Details on how error tolerances are defined using a scaled ∞-norm can be found in [196]. We find that the default settings of *NDsolve* yield approximate solutions to Eqs. (4.16)-(4.23) with residuals less than 10^{-3} for all $t \geq 0$. To further ensure the validity of numerical solutions in this chapter, we checked that they are robust to decreases in "MaxStepSize", increases in "PrecisionGoal" and "AccuracyGoal", and consistent with the analytical steady state results in Sects. 4.3.2 and 4.3.4.

4.3 Results

In this section we explore the behaviour of Eqs. (4.16)-(4.23). We present time-dependent numerical solutions of the full model in Sect. 4.3.1. We then conduct a steady state analysis of the subsystem (4.19)-(4.22) in Sect. 4.3.2. Finally, in Sect. 4.3.3, we characterise the MDM lipid distribution by deriving and then exploiting a continuum approximation of Eqs. (4.16)-(4.18).

4.3.1 Model dynamics

We generate numerical solutions across a range of values of the influx parameters σ_L and σ_H. The dynamics of the ODE subsystem (4.19)-(4.23) are shown in Fig. 4.2. At early times, $t \lesssim 0.25$ (see insets of Fig. 4.2(d, g)), we observe quasi-linear growth in $L(t)$ and $H(t)$, which reflects LDL and HDL infiltrating a lesion that is initially devoid of MDMs. The initial rise in $L(t)$ drives a rapid increase in $M(t)$ and $L_M(t)$ as MDMs are recruited to the lesion from the blood. The growth in $L(t)$ then slows substantially for $0.5 \lesssim t \lesssim 1$ due to MDM uptake. We note that this initial wave of uptake is sufficient to cause $L(t)$ to decrease in many of the cases shown, which indicates that the uptake rate exceeds the influx rate of LDL lipid during this period. For $1 \lesssim t \lesssim 2$, growth in $H(t)$ slows, indicating that at this stage the MDM population has ingested enough lipid for offloading to substantially impact the HDL capacity in the lesion. Indeed for sufficiently large values of $(\sigma_L - \sigma_H)$ (see Fig. 4.2(b, c, e, f, h, i)), intracellular lipid loads are sufficiently large that offloading causes $H(t)$ to peak and decrease thereafter. We note also that MDM cell death gives rise to a secondary increase in $L(t)$ in these cases during this time period; the increase in extracellular lipid due to cell death exceeds the loss due to uptake for sufficiently large values of σ_L relative to σ_H. Finally, we observe that $M(t)$, $L_M(t)$, $L(t)$ and $H(t)$ evolve to nonzero equilibrium values as $t \to \infty$.

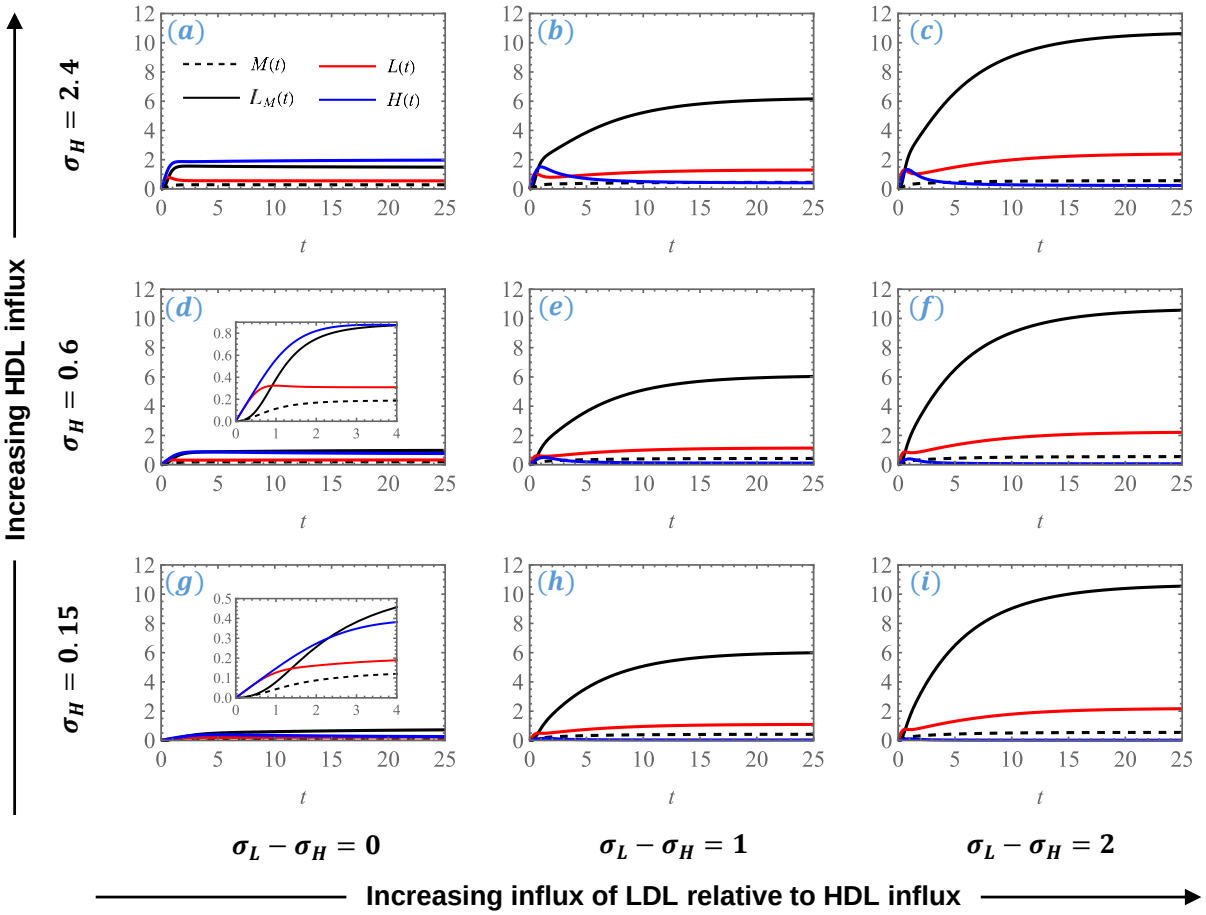


Figure 4.2: **Series of plots showing how lesion composition evolves with time for different rates of LDL and HDL entry.** The time dynamics of the MDM density, M, MDM lipid density, L_M, extracellular lipid density, L, and HDL capacity, H, are presented for a range of values of the parameters σ_L and σ_H. We consider the cases $\sigma_H = 0.15$, 0.6 and 2.4 in the bottom, middle and top rows, respectively. From left to right, the LDL influx, σ_L, is increased from σ_H to $\sigma_H + 1$ and $\sigma_H + 2$. The remaining parameter values are given in Eqs. (4.25).

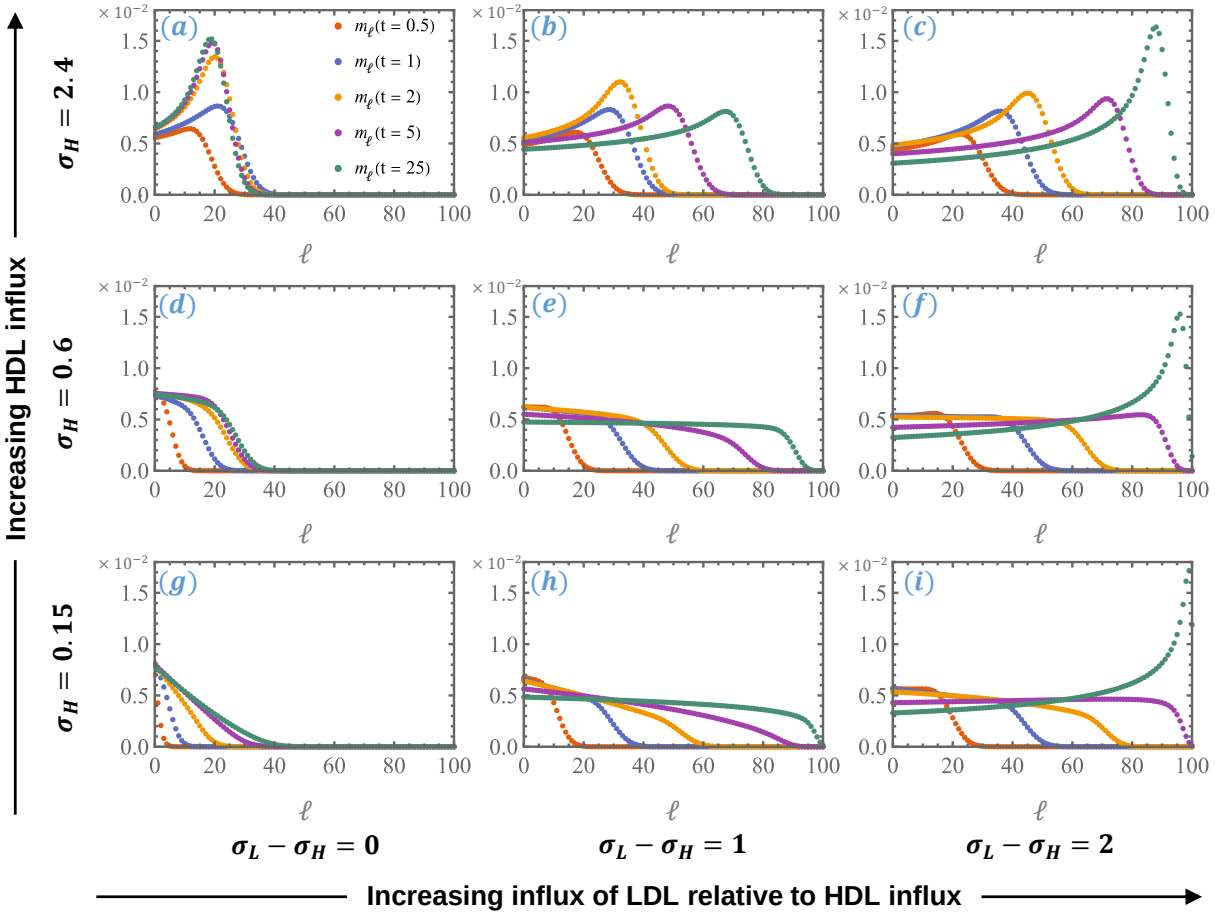


Figure 4.3: **Dynamics of the MDM lipid distribution for different rates of LDL and HDL influx.** The distribution functions, $m_\ell(t)$, $\ell = 0, 1, \ldots, \ell_{\max}$, are plotted against ℓ at the time values $t = 0.5$, 1, 2, 5 and 25 (approximately steady state). We consider the same values of σ_L and σ_H as in Fig. 4.2. The remaining parameters are set according to Eqs. (4.25).

The numerical solutions suggest that lesion lipid content at equilibrium is more sensitive to the relative influx of LDL lipid to HDL capacity, $(\sigma_L - \sigma_H)$, than to the individual influx rates σ_L and σ_H. Indeed, when $\sigma_L - \sigma_H = 2$ the trajectories of $L_M(t)$ and $L(t)$ are indistinguishable for $t \gtrsim 4$ (see Fig. 4.2(c, f, i)). We note further that larger values of $(\sigma_L - \sigma_H)$ give rise to larger increases in $L_M(t)$ than in $L(t)$ for the parameter values used in Fig. 4.2. That is, increases to the relative influx of LDL lipid to HDL capacity yield greater changes in the MDM lipid burden than the amount of extracellular lipid for these parameter values. These trends will be explored in more detail in Sect. 4.3.2.

The dynamics of the MDM lipid distribution, $m_\ell(t)$, $\ell = 0, 1, \ldots, \ell_{\max}$, are shown in Fig. 4.3. We see that $m_\ell(t)$ evolves in a wave-like manner over time towards a non-zero equilibrium. The wavefront proceeds from $\ell = 0$ at $t = 0$ to $\ell = \ell_c \in (0, \ell_{\max})$ as $t \to \infty$. We note, however, that the wavefront may change direction at later times (e.g., Fig. 4.3(a)). This is likely due to offloading to HDL, given the dominance of $H(t)$ for these parameter values (see Fig. 4.2(a)).

The lipid distribution m_ℓ adopts several qualitatively distinct profiles at equilibrium.

The equilibrium profile may be monotone decreasing in ℓ, and may be convex (as in Fig. 4.3(g)) or concave (Fig. 4.3(d, h)); it may have a quasi-uniform profile (Fig. 4.3(e)) or a peaked profile (Fig. 4.3(a, b, c, f, i)). The simulation results presented in Fig. 4.3 suggest that the location of the wavefront at steady state is sensitive to the difference $(\sigma_L - \sigma_H)$. However, the geometric features of the profile (e.g., existence of a local maximum) seem to depend on the individual magnitudes of σ_L and σ_H. For instance, the spiked profile can manifest with low (e.g., Fig. 4.3(a)), intermediate (e.g., Fig. 4.3(b)) or high (e.g., Fig. 4.3(c)) lipid loads. We study the equilibrium lipid distribution in more depth in Sect. 4.3.3.

Before proceeding to the steady state analysis, we pause to define two quantities which help to summarise the model behaviour:

$$\mu(t) := \frac{L_M(t) - M(t)}{\kappa M(t)}, \qquad f(t) := \frac{L_M(t)}{L_M(t) + L(t)}. \tag{4.26}$$

Both variables are normalised such that $0 \leq \mu(t), f(t) \leq 1$. The ratio $\mu(t)$ represents the mean MDM lipid burden, relative to the capacity for ingested lipid. Since

$$\mu = 1 - \frac{k_L L[(\kappa+1)M - L_M]}{k_L L \kappa M}, \tag{4.27}$$

we note that another interpretation for μ is the fractional decrease in the uptake rate of the MDM population due to its lipid load at time t. The ratio $f(t)$ is the fraction of lipid in the lesion that is contained within the MDM population.

The dynamics of $\mu(t)$ and $f(t)$ are shown in Fig. 4.4 for $\sigma_H = 1$ and $\sigma_L = 0.75$, 1.5, 3, 6 and 12. Both variables tend to non-zero steady state values at long times: $\mu \to \mu^\star$ and $f \to f^\star$ as $t \to \infty$. We observe that, as σ_L increases, $\mu^\star$ increases towards $\mu^\star \to 1^-$, which corresponds to a lesion with MDM lipid loads at capacity, and, consequently, 100% defective uptake. By contrast, $f^\star$ depends non-monotonically on σ_L, attaining its largest value, $f^\star \approx 0.8$, when $1.5 \lesssim \sigma_L \lesssim 3$. In order to understand these trends and those described above, we turn now to the steady state analysis.

4.3.2 Steady state analysis of the closed subsystem

Let $M^\star$, $L_M^\star$, $L^\star$ and $H^\star$ denote the steady values of the corresponding dependent variables. Expressions for these quantities can be found by setting the time derivatives to zero in Eqs. (4.19)-(4.22). We find that $M^\star$, $L_M^\star$ and $H^\star$ can be expressed in term of $L^\star$:

$$\begin{aligned} M^\star &= \frac{L^\star}{(1+\gamma)(L_c + L^\star)}, \qquad L_M^\star = \frac{k_L(\kappa+1)(L^\star)^2 - (\sigma_L - \delta_L L^\star)(1+\gamma)(L^\star + L_c)}{(1+\gamma)(1+k_L L^\star)(L^\star + L_c)}, \\ H^\star &= \frac{\sigma_H}{\delta_H + k_H(L_M^\star - M^\star)}, \end{aligned} \tag{4.28}$$

and that $L^\star$ solves a quintic equation

$$c_5(L^\star)^5 + c_4(L^\star)^4 + c_3(L^\star)^3 + c_2(L^\star)^2 + c_1 L^\star + c_0 = 0. \tag{4.29}$$

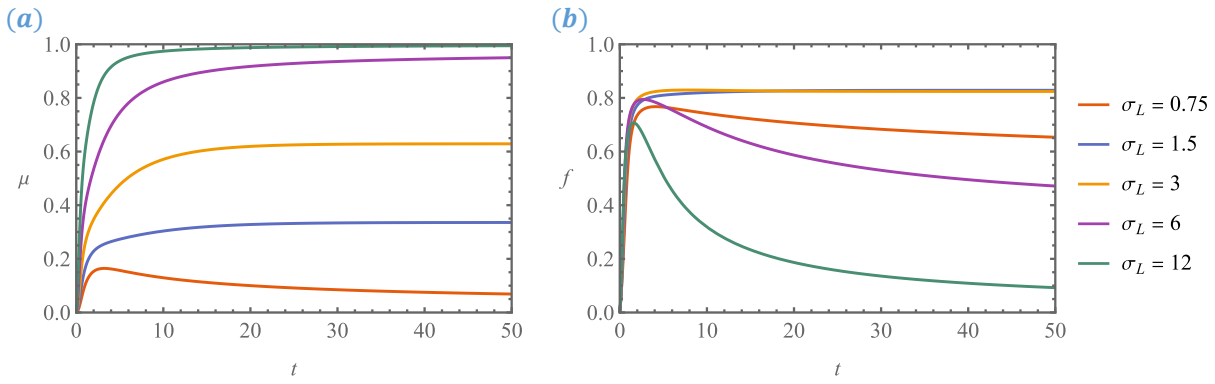


Figure 4.4: **Fractional decrease in uptake rate of MDM population due to lipid accumulation, $\mu(t)$, and proportion of lesion lipid that is intracellular, $f(t)$.** The quantities $\mu(t)$ and $f(t)$, defined in Eqs. (4.26), are plotted for the cases $\sigma_L = 0.75, 1.5, 3, 6$ and 12 with $\sigma_H = 1$. We set the remaining parameters according to Eqs. (4.25).

The coefficients c_i, $i = 1, \ldots, 5$ are complicated combinations of the model parameters:

$$c_0 := (\gamma+1)^2 L_c^2 \sigma_L(\gamma\delta_H + \delta_H + k_H(\sigma_H - (\gamma+1)\sigma_L)), \tag{4.30}$$

$$\begin{aligned} c_1 := (\gamma+1)L_c\Big[&(\gamma+1)(\gamma+2)L_c\delta_H k_L\sigma_L \\ &+ L_c k_H\Big(k_L\sigma_L(\sigma_H - \sigma_L) - \sigma_H\delta_L + 2(\gamma+1)\delta_L\sigma_L\Big) - (\gamma+1)L_c\delta_H\delta_L + \delta_H \\ &- 2k_H\sigma_L(-\sigma_H + \gamma\sigma_L + \sigma_L + 1) + 2(\gamma+1)\delta_H\sigma_L) + k_H\sigma_H\Big], \end{aligned} \tag{4.31}$$

$$\begin{aligned} c_2 := (\gamma+1)(&k_H(-L_c\sigma_H k_L((\gamma+1)L_c\delta_L + \kappa - 2) - ((\gamma+1)L_c\delta_L - 1)^2 + \sigma_H) \\ &+ L_c k_L\sigma_L(2\gamma(L_c\delta_L + \sigma_H + \kappa - 1) + 2L_c\delta_L + 2\sigma_H + \kappa - 3) \\ &+ (\gamma+1)\sigma_L(4(\gamma+1)L_c\delta_L + \sigma_H - 2) - (\gamma+1)\sigma_L^2(2L_c k_L + \gamma + 1) \\ &+ L_c\delta_H(-(\gamma+1)\delta_L((\gamma+2)L_c k_L + 2(\gamma+1)) - \gamma\kappa k_L) - 2(\gamma+1)L_c\sigma_H\delta_L \\ &+ (\gamma+1)\delta_H\sigma_L(L_c k_L(L_c k_L + 2\gamma + 4) + \gamma + 1) + (\gamma+1)\delta_H(2L_c k_L + 1)), \end{aligned} \tag{4.32}$$

$$\begin{aligned} c_3 := (\gamma+1)\delta_H(&-(\gamma+1)(\delta_L(L_c k_L(L_c k_L + 2\gamma + 4) + \gamma + 1) \\ &- k_L(L_c k_L + 2)) - \gamma\kappa k_L(L_c k_L + 1) + (\gamma+1)k_L\sigma_L(2L_c k_L + \gamma + 2)) \\ &+ k_H(k_L((\gamma+1)\sigma_L(\gamma(4L_c\delta_L + \sigma_H + 2\kappa - 2) + 4L_c\delta_L + \sigma_H + \kappa - 3) \\ &- (\gamma+1)\sigma_H(2(\gamma+1)L_c\delta_L + \kappa - 2) \\ &- (\gamma+1)^2\sigma_L^2) - (\gamma+1)(\kappa-1)L_c k_L^2(\sigma_H - \sigma_L) - \delta_L(\gamma+1)^2(2(\gamma+1)L_c\delta_L \\ &+ \sigma_H - 2(\gamma+1)\sigma_L - 2)) - ((\gamma+1)L_c\delta_L - 1)(2\gamma\kappa + (\gamma+1)(L_c\delta_L - 2) + \kappa), \end{aligned} \tag{4.33}$$

$$\begin{aligned} c_4 := (\gamma+1)\delta_H k_L(&k_L(\gamma(-2L_c\delta_L - \kappa + \sigma_L + 1) - 2L_c\delta_L + \sigma_L + 1) \\ &- (\gamma+1)(\gamma+2)\delta_L) - k_H((\gamma+1)k_L\delta_L(\gamma(2L_c\delta_L + \sigma_H + 2\kappa - 2\sigma_L - 2) \\ &+ 2L_c\delta_L + \sigma_H + \kappa - 2\sigma_L - 3) + (\kappa-1)k_L^2(\gamma(L_c\delta_L + \sigma_H + \kappa - \sigma_L - 1) \\ &+ L_c\delta_L + \sigma_H - \sigma_L - 1) + (\gamma+1)^3\delta_L^2), \end{aligned} \tag{4.34}$$

$$c_5 := -[(\gamma+1)k_L\delta_L((\gamma+1)\delta_H k_L + (\gamma+1)k_H\delta_L + (\kappa-1)k_H k_L)]. \tag{4.35}$$

We note that physically realistic steady state solutions must satisfy $L_M^\star \geq M^\star$ so that MDM lipid content is not less than the endogenous lipid content. Re-writing this condition

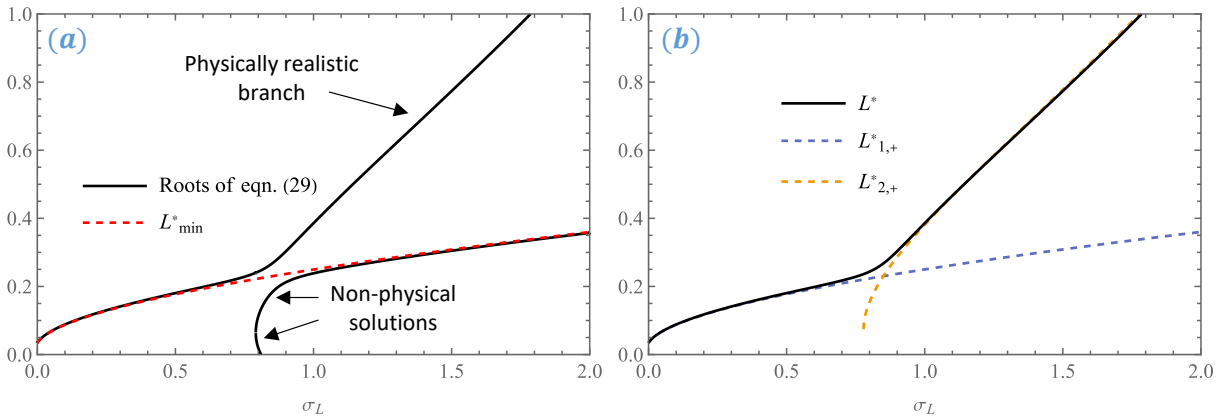


Figure 4.5: **Identifying and approximating the physical solution, $L^\star$, of the polynomial** (4.29)**.** The left plot shows the positive solutions of Eq. (4.29) as the LDL influx, σ_L, is varied. There is only one physically realistic solution which satisfies $L^\star \geq L^\star_{\text{min}}$. The right plot shows how the left and right segments of this physical solution are approximated by the asymptotic solutions, $L^\star_{1,+}$ and $L^\star_{2,+}$, respectively. We use $\sigma_H = 1$ and set the remaining parameter values according to Eqs. (4.25).

using the expressions for $L^\star_M$ and $M^\star$ in Eqs. (4.28) supplies the following inequality for $L^\star$:

$$\begin{aligned} L^\star \geq\ & \frac{1}{2\big(k_L\kappa + \delta_L(1+\gamma)\big)}\Big[\big(1+(1+\gamma)(\sigma_L - \delta_L L_c)\big) \\ & + \sqrt{\big(1+(1+\gamma)(\sigma_L-\delta_L L_c)\big)^2 + 4\big(k_L\kappa+\delta_L(1+\gamma)\big)(1+\gamma)\sigma_L L_c}\Big] \\ =:\ & L^\star_{\text{min}}. \end{aligned} \tag{4.36}$$

Hence, we seek positive solutions of the quintic (4.29) which satisfy inequality (4.36).

We used the Wolfram Mathematica routine *NSolve* to determine the positive solutions of Eq. (4.29) as σ_L varies. The results, presented in Fig. 4.5(a), show that for fixed values of σ_L, Eq. (4.29) admits a unique physically realistic solution (with $L^\star \geq L^\star_{\text{min}}$). Further, $L^\star$ increases continuously with σ_L and the solution branch can be decomposed into two main segments. On the left segment ($0 \leq \sigma_L \lesssim 0.8$ in Fig. 4.5) $L^\star$ increases slowly with σ_L and is well-approximated by $L^\star_{\text{min}}$. This regime corresponds to an HDL-dominant lesion where MDM lipid loads are minimal ($L^\star_M \approx M^\star$) due to efficient efflux. In this regime, increasing LDL influx, σ_L, has little effect on extracellular lipid accumulation at equilibrium because MDMs rapidly offload the lipid they ingest and, therefore, only contribute their endogenous lipid content to the extracellular environment upon death. For large values of σ_L ($\sigma_L \gtrsim 0.8$ in Fig. 4.5) $L^\star$ increases more rapidly with σ_L. For these lesions, the LDL influx is sufficiently large to impact the HDL capacity in the lesion at steady state.

While a closed-form expression for $L^\star$ does not exist in full generality, we can approximate the individual segments of $L^\star$ via asymptotic analysis. Specifically, we seek approximate solutions to the polynomial (4.29) in the limit $\delta_L \sim \delta_H \ll 1$. Biologically,

this corresponds to a regime in which loss of extracellular lipid and HDL capacity to non-MDM interactions is negligible. We note from Eqs. (4.30)-(4.35) that the coefficients scale as: $c_0, \ldots, c_4 = \mathcal{O}(1)$ and $c_5 = \mathcal{O}(\delta_L, \delta_H)$, so that Eq. (4.29) can be interpreted as a singular perturbation problem. We first consider the "outer" problem by setting $\delta_L, \delta_H \to 0$ in Eq. (4.29). By factorising the resulting quartic polynomial into two quadratic equations for $L^\star$, we arrive at the following solutions:

$$L^\star_{1,\pm} := \frac{\gamma\sigma_L + \sigma_L + 1 \pm \sqrt{4(\gamma+1)\kappa L_c k_L \sigma_L + (\gamma\sigma_L + \sigma_L + 1)^2}}{2\kappa k_L}, \tag{4.37}$$

$$L^\star_{2,\pm} := \frac{-b_1 \pm \sqrt{b_1^2 - 4b_0 b_2}}{2b_2}, \tag{4.38}$$

where the constants b_0, b_1 and b_2 of $L^\star_{2,\pm}$ are given by

$$\begin{aligned} b_0 &:= L_c(1+\gamma)\big[(1+\gamma)\sigma_L - \sigma_H\big], \\ b_1 &:= (\gamma+1)\big[1 + k_L L_c(\sigma_L - \sigma_H) + (1+\gamma)\sigma_L - \sigma_H\big], \\ b_2 &:= k_L\big[(1+\gamma)(1+\sigma_L - \sigma_H) - \gamma\kappa\big]. \end{aligned} \tag{4.39}$$

The remaining root is negative and scales as $L^\star_0 = \mathcal{O}(\delta_L^{-1}, \delta_H^{-1})$.

In Fig. 4.5(b) we show how the solutions $L^\star_{1,+}$ and $L^\star_{2,+}$ change as σ_L varies. We note that these expressions are good approximations for the left and right segments of $L^\star$, respectively. We note further that $L^\star_{\min}$ reduces to $L^\star_{1,+}$ in the limit $\delta_L \to 0$, which indicates that $L^\star_{1,+}$ corresponds to a regime where $L^\star_M = M^\star + \mathcal{O}(\delta_L, \delta_H)$. Substituting this result into Eqs. (4.28) shows that $H^\star = \mathcal{O}(\delta_L^{-1}, \delta_H^{-1})$ at leading order, confirming that the slower increase with σ_L on the left branch $L^\star_{1,+}$ is due to rapid lipid efflux to HDL. The expression for $L^\star_{2,+}$ is more complicated and difficult to interpret. However, we note that the coefficients (4.39) which define $L^\star_{2,+}$ only depend on the influx parameters σ_L and σ_H through the combinations $\sigma_L - \sigma_H$ and $(1+\gamma)\sigma_L - \sigma_H$. This reinforces the notion that $L^\star$ is sensitive to the relative influx of LDL lipid and HDL capacity.

In Fig. 4.6, we use the expressions (4.28) with the numerical solution for $L^\star$ in Eq. (4.29) to show how lesion composition at equilibrium changes as both σ_L and σ_H vary. We find that $M^\star$, $L^\star_M$ and $L^\star$ each increase with σ_L and decrease with σ_H. By contrast, $H^\star$ decreases with σ_L and increases with σ_H. We note that the approximately linear contours, which feature in all four plots, indicate that the dependent variables are sensitive to the difference: $\sigma_L - \sigma_H$. This suggests that the relative influx of LDL lipid to HDL capacity not only determines $L^\star$ (as indicated by the asymptotics), but lesion composition more generally. When $\sigma_L - \sigma_H \lesssim 0$ (top left in plots of Fig. 4.6), the lesion is HDL-dominant ($H^\star > 25$) with low quantities of lipid, $L^\star_M$ and $L^\star$), and a small MDM population, $M^\star$. For $0 \lesssim \sigma_L - \sigma_H \lesssim 5$ the lesion contains intermediate amounts of MDMs, lipid and HDL capacity. Finally, when $\sigma_L - \sigma_H \gtrsim 5$ the lesion is dominated by extracellular lipid ($L^\star > 25$). In this regime, HDL capacity is exhausted ($H^\star \approx 0$) and MDM lipid loads are near capacity ($L^\star_M \approx (\kappa+1)M^\star$) so that increases to the LDL lipid influx relative

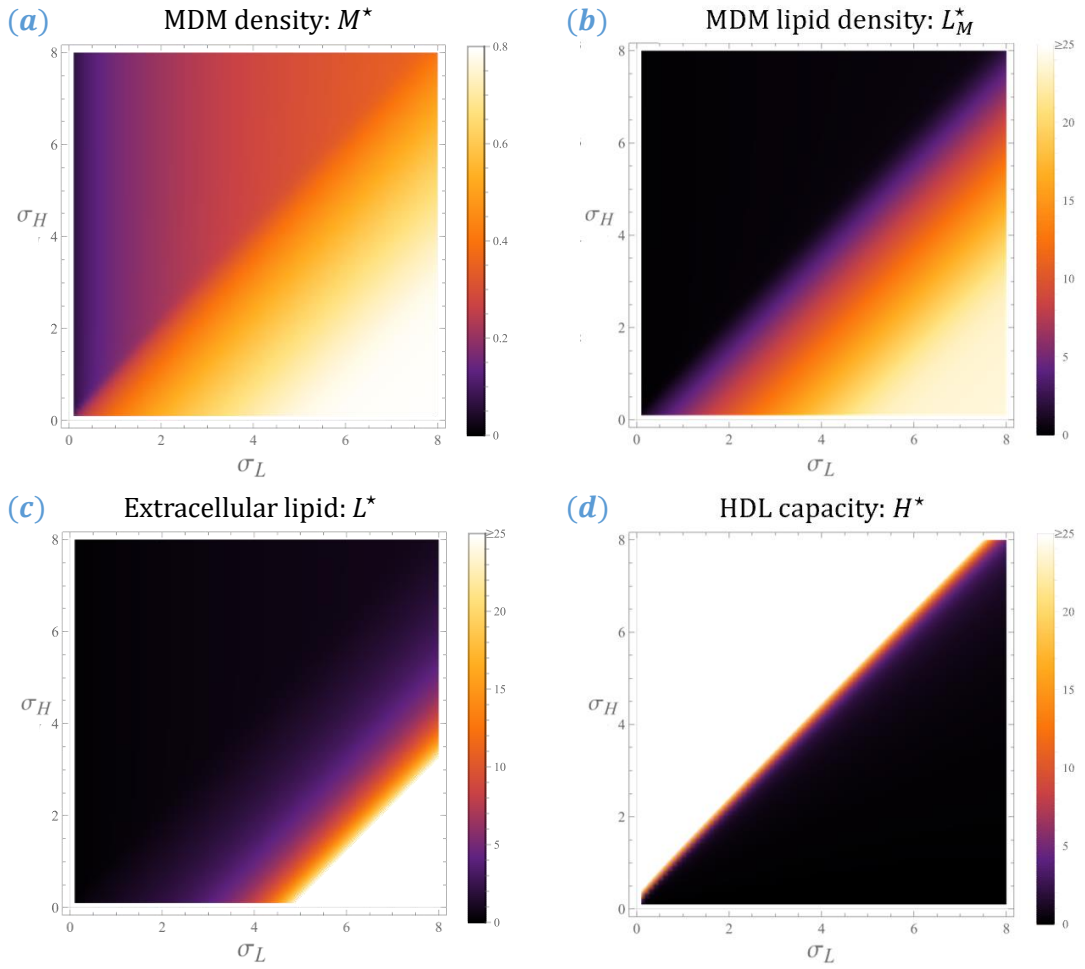


Figure 4.6: **Lesion composition is sensitive to the influxes of LDL lipid (σ_L) and HDL capacity (σ_H).** The steady state values $M^\star$, $L_M^\star$, $L^\star$ and $H^\star$ are plotted against σ_L and σ_H. Note that the approximately linear contours, which feature in all four plots, indicate that the dependent variables are sensitive to the difference $(\sigma_L - \sigma_H)$. That is, lesion composition is largely determined by the relative influx of LDL lipid to HDL capacity. Parameter values are set according to Eqs. (4.25).

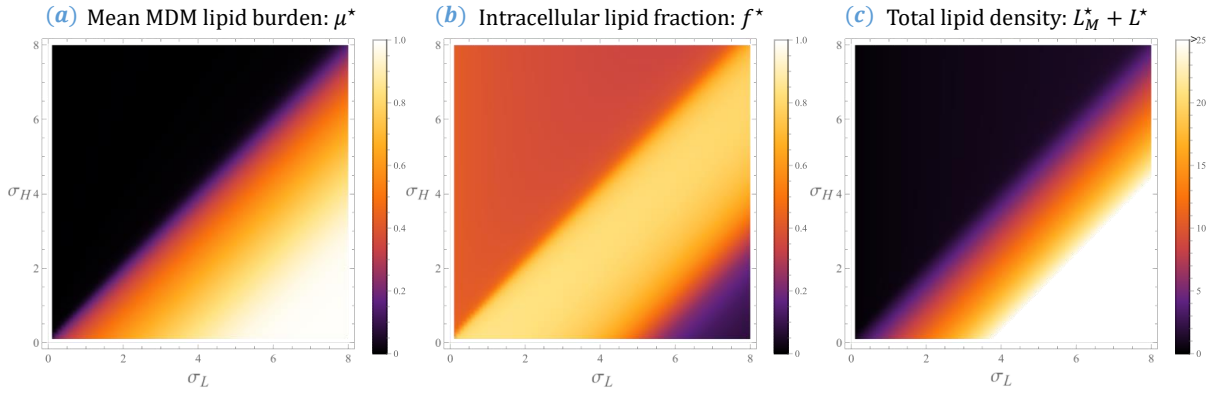


Figure 4.7: **Equilibrium lesion lipid content as the LDL and HDL influxes are varied.** We plot the normalised quantities $\mu^\star$ and $f^\star$, defined by Eqs. (4.26), and the total lesion lipid, $L_M^\star + L^\star$, against σ_L and σ_H. Note how the fraction of lipid that is intracellular, $f^\star$, is approximately constant in the band $0 \lesssim \sigma_L - \sigma_H \lesssim 5$, in which average MDM lipid burden, $\mu^\star$, and total lesion lipid, $L_M^\star + L^\star$, both vary substantially. The parameter values are set according to Eqs. (4.25).

to HDL capacity, $(\sigma_L - \sigma_H)$, directly increase the amount of extracellular lipid at steady state, $L^\star$.

We further explore lesion composition in Fig. 4.7 where we focus on the average MDM lipid burden, $\mu^\star$, the fraction of lesion lipid that is intracellular, $f^\star$, and the total lesion lipid, $L_M^\star + L^\star$, as σ_L and σ_H vary. In contrast to the trends of $\mu^\star$ and $L_M^\star + L^\star$ (which both increase with σ_L and decrease with σ_H), the fraction $f^\star$ exhibits non-monotonic dependence on both σ_L and σ_H. It follows that $f^\star$ may be a poor metric for lesion progression since it can take the same value when lesion lipid content is low or high (e.g., $f^\star \approx 0.4$ at $(\sigma_L, \sigma_H) = (2, 4)$ or $(6, 2)$). We note further that $f^\star$ is approximately constant for $0 \lesssim \sigma_L - \sigma_H \lesssim 5$, while $\mu^\star$ and $L_M^\star + L^\star$ vary substantially in this interval. This behaviour probably occurs because, in this region of parameter space, most of the lipid is contained in the MDM population (compare Figs. 4.6(b,c)), and so the primary source of extracellular lipid is cell death. Since the amount of lipid entering the extracellular environment via cell death is exactly the lipid content of the dying MDMs, cell death equalises any changes in the amounts of intracellular and extracellular lipid. Finally, the plots confirm that the lesion is dominated by extracellular lipid in the region $\sigma_L - \sigma_H \gtrsim 5$, where MDM lipid loads are comparable to the maximum lipid capacity.

4.3.3 MDM lipid distribution

It is not straightforward to analyse the lipid distribution, $m_\ell(t)$, $\ell = 0, 1, \ldots, \ell_{\max}$, by directly considering Eqs. (4.16)-(4.18). Nonetheless, we show below that the steady state values, $m_\ell^\star$, $\ell = 0, 1, \ldots \ell_{\max}$, can be obtained via the method of generating functions. We set

$$g(z,t) := \sum_{\ell=0}^{\ell_{\max}} m_\ell(t)\, z^\ell, \qquad 0 \le z \le 1. \tag{4.40}$$

By differentiating Eq. (4.40) with respect to t and substituting the ODEs (4.16)-(4.18), we find that $g(z,t)$ satisfies the following PDE:

$$\frac{\partial g}{\partial t} + (1-z)\Big[k_L L^\star\Big(\ell_{\max}\, g - z\frac{\partial g}{\partial z}\Big) - k_H H^\star \frac{\partial g}{\partial z}\Big] = 1 - (1+\gamma)g. \tag{4.41}$$

Eq. (4.41) is subject to the boundary condition

$$g(1,t) = M(t). \tag{4.42}$$

At steady state, Eqs. (4.41) and (4.42) reduce to the following non-autonomous ODE initial value problem:

$$(1-z)\Big[k_L L^\star\Big(\ell_{\max}\, g - z\frac{dg}{dz}\Big) - k_H H^\star \frac{dg}{dz}\Big] = 1 - (1+\gamma)g. \tag{4.43}$$

$$g(1) = M^\star, \tag{4.44}$$

which can be solved in terms of the hypergeometric function ${}_2F_1$:

$$g(z) = M^\star\, {}_2F_1\Big(1, -\ell_{\max}, p+2, a_c(1-z)\Big), \tag{4.45}$$

where a_c and p are the following parameter groupings:

$$a_c := \frac{k_L L^\star}{k_L L^\star + k_H H^\star}, \qquad\qquad p := \frac{1+\gamma}{k_L L^\star + k_H H^\star} - 1. \tag{4.46}$$

Series expansion of the solution (4.45) about $z = 0$ gives

$$g(z) = M^\star \sum_{\ell=0}^{\ell_{\max}} \left(\prod_{k=1}^{\ell} \frac{a_c(\ell_{\max} - k + 1)}{(p+1+k)} \right) {}_2F_1(\ell+1, \ell-\ell_{\max}, 2+\ell+p, a_c)\, z^\ell, \tag{4.47}$$

where the summation is finite because each contribution for $\ell > \ell_{\max}$ is zero. Upon comparison with definition (4.40), we obtain

$$\begin{aligned} m_\ell^\star &= M^\star \left(\prod_{k=1}^{\ell} \frac{a_c(\ell_{\max} - k + 1)}{(p+1+k)} \right) {}_2F_1(\ell+1, \ell-\ell_{\max}, 2+\ell+p, a_c), \\ &= M^\star \left(\prod_{k=1}^{\ell} \frac{a_c(\ell_{\max} - k + 1)}{(p+1+k)} \right) \sum_{n=0}^{\ell_{\max}-\ell} \frac{(\ell+1)^{(n)}(\ell-\ell_{\max})^{(n)}}{(\ell+2+p)^{(n)}} \frac{a_c^n}{n!}, \quad 0 \le \ell \le \ell_{\max}, \end{aligned} \tag{4.48}$$

where $x^{(n)} = x(x+1)\cdots(x+n-1)$ is the n-th rising factorial of x, and the product takes the value 1 for $\ell = 0$. Although the solution (4.48) is exact, the complicated dependence of $m_\ell^\star$ on the index ℓ and the model parameters makes it difficult to analyse the geometric features of the distribution (e.g., the curvature, existence of a local maximum). We show below how this information can be readily extracted from a continuum approximation of Eqs. (4.16)-(4.18).

4.3.3.1 Derivation of continuum approximation

We identify the (dimensionless) discrete lipid distribution, $m_\ell(t)$, $\ell = 0, 1, \dots \ell_{\max}$, with the function $m(a,t) \geq 0$, which is defined over a continuous structure variable, a. Specifically, we make the identifications

$$a \sim \frac{\ell}{\ell_{\max}} \qquad \text{and} \qquad m(a,t) \sim \ell_{\max}\, m_\ell(t), \tag{4.49}$$

so that $0 \leq a \leq 1$ and $m(a,t)$ is proportional to the number density of MDMs with lipid content $a_0 + \kappa a$ at time t. The structure variable is bounded such that $a = 0$ corresponds to MDMs containing only endogenous lipid and $a = 1$ to MDMs whose lipid load is at maximum capacity. Letting $\epsilon := \ell_{\max}^{-1}$, we recast the discrete Eqs. (4.17) as the following non-local equation:

$$\begin{aligned} \epsilon \frac{\partial m}{\partial t}(a,t) = {} & k_L L\big[(1-a+\epsilon)m(a-\epsilon,t) - (1-a)m(a,t)\big] \\ & + k_H H\big[(a+\epsilon)m(a+\epsilon,t) - a m(a,t)\big] - \epsilon(1+\gamma)m(a,t), \end{aligned} \tag{4.50}$$

where $\epsilon \leq a \leq 1-\epsilon$. To derive our continuum model, we expand the terms in Eq. (4.50) about $\epsilon = 0$ to obtain

$$(1-a+\epsilon)m(a-\epsilon,t) - (1-a)m(a,t) = \Big[-\frac{\partial}{\partial a} + \frac{\epsilon}{2}\frac{\partial^2}{\partial a^2}\Big]\big[(1-a)m\big] + \mathcal{O}(\epsilon^2), \tag{4.51}$$

$$(a+\epsilon)m(a+\epsilon,t) - a m(a,t) = \Big[\frac{\partial}{\partial a} + \frac{\epsilon}{2}\frac{\partial^2}{\partial a^2}\Big]\big[am\big] + \mathcal{O}(\epsilon^2). \tag{4.52}$$

Substituting Eqs. (4.51) and (4.52) into Eq. (4.50), dividing through by ϵ and retaining terms of $\mathcal{O}(\epsilon)$ yields the PDE

$$\frac{\partial m}{\partial t} = k_L L\Big[-\frac{\partial}{\partial a} + \frac{\epsilon}{2}\frac{\partial^2}{\partial a^2}\Big]\big[(1-a)m\big] + k_H H\Big[\frac{\partial}{\partial a} + \frac{\epsilon}{2}\frac{\partial^2}{\partial a^2}\Big]\big[am\big] - (1+\gamma)m. \tag{4.53}$$

Eq. (4.53) is an advection-diffusion equation. In conservation form, it reads:

$$\frac{\partial m}{\partial t} = \frac{\partial}{\partial a}\Big[D(a,t)\frac{\partial m}{\partial a} - v(a,t)m\Big] - (1+\gamma)m, \tag{4.54}$$

where the lipid content velocity, v, and diffusion coefficient, D, are defined as follows:

$$v(a,t) := k_L L(1-a) - k_H H a + \frac{\epsilon}{2}(k_L L - k_H H), \tag{4.55}$$

$$D(a,t) := \frac{\epsilon}{2}\big(k_L L(1-a) + k_H H a\big). \tag{4.56}$$

Appropriate boundary conditions are determined by considering the dynamics of the dimensionless MDM population, $M(t)$, which, in the continuum formulation, we identify with the integral:

$$M(t) \sim \int_0^1 m(a,t)\, da. \tag{4.57}$$

Integrating Eq. (4.54) with respect to $a \in (0,1)$, we deduce that

$$\frac{dM}{dt} = \Big(D\frac{\partial m}{\partial a} - vm\Big)\Big|_{a=0}^{a=1} - (1+\gamma)M. \tag{4.58}$$

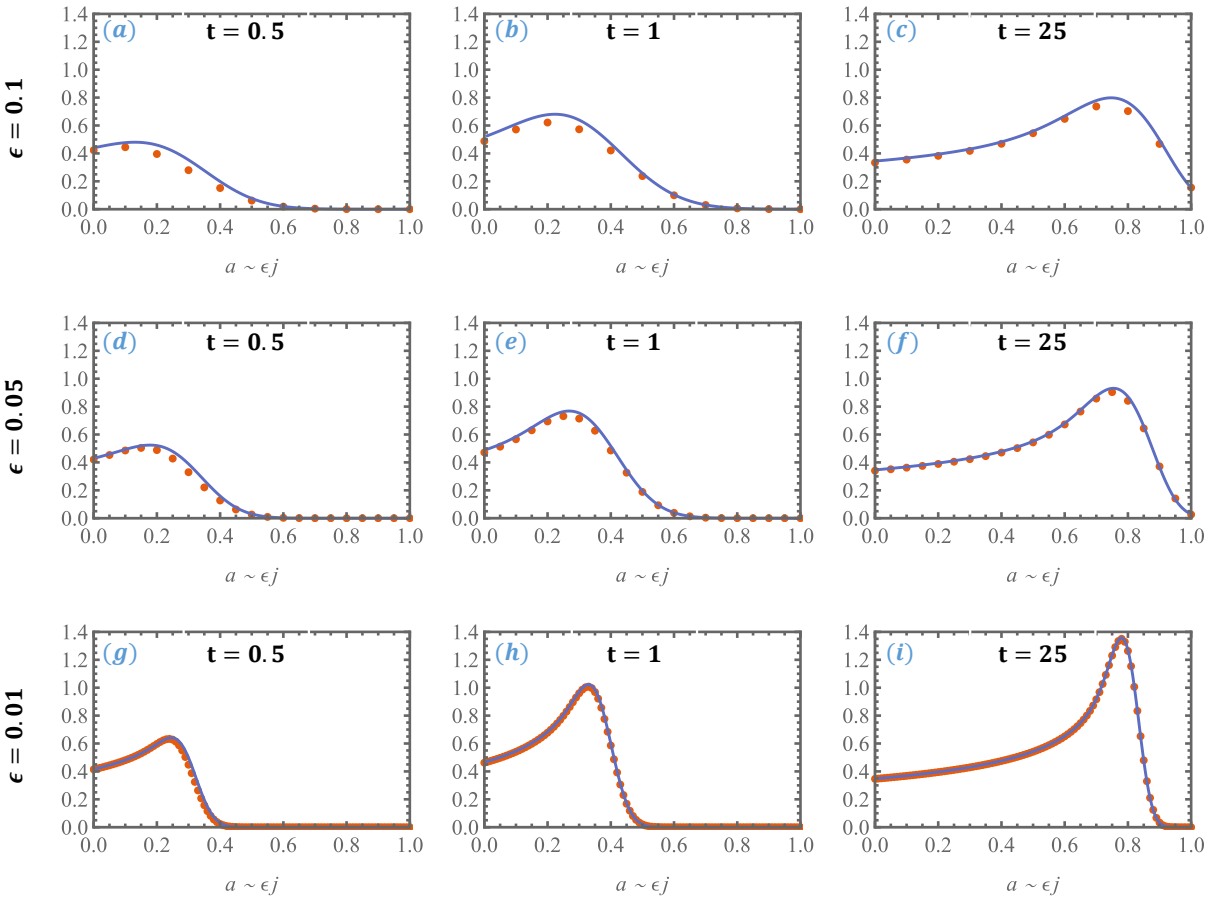


Figure 4.8: **Continuum vs. discrete models.** The output for the discrete model (4.16)-(4.23) is compared to that of the continuum model (4.54), (4.59), (4.60), (4.19)-(4.23) for $\epsilon = 0.1$, 0.05 and 0.01 in the top, middle and bottom rows, respectively. The distributions are shown at the times $t = 0.5, 1$ and 25, where the system is approximately at equilibrium. We let $\sigma_L = 3$, and set the other parameters according to Eqs. (4.25).

To ensure consistency between Eqs. (4.58) and (4.19), we set

$$\left(D\frac{\partial m}{\partial a} - vm\right)\Big|_{a=0} = -\frac{L}{L_c + L}, \qquad \text{and} \qquad \left(D\frac{\partial m}{\partial a} - vm\right)\Big|_{a=1} = 0. \tag{4.59}$$

The boundary condition at $a = 0$ ensures that the flux of MDMs at $a = 0$ is given by the MDM recruitment rate, while the no-flux condition at $a = 1$ ensures that MDMs cannot exceed the maximal lipid load $a = 1$. We note that the two boundary conditions in Eqs. (4.59) are sufficient for closure, since Eq. (4.53) is second order in a.

Finally, we impose the initial condition

$$m(a, 0) = 0, \tag{4.60}$$

and close the continuum model by coupling the PDE (4.53) to the closed ODE subsystem (4.19)-(4.22).

4.3.3.2 Comparison of discrete and continuum models

We generate numerical solutions of the continuum model, defined by Eqs. (4.54), (4.59), (4.60), (4.19)-(4.23), by using the Method of Lines with second-order central differencing

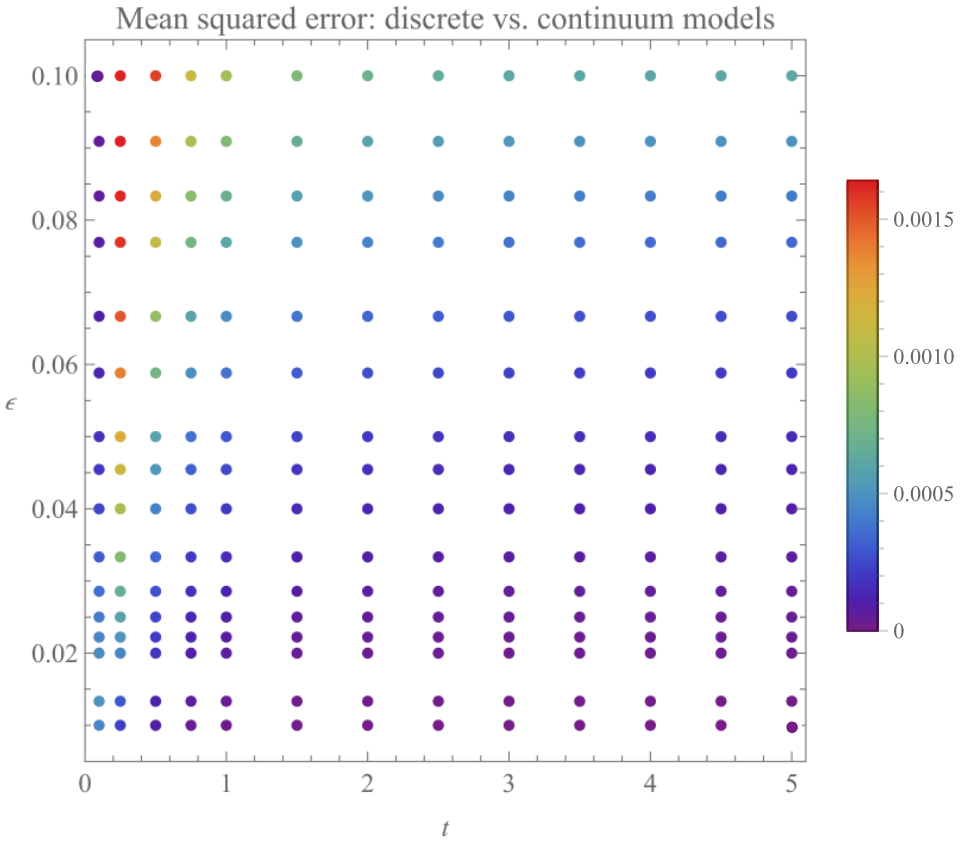


Figure 4.9: **Deviation between the discrete and continuum models.** We use Eq. (4.61) to calculate the mean squared error (MSE) across a number of sample times t and values of ϵ. The value of the MSE is indicated by the colour of the corresponding sample point. We use $\sigma_L = 3$ and $\sigma_H = 1$, and set the other parameters according to Eqs. (4.25).

for $\frac{\partial m}{\partial a}$ and $\frac{\partial^2 m}{\partial a^2}$. The output is compared to that of the discrete model (4.16)-(4.23) in Fig. 4.8. We find that the discrete and continuum models are in excellent agreement, with better consistency for smaller values of ϵ and late time points, t. We note that the value of ϵ affects the sharpness of the wavefront, but not its location, with smaller values of ϵ yielding sharper wavefronts. These observations are consistent with Eqs. (4.55) and (4.56), which show that the diffusion coefficient, $D(a,t)$, is proportional to ϵ, while the velocity, $v(a,t)$, is an $\mathcal{O}(1)$ quantity.

We quantify the deviation between the discrete and continuum models at time t by defining the mean-squared error (MSE):

$$\mathrm{MSE}(t;\,\epsilon) := \frac{1}{\ell_{\max}} \sum_{\ell=0}^{\ell_{\max}} \left(\ell_{\max} m_\ell(t) - m(\ell/\ell_{\max}, t)\right)^2, \tag{4.61}$$

where $\ell_{\max} = \epsilon^{-1}$, and $m_\ell(t)$ and $m(\cdot, t)$ are the discrete and continuum distributions, respectively. We plot the MSE in Fig. 4.9 across a number of sample times t and values of ϵ. The good agreement between the discrete and continuum models is reflected in that $\mathrm{MSE} < 2 \times 10^{-3}$ for all samples. The largest deviation between the models occurs at early times $0 < t < 1$. This transient difference is suppressed on an $\mathcal{O}(1)$ timescale.

4.3.4 Asymptotic analysis at steady state

Let $m^\star(a) = \lim_{t\to\infty} m(a,t)$ denote the steady lipid distribution for the continuum model. Setting the time derivative to zero in Eq. (4.54) and rearranging, we have that

$$\frac{\epsilon}{2}\big[a_c + (1-2a_c)a\big]\frac{d^2m^\star}{da^2} + \big[(a-a_c) + \epsilon(1-2a_c)\big]\frac{dm^\star}{da} - pm^\star = 0, \tag{4.62}$$

where the constants a_c and p are given by

$$a_c := \frac{k_L L^\star}{k_L L^\star + k_H H^\star}, \qquad\qquad p := \frac{1+\gamma}{k_L L^\star + k_H H^\star} - 1. \tag{4.63}$$

Recall that $L^\star > 0$ and $H^\star > 0$ are the steady state values of $L(t)$ and $H(t)$, respectively. It follows that $0 < a_c < 1$ and $p > -1$. We note that $a_c, p = \mathcal{O}(1)$ as $\epsilon \to 0$, since they are rational expressions of the closed subsystem variables, which are independent of ϵ.

At steady state the boundary conditions (4.59) are

$$\frac{\epsilon}{2}\frac{dm^\star}{da} - \Big[1 + \frac{\epsilon}{2}\Big(\frac{2a_c-1}{a_c}\Big)\Big]m^\star = -R, \qquad \text{at } a = 0, \tag{4.64}$$

$$\frac{\epsilon}{2}\frac{dm^\star}{da} + \Big[1 - \frac{\epsilon}{2}\Big(\frac{2a_c-1}{1-a_c}\Big)\Big]m^\star = 0, \qquad \text{at } a = 1, \tag{4.65}$$

where $R := \frac{1}{k_L(L^\star + L_c)}$ is a rescaled recruitment rate. Eqs. (4.62)-(4.65) define a singular perturbation problem with respect to the small parameter $\epsilon \ll 1$. We use the method of matched asymptotics to construct a uniformly valid approximate solution for $m^\star(a)$ in the limit $\epsilon \to 0$.

By setting $\epsilon = 0$ in Eqs. (4.62), (4.64), (4.65), we deduce that the leading order outer solutions satisfy

$$(a-a_c)\frac{dm^\star}{da} - pm^\star = 0, \tag{4.66}$$

and are subject to the Dirichlet conditions

$$m^\star(0) = R, \qquad\qquad m^\star(1) = 0. \tag{4.67}$$

The general solution to Eq. (4.66) is given by

$$m^\star(a) = K\Big(1 - \frac{a}{a_c}\Big)^p, \tag{4.68}$$

where K is a constant of integration. Since we cannot enforce both boundary conditions (4.67) simultaneously, we deduce that there are two outer solutions:

$$m^\star_{\text{left}}(a) := R\Big(1 - \frac{a}{a_c}\Big)^p, \qquad\qquad m^\star_{\text{right}}(a) := 0. \tag{4.69}$$

The left solution $m^\star_{\text{left}}(a)$ is well-defined for $0 \le a < a_c$, while $m^\star_{\text{right}}(a)$ holds in a neighbourhood of $a = 1$. We form the following composite solution:

$$m^\star_{\text{outer}}(a) := \begin{cases} R\Big(1 - \frac{a}{a_c}\Big)^p, & 0 \le a < a_c, \\ 0, & a_c < a \le 1, \end{cases} \tag{4.70}$$

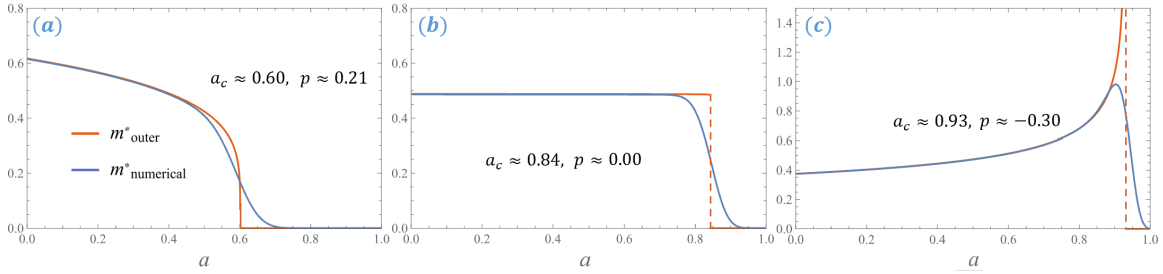


Figure 4.10: **Composite outer solution.** The outer solution (4.70) is compared with the numerical solution for $m^\star(a)$ for three values of the LDL influx, σ_L. The numerical solution is generated by solving the time-dependent system (4.54),(4.59), (4.60), (4.19)-(4.23) to $t = 200$. We use $\sigma_L = 1.3$, 1.845 and 2.5 in cases (a),(b) and (c) respectively. The red dashed line in cases (b) and (c) indicate the discontinuity of $m^\star_{\text{outer}}$ at $a = a_c$. We fix $\sigma_H = 1$ and set the remaining parameters according to Eqs. (4.25).

which ensures continuity in $m^\star_{\text{outer}}$ at $a = a_c$ for $p > 0$.

Numerical solutions of the continuum model indicate that $m^\star_{\text{outer}}(a)$ is a good approximation to $m^\star(a)$ away from the critical value $a = a_c$ (see Fig. 4.10). For $p > 0$, as in Fig. 4.10(a), the outer solution (4.70) is continuous at $a = a_c$, but the numerical solution has a smoother transition towards the zero solution as a increases. For $p = 0$, shown in Fig. 4.10(b), the solution (4.70) is piecewise constant with a discontinuity at $a = a_c$. By contrast, the numerical solution is continuous for all $0 < a < 1$ and takes on a sigmoid profile. For $p < 0$, as in Fig. 4.10(c), the solution (4.70) diverges as $a \to a_c^-$, while the numerical solution has a local maximum near $a = a_c$ in this case.

These observations suggest that we may use p and a_c to characterise the solution $m^\star(a)$ of the full Eq. (4.62). The value of p determines the geometric features of $m^\star(a)$. For $p > 0$, the solution is a decreasing function of a. The curvature is determined by whether $p > 1$, giving a concave-up $m^\star(a)$ for $0 < a \lesssim a_c$, or $0 < p < 1$, where $m^\star(a)$ is concave-down for $0 < a \lesssim a_c$. If $p = 0$, then $m^\star(a)$ is a sigmoid and constant away from $a = a_c$. Finally, if $p < 0$, then $m^\star(a)$ attains a local maximum near $a = a_c$, with the sharpness of the peak growing as $p \to (-1)^+$.

We show how p and a_c depend on σ_L and σ_H in Fig. 4.11. We find that the contours of constant a_c (Fig. 4.11(a)) are approximately linear in (σ_L, σ_H) space, and indicate that a_c increases sensitively with $(\sigma_L - \sigma_H)$. By contrast, the value of p (Fig. 4.11(b)) is non-monotonic in both σ_L and σ_H, and diverges at the origin: $p \to \infty$ as $(\sigma_L, \sigma_H) \to (0, 0)$. The critical contours, $p = 0$ and $p = 1$, are indicated so that we may partition (σ_L, σ_H) space according to the qualitative behaviour of the steady state profile of $m^\star(a)$. Consistent with the numerical results of Sect. 4.3.1, we find that $m^\star(a)$ has a peaked profile ($p < 0$) when either σ_L or σ_H are large enough. Comparison with the corresponding value of a_c reveals that peaked profiles can occur with the local maximum at low or high lipid loads (location of peak is approximately a_c). Furthermore, $m^\star(a)$ only adopts a decreasing and convex profile when σ_L and σ_H are both sufficiently small.

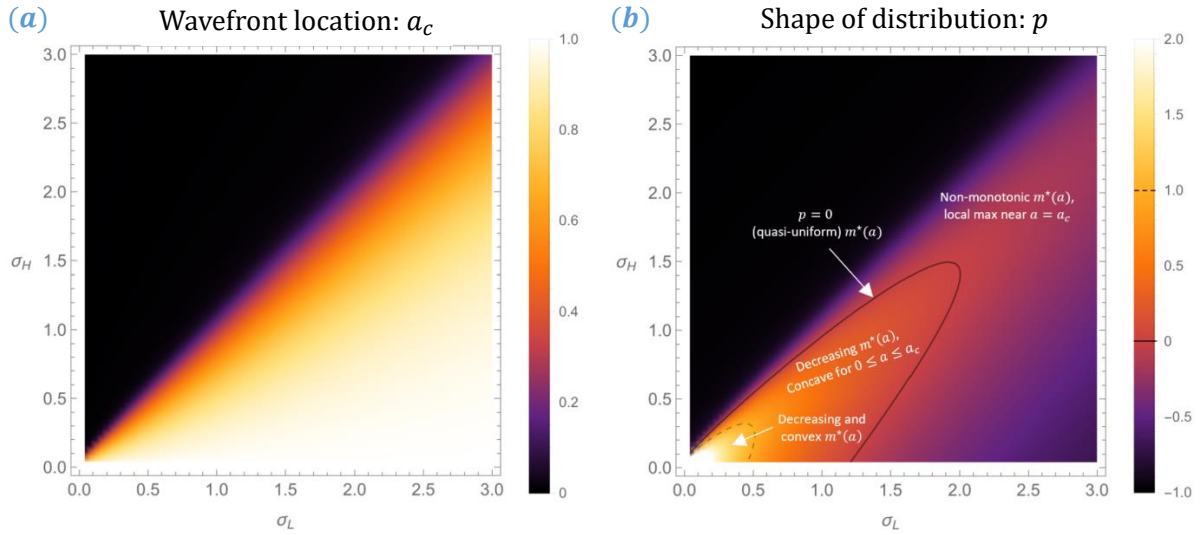


Figure 4.11: **Characterisation of the equilibrium MDM lipid distribution, $m^\star(a)$, in terms of LDL influx, σ_L, and HDL influx, σ_H.** Plot (a) shows the value of a_c, which approximates the lipid content of the most lipid-laden MDMs at equilibrium. Plot (b) indicates the value of the parameter p, which determines the shape of the distribution as indicated. Parameter values are set according to Eqs. (4.25).

To attain a uniformly valid approximation for $m^\star(a)$ over $0 < a < 1$, we define an interior variable $\tilde{a}$, such that $a = a_c + \epsilon^n \sqrt{2a_c(1-a_c)}\,\tilde{a}$ where $n > 0$ is to be specified and the coefficient of $\tilde{a}$ is chosen to simplify the interior equation. Under this change of variables, Eq. (4.62) becomes

$$\frac{\epsilon^{1-2n}}{2}\left[1 + \epsilon^n \frac{1-2a_c}{2a_c(1-a_c)}\tilde{a}\right]\frac{d^2m^\star}{d\tilde{a}^2} + \left[\epsilon^{1-n}\frac{2a_c-1}{\sqrt{2a_c(1-a_c)}} + \tilde{a}\right]\frac{dm^\star}{d\tilde{a}} - pm^\star = 0, \tag{4.71}$$

for $-\infty < \tilde{a} < \infty$. In order to match to the two outer solutions we choose n such that a term proportional to $\frac{d^2m^\star}{d\tilde{a}^2}$ becomes comparable to the $O(1)$ terms. The smallest value of n for which this occurs is $n = \frac{1}{2}$, which gives the following equation at leading order:

$$\frac{1}{2}\frac{d^2m^\star}{d\tilde{a}^2} + \tilde{a}\frac{dm^\star}{d\tilde{a}} - pm^\star = 0. \tag{4.72}$$

The general solution to Eq. (4.72) is

$$m^\star_{\text{interior}}(\tilde{a}) = e^{-\tilde{a}^2}\left[K_1 H_{-1-p}(\tilde{a}) + K_2\, {}_1F_1\left(\frac{1+p}{2}, \frac{1}{2}, \tilde{a}^2\right)\right], \tag{4.73}$$

where H and ${}_1F_1$ are the Hermite and Kummer confluent hypergeometric functions, respectively ([197, 198]). The constants of integration, K_1 and K_2, are determined by matching $m^\star_{\text{interior}}$ to the outer solutions $m^\star_{\text{left}}$ and $m^\star_{\text{right}}$, respectively. We note that Eq. (4.73) satisfies the following asymptotic relation as $\tilde{a} \to \infty$:

$$\begin{aligned} m^\star_{\text{interior}} &\sim K_2 \frac{\pi^{1/2}}{\Gamma((1+p)/2)}\tilde{a}^p \\ &= K_2 \frac{\pi^{1/2}}{\Gamma((1+p)/2)}\epsilon^{-p/2}(a-a_c)^p. \end{aligned} \tag{4.74}$$

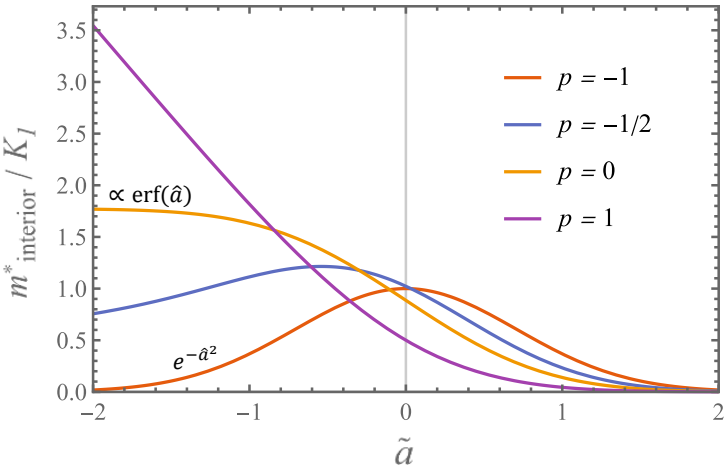


Figure 4.12: **The interior solution**. The function $e^{-\tilde{a}^2} H_{-1-p}(\tilde{a})$ from the interior solution (4.76) is shown for the values $p = -1$ (Gaussian limiting case), $-1/2$, 0 (sigmoid) and 1.

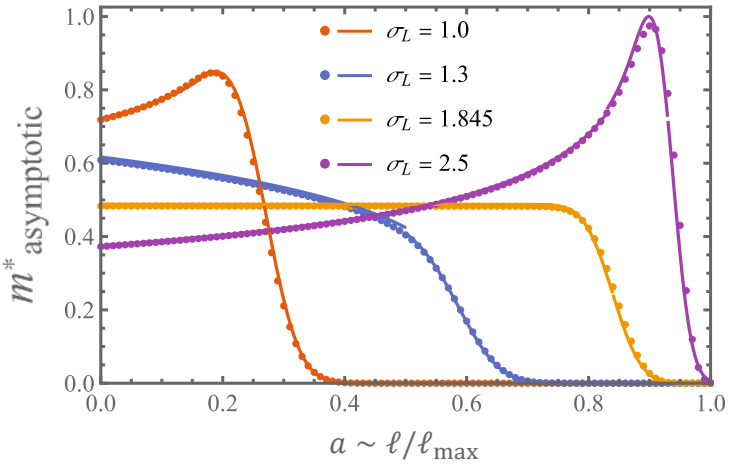


Figure 4.13: **Asymptotic solution vs. discrete model output.** The asymptotic solution of the continuum model, defined by Eq. (4.79), is plotted with the discrete model steady state distribution, $\ell_{\max} m^\star_\ell$, given by Eq. (4.48). We use $\sigma_H = 1$ and set the remaining parameter values according to Eqs. (4.25).

Comparing with $m^\star_{\text{right}}(a)$ shows that we must take $K_2 = 0$. As $\tilde{a} \to -\infty$, we use that

$$\begin{aligned} m^\star_{\text{interior}} &\sim -K_1 \pi^{1/2} \Gamma(-p) \sin(p\pi) (-\tilde{a})^p \\ &= -K_1 \pi^{1/2} \Gamma(-p) \sin(p\pi) a_c^p \epsilon^{-p/2} \Big(1 - \frac{a}{a_c}\Big)^p, \end{aligned} \tag{4.75}$$

and compare with $m^\star_{\text{left}}(a)$ to deduce that the matched interior solution is

$$m^\star_{\text{interior}}(\tilde{a}) = K_1 e^{-\tilde{a}^2} H_{-1-p}(\tilde{a}), \qquad \text{where} \quad K_1 = \frac{-R\sqrt{\pi}[2\epsilon a_c(1-a_c)]^{p/2}}{a_c^p \Gamma(-p)\sin(p\pi)}. \tag{4.76}$$

We note that $\Gamma(-p)\sin(p\pi) < 0$ for all $p > -1$ and so $K_1 > 0$.

The function $m^\star_{\text{interior}}/K_1$ in Eq. (4.76) is plotted for various values of p in Fig. 4.12. We divide by K_1 since it affects only the vertical scale of the interior solution. The function becomes increasingly asymmetric as p increases, transitioning from a bell curve

at $p = -1$, to a sigmoid at $p = 0$, and eventually a smoothed corner-like shape for $p > 0$. Consistent with these observations, we find that $m^\star_{\text{interior}}$ reduces exactly to a Gaussian in the limit $p \to (-1)^+$ and a sigmoid at $p = 0$:

$$m^\star_{\text{interior}}(\tilde{a}) \to K_1 e^{-a^2}, \qquad p \to (-1)^+; \tag{4.77}$$

$$m^\star_{\text{interior}}(\tilde{a}) = \frac{K_1\sqrt{\pi}}{2}\text{erf}(\tilde{a}), \qquad p = 0. \tag{4.78}$$

A leading order approximation for $m^\star(a)$ that is uniformly valid over $0 \leq a \leq 1$ is obtained by substituting $\tilde{a} = [2\epsilon a_c(1-a_c)]^{-1/2}(a - a_c)$ into Eq. (4.76):

$$m^\star_{\text{asymptotic}}(a) = K_1 \exp\left[-\frac{(a-a_c)^2}{2\epsilon a_c(1-a_c)}\right] H_{-1-p}\left(\frac{a-a_c}{\sqrt{2\epsilon a_c(1-a_c)}}\right). \tag{4.79}$$

We compare the matched solution (4.79) to the analytical solution (4.48) of the discrete model in Fig. 4.13. The plots show an excellent agreement between the asymptotic solution and discrete model.

4.4 Discussion

In this chapter, we presented a discretely structured model for MDM lipid accumulation in early atherosclerotic lesions. The model is formulated in terms of the extracellular lipid density, $L(t)$, the HDL lipid capacity, $H(t)$, and the MDM population, $m_\ell(t)$, which is structured by an index, $\ell = 0, 1, \ldots, \ell_{\max}$, according to lipid content. A key feature of the model is that lipid uptake and efflux events cause a finite change, Δa, to MDM lipid content. Our discretely-structured model formulation contrasts with the continuum approach proposed by Ford *et al.* [165]. It can also be reduced to a simpler, closed subsystem of ODEs for $L(t)$, $H(t)$, the total MDM density, $M(t)$, and the total MDM lipid content, $L_M(t)$.

A defining feature of our model is the treatment of MDM lipid uptake and efflux: the uptake rate is assumed to decrease linearly with lipid content, $k_L(\ell_{\max} - \ell)$, while the offloading rate increases linearly, according to $k_H\ell/\ell_{\max}$. These assumptions are consistent with current understanding that macrophages have a finite capacity for uptake due to intracellular negative-feedback signalling [94], and that intracellular cholesterol accumulation promotes the up-regulation of transporters that mediate cholesterol efflux [98]. An important consequence of our model formulation is that MDMs have a maximal lipid content, $\ell \leq \ell_{\max}$, since the uptake rate decreases to zero at $\ell = \ell_{\max}$. By contrast, the model proposed by Ford *et al.* [165] assumes that lipid uptake and efflux are independent of lipid content, and that there is no upper bound on macrophage lipid content. We further note that our simplifying assumption of linear dependence in ℓ for the uptake and efflux rates ensures the existence of a closed ODE subsystem: Eqs. (4.21)-(4.23). If the lipid-dependent rates were nonlinear in ℓ, the dynamics of $L_M(t)$ would not be expressible in terms of $M(t)$, $L_M(t)$, $L(t)$ and $H(t)$, and opportunities for mathematical analysis would be limited.

Our model analysis focused on the constants σ_L and σ_H which determine the influx of LDL lipid and HDL capacity, respectively. These parameters are expected to correlate strongly with blood LDL and HDL particle concentrations. Below, we discuss the key results in relation to the key questions posed in Sect. 4.1.

Q1.a. **How do the LDL and HDL influx rates impact lesion composition?**

Time-dependent numerical solutions showed that lesion composition develops through various stages in a manner that depends on the influx rates σ_L and σ_H. At early times, there is quasi-linear growth in $L(t)$ and $H(t)$ as LDL and HDL enter a lesion initially devoid of MDMs. The initial accumulation of extracellular lipid, $L(t)$, then drives an influx of MDMs, $M(t)$, and increases to intracellular lipid, $L_M(t)$, due to uptake. If the influx of LDL lipid relative to HDL capacity is sufficiently large ($\sigma_L - \sigma_H \gtrsim 0$), the MDM population will accumulate a substantial amount of lipid and, thereby, cause $H(t)$ to peak and decrease due to efflux. For values $\sigma_L - \sigma_H \lesssim 0$, the amount of lipid efflux is insufficient to cause $H(t)$ to decline. At long times, regardless of the values of σ_L and σ_H, the lesion develops to a nonzero equilibrium.

Steady state analysis of the subsystem (4.19)-(4.22) showed that the model has a unique physically-realistic equilibrium. Analysis of the steady state solutions indicated that the density of MDMs, $M^\star$, intracellular lipid, $L_M^\star$, extracellular lipid, $L^\star$, and HDL capacity, $H^\star$, also depend sensitively on the difference $(\sigma_L - \sigma_H)$; the model predicts that lesion composition is sensitive to the relative influx of LDL lipid relative to HDL capacity. More specifically, the steady state plots indicate that (σ_L, σ_H) space can be partitioned into three regions. Regions in which $\sigma_L - \sigma_H \lesssim 0$ correspond to healthy tissues in which the HDL capacity greatly exceeds the amounts of ingested and extracellular lipid. Where $0 \lesssim \sigma_L - \sigma_H \lesssim 5$, the HDL capacity is typically exhausted and lesions contain intermediate MDM and lipid densities. Finally, regions in which $\sigma_L - \sigma_H \gtrsim 5$ correspond to unhealthy lesions that are dominated by extracellular lipid and MDMs with lipid loads near capacity.

Q1.b. **How do the LDL and HDL influx rates impact the distribution of lipid in lesion MDMs?**

We analysed the MDM lipid distribution by deriving a continuum limit of the discrete ODEs for $m_\ell(t)$, $\ell = 0, 1, \ldots, \ell_{\max}$. The continuum model casts the MDM population as a continuous function, $m(a,t)$, where the continuous independent variable $0 \le a \le 1$ represents lipid content. The distribution $m(a,t)$ is governed by an advection-diffusion PDE (4.54) with appropriate boundary conditions (4.59).

We used the method of matched asymptotics to construct a leading order approximation to the equilibrium MDM lipid distribution, $m^\star(a)$, in the limit $\epsilon = \ell_{\max}^{-1} \to 0$.

We found that $m^\star(a)$ depends on two parameter groupings: $0 < a_c < 1$ and $p > -1$, defined in Eq. (4.63). The constant a_c approximates the maximal lipid load attained within the MDM population at equilibrium, and represents the MDM lipid load where uptake balances efflux. Near $a = a_c$, the advection velocity is $\mathcal{O}(\epsilon)$ and comparable to the diffusion terms. The quantity p determines the shape of $m^\star(a)$. Using the outer solution (4.70) as a guide, we found that $m^\star(a)$ is decreasing and convex for $p > 1$, decreasing and concave for $0 < a \lesssim a_c$ when $0 < p < 1$, quasi-uniform for $p = 0$, and unimodal with a local maximum near $a = a_c$ for $p < 0$. We note that the outer solution is discontinuous at $a = a_c$ for $p \leq 0$, and in the first derivative for $0 < p < 1$. Analysis within an interior region of $O(\epsilon^{1/2})$ width at $a = a_c$ is needed to construct a uniformly valid approximation for $m^\star(a)$, resulting in the solution (4.79). These observations highlight the importance of including second-order terms in the continuum approximation to capture the qualitative behaviour of the underlying discrete model. The second-order terms provide a diffusive effect that smooths the outer solution in the interior region where the advection velocity vanishes at leading order. We note that, overall, we have derived a uniformly valid asymptotic approximation, $m^\star_{\text{asymptotic}}$, of the continuum model steady state lipid distribution, $m^\star$, which, in turn, is a uniformly valid asymptotic approximation of the discrete model steady state lipid distribution, $m^\star_\ell$, such that

$$m^\star_{\text{asymptotic}}(\epsilon\ell) = m^\star(\epsilon\ell) + \mathcal{O}(\epsilon) = \epsilon^{-1} m^\star_\ell + \mathcal{O}(\epsilon) \quad \text{as } \epsilon = \ell_{\max}^{-1} \to 0, \tag{4.80}$$

for every $\ell = 0, 1, \ldots, \ell_{\max}$.

The parameter groupings a_c and p are sensitive to the influxes of LDL lipid (σ_L) and HDL capacity (σ_H). Like the steady state values of the reduced subsystem variables, the constant a_c increases with $(\sigma_L - \sigma_H)$; the higher the influx of LDL lipid relative to HDL capacity, the higher the lipid load of the most lipid-laden MDMs in the population. By contrast, the parameter p is non-monotonic in both σ_L and σ_H, and, hence, the shape of the distribution $m^\star(a)$ depends on the individual influxes of LDL lipid and HDL capacity. In particular, $m^\star(a)$ may adopt a peaked or quasi-uniform profile at low or high lipid loads. These results suggest that, unlike the maximally attained lipid load a_c, the geometric features of the MDM lipid distribution, such as its concavity and existence of local maximum, may be poor indicators of lesion progression.

Q2. **Can defective efferocytosis be plausibly attributed to uptake feedback in MDMs due to high lipid loads?**

Our results indicate that the uptake rate of the MDM population may become substantially diminished over time, even when the difference between the LDL lipid and HDL capacity influx rates is modest. This is mostly clearly seen in Fig. 4.7,

where we compute the fractional defect in uptake at steady state, $\mu^\star$; when $\sigma_L - \sigma_H \gtrsim 1$ the uptake efficiency drops by at least 50%. Our results further indicate that $\mu^\star$ and the approximate maximal MDM lipid burden, a_c, are highly correlated. Noting that $a_c \gtrsim 0.8$ for $\sigma_L - \sigma_H \gtrsim 1$, the model suggests that lesion MDMs may experience a decrease of 50% of more in their population-averaged uptake rate, purely due to lipid accumulation, if MDMs with lipid content near the capacity value are detected. These results indicate that uptake feedback (i.e., subcellular signalling that down-regulates uptake) in MDMs due to high lipid loads is likely to contribute to the emergence of defective efferocytosis in atherosclerotic lesions.

4.4.1 Limitations and relation to Chapters 5-7

A notable limitation of the lipid-structured model presented in this chapter is its simplistic treatment of extracellular lipid and HDL capacity. Two aspects of our formulation warrant further investigation.

- **Representation of extracellular lipid as a single species.** In practice, there are multiple sources of extracellular lipid within lesions: extracellular lipid is found within free-diffusing LDL, retained LDL, apoptotic MDMs, and necrotic debris. Each lipid species is subject to distinct kinetics, and, in particular, is ingested by MDMs at different rates. A natural question then arises: what value should be taken for k_L, the uptake rate of a combined extracellular lipid density? For simplicity and consistency with [10], we assumed that $k_L = 1$ (recall Eqs. (4.25)). By consequence, the composition of the model lesion is sensitive to the difference $(\sigma_L - \sigma_H)$. This dependence holds when the values of k_L and k_H are comparable. However, when k_L and k_H differ markedly, the model lesion composition depends on a *weighted* difference; $C\sigma_L - \sigma_H$, for some constant $C > 0$. We comment on this effect in Chapters 5-7, where we distinguish multiple forms of extracellular lipid, each with specific uptake rates.

- **Implicit treatment of blood LDL and HDL levels.** The current model does not contain blood LDL and HDL levels as explicit parameters. As clinical readouts, these quantities are desirable as components for mathematical models of atherosclerosis. The issue stems from our simplifying assumption that extracellular lipid and HDL capacity are sourced at constant rates from the blood. In practice, LDL and HDL diffuse into the lesion from the blood and may also diffuse back into the lumen depending on the concentrations on either side of the endothelium. We account for these effects in Chapters 5-7, where we use blood LDL lipid and HDL capacity as explicit parameters.

Conclusions. In this chapter we have presented a new lipid-structured model for MDMs in early atherosclerotic lesions. We showed that the overall lesion composition and distribution of lipid within the MDM population are highly sensitive to the influxes of LDL

lipid and HDL capacity. Our results support the notion that lesion lipid content is best reduced by simultaneously lowering LDL lipid levels and increasing HDL capacity levels in the blood. We also showed how the MDM lipid distribution may adopt one of several profiles at steady state. The steady state profile may be monotone decreasing (concave or convex), quasi-uniform or unimodal, depending on the influxes of LDL lipid and HDL capacity. In Chapters 5-7, we extend our lipid-structured model to account for MDM phenotype and spatial heterogeneity. Importantly, these models directly address the limitations outlined in Sect. 4.4.1 above. The models of Chapters 5-7 are formulated under a common framework that resolves the extracellular lipid into free LDL, retained LDL, apoptotic lipid and necrotic lipid. The models also share a common set of parameter values, derived from the biological literature, that includes distinct uptake rates for each form of extracellular lipid and explicitly accounts for blood LDL and HDL levels.

Chapter 5

A phenotype-lipid structured model

In this chapter, we extend the model of Chapter 4 to account for variation in both MDM phenotype *and* lipid content. The model couples the MDM dynamics to the densities of free LDL lipid, retained LDL lipid, apoptotic lipid, necrotic lipid and HDL lipid capacity, in addition to inflammatory and resolving mediators.

5.1 Introduction

MDMs in atherosclerotic lesions exhibit a continuum of inflammatory to resolving phenotypes [7]. This view supersedes the traditional dichotomous M1/M2 classification of macrophage phenotype; M1 and M2 polarisation now typically refer to the inflammatory and resolving extremes of a phenotype continuum, respectively. MDM phenotype modulation is reversible, and is largely determined by the balance between (pro-)inflammatory and (pro-)resolving mediators [7, 199]. Following the classification presented in Tabas *et al.* [199], inflammatory mediators include cytokines such as TNF and IL-1, that are secreted by MDMs upon uptake of modLDL [101], and damage associated molecular patterns (DAMPs) that are released upon the secondary necrosis of apoptotic cells [79]. Resolving mediators include the cytokines IL-10 and IL-13, and specialised pro-resolving lipid mediators. Resolving mediators are synthesised by MDMs upon apoptotic cell uptake [106] and interaction with HDL [108]. We note that LDL and HDL promote the synthesis of opposing mediator types (inflammatory and resolving respectively) and, so, are likely to induce opposing effects on MDM phenotype. Mediators are also produced by other cell types (e.g., T cells), but signalling from MDMs is likely to dominate in atherosclerotic lesions, where they are the most abundant immune cell type [200].

Motivated by the biological observations above, we use our dual-structured model to address the following questions:

Q1. **How do blood LDL and HDL levels impact lesion composition?**
   a. How do they affect the time-evolution of lesion composition?
   b. How do they affect lesion composition at steady state?

Q2. **How are phenotype and lipid content distributed among MDMs?**
   a. How do MDM phenotype and lipid content evolve over time?
   b. Are MDM phenotype and lipid content correlated?
   c. What are the qualitative features of the phenotype and lipid content marginal distributions at steady state?

The model developed in this chapter is unique in its representation of gradual phenotype modulation. Existing models of atherosclerosis which incorporate MDM phenotype do so via binary M1/M2 classification, rather than as a spectrum of values [130, 140, 148]. While these models are insightful in their ability to predict coarse-grained phenotypic features (e.g., proportion of M1-like vs. M2-like cells), the lack of intermediate states between the M1-like and M2-like phenotypes is inconsistent with the diversity of cell states revealed by single-cell RNA sequencing [190]. Other authors have proposed dual-structured mathematical models (e.g., [173–176], reviewed in [172]). A key difference between these existing models and ours relates to the time evolution of the structure variables: in most existing models, the structure variables are independent whereas in our model their time evolution is coupled.

The remainder of the chapter is structured as follows. Sect. 5.2 details the model development, including the derivation of a closed subsystem and discussion of parameter values. Sect. 5.3 contains the results of our model analysis. Key questions 1 and 2 are addressed in Sects. 5.3.1 and 5.3.2, respectively. Finally, we discuss the results and their implications in Sect. 5.4.

5.2 Model development

In this section we present a phenotype-lipid dual-structured model for MDM populations in early atherosclerosis. Model schematics for the MDM dynamics and LDL retention are given in Figs. 5.1 and 5.2, respectively.

5.2.1 Assumptions and definitions

We assume for simplicity that MDM phenotype and lipid content change by finite increments, $\Delta\phi = 1$ and $\Delta a > 0$, respectively. Specifically, we let $m_{\phi,\ell}(t)$ denote the number density of MDMs with phenotype ϕ and lipid content $a_0 + \ell\Delta a$ at time $t \geq 0$. The phenotype index runs over both positive and negative integer values: $\phi = 0, \pm 1, \ldots, \pm\phi_{\max}$. MDMs with $\phi > 0$ are pro-inflammatory and have an M1-like phenotype; those with $\phi < 0$ are resolving and have an M2-like phenotype. The extreme values $\phi = \pm\phi_{\max}$ can be interpreted as complete M1 and M2 polarisation. The lipid index runs over non-negative values: $\ell = 0, 1, \ldots, \ell_{\max}$, so that MDM lipid content ranges from their endogenous content, $a_0 \geq 0$, to a maximum value, $a_0 + \kappa$, where $\kappa := \ell_{\max}\Delta a$ is the maximum capacity for ingested lipid.

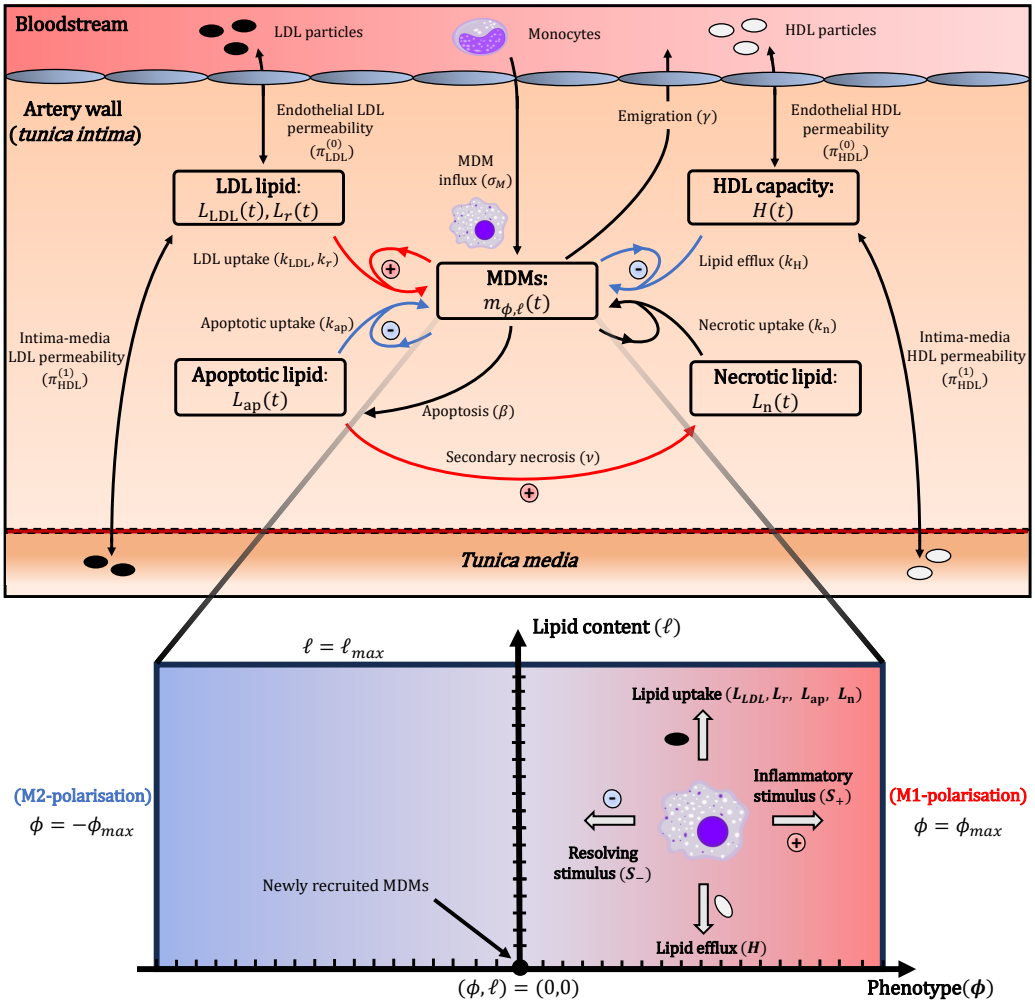


Figure 5.1: **A schematic of the MDM-lipid dynamics in the model.** Processes represented with blue arrows stimulate the secretion of resolving mediators by MDMs, while those represented by red arrow stimulate the emission of inflammatory mediators. The lower half illustrates the discrete phenotype-lipid structure space that underpins the MDM dynamics. LDL retention and constitutive mediator production by MDMs are not shown.

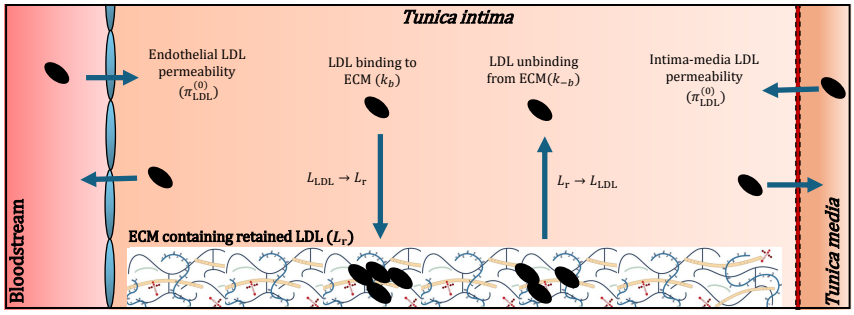


Figure 5.2: **Schematic of the LDL kinetics in absence of MDMs.** The model distinguishes between free LDL (L_{LDL}), which diffuses freely between the bloodstream, tunica intima and tunica media, and retained LDL (L_r) that is bound to the ECM within the tunica intima. We assume in Eqs. (5.7)-(5.8) that the ECM has a finite capacity for LDL retention, K_r, and that the rate of binding is proportional to the available capacity: $k_b(K_r - L_r)$.

We also introduce variables to describe the extracellular environment. We denote by $L_{LDL}(t) \geq 0$, $L_{\mathrm{r}}(t) \geq 0$, $L_{\mathrm{ap}}(t) \geq 0$ and $L_{\mathrm{n}}(t) \geq 0$ the mass densities of free LDL lipid, retained LDL lipid, apoptotic lipid and necrotic lipid respectively. We let $H(t)$ be the lipid capacity of HDL particles in the lesion. Finally, we denote by $S_+(t) \geq 0$ and $S_-(t) \geq 0$ the mass densities of inflammatory and resolving mediators respectively.

We note that all dependent variables in the model represent densities within the *tunica intima*. This is the innermost region of the artery wall where atherosclerosis develops [7]. As shown in Figs. 5.1 and 5.2, the intimal densities are nonetheless affected by the bloodstream and *tunica media* (the next layer of the artery wall) via the flux of cells and lipids. We assume for simplicity that the contents of the bloodstream and *tunica media* are static in the equations below.

5.2.2 Model equations

MDMs. We propose that the MDM population evolves according to the following ODEs:

$$\begin{aligned}\frac{d}{dt}m_{\phi,\ell} = \quad & \underbrace{\boldsymbol{k_L}\cdot\boldsymbol{L}\,\big[(\ell_{\max}-\ell+1)m_{\phi,\ell-1}-(\ell_{\max}-\ell)m_{\phi,\ell}\big]}_{\text{lipid uptake}} \\ & + \underbrace{k_H H \quad \big[(\ell+1)m_{\phi,\ell+1}-\ell m_{\phi,\ell}\big]}_{\text{lipid efflux to HDL}} \\ & + \underbrace{k_S\chi S_+\big[(\phi_{\max}-\phi+1)m_{\phi-1,\ell}-(\phi_{\max}-\phi)m_{\phi,\ell}\big]}_{\text{inflammatory phenotype modulation}} \\ & + \underbrace{k_S\chi S_-\big[(\phi_{\max}+\phi+1)m_{\phi+1,\ell}-(\phi_{\max}+\phi)m_{\phi,\ell}\big]}_{\text{resolving phenotype modulation}} \\ & + \underbrace{R_{\phi,\ell}(t)}_{\text{recruitment}} - \underbrace{(\beta+\gamma)m_{\phi,\ell}}_{\text{apoptosis and egress}},\end{aligned} \tag{5.1}$$

and closure conditions:

$$m_{\phi,-1} = m_{\phi,\ell_{\max}+1} = m_{-\phi_{\max}-1,\ell} = m_{\phi_{\max}+1,\ell} = 0, \tag{5.2}$$

for every $\phi = 0, \pm1, \ldots, \pm\phi_{\max}$ and $\ell = 0, 1, \ldots, \ell_{\max}$.

The first term on the right hand side (RHS) of Eqs. (5.1) accounts for lipid uptake. Following Chapter 4, we model lipid uptake with a mass-action treatment of the following reactions:

$$\mathrm{M}_{\phi,\ell} + \Delta a \xrightarrow{k_i(\ell_{\max}-\ell)} \mathrm{M}_{\phi,\ell+1}, \tag{5.3}$$

for every (ϕ,ℓ) and $i \in \{LDL, \mathrm{r}, \mathrm{ap}, \mathrm{n}\}$. Reactions (5.3) assume that the rate of lipid uptake decreases linearly with lipid content in a manner commensurate with available capacity. For notational brevity in Eqs. (5.1), we introduce vectors for the uptake rates, $\boldsymbol{k_L} := (k_{LDL}, k_{\mathrm{r}}, k_{\mathrm{ap}}, k_{\mathrm{n}})$, and the extracellular lipids, $\boldsymbol{L} := (L_{LDL}, L_{\mathrm{r}}, L_{\mathrm{ap}}, L_{\mathrm{n}})$, so that $\boldsymbol{k_L}\cdot\boldsymbol{L} = k_{LDL}L_{LDL} + k_{\mathrm{r}}L_{\mathrm{r}} + k_{\mathrm{ap}}L_{\mathrm{ap}} + k_{\mathrm{n}}L_{\mathrm{n}}$.

The second term of the RHS of Eqs. (5.1) accounts for lipid efflux to HDL. Again, following Chapter 4, we treat efflux with mass-action kinetics according to the reactions

$$\mathrm{M}_{\phi,\ell} \xrightarrow{k_H \ell} \mathrm{M}_{\phi,\ell-1}, \tag{5.4}$$

for every (ϕ, ℓ). The reactions (5.4) assume that the efflux rate increases linearly with lipid content.

The third and fourth terms of the RHS of Eqs. (5.1) account for MDM phenotype modulation by inflammatory and resolving mediators [7], S_+ and S_- respectively. We model phenotype modulation via the reactions

$$\mathrm{M}_{\phi,\ell} + \Delta s \to \begin{cases} \mathrm{M}_{\phi\pm1,\ell} & \text{with rate } p_\phi^\pm := k_S \chi(\phi_{\max} \mp \phi); \\ \mathrm{M}_{\phi,\ell} & \text{with rate } k_S(1 - p_\phi^\pm), \end{cases} \tag{5.5}$$

for every (ϕ, ℓ). Here k_S is the rate of mediator binding to MDM surface receptors and Δs is the mediator mass bound per interaction. We assume each mediator binding interaction stimulates a move to a new phenotype class with probability: $p_\phi^\pm = \chi(\phi_{\max} \mp \phi)$. The parameter $0 \leq \chi \leq (2\phi_{\max})^{-1}$ which modulates this probability can be interpreted as the phenotypic plasticity of the MDMs. We assume that $p_\phi^\pm$ decreases linearly to zero as $\phi \to \pm\phi_{\max}$, so that it becomes increasingly difficult for MDMs to become more polarised the more polarised they are. Biologically, this property reflects the saturation of intracellular signalling pathways when macrophages are continually exposed to inflammatory or resolving mediators.

The final terms on the RHS of Eqs. (5.1) account for MDM recruitment, apoptosis and egress. We assume that newly recruited MDMs enter the lesion from the bloodstream carrying only endogenous lipid and with an uncommitted phenotype:

$$R_{\phi,\ell}(t) := \begin{cases} \sigma_M \left(\frac{S_+}{S_+ + S_+^{\mathrm{c}50} + \rho S_-} \right) & \text{if } (\phi, \ell) = (0, 0); \\ 0 & \text{if } (\phi, \ell) \neq (0, 0). \end{cases} \tag{5.6}$$

The recruitment rate is a first-order Hill function of the inflammatory mediator density, S_+, which saturates at the maximum value σ_M. Resolving mediators, S_-, inhibit recruitment by linearly increasing the threshold for half-maximal recruitment from the basal value $S_+^{\mathrm{c}50}$; the parameter ρ governs the sensitivity of the recruitment rate to S_-. We assume for simplicity that the rates of MDM apoptosis, β, and egress, γ, are constant.

Extracellular lipids. We assume that the densities of free and retained LDL evolve

according to the ODEs

$$\begin{aligned}\frac{dL_{LDL}}{dt} = &\underbrace{\pi_L^{(0)}(L^{(0)} - L_{LDL})}_{\text{lumenal flux}} - \underbrace{\pi_L^{(1)}(L_{LDL} - L^{(1)})}_{\text{tunica media flux}} \\ &- \underbrace{k_b L_{LDL}(K_\text{r} - L_\text{r})}_{\text{retention via ECM binding}} + \underbrace{k_{-b} L_\text{r}}_{\text{unbinding}} \\ &\underbrace{- k_{LDL}\Delta a L_{LDL} \sum_{\phi,\ell}(\ell_\text{max} - \ell) m_{\phi,\ell}}_{\text{uptake by MDMs}},\end{aligned} \tag{5.7}$$

$$\begin{aligned}\frac{dL_\text{r}}{dt} = &+ k_b L_{LDL}(K_\text{r} - L_\text{r}) - k_{-b} L_\text{r} \\ &- k_\text{r}\Delta a L_\text{r} \sum_{\phi,\ell}(\ell_\text{max} - \ell) m_{\phi,\ell}.\end{aligned} \tag{5.8}$$

The first two terms on the RHS of Eq. (5.7) account for the flux of free LDL between the lesion and the lumen/tunica media. The parameters $\pi_L^{(0)}$ and $\pi_L^{(1)}$ denote the LDL exchange rate at the endothelium and internal elastic lamina, respectively. The densities of free LDL in the lumen, $L^{(0)}$, and tunica media, $L^{(1)}$, are assumed to be non-negative constants. We assume that free LDL binds to ECM proteoglycans with rate constant k_b in a capacity-limited manner, and unbinds at rate k_{-b}; the maximum capacity for LDL retention is K_r. The final terms on the RHS of Eqs. (5.7) and (5.8) account for MDM uptake of free and bound LDL via reactions (5.3).

We propose that the densities of apoptotic and necrotic lipid satisfy

$$\frac{dL_\text{ap}}{dt} = \underbrace{\beta \sum_{\phi,\ell}(a_0 + \ell\Delta a) m_{\phi,\ell}}_{\text{apoptosis}} - \nu L_\text{ap} - k_\text{ap}\Delta a L_\text{ap} \sum_{\phi,\ell}(\ell_\text{max} - \ell) m_{\phi,\ell}, \tag{5.9}$$

$$\frac{dL_\text{n}}{dt} = + \underbrace{\nu L_\text{ap}}_{\text{necrosis}} \underbrace{- k_\text{n}\Delta a L_\text{n} \sum_{\phi,\ell}(\ell_\text{max} - \ell) m_{\phi,\ell}}_{\text{uptake by MDMs}}. \tag{5.10}$$

The first term of the RHS of Eq. (5.9) accounts for lipid deposition into the extracellular space due to MDM apoptosis. We assume that apoptotic cells undergo secondary necrosis at rate ν, which provide linear sink and source terms in Eqs. (5.9) and (5.10), respectively. The final terms on the RHS of Eqs. (5.9) and (5.10) describe apoptotic and necrotic lipid uptake by MDMs.

HDL lipid capacity. We assume that the lipid capacity of the HDL particles in the lesion evolves according to

$$\frac{dH}{dt} = \underbrace{\pi_H^{(0)}(H^{(0)} - H)}_{\text{lumenal flux}} - \underbrace{\pi_H^{(1)}(H - H^{(1)})}_{\text{tunica media flux}} - \underbrace{k_H \Delta a H \sum_{\phi,\ell} \ell m_{\phi,\ell}}_{\text{lipid efflux by MDMs}}. \tag{5.11}$$

The first two terms on the RHS of Eq. (5.11) describe the flux of HDL lipid capacity (via HDL particle diffusion) between the lesion and the lumen/tunica media. For simplicity, we assume that the diffusivity of HDL particles is independent of their lipid capacity, so that $\pi_H^{(0)}$ and $\pi_H^{(1)}$ represent the common permeability of HDL particles and HDL lipid capacity at the endothelium and internal elastic lamina, respectively. The final term accounts for MDM lipid efflux to HDL particles.

Inflammatory and resolving mediators. We propose that the densities of inflammatory and resolving mediators satisfy the following ODEs:

$$\begin{aligned}\frac{dS_+}{dt} &= \underbrace{\alpha L_{\mathrm{r}}}_{\substack{\text{resident}\\ \text{signals}}} + \mu\Big[\underbrace{(k_{LDL}L_{LDL} + k_{\mathrm{r}}L_{\mathrm{r}})\Delta a \sum_{\phi,\ell}(\ell_{\max} - \ell)m_{\phi,\ell}}_{\text{LDL-stimulated emission}} + \underbrace{\nu L_{\mathrm{ap}}}_{\text{DAMPs}}\Big] \\ &\quad + \underbrace{k_c \sum_{\phi,\ell}\Big(1 + \frac{\phi}{\phi_{\max}}\Big)m_{\phi,\ell}}_{\text{MDM constitutive production}} - \underbrace{\Big[k_S\Delta s \sum_{\phi,\ell} m_{\phi,\ell} + \delta_S\Big]}_{\text{MDM binding and decay}} S_+,\end{aligned} \tag{5.12}$$

$$\begin{aligned}\frac{dS_-}{dt} &= \mu\Big[\underbrace{k_{\mathrm{ap}}\Delta a L_{\mathrm{ap}} \sum_{\phi,\ell}(\ell_{\max} - \ell)m_{\phi,\ell}}_{\text{efferocytosis-stimulated emission}} + \underbrace{k_H \Delta a H \sum_{\phi,\ell}\ell m_{\phi,\ell}}_{\text{HDL-stimulated emission}}\Big] \\ &\quad + k_c \sum_{\phi,\ell}\Big(1 - \frac{\phi}{\phi_{\max}}\Big)m_{\phi,\ell} - \Big[k_S\Delta s \sum_{\phi,\ell} m_{\phi,\ell} + \delta_S\Big]S_-.\end{aligned} \tag{5.13}$$

The first term on the RHS of Eq. (5.12) models the release of inflammatory signals by resident cells (e.g., smooth muscle cells, tissue-resident macrophages) [68]. The signal cascades which first stimulate MDM recruitment are currently unknown, but are thought to be the result of excessive LDL retention [59]. Hence, we assume for simplicity that the resident cells produce inflammatory mediators at rate proportional to the retained LDL lipid density.

Eqs. (5.12) and (5.13) also account for mediator production due to lipid activity. This includes MDM production of inflammatory mediators due to LDL uptake (both native and modified forms of LDL induce inflammatory responses in macrophages [102, 104]), and MDM production of resolving mediators upon apoptotic lipid uptake [106] and interaction with HDL [108]. We also include production of inflammatory DAMPs that are released by apoptotic bodies upon secondary necrosis [79]. We assume for simplicity that the magnitude of mediator production is proportional to the amount of lipid involved in each of the above interactions; the parameter μ represents the mediator mass produced per unit lipid.

The remaining source terms in Eqs. (5.12) and (5.13) account for constitutive mediator production by MDMs. Indeed, macrophages are potent cytokine emitters (even in the absence of stimulants [104]) and exhibit a phenotype-dependent secretion profile [105]. To account for these effects, we assume that MDMs constitutively produce mediators at the constant rate $2k_c$ per cell, but that the ratio of inflammatory to resolving mediator

production is skewed linearly according to phenotype. M1-polarised cells with $\phi = \phi_{\max}$ secrete only inflammatory mediators while M2-polarised cells with $\phi = -\phi_{\max}$ emit only resolving mediators.

We further assume that mediators bind to MDM surface receptors, according to reaction (5.5), and undergo natural decay at rate δ_S. We use a common decay rate for both inflammatory and resolving mediators since experimentally reported half-lives for inflammatory and resolving cytokines are comparable [201]. Similarly, we use a common binding rate in the absence of evidence for MDM preferential binding.

Initial conditions. We close Eqs. (5.1), (5.7)-(5.13) by supposing that at $t = 0$:

$$m_{\phi,\ell} = 0 \quad \text{for every } (\phi, \ell), \qquad L_{LDL} = L_{\mathrm{r}} = L_{\mathrm{ap}} = L_{\mathrm{n}} = H = S_{\pm} = 0. \tag{5.14}$$

The conditions (5.14) assume that the lesion is initially devoid of MDMs, extracellular lipid, HDL capacity and mediators.

5.2.3 A closed subsystem

We can derive a closed subsystem from Eqs. (5.1), (5.7)-(5.13) by defining the population variables:

$$M(t) := \sum_{\phi,\ell} m_{\phi,\ell}(t), \tag{5.15}$$

$$\hat{\Phi}_M(t) := \frac{1}{M(t)} \sum_{\phi,\ell} \Big(\frac{\phi}{\phi_{\max}}\Big) m_{\phi,\ell}(t), \tag{5.16}$$

$$\hat{L}_M(t) := \frac{1}{M(t)} \sum_{\phi,\ell} \Big(\frac{\ell}{\ell_{\max}}\Big) m_{\phi,\ell}(t). \tag{5.17}$$

Here $M(t) \geq 0$ represents the total MDM density. The quantity $-1 \leq \hat{\Phi}_M(t) \leq 1$ is the mean MDM phenotype, normalised such that $\hat{\Phi}_M = 1$ corresponds to M1-polarisation and $\hat{\Phi}_M = -1$ to M2-polarisation. Finally, $0 \leq \hat{L}_M(t) \leq 1$ is the mean MDM lipid content, normalised by the maximal capacity.

By differentiating definitions (5.15)-(5.17) with respect to time and substituting from Eqs. (5.1), we obtain ODEs for M, $\hat{\Phi}_M$ and $\hat{L}_M$:

$$\frac{dM}{dt} = \left(\frac{\sigma_M S_+}{S_+ + S_+^{\mathrm{c50}} + \rho S_-}\right) - (\beta + \gamma) M, \tag{5.18}$$

$$\frac{d\hat{\Phi}_M}{dt} = k_s \chi \big[S_+(1 - \hat{\Phi}_M) - S_-(1 + \hat{\Phi}_M)\big] - \left(\frac{\sigma_M S_+}{S_+ + S_+^{\mathrm{c50}} + \rho S_-}\right) \frac{\hat{\Phi}_M}{M}, \tag{5.19}$$

$$\frac{d\hat{L}_M}{dt} = \boldsymbol{k_L} \cdot \boldsymbol{L}\ (1 - \hat{L}_M) - k_H H \hat{L}_M \qquad - \left(\frac{\sigma_M S_+}{S_+ + S_+^{\mathrm{c50}} + \rho S_-}\right) \frac{\hat{L}_M}{M}. \tag{5.20}$$

Sink terms arise in Eqs. (5.19) and (5.20) because recruited MDMs enter the lesion with $\phi = \ell = 0$, reducing the mean (absolute) phenotype and lipid content. We can also rewrite

Eqs. (5.7)-(5.13) as follows:

$$\begin{aligned}\frac{dL_{LDL}}{dt} = {} & \pi_L^{(0)}(L^{(0)} - L_{LDL}) - \pi_L^{(1)}(L_{LDL} - L^{(1)}) \\ & - k_b L_{LDL}(K_\mathrm{r} - L_\mathrm{r}) \quad + k_{-b} L_\mathrm{r} \quad - k_{LDL}\kappa L_{LDL} M(1 - \hat{L}_M),\end{aligned} \tag{5.21}$$

$$\frac{dL_\mathrm{r}}{dt} = k_b L_{LDL}(K_\mathrm{r} - L_\mathrm{r}) - k_{-b} L_\mathrm{r} - k_\mathrm{r}\kappa L_\mathrm{r} M(1 - \hat{L}_M), \tag{5.22}$$

$$\frac{dL_\mathrm{ap}}{dt} = \beta M(1 + \kappa \hat{L}_M) - \nu L_\mathrm{ap} - k_\mathrm{ap}\kappa L_\mathrm{ap} M(1 - \hat{L}_M), \tag{5.23}$$

$$\frac{dL_\mathrm{n}}{dt} = \nu L_\mathrm{ap} - k_\mathrm{n}\kappa L_\mathrm{n} M(1 - \hat{L}_M), \tag{5.24}$$

$$\frac{dH}{dt} = \pi_H^{(0)}(H^{(0)} - H) - \pi_L^{(1)}(H - H^{(1)}) - k_H \kappa H M \hat{L}_M, \tag{5.25}$$

$$\begin{aligned}\frac{dS_+}{dt} = {} & \alpha L_\mathrm{r} + \mu\Big[(k_{LDL} L_{LDL} + k_\mathrm{r} L_\mathrm{r})\kappa M(1 - \hat{L}_M) + \nu L_\mathrm{ap}\Big] \\ & + k_c M(1 + \hat{\Phi}_M) - (k_S \Delta s M + \delta_S) S_+,\end{aligned} \tag{5.26}$$

$$\begin{aligned}\frac{dS_-}{dt} = {} & \mu\Big[k_\mathrm{ap}\kappa L_\mathrm{ap} M(1 - \hat{L}_M) + k_H \kappa H M \hat{L}_M\Big] \\ & + k_c M(1 - \hat{\Phi}_M) - (k_S \Delta s M + \delta_S) S_-.\end{aligned} \tag{5.27}$$

Eqs. (5.18)-(5.27) with the initial conditions (5.14) comprise a closed subsystem that can be solved independently of Eq. (5.1).

5.2.4 Parameter values

The parameters that appear in Eqs. (5.1),(5.18)-(5.27) are summarised in Table 5.1.

The blood densities of LDL lipid, $L^{(0)}$, and HDL lipid capacity, $H^{(0)}$, are key parameters in our model. Since these quantities are sensitive to modifiable lifestyle factors such as diet and exercise [38], we explore a range of plausible values in our analysis. The range for $L^{(0)}$ is based on the human serum LDL cholesterol distribution reported in [32], in which 99.8% of the subjects had LDL cholesterol below 280mg/dL. We multiply this figure by 78/50 to account for LDL phospholipid to obtain an upper estimate of 480mg/dL [39]. We take $H^{(0)} = 230$ mg/dL as a conservative upper bound, which exceeds the highest recorded HDL cholesterol concentrations ($\sim$193mg/dL) in a sample of 116508 individuals from the general population [202].

We consider a range of values for the LDL retention capacity, K_r, since it varies between artery wall sections [24]. As LDL retention is driven by LDL-proteoglycan binding, we estimate K_r by considering the artery wall proteoglycan density. Artery wall extracellular matrix prior to atherosclerosis-induced collagen degradation consists of 4% proteoglycan and 40% collagen [208]. Using $0.01 - 3$ mg/mL as an estimate for the collagen density (0.75 mg/mL is used to replicate the tunica intima in culture models [210]), we obtain a proteoglycan density of $0.001 - 0.3$ mg/mL. Assuming each proteoglycan molecule (est. mass 800 kDa [234]) can support a single aggregate of LDL (typical diameter 75 nm, corresponding to 0.0002 pg lipid for spherical droplets [209]), we estimate

Table 5.1: Model parameters

Parameter	Interpretation	Estimate	Source
$L^{(0)}$	Lumen LDL lipid density	$0 - 440$ mg/dL	[32, 39]
$H^{(0)}$	Lumen HDL lipid capacity	$0 - 230$ mg/dL	[202]
$\pi_L^{(0)}$	Endothelial LDL exchange rate	1.5 month^{-1}	[203, 204]
$\pi_H^{(0)}$	Endothelial HDL exchange rate	3.0 month^{-1}	[205], $\approx 2\pi_L^{(0)}$
$L^{(1)}$	Tunica media LDL lipid density	0 mg/dL	[206]
$H^{(1)}$	Tunica media HDL lipid capacity	0 mg/dL	[206], est.
$\pi_L^{(1)}$	Internal elastic lamina LDL exchange rate	4.5 month^{-1}	[207], $\approx 3\pi_L^{(0)}$
$\pi_H^{(1)}$	Internal elastic lamina HDL exchange rate	9.0 month^{-1}	[207], $\approx 3\pi_H^{(0)}$
K_r	LDL retention capacity	$15 - 7500$ mg/dL	[208–210]
k_b	LDL retention rate	0.008 dL/mg month^{-1}	[206, 211]
k_{-b}	LDL unbinding rate	1.8 month^{-1}	[206, 211]
σ_M	Maximum MDM entry rate	17000 mm^{-3} month^{-1}	[212–214]
β	MDM apoptosis rate	1.0 month^{-1}	[68, 215]
γ	MDM egress rate	0.2 month^{-1}	[214, 216], est.
ν	Secondary necrosis rate	37 month^{-1}	[217]
a_0	MDM endogenous lipid	27pg	[218, 219]
κ	MDM lipid capacity	800pg	[133], $\approx 29a_0$
k_{LDL}	LDL lipid uptake rate	0.00034 dL/mg month^{-1}	[90]
k_r	rLDL lipid uptake rate	0.023 dL/mg month^{-1}	[90]
k_ap	Apoptotic lipid uptake rate	0.060 dL/mg month^{-1}	[220, 221]
k_n	Necrotic lipid uptake rate	0.015 dL/mg month^{-1}	[222], $\approx k_\mathrm{ap}/4$
k_H	Lipid efflux rate	0.34 dL/mg month^{-1}	[223, 224]
S_+^{c50}	Mediator density for half-maximum MDM recruitment	5 ng/mL	[225, 226]
ρ	Sensitivity of MDM recruitment to resolving mediators	0.40	[227]
δ_S	Mediator natural decay rate	1600 month^{-1}	[201]
Δs	Mediator mass	17 kDa	[228]
k_s	Mediator binding rate to MDM surface receptors	8800 mL/ng month^{-1}	[229, 230]
k_c	Constitutive mediator production rate by MDMs	1.5 pg month^{-1}	[231]
μ	Mediator production per unit lipid stimulus	0.042	[231]
α	Resident inflammatory mediator production per rLDL lipid	3.5×10^{-3} month^{-1}	[68]
χ	MDM phenotypic plasticity	6.0×10^{-6}	[232]
Δa	MDM uptake/efflux increment of lipid	16 pg	[91, 233], $\in (75\mathrm{kDa}, a_0)$
$\ell_{\max}$	Maximum MDM lipid capacity per uptake/efflux increment	100	$= \kappa/\Delta a$
$\phi_{\max}$	Half the maximum number of MDM phenotype classes	50	$< (2\chi)^{-1}$

$K_{\mathrm{r}} \approx 15 - 4500$ mg/dL.

The values of the remaining parameters are fixed. We provide further details below.

- **Exchange rates**. The parameters π_L^0, π_L^1, π_H^0 and π_H^1 are obtained by dividing the respective permeabilities by the human coronary artery tunica intima thickness (~ 0.4 mm [9]). We note that the intimal thickness in mice is considerably smaller (~ 0.025 mm [235, 236]), and so murine exchange rates are higher.

- **Maximum MDM entry rate**. The parameter σ_M is based on data from monocyte transmigration experiments [212]. Specifically, Williams *et al.* observed that when human monocytes were placed above stimulated endothelial cells, approximately 20% entered the sub-endothelial layer within 1.5 hours. Multiplying this rate by 350 mm^{-3}, a typical blood monocyte density [213], gives 34000 mm^{-3} per month. Since approximately half the incoming monocytes do not differentiate into macrophages and leave the lesion within 48 hours [214], we estimate $\sigma_M = 17000$ mm^{-3} per month.

- **Uptake and efflux rates.** The uptake and efflux rates are obtained from *in vitro* experiments. We note that the free LDL uptake rate, k_{LDL}, is calibrated to data for native LDL (data for oxidised LDL yields a slightly higher but comparable estimate), while the larger rLDL uptake rate, k_{r}, is based on aggregated LDL data. This is reasonable since proteoglycan-bound LDL aggregates into lipid droplets that are more readily taken up by MDMs *in vivo* [53]. The apoptotic lipid uptake rate, k_{ap}, has been scaled down from its *in vitro* estimate by a factor 19 to account for the 19-fold deficiency in efferocytosis measured in human atherosclerotic plaques [221].

- **Mediator mass and decay.** The mediator mass, Δs, and natural decay rate, δ_S, are based on data for the inflammatory mediator TNF, which has a molecular weight of 17 kDa in its secreted form as a monomer and a 19 minute half-life [201, 228]. Other mediators have a comparable mass and half-life (e.g., 15 kDa and 20 minutes, respectively, for the resolving mediator IL-4 [201]).

- **Resident mediator production.** We estimate the rate of rLDL-stimulated mediator production from resident cells, α, using reports that MDMs are observed in murine atherosclerotic lesions within 2 weeks of high fat diet treatment [68]. The value $\alpha = 3.5 \times 10^{-3}$ per month ensures that the MDM density in our model is approximately 350 mm^{-3} (approximately the blood monocyte concentration) in 2 weeks when $L^{(0)} = 750$ mg/dL.

- **MDM phenotypic plasticity.** The parameter χ is calibrated to experiments of macrophage phenotype modulation *in vitro* [232]. Tarique *et al.* observed that

macrophages exposed to inflammatory and resolving mediators at 20 ng/mL underwent phenotypic polarisation in 2 days. We fix $\chi = 6.3 \times 10^{-4}$ so that phenotype modulation in our model occurs on this timescale (i.e., $\hat{\Phi}_M(t = 2\text{days}) = \pm 1/2$ if $S_\pm = 20\text{ng/mL}$ and $\hat{\Phi}_M(t = 0) = 0$).

- **Increments of lipid content and phenotype.** The lipid uptake/efflux increment, Δa, and maximal structure indices, $\ell_{\max}$ and $\phi_{\max}$, are model abstractions. In reality, lipid increments vary substantially depending on the specific interaction. The smallest increment is likely that associated with efflux, given that each HDL particle can store approximately 75 kDa of cholesterol. The largest increment is likely that due to apoptotic or necrotic lipid uptake, which we can assume to be smaller than the endogenous lipid content, a_0, since cellular uptake *in vivo* is typically piecemeal rather than involving whole cell engulfment [91]. We fix $\Delta a = 16$ pg as a reasonable intermediate value. This choice means that $\ell_{\max} = \kappa/\Delta a \approx 100$. The value of $\phi_{\max}$ has an upper bound of $(2\chi)^{-1} \approx 83000$ since the phenotype transition probabilities in Eqs. (5.5) must satisfy $p_\phi^\pm \leq 1$. We fix $\phi_{\max} = 50$ so that phenotype and lipid content are equally resolved in our model.

5.2.5 Non-dimensionalisation

We recast the model in terms of the following dimensionless variables:

$$\begin{aligned} &\tilde{t} := \beta t, && \tilde{m}_{\phi,\ell}(\tilde{t}) := \frac{\beta}{\sigma_M} m_{\phi,\ell}(t), && \tilde{M}(\tilde{t}) := \frac{\beta}{\sigma_M} M(t), \\ &\tilde{\boldsymbol{L}}(\tilde{t}) := \frac{\beta}{a_0 \sigma_M} \boldsymbol{L}(t), && \tilde{H}(\tilde{t}) := \frac{\beta}{a_0 \sigma_M} H(t), && \tilde{S}_\pm(\tilde{t}) := \frac{1}{S_+^{\text{c50}}} S_\pm(t). \end{aligned} \tag{5.28}$$

This scaling measures time in units of mean MDM lifespan, $\beta^{-1} \approx 1\,\text{month}$, and MDM densities relative to the maximum influx per MDM lifespan, $\sigma_M \beta^{-1} \approx 17000\ \text{mm}^{-3}$. We express the extracellular lipid densities and HDL lipid capacity relative to the maximum influx of MDM endogenous lipid per MDM lifespan, $a_0 \sigma_M \beta^{-1} \approx 45$ mg/dL. Mediator densities are measured relative to the density for half-maximal MDM recruitment, $S_+^{\text{c50}} \approx 5$ ng/mL. We also introduce a number of dimensionless parameters in Table 5.2.

Applying the non-dimensionalisation (5.28) and definitions of Table 5.2, and dropping the tildes for notational convenience, we obtain the following dimensionless ODEs for the MDM population:

$$\begin{aligned} \frac{d}{dt} m_{\phi,\ell} = \quad & \boldsymbol{k_L} \cdot \boldsymbol{L} \big[(\ell_{\max} - \ell + 1) m_{\phi,\ell-1} - (\ell_{\max} - \ell) m_{\phi,\ell} \big] \\ & + k_H H \ \big[(\ell + 1) m_{\phi,\ell+1} - \ell m_{\phi,\ell} \big] \\ & + \chi S_+ \ \big[(\phi_{\max} - \phi + 1) m_{\phi-1,\ell} - (\phi_{\max} - \phi) m_{\phi,\ell} \big] \\ & + \chi S_- \ \big[(\phi_{\max} + \phi + 1) m_{\phi+1,\ell} - (\phi_{\max} + \phi) m_{\phi,\ell} \big] \\ & + R_{\phi,\ell} - (1 + \gamma) m_{\phi,\ell}, \end{aligned} \tag{5.29}$$

Table 5.2: Dimensionless parameters in the rescaled Eqs. (5.29)-(5.41)

Parameter	Definition	Interpretation	Estimate
$\tilde{L}^\star$	$\frac{\beta}{a_0\sigma_M}L^{(0)}$	Lumen LDL lipid density	$0-10$
$\tilde{H}^\star$	$\frac{\beta}{a_0\sigma_M}H^{(0)}$	Lumen HDL lipid capacity	$0-5$
$\tilde{K}_{\mathrm{r}}$	$\frac{\beta}{a_0\sigma_M}K_r$	LDL retention capacity	$0.3-100$
$\tilde{\pi}_L^{(0)}$	$\frac{1}{\beta}\pi_L^{(0)}$	Endothelial LDL exchange rate	1.5
$\tilde{\pi}_H^{(0)}$	$\frac{1}{\beta}\pi_H^{(0)}$	Endothelial HDL exchange rate	3.0
$\tilde{\pi}_L^{(1)}$	$\frac{1}{\beta}\pi_L^{(1)}$	Internal elastic lamina LDL exchange rate	4.5
$\tilde{\pi}_H^{(1)}$	$\frac{1}{\beta}\pi_H^{(1)}$	Internal elastic lamina HDL exchange rate	9.0
$\tilde{k}_b$	$\frac{a_0\sigma_M}{\beta^2}k_b$	LDL retention rate	2.7
$\tilde{k}_{-b}$	$\frac{1}{\beta}k_{-b}$	LDL unbinding rate	1.8
$\tilde{\gamma}$	$\frac{1}{\beta}\gamma$	MDM egress rate	0.2
$\tilde{\nu}$	$\frac{1}{\beta}\nu$	Secondary necrosis rate	37
$\tilde{\kappa}$	$\frac{1}{a_0}\kappa$	MDM lipid capacity per unit endogenous lipid	29
$\tilde{k}_{LDL}$	$\frac{a_0\sigma_M}{\beta^2}k_{LDL}$	LDL uptake rate	0.016
$\tilde{k}_{\mathrm{r}}$	$\frac{a_0\sigma_M}{\beta^2}k_{\mathrm{r}}$	rLDL uptake rate	1.1
$\tilde{k}_{\mathrm{ap}}$	$\frac{a_0\sigma_M}{\beta^2}k_{\mathrm{ap}}$	Apoptotic lipid uptake rate	5.5
$\tilde{k}_{\mathrm{n}}$	$\frac{a_0\sigma_M}{\beta^2}k_{\mathrm{n}}$	Necrotic lipid uptake rate	1.4
$\tilde{k}_H$	$\frac{a_0\sigma_M}{\beta^2}k_H$	Lipid efflux rate	16
$\tilde{\rho}$	ρ	MDM influx sensitivity to resolving mediators	0.4
$\tilde{k}_S$	$\frac{\sigma_M\Delta_S}{\beta^2}k_S$	Mediator binding rate to MDM receptors	47
$\tilde{\delta}_S$	$\frac{1}{\beta}\delta_S$	Mediator natural decay rate	1600
$\tilde{k}_c$	$\frac{\sigma_M}{S_+^{\mathrm{c50}}\beta^2}k_c$	Constitutive MDM mediator production rate	5100
$\tilde{\mu}$	$\frac{a_0\sigma_M}{S_+^{\mathrm{c50}}\beta}\mu$	Lipid-stimulated mediator production	9200
$\tilde{\alpha}$	$\frac{a_0\sigma_M}{S_+^{\mathrm{c50}}\beta^2}\alpha$	Resident mediator production per rLDL lipid	850
$\tilde{\chi}$	$\frac{k_S S_+^{\mathrm{c50}}}{\sigma_M}\chi$	MDM phenotypic plasticity	0.28
$\phi_{\max}$	$\phi_{\max}$	MDM phenotype resolution	50
$\ell_{\max}$	$\ell_{\max}$	MDM maximum lipid capacity	100

where

$$R_{\phi,\ell} := \begin{cases} \frac{S_+}{S_+ + 1 + \rho S_-} & \text{if } (\phi,\ell) = (0,0); \\ 0 & \text{if } (\phi,\ell) \neq (0,0), \end{cases} \tag{5.30}$$

$$m_{\phi,-1} = m_{\phi,\ell_{\max}+1} = m_{-\phi_{\max}-1,\ell} = m_{\phi_{\max}+1,\ell} = 0, \tag{5.31}$$

for every $\phi = 0, \pm 1, \ldots, \pm\phi_{\max}$ and $\ell = 0, 1, \ldots, \ell_{\max}$, and $\boldsymbol{k_L} \cdot \boldsymbol{L} = k_{LDL} L_{LDL} + k_{\mathrm{r}} L_{\mathrm{r}} + k_{\mathrm{ap}} L_{\mathrm{ap}} + k_{\mathrm{n}} L_{\mathrm{n}}$. The remaining variables solve the closed subsystem

$$\frac{dM}{dt} = \frac{S_+}{S_+ + 1 + \rho S_-} - (1+\gamma) M, \tag{5.32}$$

$$\frac{d\hat{\Phi}_M}{dt} = \chi\big[S_+(1-\hat{\Phi}_M) - S_-(1+\hat{\Phi}_M)\big] - \Big(\frac{S_+}{S_+ + 1 + \rho S_-}\Big)\frac{\hat{\Phi}_M}{M}, \tag{5.33}$$

$$\frac{d\hat{L}_M}{dt} = \boldsymbol{k_L} \cdot \boldsymbol{L}(1-\hat{L}_M) - k_H H \hat{L}_M - \Big(\frac{S_+}{S_+ + 1 + \rho S_-}\Big)\frac{\hat{L}_M}{M}, \tag{5.34}$$

$$\begin{aligned} \frac{dL_{LDL}}{dt} = {} & \pi_L^{(0)}(L^\star - L_{LDL}) - \pi_L^{(1)} L_{LDL} \\ & - k_b L_{LDL}(K_{\mathrm{r}} - L_{\mathrm{r}}) + k_{-b} L_{\mathrm{r}} - k_{LDL}\kappa L_{LDL} M(1-\hat{L}_M), \end{aligned} \tag{5.35}$$

$$\frac{dL_{\mathrm{r}}}{dt} = k_b L_{LDL}(K_{\mathrm{r}} - L_{\mathrm{r}}) - k_{-b} L_{\mathrm{r}} - k_{\mathrm{r}}\kappa L_{\mathrm{r}} M(1-\hat{L}_M), \tag{5.36}$$

$$\frac{dL_{\mathrm{ap}}}{dt} = M(1+\kappa\hat{L}_M) - \nu L_{\mathrm{ap}} - k_{\mathrm{ap}}\kappa L_{\mathrm{ap}} M(1-\hat{L}_M), \tag{5.37}$$

$$\frac{dL_{\mathrm{n}}}{dt} = \nu L_{\mathrm{ap}} - k_{\mathrm{n}}\kappa L_{\mathrm{n}} M(1-\hat{L}_M), \tag{5.38}$$

$$\frac{dH}{dt} = \pi_H^{(0)}(H^\star - H) - \pi_L^{(1)} H - k_H \kappa H M \hat{L}_M, \tag{5.39}$$

$$\begin{aligned} \frac{dS_+}{dt} = {} & \alpha L_{\mathrm{r}} + \mu\Big[(k_{LDL} L_{LDL} + k_{\mathrm{r}} L_{\mathrm{r}})\kappa M(1-\hat{L}_M) + \nu L_{\mathrm{ap}}\Big] \\ & + k_c M(1+\hat{\Phi}_M) - (k_S M + \delta_S) S_+, \end{aligned} \tag{5.40}$$

$$\begin{aligned} \frac{dS_-}{dt} = {} & \mu\Big[k_{\mathrm{ap}}\kappa L_{\mathrm{ap}} M(1-\hat{L}_M) + k_H \kappa H M \hat{L}_M\Big] \\ & + k_c M(1-\hat{\Phi}_M) - (k_S M + \delta_S) S_-. \end{aligned} \tag{5.41}$$

Finally, we assume that at $t = 0$:

$$m_{\phi,\ell} = 0 \quad \text{for every } (\phi,\ell), \qquad L_{LDL} = L_{\mathrm{r}} = L_{\mathrm{ap}} = L_{\mathrm{n}} = H = S_\pm = 0. \tag{5.42}$$

5.2.6 Numerical solutions and timescales

The dimensionless parameters in Table 5.2 span several orders of magnitude. In particular, the mediator parameters α, δ_S, k_S and μ are considerably larger than the other constants. Numerical solutions of Eqs. (5.29)-(5.41) consequently require small timesteps to maintain stability. We address this issue in our numerical solutions, computed with Wolfram Mathematica, by using the routine *NDSolve* with the "StiffnessSwitching" option. To ensure the validity of numerical solutions, we checked that the output of *NDSolve* was robust to decreases in "MaxStepSize", increases in "PrecisionGoal" and "AccuracyGoal", and consistent with the steady state solutions (computed with *NSolve*) in Sect. 5.3.1.2 and the analytical steady state results in Sect. 5.3.2.4.

We note that another way to reduce numerical stiffness is to approximate the mediator dynamics via separation of timescales. With $\delta_S^{-1} \ll 1$ and assuming that α, k_S, $\mu = \mathcal{O}(\delta_S)$, it is straightforward to show that $S_\pm$ satisfy the following uniformly-valid quasi-steady state approximations:

$$\begin{aligned} S_+ \sim\ & \hat{\alpha} L_{\mathrm{r}} + \hat{\mu}\big[(k_{LDL} L_{LDL} + k_{\mathrm{r}} L_{\mathrm{r}})\kappa M(1-\hat{L}_M) + \nu L_{\mathrm{ap}}\big] \\ & + \hat{k}_c M(1+\hat{\Phi}_M), \end{aligned} \tag{5.43}$$

$$S_- \sim\ \hat{\mu}\kappa M\big[k_{\mathrm{ap}} L_{\mathrm{ap}}(1-\hat{L}_M) + k_H H \hat{L}_M\big] + \hat{k}_c M(1-\hat{\Phi}_M), \text{ as } \delta_S^{-1} \to 0, \tag{5.44}$$

where $\hat{\alpha} := \alpha/\delta_S$, $\hat{\mu} := \mu/\delta_S$ and $\hat{k}_c := k_c/\delta_S$. Although approximations (5.43)-(5.44) are not used for the simulations presented in Sect. 5.3, they reveal that, at leading order, the mediator densities are proportional to their net rates of production.

5.3 Results

We present the results in two sections. In Sect. 5.3.1 we analyse the subsystem (5.32)-(5.41) to generate insight into lesion composition. In Sect. 5.3.2 we focus on the MDM phenotype-lipid distribution.

5.3.1 Lesion composition

We begin our analysis of lesion composition by computing time-dependent solutions of the subsystem (5.32)-(5.41); the results are presented in Sect. 5.3.1.1. In Sect. 5.3.1.2 we then analyse the impact of the key parameters: $L^\star$, $H^\star$ and K_{r} on the steady state values.

5.3.1.1 Time evolution

Two typical numerical solutions of the subsystem (5.32)-(5.41) are shown in Fig. 5.3. The left and right solutions respectively correspond to healthy ($L^\star = 3$, $H^\star = 2$) and unhealthy ($L^\star = 4$, $H^\star = 0.5$) blood levels of LDL lipid and HDL capacity. We set $K_{\mathrm{r}} = 25$ for both cases. The quantity $L(t)$ in plots (d) and (i) is the total extracellular lipid density:

$$L(t) := L_{LDL}(t) + L_{\mathrm{r}}(t) + L_{\mathrm{ap}}(t) + L_{\mathrm{n}}(t), \tag{5.45}$$

whereas plots (e) and (j) show the components of the total lesion lipid content:

$$L_{\mathrm{tot}}(t) := L_{LDL}(t) + L_{\mathrm{r}}(t) + \big[1 + \kappa \hat{L}_M(t)\big] M(t) + L_{\mathrm{ap}}(t) + L_{\mathrm{n}}(t), \tag{5.46}$$

which includes MDM lipid. The model dynamics can be broadly divided into three phases that we detail below.

The first weeks, $0 < t < 0.5$, are characterised by the influx of LDL, HDL and MDMs. LDL and HDL enter the lesion first at $t = 0$ (see initial rise in $L(t)$ and $H(t)$ in Figs. 5.3 (d, i)). The lesion is initially dominated by free LDL for $0 < t < 0.02$, due to LDL influx from the blood, and rLDL for $0.02 < t < 0.1$, due to LDL retention to ECM proteoglycans

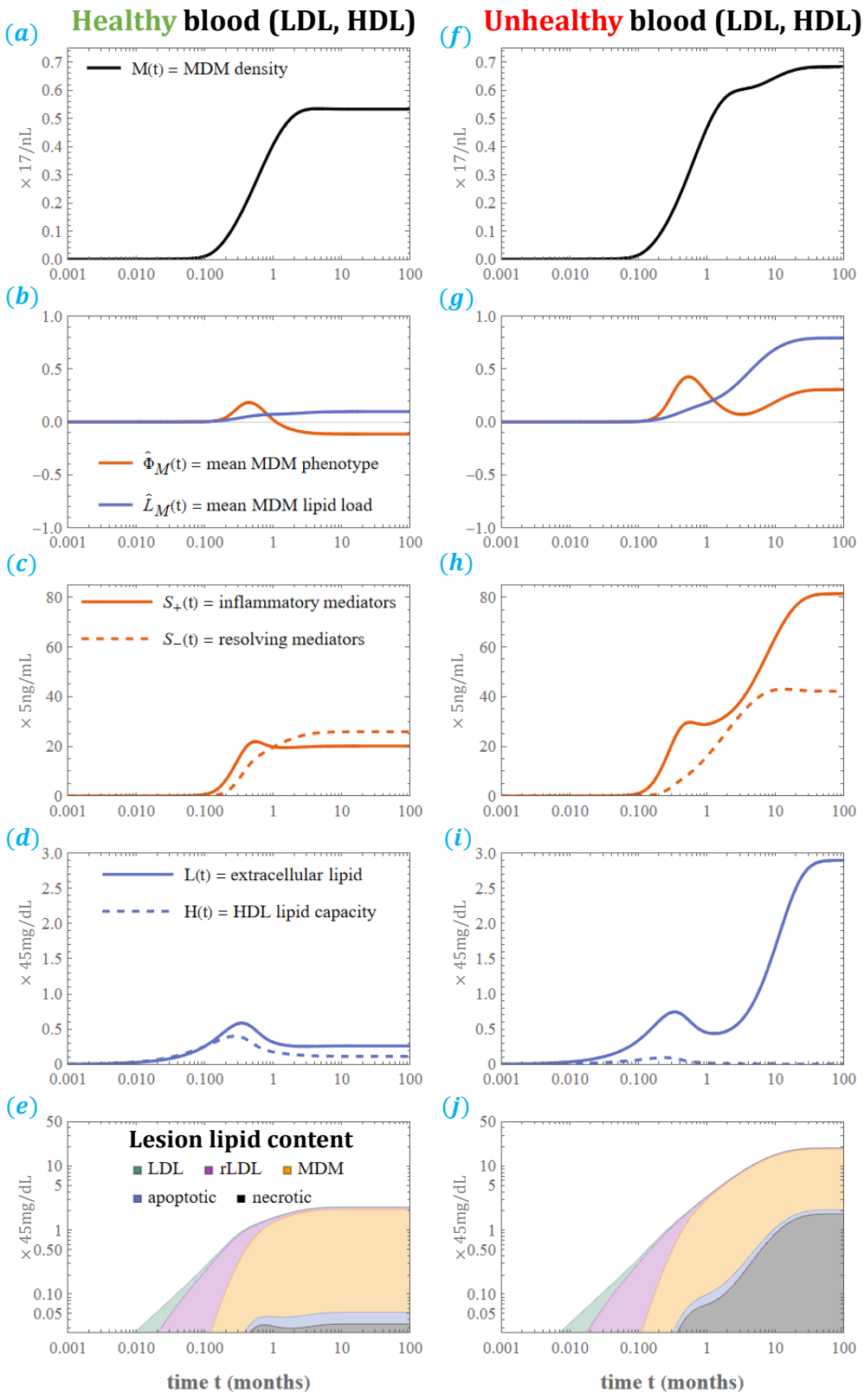


Figure 5.3: **Time evolution of lesion composition.** Plots (a)-(j) show numerical solutions of Eqs. (5.32)-(5.41) for a case with healthy LDL to HDL balance: $L^\star = 3$, $H^\star = 2$ (left), and unhealthy LDL to HDL balance: $L^\star = 4$, $H^\star = 0.5$ (right). The system tends to a non-zero steady state as $t \to \infty$ with values that depend sensitively on $L^\star$ and $H^\star$. We set $K_r = 25$ for both cases. Note the logarithmic scale for time, t, and the lipid densities in plots (e) and (j).

(Figs. 5.3 (e, j)). The increase in rLDL drives an increase in inflammatory mediator density (Figs. 5.3 (c, h)) that stimulates MDM recruitment; MDMs infiltrate the lesion in substantial numbers from $t > 0.1$ (Figs. 5.3 (a, f)). In the initial period following MDM influx, $0.1 < t < 0.5$, there is an increase in MDM lipid content and phenotype (Figs. 5.3 (b, g)), and corresponding increase in MDM lipid relative to rLDL lipid (Figs. 5.3 (e, j)). These changes are driven by MDM uptake of rLDL and interaction with inflammatory mediators. We note that rLDL uptake stimulates inflammatory mediator production, and, consequently, further stimulates inflammatory MDM phenotype modulation.

The period $0.5 < t < 2$ is characterised by MDM modulation towards resolving phenotypes (Figs. 5.3 (b, g)). This phenotype change is driven by increased production of resolving mediators, relative to inflammatory mediators (Figs. 5.3 (c, h)). Resolving mediator production is partly stimulated by increased HDL efflux during this period; MDMs have ingested enough lipid by this stage for efflux to cause HDL capacity to decline (Figs. 5.3 (d, i)). Resolving mediators are also produced due to MDM uptake of apoptotic lipid (i.e., efferocytosis), which first appears during this period due to MDM death.

For $2 < t < \infty$, the model tends to a non-zero steady state in a manner sensitive to parameter values. For healthier balances of blood LDL lipid and HDL capacity $(L^\star, H^\star)$: mean MDM lipid content increases to a small non-zero value and mean MDM phenotype remains negative (i.e., resolving) (Fig. 5.3(b)), resolving mediators outbalance inflammatory mediators (Fig. 5.3(c)), extracellular lipid levels are low and comparable to HDL capacity (Fig. 5.3(d)). Lesion lipid content is less than the blood LDL density: $L_{\text{tot}}(t \to \infty) \approx 2.5 < L^\star = 3$ (Fig. 5.3(e)). By contrast, when $L^\star$ is sufficiently high relative to $H^\star$ (quantified in Sect. 5.3.1.2): MDM densities are greater (Fig. 5.3(f)), mean MDM lipid content increases to a large value and mean MDM phenotype is positive (i.e., inflammatory) (Fig. 5.3(g)), inflammatory mediators outbalance resolving mediators (Fig. 5.3(h)), HDL capacity is largely exhausted while extracellular lipid levels remain substantial (Fig. 5.3(i)), and lesion lipid densities are greater than blood LDL densities: $L_{\text{tot}}(t \to \infty) \approx 20 > L^\star = 4$ (Fig. 5.3(j)).

In Fig. 5.4 we show how the LDL retention capacity, K_{r}, impacts the timescale of lesion development. The left plot depicts the time to steady state, defined numerically as the smallest time t for which $\sqrt{\sum_i \left(\frac{1}{y_i}\frac{dy_i}{dt}\right)^2} \leq 10^{-8}$, where the sum is taken over all subsystem variables: $\boldsymbol{y} = (M, \hat{\Phi}_M, \hat{L}_M, H, \boldsymbol{L}, S_\pm)$. The time to steady state increases with K_{r} and is greater for the unhealthy case ($L^\star = 4.0$, $H^\star = 0.5$) than the healthy case ($L^\star = 3.0, H^\star = 2$) for all $K_{\text{r}} \leq 100$. The right plot shows the time, t_{M}, for MDM lipid to exceed 450mg/dL (the smallest t satisfying $(1 + \kappa \hat{L}_M(t))M(t) > 10$), which we use as a proxy for fatty streak onset. We find that increases to K_{r} yield smaller values of t_{M}; regions with higher LDL retention capacity develop fatty streaks earlier. Moreover, if K_{r} is sufficiently small, the MDM lipid density never exceeds the 450mg/dL threshold; fatty streaks will not develop in regions of sufficiently low LDL retention capacity.

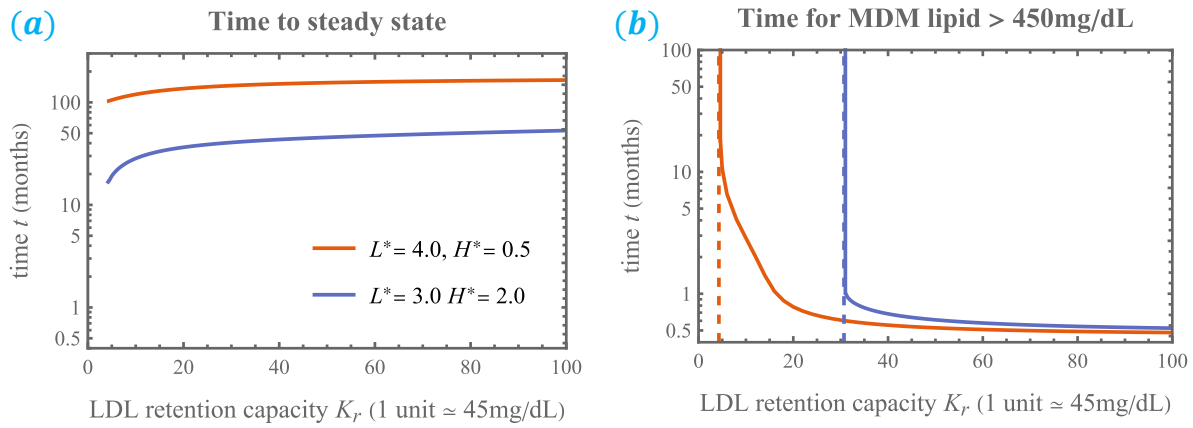


Figure 5.4: **LDL retention capacity modulates the timescale of lesion development.** Plot (a) shows how time to steady state increases with K_r. Plot (b) shows how the time for MDM lipid to exceed 450mg/dL, a proxy for fatty streak onset, decreases with K_r.

5.3.1.2 Steady state solutions

The results of Sect. 5.3.1.1 show that the model tends to a non-zero equilibrium as $t \to \infty$. Steady state solutions to the subsystem (5.32)-(5.41) are computed numerically via the Mathematica *FindRoot* routine.

Fig. 5.5 illustrates how blood levels of LDL lipid, $L^\star$, and HDL capacity, $H^\star$, impact the model lesion at steady state. Lesion composition becomes more pathological as $L^\star$ increases and $H^\star$ decreases; MDM density, mean phenotype, lipid content and total lipid content each monotonically increase with $L^\star$ and decrease with $H^\star$, while HDL capacity monotonically decreases with $L^\star$ and increases with $H^\star$. We note that all plots exhibit regions in which the contours are approximately linear. For the case $K_\mathrm{r} = 25$ shown, these contours take the form $0.4L^\star - H^\star =$ constant. The greater weighting on $H^\star$ in the linear combination reflects the higher value of the dimensionless lipid efflux rate, k_H, relative to the uptake rates in Table 5.2. Values of $(L^\star, H^\star)$ above the $\hat{\Phi}_M = 0$ contour ($0.4L^\star - H^\star \approx 0.4$) yield healthy lesions with smaller MDM densities, resolving mean phenotypes and small mean lipid loads. Lesion lipid content is low and HDL capacity remains substantial. Values of $(L^\star, H^\star)$ below the $\hat{\Phi}_M = 0$ contour yield pathological lesions with higher MDM densities, inflammatory mean phenotypes and higher mean lipid loads. Lesion lipid content is also large. These markers of pathology each increase with $0.4L^\star - H^\star$. By contrast the HDL capacity is exhausted in this region.

Fig. 5.6 shows how the LDL retention capacity, K_r, impacts lesion composition at steady state. We find that MDM density, MDM mean phenotype and MDM lipid content increase non-linearly with K_r. These trends are amplified when the values $(L^\star, H^\star)$ are more pathological (i.e., $0.4L^\star - H^\star$ is larger). HDL capacity instead decreases with K_r. Moreover, total lesion lipid content increases or decreases with K_r, depending on whether the values $(L^\star, H^\star)$ are pathological or healthy, respectively. This difference arises because higher LDL retention capacities give rise to higher MDM densities, due partially to

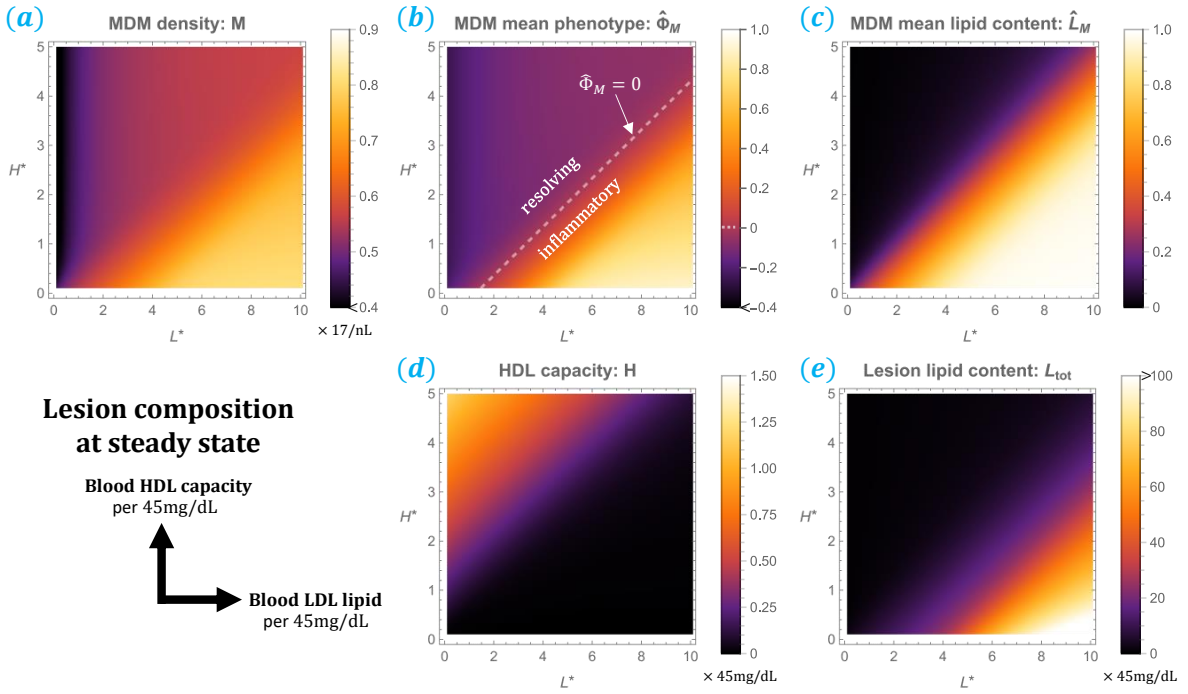


Figure 5.5: **Lesion composition at steady state depends on the bloodstream balance of LDL lipid ($L^\star$) to HDL capacity ($H^\star$).** The plots depict solutions to Eqs. (5.32)-(5.41) at equilibrium across a uniform grid of values for $(L^\star, H^\star)$. We use a grid resolution of 0.2×0.1 and assume $K_\mathrm{r} = 25$. Note that the markers of pathology: M, $\hat{\Phi}_M$, $\hat{L}_M$ and L_tot, each increase with $L^\star$ and decrease with $H^\star$.

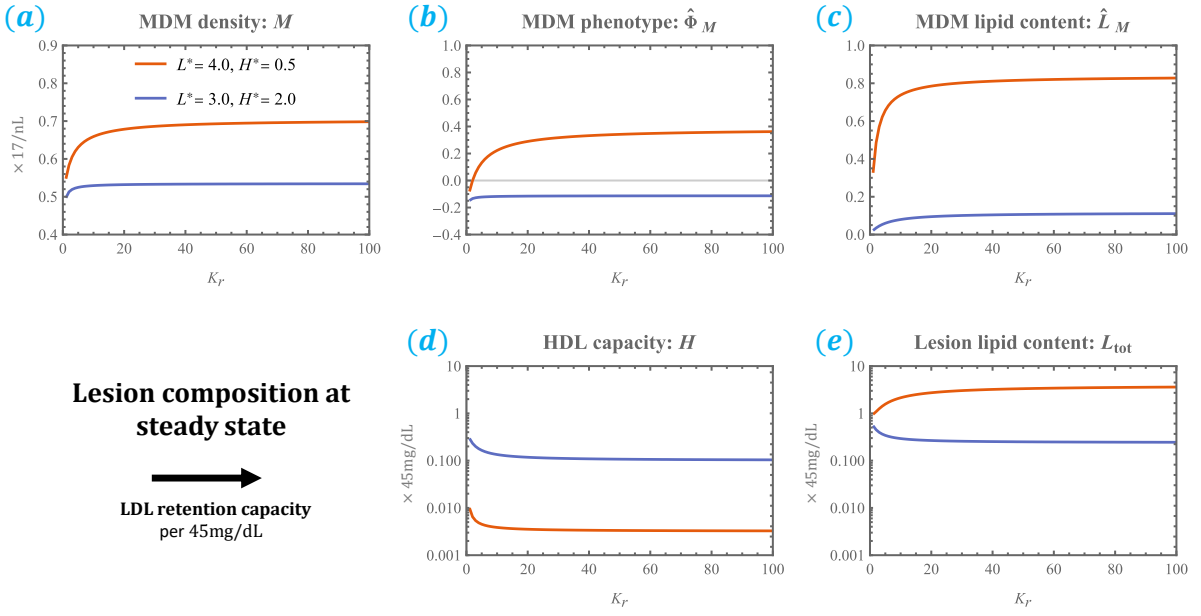


Figure 5.6: **Lesion composition at steady state varies with LDL retention capacity (K_r).** The plots show solutions to Eqs. (5.32)-(5.41) at steady state across $0.3 \leq K_\mathrm{r} \leq 100$. We show a case with healthy LDL to HDL balance: $L^\star = 3.0$, $H^\star = 2.0$, and a case with unhealthy LDL to HDL balance: $L^\star = 4.0$, $H^\star = 0.5$.

elevated signalling by resident cells. In healthy cases, HDL capacity remains substantial so that MDMs provide a net reduction in lesion lipid content by consuming extracellular lipid and efficiently offloading to HDL. In pathological cases, HDL capacity is exhausted and lipid taken up by MDMs can only leave the lesion via MDM egress. This makes MDMs net contributors to lesion lipid content; on average, they remove less lipid from the lesion than they supply via their endogenous lipid content.

5.3.2 MDM phenotype-lipid distribution

We now turn to Eqs. (5.29) to study how phenotype and lipid content are distributed amongst lesion MDMs. After presenting numerical solutions for $m_{\phi,\ell}(t)$ in Sect. 5.3.2.1, we derive a continuum approximation of Eqs. (5.29) in Sect. 5.3.2.2 to make analytical progress. In Sect. 5.3.2.3 we show how analysis of the leading-order advective dynamics enables us to characterise the expected trajectories of MDMs through phenotype-lipid space. Finally, in Sect. 5.3.2.4 we analyse the MDM distribution at steady state.

5.3.2.1 Time evolution

In Fig. 5.7 we present the dynamics of the MDM phenotype-lipid distribution, $m_{\phi,\ell}(t)$, for the cases shown in Fig. 5.3. At early times, $0 \leq t \leq 0.2$, the distribution evolves in a wave-like manner, from $(\phi, \ell) = (0, 0)$, in the direction of increasing ϕ and ℓ due to the initial phase of LDL influx and uptake noted in Sect. 5.3.1.1. At later times ($0.5 \leq t \leq 2$), the distribution moves leftwards, becoming concentrated at lower values of ϕ. This resolving phenotype modulation reflects greater production of resolving mediators, S_-, relative to inflammatory mediators, S_+, in this phase (c.f. Fig. 5.3 (e,h)). At longer times, the distribution settles to a steady state. In the healthy case, lipid loads increase slightly and phenotypes remain resolving as the lesion tends to equilibrium. In the unhealthy case, lipid loads increase substantially and phenotypes become more inflammatory towards equilibrium.

We note that the MDM distribution, in both cases and at all times, is concentrated about a central curve which begins at the origin $(\phi, \ell) = (0, 0)$ and terminates at an interior point in (ϕ, ℓ) space. This feature indicates that phenotype and lipid content are non-linearly correlated. At steady state, this correlation is monotonic but may be negative (as in case (a)) or positive (as in case (b)) depending on model parameters.

It is not straightforward to understand how the MDM distributions in Fig. 5.7 arise by directly considering Eqs. (5.29). In order to make progress, we consider a continuum approximation of Eqs. (5.29) in the analysis below.

5.3.2.2 Continuum approximation

We associate the discretely structured MDM distribution, $m_{\phi,\ell}(t)$, $\phi = 0, \pm 1, \ldots, \pm\phi_{\max}$, $\ell = 0, 1, \ldots, \ell_{\max}$, with a function $m(\tilde{\phi}, \tilde{\ell}, t) \geq 0$ of two continuous structure variables, $\tilde{\phi}$

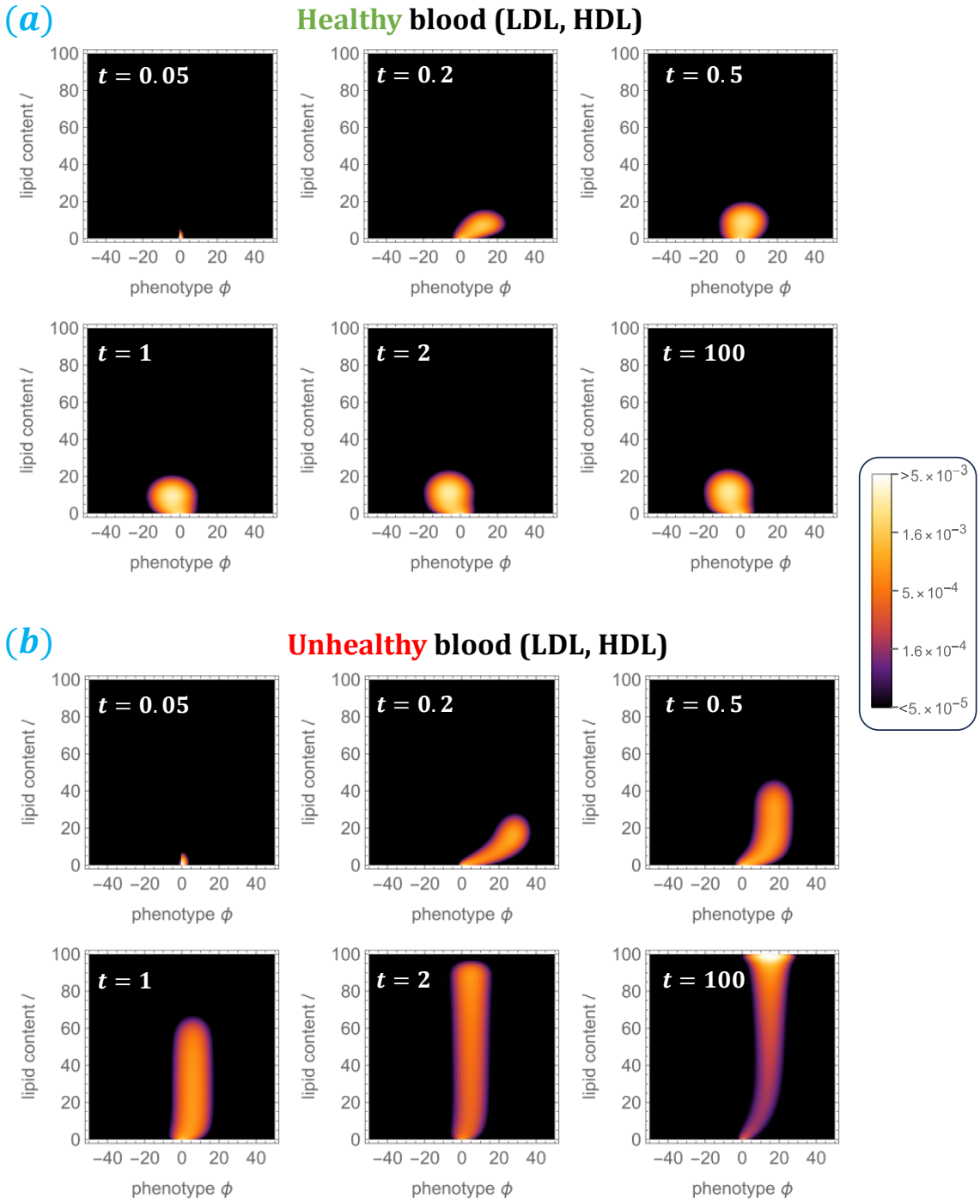


Figure 5.7: **MDM phenotype-lipid distribution dynamics for two typical simulations.** The plots show numerical solutions of Eqs. (5.29) for $m_{\phi,\ell}(t)$ for a case with healthy LDL to HDL balance (a): $L^\star = 3.0$, $H^\star = 2.0$, and unhealthy LDL to HDL balance (b): $L^\star = 4.0$, $H^\star = 0.5$. We use $K_\mathrm{r} = 25$ for both simulations. At steady state (see $t = 100$), the distribution may skew towards resolving (case (a)) or inflammatory (case (b)) phenotypes.

and $\tilde{\ell}$, and time t. Specifically, we make the identifications

$$\tilde{\phi} \sim \frac{\phi}{\phi_{\max}}, \qquad \tilde{\ell} \sim \frac{\ell}{\ell_{\max}}, \qquad m(\tilde{\phi}, \tilde{\ell}, t) \sim \phi_{\max}\, \ell_{\max}\, m_{\phi,\ell}(t). \tag{5.47}$$

Here $\tilde{\phi} \in [-1, 1]$ and $\tilde{\ell} \in [0, 1]$, so that $\tilde{\phi} = -1$ corresponds to fully M2-polarised MDMs, $\tilde{\phi} = 1$ to fully M1-polarised MDMs, $\tilde{\ell} = 0$ to MDMs with only endogenous lipid, and $\tilde{\ell} = 1$ to MDMs at maximal lipid content. The function $m(\tilde{\phi}, \tilde{\ell}, t)$ can be interpreted as the number density of MDMs across a continuous phenotype-lipid structure space, with scaling such that we may identify

$$M(t) = \sum_{\phi,\ell} m_{\phi,\ell}(t) \sim \int_0^1 \int_{-1}^1 m(\tilde{\phi}, \tilde{\ell}, t)\, d\tilde{\phi}\, d\tilde{\ell}. \tag{5.48}$$

We seek an expansion of Eqs. (5.29) in the limit $\ell_{\max} \sim \phi_{\max} \to \infty$. More precisely, we set $\epsilon := \ell_{\max}^{-1} \ll 1$ and assume that $\theta := \phi_{\max}/\ell_{\max} = \mathcal{O}(1)$ as $\epsilon \to 0$. Substituting the identifications (5.47) into Eqs. (5.29), Taylor-expanding about $\epsilon = 0$, and neglecting $\mathcal{O}(\epsilon^2)$ terms, yields the advection-diffusion PDE

$$\frac{\partial m}{\partial t} = \nabla \cdot (\boldsymbol{D} \nabla m - \boldsymbol{v} m) - (1 + \gamma) m, \tag{5.49}$$

where $\nabla = \left(\frac{\partial}{\partial \tilde{\phi}}, \frac{\partial}{\partial \tilde{\ell}}\right)^T$, and the velocity vector, $\boldsymbol{v}$, and diffusivity matrix, $\boldsymbol{D}$, are respectively:

$$\boldsymbol{v} = \begin{bmatrix} \chi(S_+ - S_-) - \chi(S_+ + S_-)\tilde{\phi} \\ \boldsymbol{k_L} \cdot \boldsymbol{L} - (\boldsymbol{k_L} \cdot \boldsymbol{L} + k_H H)\tilde{\ell} \end{bmatrix} + \frac{\epsilon}{2} \begin{bmatrix} \theta\chi(S_+ - S_-) \\ \boldsymbol{k_L} \cdot \boldsymbol{L} - k_H H \end{bmatrix}, \tag{5.50}$$

$$\boldsymbol{D} = \frac{\epsilon}{2} \begin{bmatrix} \theta\chi\big[(S_+ + S_-) - (S_+ - S_-)\tilde{\phi}\big] & 0 \\ 0 & \boldsymbol{k_L} \cdot \boldsymbol{L} - (\boldsymbol{k_L} \cdot \boldsymbol{L} - k_H H)\tilde{\ell} \end{bmatrix}. \tag{5.51}$$

We note that Eq. (5.49) is advection-dominant since $\mathbf{v} = \mathcal{O}(1)$ and $\mathbf{D} = \mathcal{O}(\epsilon)$.

We derive boundary conditions for Eq. (5.49) by requiring that the dynamics of the MDM population, $M(t)$, as defined by Eq. (5.32), are consistent with those of the continuous MDM distribution (5.48). Integrating Eq. (5.49) over $(\tilde{\phi}, \tilde{\ell}) \in \mathcal{R} := [-1, 1] \times [0, 1]$ and applying the divergence theorem yields

$$\frac{dM}{dt} = \oint_{\partial\mathcal{R}} (D\nabla m - vm) \cdot \mathbf{n}\, ds - (1 + \gamma) M, \tag{5.52}$$

where $\mathbf{n}$ is the outwards pointing normal vector. We set

$$(D\nabla m - vm) \cdot (\pm 1, 0)^T = 0 \quad \text{on } \tilde{\phi} = \pm 1, \tag{5.53}$$

$$(D\nabla m - vm) \cdot (0, +1)^T = 0 \quad \text{on } \tilde{\ell} = 1, \tag{5.54}$$

$$(D\nabla m - vm) \cdot (0, -1)^T = R_{0,0} \cdot \delta_0(\tilde{\phi}) \quad \text{on } \tilde{\ell} = 0. \tag{5.55}$$

Eqs. (5.53) and (5.54) are no-flux conditions so that MDMs cannot enter or leave the system by exceeding the phenotype bounds $\tilde{\phi} = \pm 1$ or maximal lipid content $\tilde{\ell} = 1$, respectively. We use the Dirac-delta distribution, δ_0, in Eq. (5.55) to ensure that MDMs enter the lesion at the origin $(\tilde{\phi}, \tilde{\ell}) = (0, 0)$.

5.3.2.3 Advection at leading order

Eq. (5.49) reduces to a hyperbolic PDE at leading order as $\epsilon \to 0$:

$$\begin{aligned}\frac{\partial m}{\partial t} + \chi \frac{\partial}{\partial \tilde{\phi}}\Big[\Big((S_+ - S_-) - (S_+ + S_-)\tilde{\phi}\Big)m\Big] \\ + \frac{\partial}{\partial \tilde{\ell}}\Big[\Big(\boldsymbol{k_L}\cdot\boldsymbol{L} - (\boldsymbol{k_L}\cdot\boldsymbol{L} + k_H H)\tilde{\ell}\Big)m\Big] = -(1+\gamma)m.\end{aligned} \tag{5.56}$$

Eq. (5.56) describes the advection, in $(\tilde{\phi}, \tilde{\ell})$ space, of MDMs according to a time-dependent velocity field:

$$\frac{d\tilde{\phi}}{dt} = \chi\big[(S_+ - S_-) - (S_+ + S_-)\tilde{\phi}\big], \tag{5.57}$$

$$\frac{d\tilde{\ell}}{dt} = \boldsymbol{k_L}\cdot\boldsymbol{L} - (\boldsymbol{k_L}\cdot\boldsymbol{L} + k_H H)\tilde{\ell}, \tag{5.58}$$

where the coefficients: $S_\pm(t)$, $\boldsymbol{L}(t)$ and $H(t)$, are time-dependent solutions of the subsystem (5.32)-(5.41).

The dynamics of the velocity field defined by Eqs. (5.57)-(5.58) are illustrated in Fig. 5.8. A striking feature of the plots is that, at all times, the vector field has a single point $(\tilde{\phi}_\times, \tilde{\ell}_\times)$ of zero instantaneous velocity. This time-dependent point represents the target phenotype and lipid content that MDMs are driven towards by advection. Setting time derivatives to zero in Eqs. (5.57)-(5.58), and solving for $\tilde{\phi}$ and $\tilde{\ell}$ shows that

$$\tilde{\phi}_\times(t) := \frac{S_+(t) - S_-(t)}{S_+(t) + S_-(t)}, \qquad \tilde{\ell}_\times(t) := \frac{\boldsymbol{k_L}\cdot\boldsymbol{L}(t)}{\boldsymbol{k_L}\cdot\boldsymbol{L}(t) + k_H H(t)}. \tag{5.59}$$

The time-evolution of the zero velocity point, given by Eqs. (5.59), is shown in Fig. 5.8(c). We find that $(\tilde{\phi}_\times, \tilde{\ell}_\times)$ first moves from an inflammatory position towards resolving phenotypes. This initial transition occurs because resolving mediator production by MDMs opposes the initially pure inflammatory environment due to rLDL-stimulated resident cells. When the LDL to HDL balance is healthy, the target phenotype becomes resolving and the target lipid content increases towards towards a low steady state value. When the LDL to HDL balance is unhealthy, the target phenotype remains inflammatory and the target lipid content increases to a large value as the system evolves to its steady state. We note further that $(\tilde{\phi}_\times, \tilde{\ell}_\times)$ aligns well with the MDM distribution end points shown in Fig. 5.7.

Since MDMs enter the model lesion with minimal lipid content and a neutral phenotype, we are particularly interested in solutions to Eqs. (5.57)-(5.58), which satisfy the initial conditions

$$\tilde{\phi}(t^\star) = 0, \qquad \tilde{\ell}(t^\star) = 0. \tag{5.60}$$

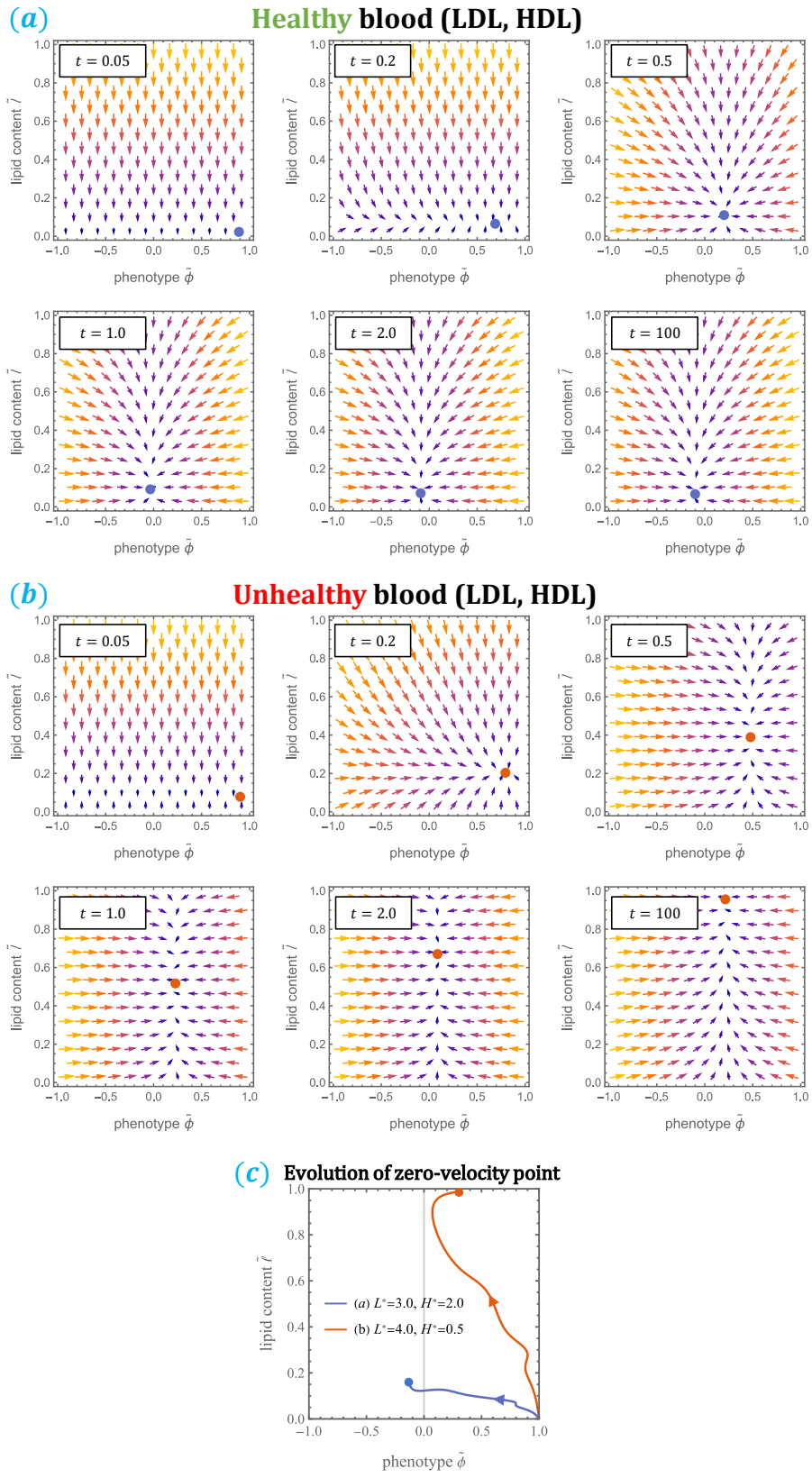


Figure 5.8: **Dynamics of the MDM phenotype-lipid velocity field.** The vector field plots illustrate the right hand side of Eqs. (5.57)-(5.58) using the numerical solutions of the subsystem (5.32)-(5.41) shown in Fig. 5.3. The velocity magnitude is indicated by larger arrows and brighter colours. The point of instantaneous zero velocity is indicated by a circle at each time point in (a) and (b), and plotted against time in (c). We fix $K_{\mathrm{r}} = 25$ and use $L^\star = 4.0$, $H^\star = 0.5$ for (a) and $L^\star = 3.0$, $H^\star = 2.0$ for (b).

Such solutions represent the trajectory of MDMs that enter the lesion at time $t = t^\star$ in the limit $\epsilon \to 0$. They can be expressed in terms of the subsystem variables as follows:

$$\tilde{\phi}(t) = I_1(t)^{-1} \int_{t^\star}^{t} \chi\big(S_+(\tau) - S_-(\tau)\big) I_1(\tau) d\tau, \tag{5.61}$$

$$\tilde{\ell}(t) = I_2(t)^{-1} \int_{t^\star}^{t} \boldsymbol{k_L} \cdot \boldsymbol{L}(\tau) I_2(\tau) d\tau, \qquad t \geq t^\star, \tag{5.62}$$

where $I_1(t)$ and $I_2(t)$ are integrating factors:

$$I_1(t) := e^{\int_{t^\star}^{t} \chi\left(S_+(\tau)+S_-(\tau)\right) d\tau}, \qquad I_2(t) := e^{\int_{t^\star}^{t} \left(\boldsymbol{k_L}\cdot\boldsymbol{L}(\tau)+k_H H(\tau)\right) d\tau}.$$

We use numerical solutions of the subsystem (5.32)-(5.44) to evaluate Eqs. (5.61)-(5.62) in Fig. 5.9. As MDMs travel along the trajectories shown, they emigrate from the lesion and die via apoptosis at the constant rate $(1 + \gamma)$. The proportion of the MDMs which enter the lesion at time $t = t^\star$ that are still alive and in the lesion at time $t \geq t^\star$ is given by $e^{-(1+\gamma)(t-t^\star)}$. This proportion is represented in Fig. 5.9 by the opacity of the curves. The plots illustrate that MDMs which enter the lesion early (e.g., at $t^\star = 0.2$) can be expected to first transition from phenotypic neutrality to an inflammatory state, before evolving to either a resolving phenotype with low lipid load (case (a)), or a milder inflammatory phenotype with high lipid load (case b). The trajectories of MDMs that enter the lesion at later times are typically monotonic, in contrast to the looping trajectories of MDMs that enter at earlier times. We note in particular that trajectories with $t^\star = 100$ (near steady state) align well with the centre line of the MDM distributions (c.f. Fig. 5.7 at $t = 100$).

5.3.2.4 Steady state solutions

It is straightforward to show that $m^\star(\tilde{\phi}, \tilde{\ell})$, the steady state solution of Eq. (5.49), satisfies

$$\begin{aligned} \frac{\epsilon\theta q}{2} \frac{\partial^2}{\partial \tilde{\phi}^2}\Big[(1-\tilde{\phi}_\infty\tilde{\phi})m^\star\Big] + \frac{\epsilon}{2}\frac{\partial^2}{\partial \tilde{\ell}^2}\Big[\Big(\tilde{\ell}_\infty - (2\tilde{\ell}_\infty - 1)\tilde{\ell}\Big)m^\star\Big] \\ - q(\tilde{\phi}_\infty - \tilde{\phi})\frac{\partial m^\star}{\partial \tilde{\phi}} - (\tilde{\ell}_\infty - \tilde{\ell})\frac{\partial m^\star}{\partial \tilde{\ell}} - (p-q)m^\star = 0, \end{aligned} \tag{5.63}$$

where the constants $\tilde{\phi}_\infty$, $\tilde{\ell}_\infty$, q and p are defined in terms of model parameters and the equilibrium values of the subsystem variables:

$$\begin{aligned} \tilde{\phi}_\infty &:= \frac{S_+ - S_-}{S_+ + S_-}, \qquad & \tilde{\ell}_\infty &:= \frac{\boldsymbol{k_L}\cdot\boldsymbol{L}}{\boldsymbol{k_L}\cdot\boldsymbol{L} + k_H H}, \\ q &:= \frac{\chi(S_+ + S_-)}{\boldsymbol{k_L}\cdot\boldsymbol{L} + k_H H}, \qquad & p &:= -1 + \frac{1+\gamma}{\boldsymbol{k_L}\cdot\boldsymbol{L} + k_H H}. \end{aligned} \tag{5.64}$$

We note that $\tilde{\phi}_\infty \in (-1, 1)$ and $\tilde{\ell}_\infty \in (0, 1)$ coincide exactly with the target phenotype and lipid content, $\tilde{\phi}_\times$ and $\tilde{\ell}_\times$, respectively (c.f. Eqs. (5.59) at steady state). We note also that $p \in (-1, \infty)$ and $q \in (0, \infty)$. The boundary conditions (5.53)-(5.55) become

$$J_\phi|_{\tilde{\phi}=-1} = 0, \qquad J_\phi|_{\tilde{\phi}=1} = 0, \qquad J_\ell|_{\tilde{\ell}=1} = 0, \qquad J_\ell|_{\tilde{\ell}=0} = \Big(\frac{\tilde{\ell}_\infty R_{0,0}}{\boldsymbol{k_L}\cdot\boldsymbol{L}}\Big)\cdot\delta_0(\tilde{\phi}), \tag{5.65}$$

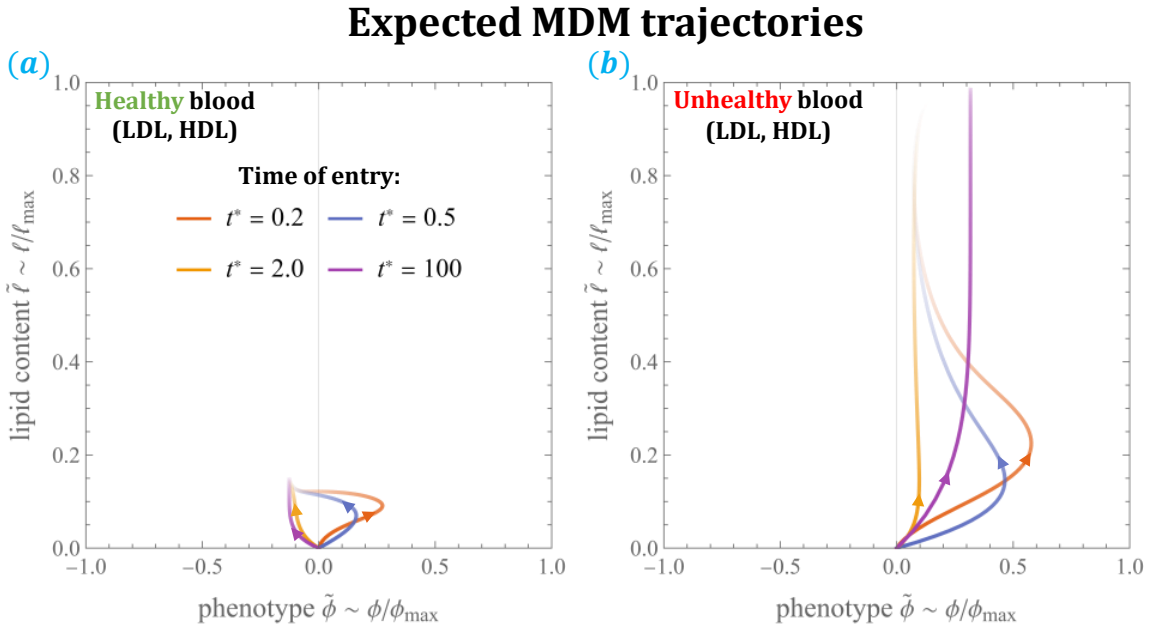


Figure 5.9: **Expected trajectory through phenotype-lipid space of MDMs that enter the lesion at time $t = t^\star$.** The curves are numerical solutions to Eqs. (5.57)-(5.60). The opacity of each point on the curves represents the probability that MDMs travel through that point before either dying or emigrating from the lesion. Note how MDMs which enter at later times have simple monotonic trajectories, in contrast to those that enter earlier.

where the dimensionless fluxes are given by

$$J_\phi = q(\tilde{\phi}_\infty - \tilde{\phi})m^\star - \frac{\epsilon\theta q}{2}\frac{\partial}{\partial\tilde{\phi}}\Big[(1-\tilde{\phi}_\infty\tilde{\phi})m^\star\Big], \tag{5.66}$$

$$J_\ell = (\tilde{\ell}_\infty - \tilde{\ell})m^\star - \frac{\epsilon}{2}\frac{\partial}{\partial\tilde{\ell}}\Big[\big(\tilde{\ell}_\infty - (2\tilde{\ell}_\infty - 1)\tilde{\ell}\big)m^\star\Big]. \tag{5.67}$$

Rather than searching for a closed-form solutions to Eq. (5.63) in full generality, we characterise the solutions via asymptotic analysis in the limit $\epsilon \to 0$. More specifically, we derive equations for the central curve of the MDM distribution and marginal distributions with respect to lipid content, $W(\tilde{\ell})$, and phenotype, $V(\tilde{\phi})$, where

$$W(\tilde{\ell}) := \int_{-1}^{1} m^\star(\tilde{\phi},\tilde{\ell})\,d\tilde{\phi}, \qquad V(\tilde{\phi}) := \int_{0}^{1} m^\star(\tilde{\phi},\tilde{\ell})\,d\tilde{\ell}. \tag{5.68}$$

Finally, we consider the impact of the LDL lipid and HDL capacity blood densities, $L^\star$ and $H^\star$, respectively. The results are summarised in Figs. 5.10 and 5.11.

Central curve. We determine the curve about which $m^\star(\tilde{\phi},\tilde{\ell})$ is centred by considering Eq. (5.63) at leading order. When $\epsilon = 0$, Eq. (5.63) reduces to a first order hyperbolic PDE, with characteristics that satisfy the equation

$$\frac{d\tilde{\phi}}{d\tilde{\ell}} = \frac{q(\tilde{\phi}_\infty - \tilde{\phi})}{\tilde{\ell}_\infty - \tilde{\ell}}. \tag{5.69}$$

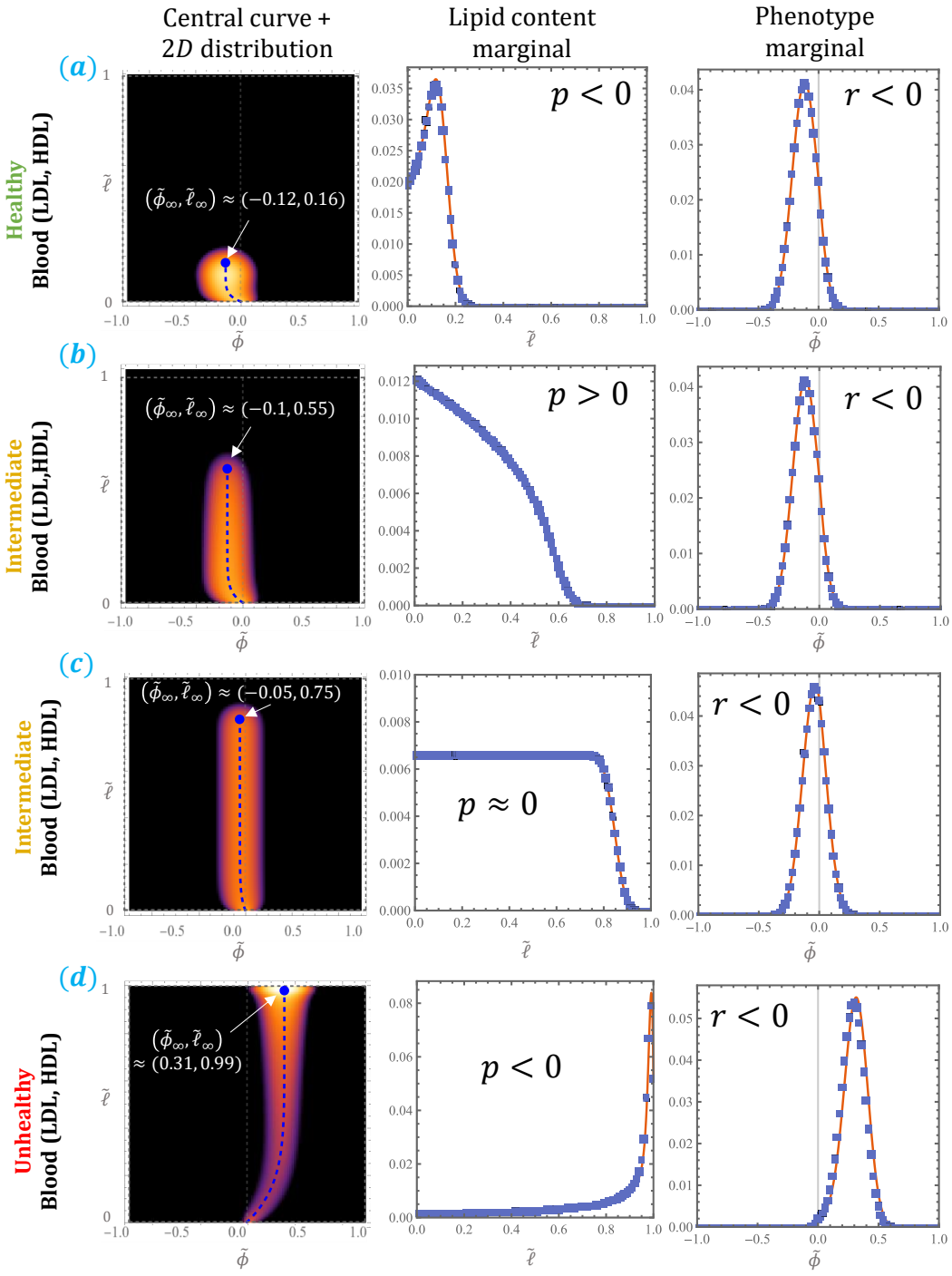


Figure 5.10: **Comparison of continuum analytical results to numerical solutions for the discrete MDM distribution, $m_{\phi,\ell}$, at steady state.** Cases (a)-(d) use the values $(L^\star, H^\star) = (3, 2)$, $(1.8, 0.8)$, $(2.5, 0.77)$ and $(4, 0.5)$ and are ordered roughly by pathology. The first column overlays Eq. (5.70) for the central curve with $m_{\phi,\ell}$ (same colour legend as in Fig. 5.7). The second and third columns compare the exact solutions for the lipid content and phenotype marginals, given by Eqs. (5.73) and (5.83), respectively, with the discrete marginals. We set $K_\mathrm{r} = 25$ for all cases.

Solving Eq. (5.69) subject to $\tilde{\phi}(\tilde{\ell}=0)=0$ yields

$$\tilde{\phi}=\tilde{\phi}_c(\tilde{\ell}):=\tilde{\phi}_\infty\left[1-\left(1-\frac{\tilde{\ell}}{\tilde{\ell}_\infty}\right)^q\right]. \tag{5.70}$$

In the first column of Fig. 5.10, the solution (5.70) is superimposed on numerical solutions for $m_{\phi,\ell}$ at steady state, showing good agreement with the centre of the MDM distributions.

Eq. (5.70) confirms that, at steady state, phenotype and lipid content are monotonically correlated via a power law. The correlation is positive when $\tilde{\phi}_\infty>0$ and negative when $\tilde{\phi}_\infty<0$. Equivalently, using the first of Eqs. (5.64), if inflammatory mediators dominate resolving ones ($S_+>S_-$) then MDMs with higher lipid loads have a more inflammatory phenotype; if, however, resolving mediators dominate ($S_+<S_-$) then MDMs with higher lipid loads have a more resolving phenotype. The nonlinearity of the correlation is determined by the constant q, which measures the relative amount of mediator-MDM activity to lipid-MDM activity.

Distribution of lipid content: Integrating Eqs. (5.63) and (5.65) with respect to $\tilde{\phi}\in[-1,1]$ yields the following ODE for $W(\tilde{\ell})$:

$$\frac{\epsilon}{2}\frac{d^2}{d\tilde{\ell}^2}\Big[\big(\tilde{\ell}_\infty-(2\tilde{\ell}_\infty-1)\,\tilde{\ell}\,\big)W\Big]-(\tilde{\ell}_\infty-\tilde{\ell})\frac{dW}{d\tilde{\ell}}-pW=0, \tag{5.71}$$

and the boundary conditions:

$$-\frac{\epsilon}{2}\frac{d}{d\tilde{\ell}}\Big[\big(\tilde{\ell}_\infty-(2\tilde{\ell}_\infty-1)\,\tilde{\ell}\big)\,W\Big]+(\tilde{\ell}_\infty-\tilde{\ell})W=\begin{cases}\frac{\tilde{\ell}_\infty R_{0,0}}{\boldsymbol{k_L\cdot L}} & \text{at } \tilde{\ell}=0,\\ 0 & \text{at } \tilde{\ell}=1.\end{cases} \tag{5.72}$$

Eq. (5.71) admits an exact solution (found via the Mathematica *DSolve* routine):

$$W(\tilde{\ell})=e^{-f(\tilde{\ell})}\Big[K_1U_p^{2-f(\tilde{\ell}_\infty)}(f(\tilde{\ell}))+K_2\mathcal{L}_{-p}^{1-f(\tilde{\ell}_\infty)}(f(\tilde{\ell}))\Big], \tag{5.73}$$

where f is the function

$$f(\tilde{\ell}):=\frac{2}{(1-2\tilde{\ell}_\infty)\epsilon}\left[\tilde{\ell}+\left(\frac{\tilde{\ell}_\infty}{1-2\tilde{\ell}_\infty}\right)\right], \tag{5.74}$$

$U_a^b(z)$ is the confluent hypergeometric function and $\mathcal{L}_a^b(z)$ the generalised Laguerre polynomial. The constants K_1 and K_2 are determined by substituting Eq. (5.73) into the boundary conditions (5.72); exact expressions are readily obtained via the Mathematica *Solve* routine, but are too involved to be insightful and so are omitted here for brevity. We compare the solution (5.73) to numerical solutions of the discrete model in the second column of Fig. 5.10, showing excellent agreement.

The form of Eq. (5.73) makes it difficult to understand how $W(\tilde{\ell})$ depends on the constants defined in Eqs. (5.64). Nonetheless, analysis of the leading order "outer" solution shows how the qualitative behaviour of $W(\tilde{\ell})$ depends on p and $\tilde{\ell}_\infty$. Here we

follow the asymptotic analysis in Chapter 4. Setting $\epsilon = 0$ in Eq. (5.71) admits the following solution:

$$W_{\text{outer}}(\tilde{\ell}) = K_3\left(1 - \frac{\tilde{\ell}}{\tilde{\ell}_\infty}\right)^p, \tag{5.75}$$

where $K_3 \geq 0$ is a constant of integration. Eq. (5.75) admits three possible behaviours as $\tilde{\ell} \to \tilde{\ell}_\infty$ from below. For $p > 0$, W_{outer} decreases monotonically to zero (with non-zero derivative if $p < 2$); for $p = 0$, W_{outer} is constant; and for $p < 0$, W_{outer} diverges to $+\infty$. The full solution does not exhibit such discontinuities at $\tilde{\ell} = \tilde{\ell}_\infty$ due to the regularising effects of the second derivative term. The corresponding behaviour for $W(\tilde{\ell})$ is as follows. For $p > 0$, W decreases monotonically and smoothly to zero near $\tilde{\ell} = \tilde{\ell}_\infty$ (Fig. 5.10(b)); for $p = 0$, W takes a quasi-uniform sigmoidal profile with a rapid decrease to zero near $\tilde{\ell} = \tilde{\ell}_\infty$ (Fig. 5.10(c)); and for $p < 0$, W increases monotonically before attaining a local maximum near $\tilde{\ell} = \tilde{\ell}_\infty$ (Fig. 5.10 (a,d)). In the above, "near $\tilde{\ell} = \tilde{\ell}_\infty$" means an $\mathcal{O}(\epsilon^{\frac{1}{2}})$ neighbourhood of $\tilde{\ell} = \tilde{\ell}_\infty$. This scaling can be derived by searching for an inner variable $\hat{\ell} = (\tilde{\ell} - \tilde{\ell}_\infty)/\epsilon^n$ for some $\hat{\ell} = \mathcal{O}(1)$ in Eq. (5.71); an exponent $n = \frac{1}{2}$ is required to bring the second derivative into the dominant balance.

Distribution of phenotype: Integrating Eqs. (5.63) and (5.65) with respect to $\tilde{\ell} \in [0, 1]$ gives the following boundary value problem for $V(\tilde{\phi})$:

$$\frac{\epsilon\theta}{2}\frac{d^2}{d\tilde{\phi}^2}\left[(1 - \tilde{\phi}_\infty\tilde{\phi})V\right] - (\tilde{\phi}_\infty - \tilde{\phi})\frac{dV}{d\tilde{\phi}} - rV = -\frac{\tilde{\ell}_\infty R_{0,0}}{q\boldsymbol{k_L}\cdot\boldsymbol{L}}\cdot\delta_0(\tilde{\phi}), \tag{5.76}$$

$$-\frac{\epsilon\theta}{2}\frac{\partial}{\partial\tilde{\phi}}\left[(1 - \tilde{\phi}_\infty\tilde{\phi})V\right] + (\tilde{\phi}_\infty - \tilde{\phi})V = 0 \quad \text{at } \tilde{\phi} = \pm 1, \tag{5.77}$$

where $r := -1 + \frac{p+1}{q}$. As in the derivation of a Green's function, we first recast the Dirac-delta source, which describes MDM recruitment, as a jump condition. That is, we seek a solution of the form

$$V(\tilde{\phi}) = \begin{cases} V_-(\tilde{\phi}), & -1 \leq \tilde{\phi} \leq 0; \\ V_+(\tilde{\phi}), & 0 \leq \tilde{\phi} \leq 1, \end{cases} \tag{5.78}$$

where $V_\pm$ solve the ODE

$$\frac{\epsilon\theta}{2}\frac{d^2}{d\tilde{\phi}^2}\left[(1 - \tilde{\phi}_\infty\tilde{\phi})V_\pm\right] - (\tilde{\phi}_\infty - \tilde{\phi})\frac{dV_\pm}{d\tilde{\phi}} - rV_\pm = 0, \tag{5.79}$$

and satisfy

$$V_-(0) = V_+(0) \tag{5.80}$$

$$V_-'(0) = V_+'(0) + \frac{2\tilde{\ell}_\infty R_{0,0}}{\epsilon\theta q\boldsymbol{k_L}\cdot\boldsymbol{L}} \tag{5.81}$$

$$-\frac{\epsilon\theta}{2}\left[(1 - \tilde{\phi}_\infty\tilde{\phi})V_\pm\right]' + (\tilde{\phi}_\infty - \tilde{\phi})V_\pm = 0 \quad \text{at } \tilde{\phi} = \pm 1. \tag{5.82}$$

The exact solution for Eq. (5.79) can be written as

$$V_{\pm}(\tilde{\phi}) = J_{\pm,1} U_{-r}^{1+g(\tilde{\phi}_\infty)}(g(\tilde{\phi})) + J_{\pm,2} \mathcal{L}_r^{g(\tilde{\phi}_\infty)}(g(\tilde{\phi})), \tag{5.83}$$

where

$$g(\tilde{\phi}) := \frac{2(\tilde{\phi}_\infty \tilde{\phi} - 1)}{\epsilon \theta \tilde{\phi}_\infty^2}. \tag{5.84}$$

Expressions for the constants $J_{\pm,1}$, $J_{\pm,2}$ can be found by substituting Eq. (5.83) into conditions (5.80)-(5.82). As for $W(\tilde{\ell})$, they are too complicated to be insightful and are omitted for brevity. The comparison of solutions (5.83) with the discrete model output in column 3 of Fig. 5.10 shows good agreement. We note that the jump condition amounts to a small reduction in slope at $\tilde{\phi} = 0$ that is almost imperceptible for the parameter values in Table 5.1.

Following the analysis of $W(\tilde{\ell})$, we compute the leading order "outer" solution to Eq. (5.76):

$$V_{\text{outer}} = J_3 \Big(1 - \frac{\tilde{\phi}}{\tilde{\phi}_\infty}\Big)^r. \tag{5.85}$$

Eq. (5.85) is of the same form as Eq. (5.75); $\tilde{\phi}_\infty$ and r play the same roles for V as $\tilde{\ell}_\infty$ and p play for W. The main difference, as shown in Fig. 5.10, is that only the case $r < 0$ manifests in numerical solutions. Consequently, $V(\tilde{\phi})$ always attains a local maximum in a small (again $\mathcal{O}(\epsilon^{\frac{1}{2}})$) neighbourhood of $\tilde{\phi} = \tilde{\phi}_\infty$. This observation is supported by the numerical results below.

Impact of blood LDL lipid and HDL capacity levels. We conclude our steady state analysis by examining how the qualitative form of the MDM distribution changes as $L^\star$ and $H^\star$ vary. The results are summarised in Fig. 5.11 where we plot the parameter groupings in Eqs. (5.64) against $L^\star$ and $H^\star$; the four cases shown in Fig. 5.10 are also indicated. Recall that p and r determine the overall shape (e.g., whether they attain a local maximum) of the lipid and phenotype marginal distributions, $W(\tilde{\ell})$ and $V(\tilde{\phi})$ respectively, while $\tilde{\phi}_\infty$, $\tilde{\ell}_\infty$ and q determine the central curve.

We note first how r and p vary with $L^\star$ and $H^\star$. The value of r decreases monotonically with $L^\star$ and is less sensitive to $H^\star$. Importantly, we find that $r < 0$ for all $L^\star \in (0, 10)$ and $H^\star \in (0, 5)$, indicating that the phenotype marginal attains a local maximum near $\tilde{\phi} = \tilde{\phi}_\infty$ across the range of physiologically plausible values for blood LDL lipid and HDL capacity. By contrast, $p \geq 0$ for values of $(L^\star, H^\star)$ sufficiently close to the origin. This suggests that monotone decreasing and sigmoidal lipid marginals only occur when blood levels of LDL lipid and HDL capacity are both sufficiently low; otherwise the lipid marginal attains a local maximum near $\tilde{\ell} = \tilde{\ell}_\infty$.

The target phenotype, $\tilde{\phi}_\infty$, and lipid content, $\tilde{\ell}_\infty$, both increase with $L^\star$ and decrease with $H^\star$. In particular, their plots exhibit the linear contours prominent in Fig. 5.5;

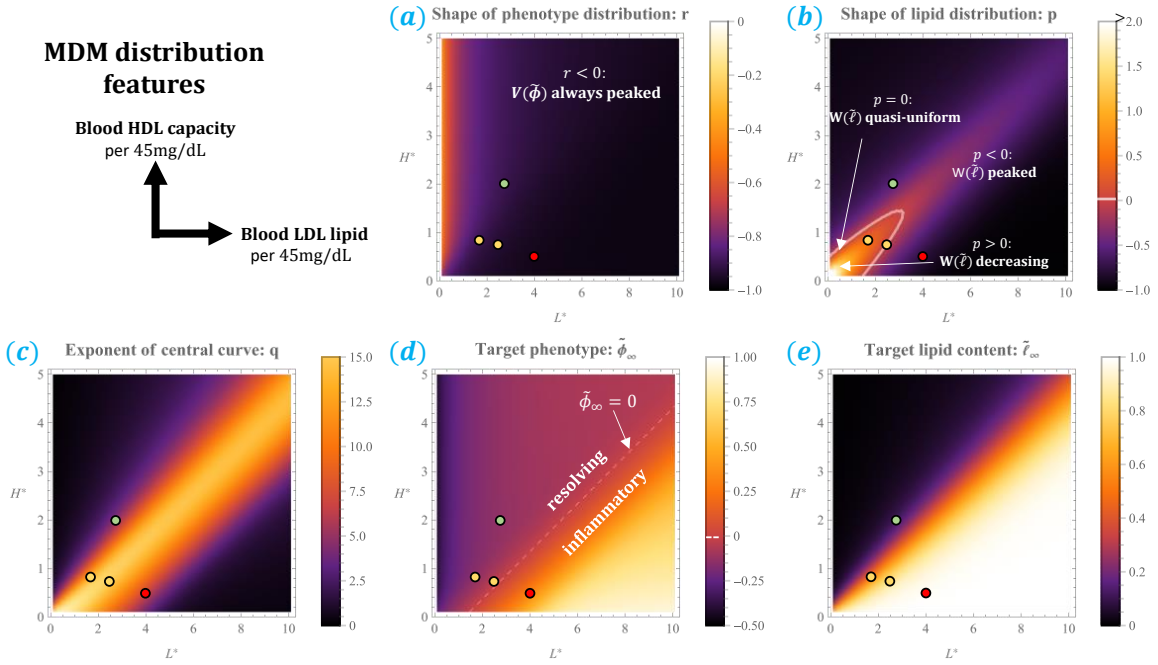


Figure 5.11: **Impact of blood LDL lipid ($L^\star$) and HDL capacity ($H^\star$) on the qualitative features of the MDM distribution.** The values were computed by combining the results shown in Fig. 5.5 with the formulae (5.64) and $r = -1 + \frac{p+1}{q}$. The four cases presented in Fig. 5.10 are also indicated: $(L^\star, H^\star) = (3, 2)$, $(1.8, 0.8)$, $(2.5, 0.77)$ and $(4, 0.5)$.

increases to the relative level of LDL lipid to HDL capacity raise both these markers of pathology.

Finally, we note that the exponent, q, of the central curve is largest when $L^\star$ and $H^\star$ are comparable. This causes the central curve to appear straighter (i.e., $\tilde{\phi}_c(\tilde{\ell}) \approx \tilde{\phi}_\infty$ except for the smallest values of $\tilde{\ell}$) in cases of intermediate pathology. Indeed, in Fig. 5.10 the intermediate cases (b) and (c) are notably straighter than the unhealthy case (d).

5.4 Discussion

In this chapter we have developed a mathematical model for early atherosclerosis in which the MDM population is structured by phenotype, ϕ, and lipid content, ℓ. This framework allows for incremental changes in phenotype and lipid content, which contrasts their treatment as binary variables in much of the existing modelling literature. The model couples the MDM dynamics to the densities of free LDL lipid, $L_{LDL}(t)$, retained LDL lipid, $L_{\mathrm{r}}(t)$, apoptotic lipid, $L_{\mathrm{ap}}(t)$, necrotic lipid, $L_{\mathrm{n}}(t)$, HDL capacity, $H(t)$, inflammatory mediators, $S_+(t)$, and resolving mediators, $S_-(t)$. These variables form a closed subsystem of ODEs when coupled with the MDM density, $M(t)$, mean phenotype, $\hat{\Phi}_M(t)$, and mean lipid content, $\hat{L}_M(t)$. This subsystem can be solved independently of the structured MDM population, $m_{\phi,\ell}(t)$.

We parameterised the model using data from the biological literature. Where possible, we used human *in vivo* data (e.g., blood measurements for $L^{(0)}$ and $H^{(0)}$) or *ex vivo* data (e.g., surgical data for $\pi_L^{(0)}$ and postmortem data for $L^{(1)}$ and $H^{(1)}$). However, the majority of the model parameters are calibrated to *in vitro* experiments. We prioritised studies with human cell lines (e.g., for a_0, k_{LDL}, k_{r}, k_H, S_+^{c50}, ρ), and used data from nonhuman cell lines when necessary (e.g., murine data for κ, k_{ap} and k_{n}). Since the point estimates in Table 5.1 are likely to carry high degrees of uncertainty, we have cautiously interpreted the results of the current study by focusing on trends rather than precise quantitative outputs.

Our model analysis focused on the impact of three dimensionless parameters: $L^\star$, $H^\star$ and K_{r}. The quantities $L^\star$ and $H^\star$ are proportional to the blood densities of LDL lipid and HDL capacity, respectively. These vary considerably according to genetic and lifestyle factors. We explored values in the range $L^\star \in (0, 10)$ and $H^\star \in (0, 5)$; the upper bounds correspond to densities of 450 and 225mg/dL, respectively. The quantity K_{r} is proportional to the capacity for LDL lipid retention. This varies according to the specific region of artery wall under consideration. We explored values $K_{\mathrm{r}} \in (0.3, 100)$, which span athero-resistant regions with capacity 15mg/dL to athero-prone regions with capacity 7500mg/dL.

We discuss our findings below in relation to the key questions posed in Sect. 5.1 .

Q1.a. **How do blood LDL and HDL levels affect the time-evolution of lesion composition?** Time-dependent numerical solutions revealed that the model lesion evolves in three phases. The first phase (approx. $0 < t < 0.5$ MDM lifespans) consists of the initial influx of LDL, HDL and, subsequently, MDMs. MDM lipid loads are small but increasing and the mean MDM phenotype is inflammatory. The second phase (approx. $0.5 < t < 2$ MDM lifespans) is characterised by modulation towards resolving MDM phenotypes and a slower rise of MDM lipid content. These phases are consistent with observations of macrophage behaviour during acute inflammation; macrophages first adopt inflammatory phenotypes and transition to resolving phenotypes during a phase of inflammatory resolution and tissue repair [237]. To the best of our knowledge, the present model is the first to capture this transition as an emergent property of the dynamics. Rather than completely resolving, however, the model lesion enters a final phase (approx. $2 < t < 100$ MDM lifespans) in which the dynamics tend to a nonzero steady state. If blood LDL lipid is low relative to HDL capacity, the lesion tends to a healthy state with low lipid burden and resolving phenotypes. This behaviour suggests that the well-documented spontaneous regression of many early atherosclerotic lesions [238] may simply be the natural and expected progression under a healthy blood lipoprotein balance. By contrast, when blood LDL lipid is high relative to HDL capacity, MDM lipid loads increase to equilibrium and the model lesion accumulates necrotic lipid. Overall,

the three-phase dynamics support the idea that chronic inflammation in atherosclerosis can be understood as an acute inflammatory response to LDL retention with incomplete resolution [239].

We also studied the impact of LDL retention capacity on the timescale of atherosclerosis development. In particular, we computed the time for MDM lipid to exceed a density of 450mg/dL; we use this lipid density as a proxy for fatty streak formation, which is characterised by the appearance of foam cells [27]. Our results indicate that this time decreases with LDL retention capacity; fatty streak onset in the model lesion occurs earlier for regions of high LDL retention. This finding is consistent with observations of the murine aortic arch in which regions of lower retention capacity (e.g., central zone of the arch) developed atherosclerosis later than regions of high retention (e.g., dorsal and ventral zones) [24].

Q1.b. **How do blood LDL and HDL levels affect lesion composition at steady state?** Analysis of steady state solutions revealed how equilibrium lesion composition depends on the parameters $L^\star$, $H^\star$ and K_r. The results indicate that the degree of pathology is largely determined by a linear combination of the form: $0.4L^\star - H^\star$; it is the (weighted) *relative* value of LDL lipid to HDL capacity in the blood that matters. The greater weighting on $H^\star$ in the linear combination reflects the higher value of the dimensionless lipid efflux rate, k_H, relative to the uptake rates in Table 5.2. Hence, the increased amount of lipid efflux promoted by a rise in blood HDL lipid capacity is greater than the increase in lesion lipid content by an equal rise in blood LDL lipid density. Overall, the model predicts that early atherosclerotic lesions regress when blood LDL lipid density decreases or blood HDL capacity increases. The degree of pathology also generally increases with K_r. Regions of higher LDL retention capacity exhibit greater MDM densities, more inflammatory MDM phenotypes and higher MDM lipid loads.

Q2.a. **How do MDM phenotype and lipid content evolve over time?** We analysed the MDM distribution by deriving a continuum analogue of the discrete Eqs. (5.29) for $m_{\phi,\ell}(t)$. Analysis of the continuum model showed that the time-evolution of phenotype and lipid content for individual MDMs depends on the time of entry into the lesion. MDMs which enter the lesion at early times typically first transition from phenotypic neutrality to an inflammatory state, and then to a resolving state (if the blood LDL to HDL balance is healthy) or to a milder inflammatory state (if the LDL to HDL balance is unhealthy). The trajectories of MDMs which enter the lesion at later times are monotonic (in phenotype-lipid structure space) and follow the central curve of the equilibrium MDM distribution. These results suggest that MDMs which enter the lesion during early stages of lesion development experience

a greater amount of phenotype modulation throughout their lifespan than those entering at later times.

Q2.b. **Are MDM phenotype and lipid content correlated?** The asymptotic analysis presented in Sect. 5.3.2.4 showed that MDM phenotype and lipid content are correlated via a power law at steady state. If LDL lipid density dominates HDL capacity in the blood, lipid-laden MDMs have a more inflammatory phenotype than lipid-poor MDMs, while if blood LDL lipid density is sufficiently low, lipid-laden MDMs have a more resolving phenotype than MDMs with a lower lipid burden. The non-linearity of the correlation is determined by a constant, q, that measures the relative amount of lipid activity to mediator activity in the lesion (made precise by Eq. (5.64)). Although we did not pursue a time-dependent mathematical analysis, numerical solutions (e.g., Fig. 5.7) demonstrated that the MDM phenotype-lipid distribution is always concentrated about a central curve, indicating that a monotone correlation between phenotype and lipid content holds for all times. These findings are consistent with the recent discovery of PLIN2$^{\text{hi}}$/TREM1$^{\text{hi}}$ macrophages in human lesions, for which the transcriptional signatures of lipid loading and inflammation are coupled [190].

Q2.c. **What are the qualitative features of the phenotype and lipid content marginal distributions at steady state?** Further analysis in Sect. 5.3.2.4 showed that the phenotype marginal distribution always attains a single local maximum. The location of the maximum, which represents the most common phenotype in the lesion, is a close approximation to the "target" phenotype that MDMs are driven towards by the extracellular environment over their lifetime. By contrast, the lipid marginal distribution varies more in shape as $L^\star$ and $H^\star$ are varied; it may exhibit a local maximum, adopt a quasi-uniform profile, or decrease monotonically according to the value of p, a constant which quantifies the amount of MDM-lipid activity in the lesion.

Conclusions. In this chapter we have presented a new mathematical model for early atherosclerosis in which the MDM population is structured according to phenotype and lipid content. The model indicates that lesion composition depends sensitively on the (weighted) relative density of LDL lipid to HDL capacity in the blood, and the LDL retention capacity of the artery wall. Numerical and asymptotic results show that, at steady state, MDM phenotype and lipid content are monotonically correlated via a power law, the phenotype marginal distribution is unimodal, and the lipid content distribution may attain a unimodal, quasi-uniform or decreasing profile. The findings discussed above develop the current understanding of macrophage phenotype and lipid content heterogeneity in early atherosclerotic lesions. In the following chapter, we consider an additional aspect of macrophage heterogeneity, namely spatial variation.

Chapter 6

A spatially-resolved lipid structured model

In this chapter, we extend the lipid-structured model of Chapter 4 to account for spatial heterogeneity. The model uses the principle of mass conservation to couple the MDM dynamics to the densities of free LDL lipid, retained LDL lipid, apoptotic lipid, necrotic lipid, HDL lipid capacity, in addition to inflammatory mediators.

6.1 Introduction

Understanding the spatial distribution of lipid and MDMs in atherosclerotic lesions is a topic of current research. Data on spatial variation in early mouse lesions is limited since murine artery walls do not undergo diffuse intimal thickening; the intima width is 10-20 fold shorter in mice (~ 0.025mm [235, 236]) compared to humans ($\sim 0.25 - 50$mm [9, 204]). Nonetheless, murine bead tracking studies have been conducted by Williams *et al.* [68], which suggest that MDMs undergo limited spatial movement in both progressing and regressing lesions. In this chapter, we focus instead on spatial variation within human lesions.

Spatially resolved data on lipid and MDM accumulation in early human lesions is also scarce. The only study which presents such data, that we are aware of, is by Nakashima *et al.* [9]. Their images of lipid and MDM densities in early human coronary lesions are shown in Fig. 6.1. Inspection of the lipid densities in Fig. 6.1(b,e,h) shows that lipid first accumulates deep in the intima, towards the media. Nakashima *et al.* note that biglycan, an extracellular matrix proteoglycan, occurs in the same spatial location as the early distribution of lipids, suggesting that the early deposition profile is due to a non-uniform LDL retention capacity. The images in Fig. 6.1(k, n, q) show a second wave of lipid influx that coincides with the later influx of MDMs (c.f. (l, o, r)). The MDM density remains localised to the intima, with negligible numbers of macrophages near the medial boundary. More recent work by Nakagawa *et al.* [110] further supports the hypothesis that MDMs do not traverse into the media from the intima. We further note that both the lipid and MDM densities appear to attain a peak within the intima at the "PIT with

foam cells" stage (see (q) and (r)). This region of greatest lipid density approximately coincides with that of greatest MDM density. The primary goal of the present study is to identify mechanisms which may explain how these spatial profiles arise.

Of particular relevance is the impact of lipid ingestion on MDM behaviour. We note first that lipid-laden MDMs exhibit a decreased lifespan relative to unladen MDMs. This is due to the cytotoxicity of free cholesterol, which promotes controlled cell death (apoptosis) [78]. Lipid-laden MDMs are also less mobile than unladen MDMs, due in part to cytoskeletal changes [240, 241]. Both effects are likely to impact the spatial distribution of MDMs (and consequently, lipid) since the distribution of MDM lipid content is unlikely to be spatially uniform. The impact of these lipid-dependent effects on the MDM and lipid spatial distributions is presently unknown, and another focus of the present study.

By extending the lipid-structured model of Chapter 4 to account for simultaneous variation in MDM lipid content and spatial position, we derive a continuum model and address the following key questions:

Q1. **When does our model qualitatively reproduce the densities in Fig. 6.1?**

Q2. **What are the effects of introducing lipid content-dependence to MDM lifespan and mobility?**

Q3. **How does MDM lipid content vary with spatial depth?**

The model developed in this chapter contributes to the large literature on spatial PDE models of atherosclerosis (e.g., [136, 139, 141, 144, 146, 151, 242], reviewed in Chapter 3). With the notable exceptions of Fok [144] and Mirzaei *et al.* [242], the existing spatial PDE models have not been compared to available images of lesion formation. No models have accounted for the Nakashima images shown in Fig. 6.1. Moreover, existing spatial models that account for MDM lipid uptake use a binary treatment of MDM lipid content by distinguishing between lipid-poor MDMs, simply called "macrophages", and lipid-laden MDMs, called "foam cells". The existing models that capture gradual MDM lipid accumulation using a lipid-structured framework are not spatially resolved [165, 166, 184, 185].

The remainder of this chapter is structured as follows. Sect. 6.2 explains the model development. Sect. 6.3 contains the results. We consider the model in increasing complexity by introducing lipid content-dependent lifespan and mobility one at a time, and then simultaneously. Finally, in Sect. 6.4 we discuss the results and how they address the above questions.

6.2 Model development

In this section we present a spatially-resolved model for lipids and MDMs in early atherosclerosis. The MDM population is further structured according to lipid content. A model schematic is given in Fig. 6.2.

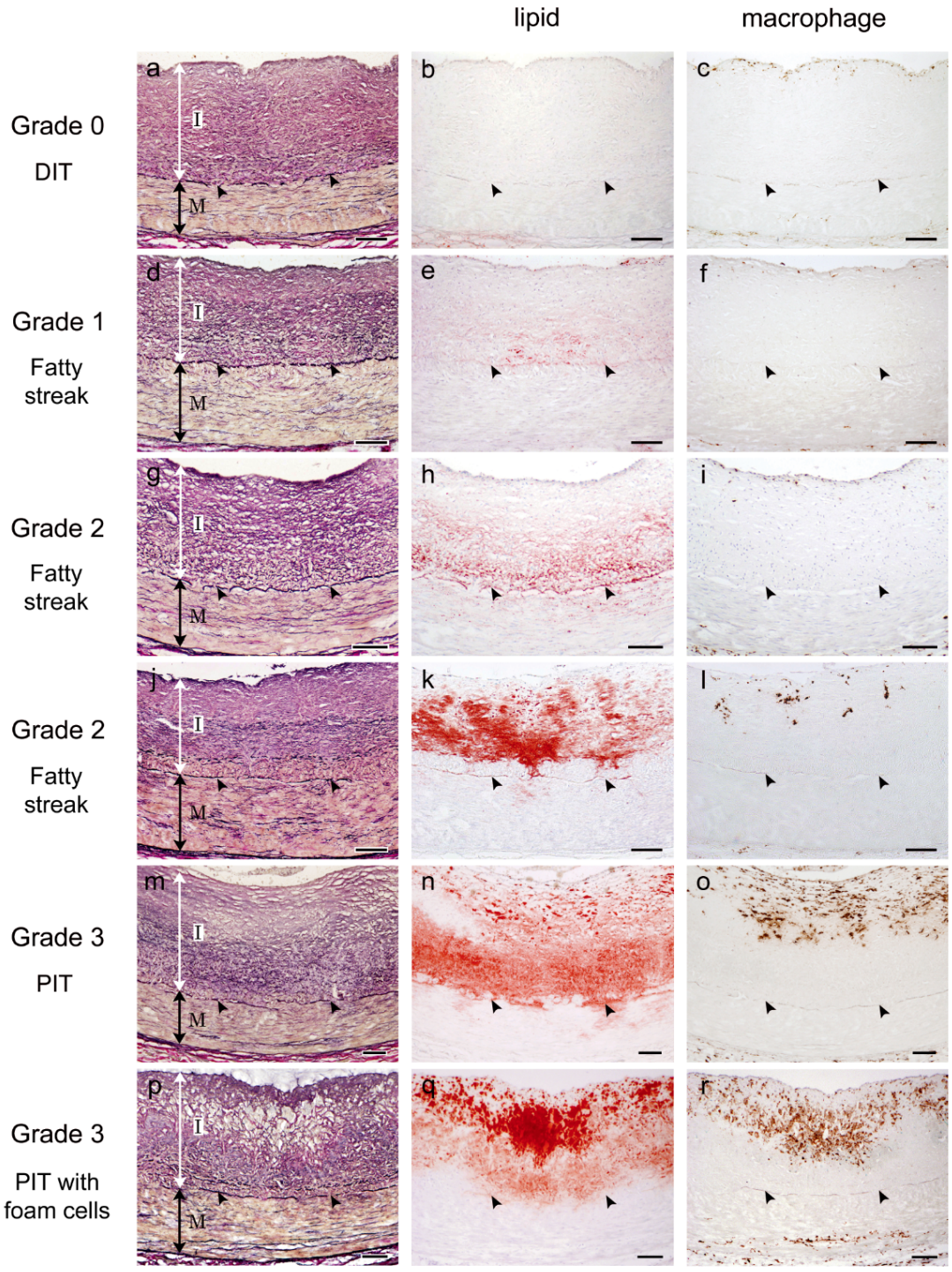


Figure 6.1: **Early stages of human coronary atherosclerosis.** The images show representative lipid and macrophage densities across six stages of lipid accumulation. The endothelium is at the top of each image, and corresponds to $x = 0$ in our model. The internal elastic lamina (IEL) which separates the tunica intima (labelled "I") from the tunica media (labelled "M") is marked with black arrows, and corresponds to $x = X$. Note how lipid first accumulates deep in the tunica intima. The lipid and macrophage densities eventually both peak within the tunica intima, in plots (q) and (r) respectively. Bars on the bottom-right represent 0.1mm. Reproduced, with permission, from Nakashima *et al.* [9].

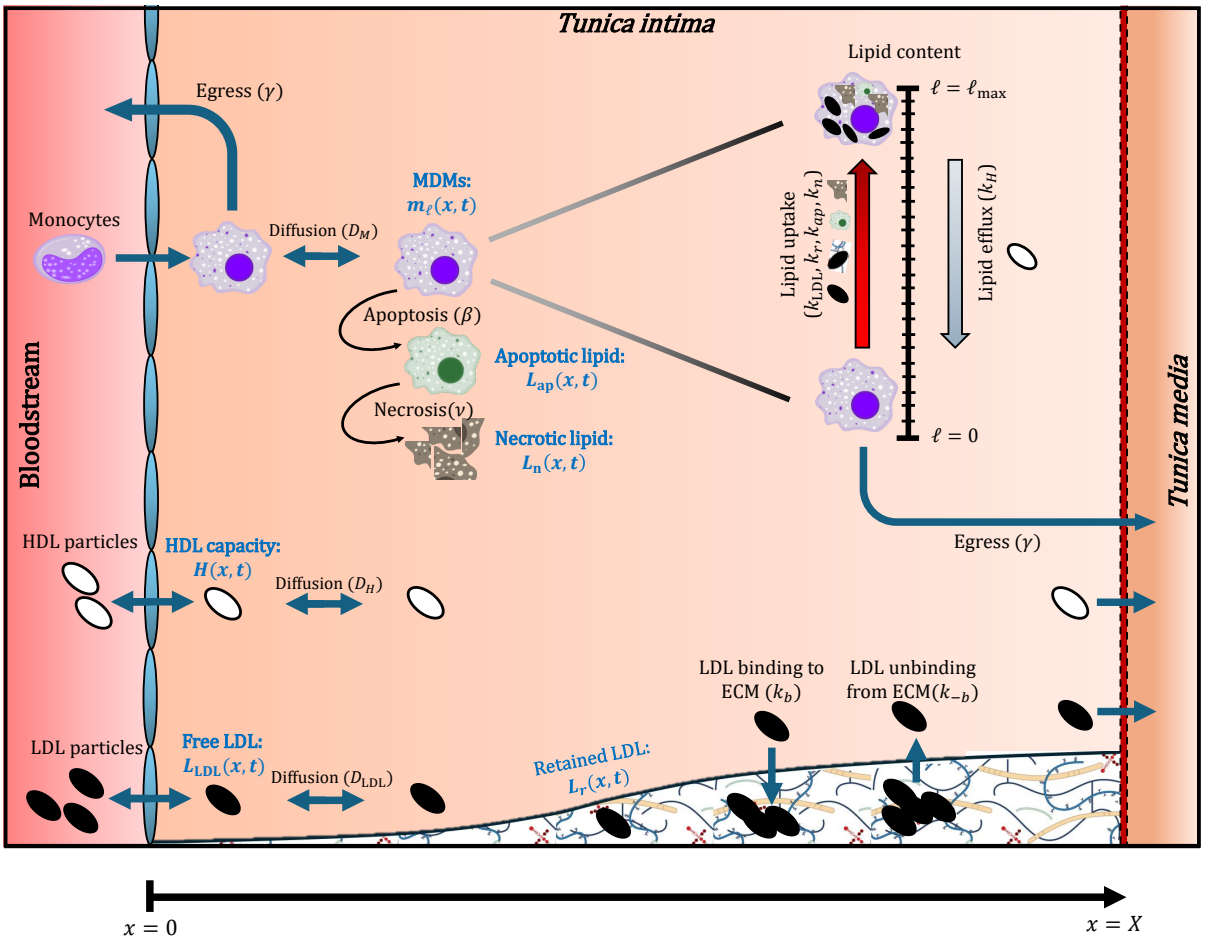


Figure 6.2: **Schematic depiction of the model.** The spatial domain is the *tunica intima*, which is bordered by the bloodstream at the endothelium, $x = 0$, and the *tunica media* at the IEL, $x = X$. The dependent variables are highlighted in blue. The discrete lipid-structured MDM population is illustrated in the top-right; MDMs increase their ℓ-index via lipid uptake, and decrease their ℓ-index via lipid efflux to HDL. Note also the non-uniform LDL retention capacity due to abundant LDL-retaining proteoglycans towards the *tunica media*. We omit the smaller diffusivities of apoptotic and necrotic lipid, and the lipid-dependence of MDM mobility and apoptosis for legibility.

6.2.1 Assumptions and definitions

We formulate the model as a system of partial differential equations, with associated boundary and initial conditions. The equations are defined in one spatial dimension, $0 \leq x \leq X$, which represents distance from the endothelium ($x = 0$) to the IEL ($x = X$). This Cartesian formulation assumes that the domain is sufficiently far from the edges of the lesion that net circumferential and axial motions are negligible. We assume for simplicity that the domain length is fixed. This approximation is reasonable for early lesions but is unlikely to hold for late-stage plaques.

We further assume that MDMs take up and offload lipid in finite increments of mass $\Delta a > 0$, and structure the MDM population according to lipid content. Specifically, we let $m_\ell(x,t) \geq 0$ denote the density of MDMs with lipid content $a_0 + \ell\Delta a$ at position x and time $t \geq 0$. The index ℓ runs over non-negative values: $\ell = 0, 1, \ldots, \ell_{\max}$, so that MDM lipid content ranges from $a_0 \geq 0$, the endogenous content, to $a_0 + \kappa$, where $\kappa = \ell_{\max}\Delta a$ is the maximum amount of lipid that an MDM can ingest.

We introduce additional dependent variables to describe the extracellular environment. We denote by $L_{LDL}(x,t) \geq 0$, $L_{\mathrm{r}}(x,t) \geq 0$, $L_{\mathrm{ap}}(x,t) \geq 0$ and $L_{\mathrm{n}}(x,t) \geq 0$ the mass densities of free LDL lipid, retained LDL lipid, apoptotic lipid and necrotic lipid respectively. We let $H(x,t)$ be the lipid capacity of HDL particles in the lesion. Finally, we denote by $S(x,t) \geq 0$ the mass density of inflammatory mediators.

6.2.2 Model equations

MDMs. We propose that the MDM population evolves according to the following PDEs:

$$\begin{aligned}\frac{\partial m_\ell}{\partial t} = &\underbrace{D_M\left[1 - \psi_D\Big(\frac{\ell}{\ell_{\max}}\Big)\right]\frac{\partial^2 m_\ell}{\partial x^2}}_{\text{diffusion}} - \underbrace{\frac{\beta m_\ell}{1 - \psi_\beta\big(\frac{\ell}{\ell_{\max}}\big)}}_{\text{apoptosis}} \\ &+ \underbrace{\boldsymbol{k_L}\cdot\boldsymbol{L}\,\left[(\ell_{\max} - \ell + 1)m_{\ell-1} - (\ell_{\max} - \ell)m_\ell\right]}_{\text{lipid uptake}} \\ &+ \underbrace{k_H H \quad \left[(\ell+1)m_{\ell+1} - \ell m_\ell\right]}_{\text{lipid efflux to HDL}},\end{aligned} \tag{6.1}$$

for all $0 \leq x \leq 1$ and $t \geq 0$. Eqs. (6.1) hold for $\ell = 0, 1, \ldots, \ell_{\max}$, subject to the closure conditions:

$$m_{-1} = m_{\ell_{\max}+1} = 0. \tag{6.2}$$

The first term on the RHS of Eqs. (6.1) describes MDM transport by random motion. We assume that MDM mobility decreases linearly with ℓ so that MDMs with low lipid loads are more mobile than lipid-laden cells; macrophage mobility decreases upon conversion to foam cells [240]. The parameter $0 \leq \psi_D \leq 1$ determines how sensitive MDM diffusion is to lipid load. If $\psi_D = 0$ then there is no lipid-dependence and all MDMs have diffusion coefficient D_M. When $\psi_D > 0$, MDM diffusivity decreases from D_M at $\ell = 0$ to

$D_M(1-\psi_D)$ at $\ell = \ell_{\max}$. When $\psi_D = 1$, the MDMs are fully lipid laden and, as a result, immobile.

The second term on the RHS of Eqs. (6.1) represents MDM apoptosis. We suppose that the apoptosis rate is an increasing function of ℓ, so that lipid-laden macrophages die more frequently than those with lower lipid loads, due to the cytotoxicity of free cholesterol [78]. More specifically, we assume that the mean MDM lifespan decreases linearly with ℓ, from β^{-1} when $\ell = 0$ to $\beta^{-1}(1-\psi_\beta)$ when $\ell = \ell_{\max}$. The parameter $0 \leq \psi_\beta \leq 1$ determines the sensitivity of mean lifespan on lipid content; if $\psi_\beta = 0$ then all MDMs share a common mean lifespan, β^{-1}, regardless of their lipid content, whereas if $\psi_\beta = 1$ then the MDM mean lifespan decreases to zero at $\ell = \ell_{\max}$ (MDMs at capacity die instantly, giving $m_{\ell_{\max}} = 0$). Our formulation assumes that the apoptosis rate increases with ℓ. This nonlinear dependence is reasonable since lipid handling is a normal macrophage function and lipid-induced apoptosis is a response to *excess* lipid accumulation [98]. Therefore, increases in lower lipid loads are likely to have less of an impact on macrophage viability than increases in lipid-laden cells.

The third term on the RHS of Eqs. (6.1) accounts for lipid uptake. Following [10], we model lipid uptake by applying the Law of Mass Action to the following reactions:

$$\mathrm{M}_\ell + \Delta a \xrightarrow{k_i(\ell_{\max}-\ell)} \mathrm{M}_{\ell+1}, \tag{6.3}$$

for $\ell = 0, 1, \ldots \ell_{\max}$ and $i \in \{LDL, \mathrm{r}, \mathrm{ap}, \mathrm{n}\}$. Reactions (6.3) assume that the rate of lipid uptake decreases linearly with lipid content, at a rate which is proportional to the available capacity. For notational brevity in Eqs.(6.1), we introduce vectors for the uptake rates, $\boldsymbol{k_L} := (k_{LDL}, k_\mathrm{r}, k_\mathrm{ap}, k_\mathrm{n})$, and the extracellular lipids, $\boldsymbol{L} := (L_{LDL}, L_\mathrm{r}, L_\mathrm{ap}, L_\mathrm{n})$, so that $\boldsymbol{k_L} \cdot \boldsymbol{L} = k_{LDL}L_{LDL} + k_\mathrm{r}L_\mathrm{r} + k_\mathrm{ap}L_\mathrm{ap} + k_\mathrm{n}L_\mathrm{n}$.

The final term on the RHS of Eqs. (6.1) accounts for lipid efflux to HDL. Again, following [10], we treat efflux with mass-action kinetics according to the reactions

$$\mathrm{M}_\ell \xrightarrow{k_H \ell} \mathrm{M}_{\ell-1}, \tag{6.4}$$

for $\ell = 0, 1, \ldots \ell_{\max}$. In reactions (6.4), we assume that the efflux rate increases linearly with lipid content.

We close Eqs. (6.1) by imposing the following boundary conditions for $\ell = 0, 1, \ldots, \ell_{\max}$:

$$-D_M \frac{\partial m_\ell}{\partial x} = \begin{cases} R(t)\delta_{\ell,0} - \gamma m_\ell & \text{at } x = 0; \\ \gamma m_\ell & \text{at } x = X, \end{cases} \tag{6.5}$$

where $\delta_{\ell,0}$ is the Kronecker-Delta. Eqs. (6.5) assume that newly recruited MDMs enter the lesion at $x = 0$ with only their endogenous lipid content at rate $R(t)$. The recruitment rate is a first-order Hill function of the inflammatory mediator density at the endothelium:

$$R(t) := \frac{\sigma_M S(0,t)}{S_{\mathrm{c}50} + S(0,t)}, \tag{6.6}$$

with a maximal recruitment rate of σ_M and half-maximal recruitment occurring when $S(0,t) = S_{\text{c50}}$. Eqs. (6.5) also account for MDM egress through either boundary. More specifically, we assume that MDMs at $x = 0, X$ exit the lesion at a rate proportional to their mobility: $\gamma\big[1 - \psi_D\big(\frac{\ell}{\ell_{\max}}\big)\big]$. Since internal elastic lamina egress rates have not been measured, to the best of our knowledge, we assume for simplicity that egress rates at $x = 0$ and $x = X$ are equal. We state initial conditions for m_ℓ together with the other variables later in this section.

Extracellular lipids. We assume the densities of free and retained LDL evolve according to the PDEs

$$\begin{aligned}\frac{\partial L_{\scriptscriptstyle LDL}}{\partial t} = \underbrace{D_{\scriptscriptstyle LDL}\frac{\partial^2 L_{\scriptscriptstyle LDL}}{\partial x^2}}_{\text{diffusion}} &- \underbrace{k_b L_{\scriptscriptstyle LDL}[K_{\text{r}}(x) - L_{\text{r}}]}_{\text{retention via ECM binding}} + \underbrace{k_{-b} L_{\text{r}}}_{\text{unbinding}} \\ &\underbrace{- k_{\scriptscriptstyle LDL}\Delta a L_{\scriptscriptstyle LDL}\sum_{\ell=0}^{\ell_{\max}}(\ell_{\max} - \ell)m_\ell}_{\text{uptake by MDMs}},\end{aligned} \tag{6.7}$$

$$\frac{\partial L_{\text{r}}}{\partial t} = k_b L_{\scriptscriptstyle LDL}[K_{\text{r}}(x) - L_{\text{r}}] - k_{-b} L_{\text{r}} - k_{\text{r}}\Delta a L_{\text{r}}\sum_{\ell=0}^{\ell_{\max}}(\ell_{\max} - \ell)m_\ell. \tag{6.8}$$

The first term in Eq. (6.7) accounts for random motion of free LDL, with diffusivity $D_{\scriptscriptstyle LDL}$. We also assume that free LDL binds to ECM proteoglycans with rate constant k_b in a capacity-limited manner, and unbinds at rate k_{-b}. Motivated by Fig. 6.1, we suppose that the capacity for LDL retention $K_r(x)$ is a sigmoidal function of position:

$$K_{\text{r}}(x) := \bar{K}_r \cdot \left(\frac{2}{1 + e^{\theta(1/2 - x/X)}}\right), \quad \text{where } \bar{K}_r = \frac{1}{X}\int_0^X K_r(x)dx. \tag{6.9}$$

Here $\bar{K}_r$ is the mean rLDL capacity in the intima and $\theta > 0$ determines the steepness of $K_{\text{r}}(x)$ (plots of the functional form for $K_r(x)/\bar{K}_r$ are shown in Fig. 6.3). The final terms in Eqs. (6.7)-(6.8) account for MDM uptake via reactions (6.3).

We close Eq. (6.7) by imposing the following boundary conditions:

$$-D_{\scriptscriptstyle LDL}\frac{\partial L_{\scriptscriptstyle LDL}}{\partial x} = \begin{cases} P_L^{(0)}(L^\star - L_{\scriptscriptstyle LDL}) & \text{at } x = 0; \\ P_L^{(1)}(L_{\scriptscriptstyle LDL} - 0) & \text{at } x = X. \end{cases} \tag{6.10}$$

Eqs. (6.10) account for the exchange of free LDL between the tunica intima and the lumen/tunica media. Parameters $P_L^{(0)}$ and $P_L^{(1)}$ denote the permeability to free LDL of the endothelium and internal elastic lamina, respectively. We assume that the blood density of LDL lipid is given by a constant $L^\star$. Motivated by human data reported by Smith *et al.* [206], we suppose further that the density of LDL lipid in the tunica media is negligible.

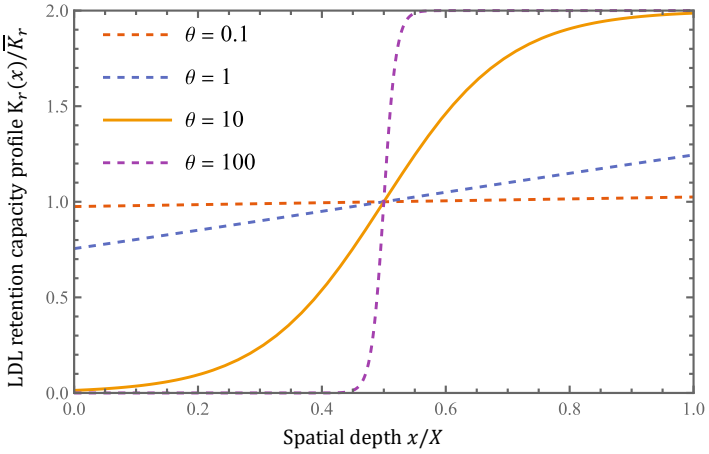


Figure 6.3: **Spatial dependence of the LDL retention capacity, defined in Eq. (6.9).** Higher values of θ increase the sharpness of the step. We choose $\theta = 10$ for our numerical simulations to mimic the smooth increase in LDL retention with depth seen in Fig. 6.1(e,h).

We propose that the apoptotic and necrotic lipid densities satisfy

$$\frac{\partial L_{\rm ap}}{\partial t} = \underbrace{D_{\rm ap}\frac{\partial^2 L_{\rm ap}}{\partial x^2}}_{\text{diffusion}} + \sum_{\ell=0}^{\ell_{\max}} \Bigg[\underbrace{\frac{\beta(a_0+\ell\Delta a)}{1-\psi_\beta(\frac{\ell}{\ell_{\max}})}}_{\text{apoptosis}} - \underbrace{k_{\rm ap}\Delta a L_{\rm ap}(\ell_{\max}-\ell)}_{\text{uptake by MDMs}} \Bigg] m_\ell - \underbrace{\nu L_{\rm ap}}_{\text{necrosis}}, \tag{6.11}$$

$$\frac{\partial L_{\rm n}}{\partial t} = D_{\rm n}\frac{\partial^2 L_{\rm n}}{\partial x^2} + \nu L_{\rm ap} - k_{\rm n}\Delta a L_{\rm n}\sum_{\ell=0}^{\ell_{\max}}(\ell_{\max}-\ell)m_\ell. \tag{6.12}$$

The terms on the first line of the RHS of Eq. (6.11) account for diffusion, lipid deposition due to MDM apoptosis and uptake by MDMs according to reactions (6.3). We further assume that apoptotic cells undergo secondary necrosis at rate ν, which provides linear sink and source terms in Eqs.(6.11) and (6.12), respectively.

We close Eqs. (6.11)-(6.12) by imposing the following boundary conditions:

$$\frac{\partial L_{\rm ap}}{\partial x} = \frac{\partial L_{\rm n}}{\partial x} = 0 \quad \text{at } x = 0, X. \tag{6.13}$$

Eqs. (6.13) assume for simplicity that the endothelium and internal elastic lamina are impermeable to both apoptotic and necrotic lipid.

HDL lipid capacity. We assume that the lipid capacity of the HDL particles is governed by the following PDE:

$$\frac{\partial H}{\partial t} = \underbrace{D_H\frac{\partial^2 H}{\partial x^2}}_{\text{diffusion}} \quad \underbrace{- k_H\Delta a H\sum_{\ell=0}^{\ell_{\max}}\ell m_\ell}_{\text{lipid efflux by MDMs}}. \tag{6.14}$$

Eq. (6.14) accounts for HDL diffusion and MDM lipid efflux via reactions (6.4).

We close Eq. (6.14) by imposing the following boundary conditions:

$$-D_H\frac{\partial H}{\partial x} = \begin{cases} P_H^{(0)}(H^\star - H) & \text{at } x = 0; \\ P_H^{(1)}(H - 0) & \text{at } x = X. \end{cases} \tag{6.15}$$

Eqs. (6.15) describe the flux of HDL lipid capacity between the tunica intima and the lumen/tunica media. The constants $P_H^{(0)}$ and $P_H^{(1)}$ denote the permeability to HDL of the endothelium and internal elastic lamina, respectively. We assume that the blood density of HDL lipid capacity is a constant $H^\star$. Similar to our treatment of LDL lipid, we assume that the HDL lipid capacity density in the tunica media is negligible.

Inflammatory mediators. Finally, we propose that the density of inflammatory mediators S evolves according to the following PDE:

$$\frac{\partial S}{\partial t} = \underbrace{D_S \frac{\partial^2 S}{\partial x^2}}_{\text{diffusion}} + \underbrace{\alpha L_{\text{r}}}_{\substack{\text{resident response} \\ \text{to LDL retention}}} - \underbrace{\delta_S S}_{\text{natural decay}} . \tag{6.16}$$

The first term on the RHS of Eq. (6.16) accounts for mediator diffusion, with diffusion constant D_S. Consistent with the response-to-retention hypothesis, we assume that inflammatory mediators are produced by resident cells at a rate proportional to the density of rLDL; the signal cascades which first stimulate MDM recruitment are, as yet, unknown, but are thought to be the result of excessive LDL retention [59]. Finally, we assume that inflammatory mediators undergo natural decay at rate δ_S.

We close Eq. (6.16) with the boundary conditions

$$-D_S \frac{\partial S}{\partial x} = \begin{cases} P_S^{(0)}(0 - S) & \text{at } x = 0; \\ P_S^{(1)}(S - 0) & \text{at } x = X. \end{cases} \tag{6.17}$$

In Eqs. (6.17) we assume, for simplicity, that the mediator densities in the lumen and tunica media are negligible, and that mediators leave the lesion via the endothelium and internal elastic lamina with permeabilities $P_S^{(0)}$ and $P_S^{(1)}$ respectively.

Initial conditions. We impose the following conditions at $t = 0$:

$$m_\ell = 0 \quad \forall \ell = 0, 1, \ldots, \ell_{\max}, \qquad L_{LDL} = L_{\text{r}} = L_{\text{ap}} = L_{\text{n}} = H = S = 0. \tag{6.18}$$

Eqs. (6.18) assert that the model lesion is initially devoid of MDMs, extracellular lipid, HDL and inflammatory mediators.

6.2.3 Total MDM density and lipid content

It will be useful, when discussing our results, to define the total MDM density, $M(x,t)$, and MDM lipid content, $L_M(x,t)$:

$$M(x,t) := \sum_{\ell=0}^{\ell_{\max}} m_\ell(x,t), \qquad L_M(x,t) := \sum_{\ell=0}^{\ell_{\max}} (a_0 + \ell \Delta a) m_\ell(x,t). \tag{6.19}$$

Differentiating Eqs. (6.19) with respect to t and substituting Eqs. (6.1) gives

$$\frac{\partial M}{\partial t} = D_M \frac{\partial^2}{\partial x^2}\left[M - \psi_D \sum_{\ell=0}^{\ell_{\max}} \frac{\ell m_\ell}{\ell_{\max}}\right] - \beta\left[M + \psi_\beta \sum_{\ell=0}^{\ell_{\max}} \frac{\ell m_\ell}{\ell_{\max} - \psi_\beta \ell}\right], \tag{6.20}$$

$$\begin{aligned}\frac{\partial L_M}{\partial t} = {} & D_M \frac{\partial^2}{\partial x^2}\left[L_M - \psi_D \sum_{\ell=0}^{\ell_{\max}} \frac{(a_0 + \ell\Delta a)\ell m_\ell}{\ell_{\max}}\right] + \boldsymbol{k_L} \cdot \boldsymbol{L}[(\kappa + a_0)M - L_M] \\ & - \beta\left[L_M + \ \psi_\beta \sum_{\ell=0}^{\ell_{\max}} \frac{(a_0 + \ell\Delta a)\ell m_\ell}{\ell_{\max} - \psi_\beta \ell}\right] - k_H H(L_M - a_0 M).\end{aligned} \tag{6.21}$$

The RHS terms in Eq. (6.20) account for MDM diffusion and apoptosis. The RHS terms in Eq. (6.21) describe diffusion of MDM lipid, lipid uptake, apoptosis and lipid efflux, respectively. We may also rewrite Eqs. (6.7), (6.8), (6.11), (6.12), (6.14) and (6.16) as

$$\frac{\partial L_{LDL}}{\partial t} = D_{LDL} \frac{\partial^2 L_{LDL}}{\partial x^2} - k_b L_{LDL}[K_{\mathrm{r}}(x) - L_{\mathrm{r}}] + k_{-b} L_r - k_{LDL} L_{LDL}[(\kappa + a_0)M - L_M], \tag{6.22}$$

$$\frac{\partial L_{\mathrm{r}}}{\partial t} = k_b L_{LDL}[K_{\mathrm{r}}(x) - L_{\mathrm{r}}] - k_{-b} L_r - k_{\mathrm{r}} L_{\mathrm{r}}[(\kappa + a_0)M - L_M], \tag{6.23}$$

$$\begin{aligned}\frac{\partial L_{\mathrm{ap}}}{\partial t} = {} & D_{\mathrm{ap}} \frac{\partial^2 L_{\mathrm{ap}}}{\partial x^2} + \beta\left[L_M + \psi_\beta \sum_{\ell=0}^{\ell_{\max}} \frac{(a_0 + \ell\Delta a)\ell m_\ell}{\ell_{\max} - \psi_\beta \ell}\right] \\ & - \nu L_{\mathrm{ap}} - k_{\mathrm{ap}} L_{\mathrm{ap}}[(\kappa + a_0)M - L_M],\end{aligned} \tag{6.24}$$

$$\frac{\partial L_{\mathrm{n}}}{\partial t} = D_{\mathrm{n}} \frac{\partial^2 L_{\mathrm{n}}}{\partial x^2} + \nu L_{\mathrm{ap}} - k_{\mathrm{n}} L_{\mathrm{n}}[(\kappa + a_0)M - L_M], \tag{6.25}$$

$$\frac{\partial H}{\partial t} = D_H \frac{\partial^2 H}{\partial x^2} - k_H H(L_M - a_0 M), \tag{6.26}$$

$$\frac{\partial S}{\partial t} = D_S \frac{\partial^2 S}{\partial x^2} + \alpha L_{\mathrm{r}} - \delta_S S. \tag{6.27}$$

Eqs. (6.20)-(6.27) form a closed subsystem when MDM diffusion and apoptosis are lipid content-independent ($\psi_D = \psi_\beta = 0$); otherwise they are coupled to Eqs. (6.1). We derive boundary conditions for M and L_M by differentiating Eqs. (6.19) with respect to x and substituting Eqs. (6.5):

$$-D_M \frac{\partial M}{\partial x} = \begin{cases} R(t) - \gamma M & \text{at } x = 0; \\ \gamma M & \text{at } x = X, \end{cases} \tag{6.28}$$

$$-D_M \frac{\partial L_M}{\partial x} = \begin{cases} a_0 R(t) - \gamma L_M & \text{at } x = 0; \\ \gamma L_M & \text{at } x = X. \end{cases} \tag{6.29}$$

The boundary conditions (6.10), (6.13), (6.15) and (6.17) for the remaining dependent variables are unchanged.

6.2.4 Parameter values

The model parameters are summarised in Table 6.1. Parameters above the dotted lines are in common with, or have direct analogues to, the parameters in Chapter 5. In particular, we explore a range of plausible values for the lumen blood densities of LDL lipid, $L^\star =$

Table 6.1: Model parameters

Parameter	Interpretation	Estimate	Source
$L^\star$	Lumen LDL lipid density	$0 - 440$ mg/dL	[32, 39]
$H^\star$	Lumen HDL lipid capacity	$0 - 230$ mg/dL	[202]
$P_L^{(0)}$	Endothelial permeability to LDL	0.37 mm month^{-1}	[203, 204]
$P_H^{(0)}$	Endothelial permeability to HDL	0.74 mm month^{-1}	[205]
$P_L^{(1)}$	IEL permeability to LDL	1.1 mm month^{-1}	[207]
$P_H^{(1)}$	IEL permeability to HDL	2.2 mm month^{-1}	[207]
$P_S^{(0)}$	Endothelial permeability to mediators	5.0 mm month^{-1}	[243]
$P_S^{(1)}$	IEL permeability to mediators	15 mm month^{-1}	[207]
$\overline{K}_r$	Mean LDL retention capacity	1900 mg/dL	[208, 210]
k_b	LDL retention rate	0.008 dL/mg month^{-1}	[206, 211]
k_{-b}	LDL unbinding rate	1.8 month^{-1}	[206, 211]
σ_M	Maximum MDM entry rate	6800 mm^{-2} month^{-1}	[212, 214]
β	Unladen MDM apoptosis rate	1.0 month^{-1}	[68, 215]
γ	Unladen MDM egress rate	0.08 mm month^{-1}	[214, 216]
ν	Secondary necrosis rate	37 month^{-1}	[217]
a_0	MDM endogenous lipid	27pg	[218, 219]
κ	MDM lipid capacity	800pg	[133]
k_{LDL}	LDL lipid uptake rate	0.00034 dL/mg month^{-1}	[90]
k_r	rLDL lipid uptake rate	0.023 dL/mg month^{-1}	[90]
k_ap	Apoptotic lipid uptake rate	0.060 dL/mg month^{-1}	[220, 221]
k_n	Necrotic lipid uptake rate	0.015 dL/mg month^{-1}	[222]
k_H	Lipid efflux rate	0.34 dL/mg month^{-1}	[223, 224]
S^{c50}	Mediator density for half-maximum MDM influx	5 ng/mL	[225, 226]
δ_S	Mediator natural decay rate	1600 month^{-1}	[201]
α	Resident inflammatory mediator production per rLDL lipid	3.5×10^{-5} month^{-1}	[68]
Δa	MDM uptake/efflux increment of lipid	16 pg	[91, 233]
$\ell_{\max}$	MDM lipid capacity per Δa	100	$= \kappa/\Delta a$
X	Tunica intima width	0.40 mm	[9]
θ	LDL retention profile shape	10	[9]
D_M	Diffusivity of unladen MDMs	0.02 mm^2 month^{-1}	[244]
D_ap	Diffusivity of apoptotic cells	0.005 mm^2 month^{-1}	est.
D_n	Diffusivity of necrotic cells	0.005 mm^2 month^{-1}	est.
D_{LDL}	Diffusivity of free LDL	9.2 mm^2 month^{-1}	[143]
D_H	Diffusivity of HDL	22 mm^2 month^{-1}	[143]
D_S	Diffusivity of mediators	500 mm^2 month^{-1}	[245]
ψ_D	MDM mobility sensitivity to lipid load	$\in [0, 1]$	-
ψ_β	MDM lifespan sensitivity to lipid load	$\in [0, 1]$	-

$0 - 440$mg/dL, and HDL lipid capacity, $H^\star = 0 - 230$mg/dL; their values depend on lifestyle choices (e.g., diet) and, as such, are modifiable in practice. The parameters below the dotted lines do not have analogues in Chapter 5. We briefly explain their estimated values below.

Our estimate of the tunica intima width, $X \approx 0.40$mm, is derived from Fig. 6.1. These images indicate that tunica intima width does not vary substantially during the early stages of disease progression. Regarding the variation in LDL retention with distance from the lumen, we further estimate $\theta = 10$ from these images, as this value ensures that $K_r(x)$ increases smoothly with depth (see Eq. (6.9) and Fig. 6.3).

The diffusivity parameters vary substantially in magnitude. The value for lipid-unladen MDMs, $D_M = 0.014$ mm^2 month^{-1}, derives from data on macrophage migration paths in [244]. We assume that the diffusivity of apoptotic and necrotic cells, $D_{\text{ap}} = D_{\text{n}} = 0.003$ mm^2 month^{-1}, is smaller than that of MDMs since dead cells do not move as independent agents. The diffusivities of free LDL, $D_{LDL} = 9.2$mm^2 month^{-1}, HDL, $D_H = 22$mm^2 month^{-1}, and mediators, $D_S = 500$mm^2 month^{-1}, are substantially higher.

6.2.5 Non-dimensionalisation

We define

$$\tilde{x} := \frac{x}{X}, \qquad\qquad \tilde{t} := \beta t, \tag{6.30}$$

so that spatial depth, $0 \leq \tilde{x} \leq 1$, is measured relative to the width of the tunica intima, $X \approx 0.40$mm, and time, $\tilde{t} \geq 0$, is measured in units of the mean lifespan of lipid-unladen MDMs, $\beta^{-1} \approx 1$month. We scale the remaining variables as follows:

$$\begin{aligned}
\tilde{m}_\ell(\tilde{x},\tilde{t}) &:= \frac{\beta X}{\sigma_M} m_\ell(x,t), & \tilde{M}(\tilde{x},\tilde{t}) &:= \frac{\beta X}{\sigma_M} M(x,t),\\
\tilde{L}_M(\tilde{x},\tilde{t}) &:= \frac{\beta X}{a_0\sigma_M} L_M(x,t), & \tilde{\boldsymbol{L}}(\tilde{x},\tilde{t}) &:= \frac{\beta X}{a_0\sigma_M} \boldsymbol{L}(x,t),\\
\tilde{H}(\tilde{x},\tilde{t}) &:= \frac{\beta X}{a_0\sigma_M} H(x,t), & \tilde{S}(\tilde{x},\tilde{t}) &:= \frac{1}{S^{\text{c50}}} S(x,t).
\end{aligned} \tag{6.31}$$

Eqs. (6.31) scale the MDM densities relative to the maximum influx per (lipid-unladen) MDM lifespan, $\sigma_M X^{-1}\beta^{-1} \approx 17000$mm^{-3}. The lipid densities and HDL capacity are measured relative to the maximum influx of MDM endogenous lipid per MDM lifespan, $a_0\sigma_M X^{-1}\beta^{-1} \approx 45$ mg/dL. The inflammatory mediator density is scaled relative to the density for half-maximal MDM recruitment, $S^{\text{c50}} \approx 5$ ng/mL. We also introduce a number of dimensionless parameters in Table 6.2.

Applying the non-dimensionalisation (6.31) and definitions of Table 6.2, and dropping the tildes for notational convenience, we obtain the following dimensionless PDEs for the

Table 6.2: Dimensionless parameters in Eqs. (6.32)-(6.50)

Parameter	Definition	Interpretation	Estimate
$\tilde{L}^\star$	$\frac{\beta}{a_0\sigma_M}L^\star$	Lumen LDL lipid density	$0-10$
$\tilde{H}^\star$	$\frac{\beta}{a_0\sigma_M}H^\star$	Lumen HDL lipid capacity	$0-5$
$\tilde{K}_{\mathrm{r}}$	$\frac{\beta}{a_0\sigma_M}\overline{K}_r$	Mean LDL retention capacity	25
$\tilde{P}_L^{(0)}$	$\frac{1}{X\beta}P_L^{(0)}$	Endothelial LDL permeability	0.9
$\tilde{P}_H^{(0)}$	$\frac{1}{X\beta}P_H^{(0)}$	Endothelial HDL permeability	1.8
$\tilde{P}_S^{(0)}$	$\frac{1}{X\beta}P_S^{(0)}$	Endothelial mediator permeability	13
$\tilde{P}_L^{(1)}$	$\frac{1}{X\beta}P_L^{(1)}$	Internal elastic lamina LDL permeability	2.7
$\tilde{P}_H^{(1)}$	$\frac{1}{X\beta}P_H^{(1)}$	Internal elastic lamina HDL permeability	5.4
$\tilde{P}_S^{(1)}$	$\frac{1}{X\beta}P_S^{(1)}$	Internal elastic lamina mediator permeability	38
$\tilde{k}_b$	$\frac{a_0\sigma_M}{\beta^2}k_b$	LDL retention rate	2.7
$\tilde{k}_{-b}$	$\frac{1}{\beta}k_{-b}$	LDL unbinding rate	1.8
$\tilde{\gamma}$	$\frac{1}{\beta}\gamma$	MDM egress rate	0.2
$\tilde{\nu}$	$\frac{1}{\beta}\nu$	Secondary necrosis rate	37
$\tilde{\kappa}$	$\frac{1}{a_0}\kappa$	MDM lipid capacity per unit endogenous lipid	29
$\tilde{k}_{LDL}$	$\frac{a_0\sigma_M}{\beta^2}k_{LDL}$	LDL uptake rate	0.016
$\tilde{k}_{\mathrm{r}}$	$\frac{a_0\sigma_M}{\beta^2}k_{\mathrm{r}}$	rLDL uptake rate	1.1
$\tilde{k}_{\mathrm{ap}}$	$\frac{a_0\sigma_M}{\beta^2}k_{\mathrm{ap}}$	Apoptotic lipid uptake rate	5.5
$\tilde{k}_{\mathrm{n}}$	$\frac{a_0\sigma_M}{\beta^2}k_{\mathrm{n}}$	Necrotic lipid uptake rate	1.4
$\tilde{k}_H$	$\frac{a_0\sigma_M}{\beta^2}k_H$	Lipid efflux rate	16
$\tilde{\delta}_S$	$\frac{1}{\beta}\delta_S$	Mediator natural decay rate	1600^*
$\tilde{\alpha}$	$\frac{a_0\sigma_M}{S^{\mathrm{c}50}\beta^2}\alpha$	Resident mediator production per rLDL lipid	850^*
$\ell_{\max}$	$\ell_{\max}$	MDM maximum lipid capacity	100
$\tilde{\theta}$	θ	LDL retention profile shape	10
$\tilde{D}_M$	$\frac{1}{\beta X^2}D_M$	Diffusivity of unladen MDMs	0.12
D_{ap}	$\frac{1}{\beta X^2}D_{\mathrm{ap}}$	Diffusivity of apoptotic cells	0.03
D_{n}	$\frac{1}{\beta X^2}D_{\mathrm{n}}$	Diffusivity of necrotic cells	0.03
$\tilde{D}_{LDL}$	$\frac{1}{\beta X^2}D_{LDL}$	Diffusivity of free LDL	58
$\tilde{D}_H$	$\frac{1}{\beta X^2}D_H$	Diffusivity of HDL	140
$\tilde{D}_S$	$\frac{1}{\beta X^2}D_S$	Diffusivity of mediators	3600^*
$\tilde{\psi}_D$	ψ_D	Sensitivity of MDM diffusivity to lipid load	$\in[0,1]$
$\tilde{\psi}_\beta$	ψ_D	Sensitivity of MDM lifespan to lipid load	$\in[0,1]$

MDM population:

$$\begin{aligned}\frac{\partial m_\ell}{\partial t} &= D_M\Big[1-\psi_D\Big(\frac{\ell}{\ell_{\max}}\Big)\Big]\frac{\partial^2 m_\ell}{\partial x^2} - \frac{m_\ell}{1-\psi_\beta\big(\frac{\ell}{\ell_{\max}}\big)} \\ &\quad + \boldsymbol{k_L}\cdot\boldsymbol{L}\ \big[(\ell_{\max}-\ell+1)m_{\ell-1} - (\ell_{\max}-\ell)m_\ell\big] \\ &\quad + k_H\ \ H\big[(\ell+1)m_{\ell+1} - \ell m_\ell\big],\end{aligned} \tag{6.32}$$

where

$$m_{-1} = m_{\ell_{\max}+1} = 0, \tag{6.33}$$

for every $\ell = 0, 1, \ldots, \ell_{\max}$. The remaining variables satisfy the PDEs

$$\frac{\partial M}{\partial t} = D_M\frac{\partial^2}{\partial x^2}\Big[M - \psi_D\sum_{\ell=0}^{\ell_{\max}}\tilde{\ell}m_\ell\Big] - \Big[M + \psi_\beta\sum_{\ell=0}^{\ell_{\max}}\frac{\tilde{\ell}m_\ell}{1-\psi_\beta\tilde{\ell}}\Big], \tag{6.34}$$

$$\begin{aligned}\frac{\partial L_M}{\partial t} &= D_M\frac{\partial^2}{\partial x^2}\Big[L_M - \psi_D\sum_{\ell=0}^{\ell_{\max}}(1+\kappa\tilde{\ell})\tilde{\ell}m_\ell\Big] + \boldsymbol{k_L}\cdot\boldsymbol{L}[(\kappa+1)M - L_M] \\ &\quad - \Big[L_M + \psi_\beta\sum_{\ell=0}^{\ell_{\max}}\frac{(1+\kappa\tilde{\ell})\tilde{\ell}m_\ell}{1-\psi_\beta\tilde{\ell}}\Big] - k_H\,H(L_M - M),\end{aligned} \tag{6.35}$$

$$\frac{\partial L_{LDL}}{\partial t} = D_{LDL}\frac{\partial^2 L_{LDL}}{\partial x^2} - k_b L_{LDL}[K_{\mathrm{r}}(x) - L_{\mathrm{r}}] + k_{-b}L_r - k_{LDL}L_{LDL}[(\kappa+1)M - L_M], \tag{6.36}$$

$$\frac{\partial L_{\mathrm{r}}}{\partial t} = k_b L_{LDL}[K_{\mathrm{r}}(x) - L_{\mathrm{r}}] - k_{-b}L_r - k_{\mathrm{r}}L_{\mathrm{r}}[(\kappa+1)M - L_M], \tag{6.37}$$

$$\begin{aligned}\frac{\partial L_{\mathrm{ap}}}{\partial t} &= D_{\mathrm{ap}}\frac{\partial^2 L_{\mathrm{ap}}}{\partial x^2} + \Big[L_M + \psi_\beta\sum_{\ell=0}^{\ell_{\max}}\frac{(1+\kappa\tilde{\ell})\tilde{\ell}m_\ell}{1-\psi_\beta\tilde{\ell}}\Big] \\ &\quad - \nu L_{\mathrm{ap}} - k_{\mathrm{ap}}L_{\mathrm{ap}}[(\kappa+1)M - L_M],\end{aligned} \tag{6.38}$$

$$\frac{\partial L_{\mathrm{n}}}{\partial t} = D_{\mathrm{n}}\frac{\partial^2 L_{\mathrm{n}}}{\partial x^2} + \nu L_{\mathrm{ap}} - k_{\mathrm{n}}L_{\mathrm{n}}[(\kappa+1)M - L_M], \tag{6.39}$$

$$\frac{\partial H}{\partial t} = D_H\frac{\partial^2 H}{\partial x^2} - k_H H(L_M - M), \tag{6.40}$$

$$\frac{\partial S}{\partial t} = D_S\frac{\partial^2 S}{\partial x^2} + \alpha L_{\mathrm{r}} - \delta_S S, \tag{6.41}$$

where $\tilde{\ell} := \ell/\ell_{\max}$ and

$$K_{\mathrm{r}}(x) := \bar{K}_{\mathrm{r}}\cdot\left(\frac{2}{1+e^{\theta(1/2-x)}}\right). \tag{6.42}$$

We impose the following boundary conditions:

$$-D_M\frac{\partial m_\ell}{\partial x} = \begin{cases} \frac{S}{1+S}\cdot\delta_{\ell,0} - \gamma m_\ell & \text{at } x=0; \\ \gamma m_\ell & \text{at x=1,} \end{cases} \qquad \forall \ell = 0,1,\dots \ell_{\max}, \tag{6.43}$$

$$-D_M\frac{\partial M}{\partial x} = \begin{cases} \frac{S}{1+S} - \gamma M & \text{at } x=0; \\ \gamma M & \text{at x=1,} \end{cases} \tag{6.44}$$

$$-D_M\frac{\partial L_M}{\partial x} = \begin{cases} \frac{S}{1+S} - \gamma L_M & \text{at } x=0; \\ \gamma L_M & \text{at x=1,} \end{cases} \tag{6.45}$$

$$-D_{LDL}\frac{\partial L_{LDL}}{\partial x} = \begin{cases} P_L^{(0)}(L^\star - L_{LDL}) & \text{at } x=0; \\ P_L^{(1)}(L_{LDL} - 0) & \text{at } x=1, \end{cases} \tag{6.46}$$

$$\frac{\partial L_{\rm ap}}{\partial x} = \frac{\partial L_{\rm n}}{\partial x} = 0 \quad \text{at } x=0,1, \tag{6.47}$$

$$-D_H\frac{\partial H}{\partial x} = \begin{cases} P_H^{(0)}(H^\star - H) & \text{at } x=0; \\ P_H^{(1)}(H - 0) & \text{at } x=1, \end{cases} \tag{6.48}$$

$$-D_S\frac{\partial S}{\partial x} = \begin{cases} P_S^{(0)}(0 - S) & \text{at } x=0; \\ P_S^{(1)}(S - 0) & \text{at } x=1, \end{cases} \tag{6.49}$$

and close the model with the following initial conditions at $t = 0$:

$$\begin{aligned} &m_\ell = 0 \quad \forall \ell = 0,1,\dots,\ell_{\max}, \\ &M = L_M = L_{LDL} = L_{\rm r} = L_{\rm ap} = L_{\rm n} = H = S = 0. \end{aligned} \tag{6.50}$$

6.2.6 Separation of timescales

The parameters in Table 6.2 span several orders of magnitude. In particular, the mediator parameters δ_S, α and D_S are substantially larger than the other constants. This discrepancy means that numerical simulations require small timesteps to maintain stability. To improve numerical efficiency and derive analytical insight into model behaviour, we approximate the mediator dynamics via separation of timescales. Accordingly, we define

$$\epsilon := \delta_S^{-1} = 6.25\times10^{-4} \ll 1, \qquad \alpha = \epsilon^{-1}\hat{\alpha}, \qquad D_S = \epsilon^{-1}\hat{D}_S, \tag{6.51}$$

and consider the limit $\epsilon \to 0$ where $\hat{\alpha}$, $\hat{D}_S = \mathcal{O}(1)$ as $\epsilon \to 0$. In this limit, Eqs. (6.41) and (6.49) become

$$\epsilon\frac{\partial S}{\partial t} = \hat{D}_S\frac{\partial^2 S}{\partial x^2} + \hat{\alpha}L_r - \hat{\delta}_S S, \qquad -\hat{D}_S\frac{\partial S}{\partial x} = \epsilon\begin{cases} P_S^{(0)}(0-S) & \text{at } x=0; \\ P_S^{(1)}(S-0) & \text{at } x=1. \end{cases} \tag{6.52}$$

Substituting the expansion $S = S^{(0)} + \epsilon S^{(1)} + \dots$ into Eqs. (6.52) and balancing the leading order terms gives

$$0 = \hat{D}_S\frac{\partial^2 S^{(0)}}{\partial x^2} + \hat{\alpha}L_r - \hat{\delta}_S S^{(0)}, \qquad \frac{\partial S^{(0)}}{\partial x} = 0 \quad \text{at } x=0,1. \tag{6.53}$$

Hence, S satisfies a quasi-steady approximation with no-flux boundary conditions at leading order. Eqs. (6.53) can be solved in terms of $L_{\mathrm{r}}(x,t)$ using variation of parameters:

$$\begin{aligned} S^{(0)}(x,t) = \frac{\hat{\alpha}}{\sqrt{\hat{D}_S}}\Bigg[\int_x^1 L_r(\xi,t)\sinh\left(\frac{x-\xi}{\sqrt{\hat{D}_S}}\right)d\xi \\ + \operatorname{csch}\Big(\frac{1}{\sqrt{\hat{D}_S}}\Big)\cosh\left(\frac{1-x}{\sqrt{\hat{D}_S}}\right)\int_0^1 L_{\mathrm{r}}(\xi,t)\cosh\left(\frac{\xi}{\sqrt{\hat{D}_S}}\right)d\xi\Bigg]. \end{aligned} \tag{6.54}$$

Since S is only coupled to the model via its value at $x = 0$ in Eqs. (6.43)-(6.45), we substitute $x = 0$ into Eq. (6.54) and simplify to obtain

$$S(0,t) \sim \frac{\hat{\alpha}}{\sqrt{\hat{D}_S}\sinh\left(\frac{1}{\sqrt{\hat{D}_S}}\right)}\int_0^1 L_{\mathrm{r}}(x,t)\cdot\cosh\left(\frac{1-x}{\sqrt{\hat{D}_S}}\right)dx, \quad \text{as } \epsilon \to 0. \tag{6.55}$$

Eq. (6.55) shows that, at leading order, the mediator density at the endothelium is a weighted integral of the rLDL density across the lesion. The rLDL density closer to $x = 0$ is weighted more strongly than that near $x = 1$ to account for the decay of mediators as they diffuse towards the endothelium.

6.2.7 Numerical scheme

We use the method of lines, with spatial discretisation $\Delta x = 0.02$, to obtain numerical solutions of the reduced model, which comprises PDEs (6.32)-(6.40), boundary conditions (6.44)-(6.48), initial conditions (6.50) and expression (6.55) for $S(0,t)$. We approximate the spatial derivatives with a second-order central finite difference, and the integral in Eq. (6.55) with the Trapezoidal Rule. We solve the resulting ODE system with the *NDSolve* routine in Wolfram Mathematica. To ensure the validity of numerical solutions, we checked that the output of *NDSolve* was robust to decreases in Δx (i.e. the spatial discretisation), "MaxStepSize" (i.e. the temporal discretisation), increases in "PrecisionGoal" and "AccuracyGoal", and consistent with the steady state solutions for $\psi_\beta = \psi_D = 0$ in Sect. 6.3.1.

6.3 Results

We present the results in four sections. We consider the case $\psi_D = \psi_\beta = 0$ in Sect. 6.3.1. Our analysis shows that this model, with lipid-independent MDM mobility and apoptosis, captures the overall time course of lesion development, but does not qualitatively reproduce the spatial densities seen in the Nakashima images (Fig. 6.1). We then examine the impact at steady state of lipid-dependent apoptosis alone, $\psi_\beta > 0 = \psi_D$, and lipid-dependent mobility alone, $\psi_D > 0 = \psi_\beta$, in Sects. 6.3.2 and 6.3.3 respectively. Our results show that lipid-dependent apoptosis alone cannot reproduce the observed spatial densities, but high sensitivities to lipid-dependent mobility are sufficient. Finally, in Sect. 6.3.4 we consider the model output when both apoptosis and diffusion are lipid-dependent: $\psi_\beta, \psi_D > 0$.

6.3.1 Lipid-independent MDM kinetics: $\psi_D = \psi_\beta = 0$

Results from a typical simulation for the case $\psi_D = \psi_\beta = 0$ are presented in Fig. 6.4. We fix $L^\star = 4$ and $H^\star = 0.5$ so that LDL lipid dominates HDL capacity in the blood. The plots in column (a) show the components of the total lipid density:

$$L_{\text{tot}}(x,t) := L_{\scriptscriptstyle LDL}(x,t) + L_{\text{r}}(x,t) + L_M(x,t) + L_{\text{ap}}(x,t) + L_{\text{n}}(x,t), \tag{6.56}$$

while the quantities in plot (e) are the mean lipid density and HDL lipid capacity, respectively given by

$$\overline{L}_{\text{tot}}(t) := \int_0^1 L_{\text{tot}}(x,t)dx, \qquad \overline{H}_{\text{tot}}(t) := \int_0^1 H(x,t)dx. \tag{6.57}$$

The time evolution of the lipid densities is shown in Fig. 6.4(a). At early times ($t \leq 1$), the lesion accumulates rLDL deep in the wall. This behaviour, consistent with the Nakashima images (Fig. 6.1), occurs due to the influx of free LDL at $x = 0$ and its subsequent binding to ECM proteoglycans. The high diffusivity of free LDL ($D_{\text{LDL}} = 57$), ensures that spatial variation in free LDL is small and so the spatial profile of rLDL is dominated by the non-uniform retention capacity, $K_{\text{r}}(x)$, defined in Eq. (6.42). Moreover, the proportion of free LDL to rLDL is very small due to the large mean retention capacity ($\overline{K}_{\text{r}} = 25$), relative to blood LDL density ($L^\star = 4$). In the months following LDL accumulation ($1 \leq t \leq 5$), the MDM lipid density grows markedly due to rLDL uptake. The lesion also accumulates apoptotic and necrotic lipid at this stage due to MDM death. The ratio of apoptotic to necrotic lipid is also small, due mainly to the high secondary necrosis rate, $\nu = 37$. Finally, the model tends to a nonzero steady state as $t \to \infty$. The lesion is approximately at steady state within $t = 100$ MDM lifespans (see Fig. 6.4(e), noting the logarithmic scale). The lesion continues to accumulate necrotic lipid deep in the intima during this final stage. We note that steady state in our model approximately corresponds to the onset of pathological intimal thickening (PIT) in human lesions, which follows the establishment of the MDM population during the fatty streak stage (within which our model dynamics take place).

The time evolution of the MDM density is given in Fig. 6.4(b). The MDM density grows over time and maintains a monotonically decreasing spatial profile. As expected, $M(x,t)$ attains its maximum value at $x = 0$, where MDMs enter the lesion, and fixing $\psi_D = \psi_\beta = 0$ ensures that their movement and death are decoupled from lipid content. We note that $M(x,t)$ decreases with x sufficiently smoothly that $M(1,t) > 0$ for t large; indeed $M(1,100) \approx 0.1 \times M(0,100)$ for the simulation in Fig. 6.4. Hence, by contrast to the Nakashima images, the model predicts that a substantial portion of MDMs eventually emigrate to the tunica media.

The dynamics of the lipid-spatial MDM distribution, $m_\ell(x,t)$, are shown in Fig. 6.4(c). At early times, $t \leq 1$, the distribution grows in a wave-like manner from the origin towards higher values of ℓ and x. This behaviour reflects the early increase in MDM lipid

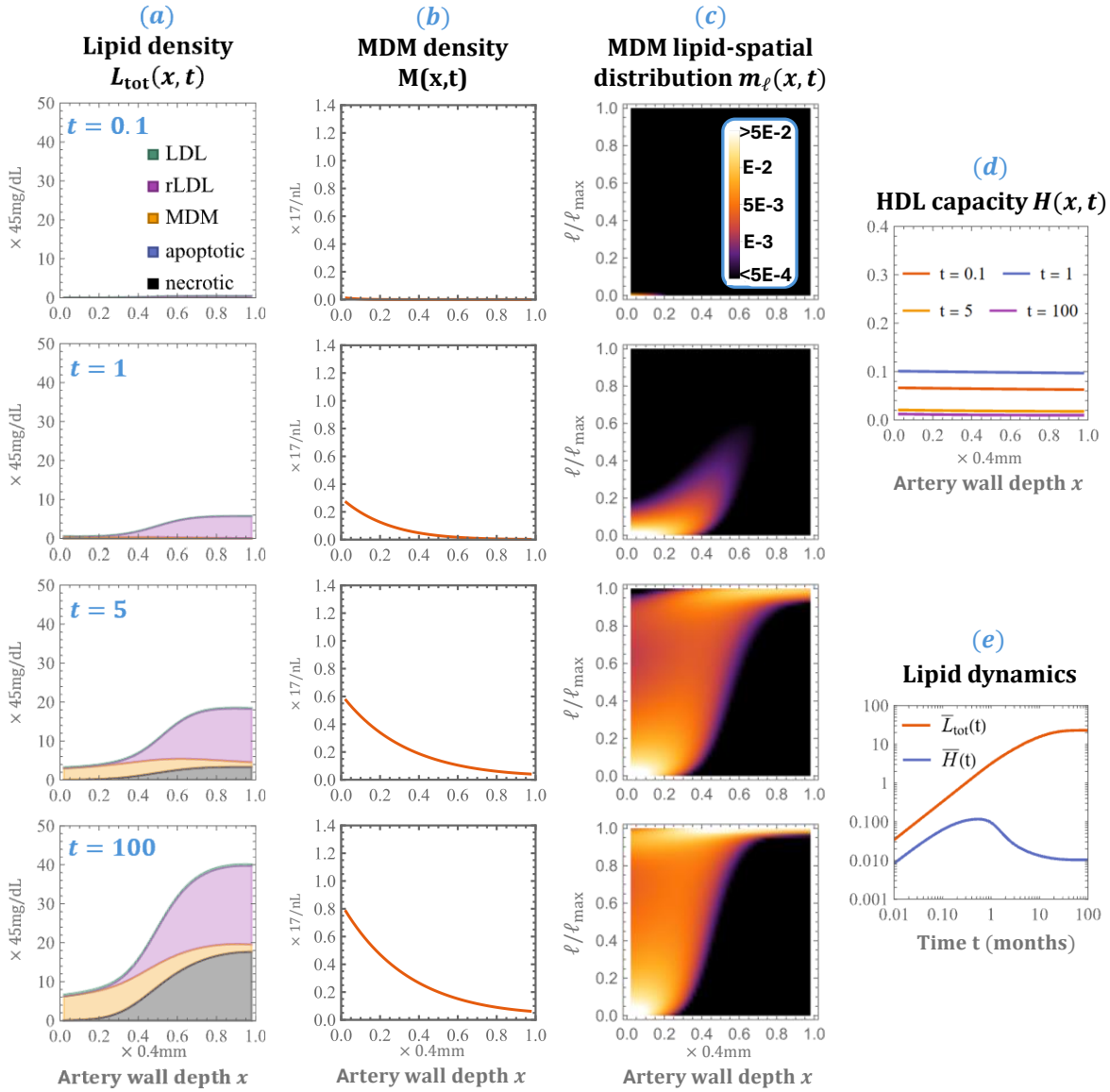


Figure 6.4: **Time evolution of the model lesion when MDM mobility and apoptosis are independent of lipid content: $\psi_{\mathbf{D}} = \psi_\beta = \mathbf{0}$.** Columns (a), (b) and (c) respectively show the lipid densities, MDM density and MDM lipid-spatial distribution at times $t = 0.1$, 1, 5 and 100. Plot (d) shows the spatial uniformity of HDL capacity. Finally, plot (e) shows the time-evolution of the mean total lipid density and HDL capacity, as defined by Eqs. (6.57). Note how, in contrast to the Nakashima images, the lipid density monotonically increases with x, and the MDM density monotonically decreases with x for all $t > 0$. We use $L^\star = 4$ and $H^\star = 0.5$.

content due to rLDL uptake and concurrent diffusion into the lesion. As t increases, the distribution stretches towards $(x, \ell/\ell_{\max}) = (1, 1)$, reflecting a growth in the number of lipid-laden MDMs deep in the lesion. We note that $m_\ell(x, t)$ is concentrated on higher values of ℓ as x increases; MDMs deeper in the lesion typically contain a higher lipid content than those nearer the endothelium. For $5 \leq t \leq 100$ the MDM distribution also extends towards $(x, \ell/\ell_{\max}) = (0, 1)$. This behaviour is partially due to the diffusion of lipid-laden MDMs from deeper in the lesion back towards the endothelium as the model tends to steady state.

Fig. 6.4(d) shows that the HDL capacity, $H(x, t)$, is approximately spatially uniform for all $t > 0$. This is due to the large HDL diffusivity, $D_H = 140$. Indeed, if $D_H = \epsilon^{-1}\hat{D}_H$ for some $\hat{D}_H = \mathcal{O}(1)$ as $\epsilon \to 0$ (recall $\epsilon := \delta_S^{-1} \ll 1$), then Eqs. (6.40) and (6.48) become

$$\epsilon \frac{\partial H}{\partial t} = \hat{D}_H \frac{\partial^2 H}{\partial x^2} - \epsilon k_H H(L_M - M) \tag{6.58}$$

$$-\hat{D}_H \frac{\partial H}{\partial x} = \epsilon \begin{cases} P_H^{(0)}(H^\star - H) & \text{at } x = 0; \\ P_H^{(1)} H & \text{at } x = 1. \end{cases} \tag{6.59}$$

Substituting $H = H^{(0)} + \epsilon H^{(1)} + \dots$ into Eqs. (6.58) and (6.59), and balancing the leading order terms shows that

$$\frac{\partial^2 H^{(0)}}{\partial x^2} = 0, \quad \left.\frac{\partial H^{(0)}}{\partial x}\right|_{x=0,1} = 0, \qquad \implies H^{(0)} = H^{(0)}(t). \tag{6.60}$$

Hence, the HDL lipid capacity is spatially uniform at leading order. To derive the dynamics of $H^{(0)}(t)$, we balance the $\mathcal{O}(\epsilon)$ terms in Eq. (6.58) and integrate with respect to $x \in (0, 1)$. Doing so gives

$$\int_0^1 \frac{\partial H^{(0)}}{\partial t} dx = \hat{D}_H \left.\frac{\partial H^{(1)}}{\partial x}\right|_{x=0}^{x=1} - k_H H^{(0)} \int_0^1 (L_M - M) dx. \tag{6.61}$$

Using result Eq. (6.60) to simplify the left-hand side, and Eq. (6.59) at $\mathcal{O}(\epsilon)$ to evaluate the boundary terms on the right-hand side, we find that

$$H(x, t) \sim H^{(0)}(t) \quad \text{as } \epsilon \to 0, \tag{6.62}$$

where

$$\frac{dH^{(0)}}{dt} = P_H^{(0)}(H^\star - H^{(0)}) - P_H^{(1)} H^{(0)} - k_H H^{(0)} \int_0^1 (L_M - M) dx. \tag{6.63}$$

Eqs. (6.62) and (6.63) express that, at leading order, the HDL density is spatially uniform and evolves according to the rates of exchange with the bloodstream, tunica media and total efflux by MDMs across the lesion $x \in (0, 1)$. These mechanisms give rise to the non-monotonic dynamics seen in Fig. 6.4(e); HDL capacity initially grows from zero due to influx from the blood, and decreases once MDMs have ingested enough lipid for the combined rates of efflux and loss to the tunica media exceed the influx from the bloodstream. By contrast, the mean lipid density across the lesion increases monotonically with

t; the lesion becomes more lipid laden with time.

Steady state. Typical steady state solutions when $\psi_D = \psi_\beta = 0$ are shown in Fig. 6.5. Again, we note that the steady state MDM density decreases monotonically with x. We prove this result by direct calculation. At steady state, Eqs. (6.34) and (6.44) become

$$0 = D_M \frac{d^2M}{dx^2} - M, \qquad -D_M \frac{dM}{dx} = \begin{cases} \frac{S_\infty}{1+S_\infty} - \gamma M & \text{at } x = 0; \\ \gamma M & \text{at } x = 1, \end{cases} \tag{6.64}$$

where $S_\infty := \lim_{t\to\infty} S(0,t)$ is the limiting value of Eq. (6.55). The boundary value problem (6.64) admits the exact solution

$$M(x) = A\cosh\left(\frac{1-x}{\sqrt{D_M}}\right) + B\sinh\left(\frac{1-x}{\sqrt{D_M}}\right), \tag{6.65}$$

where A and B are positive constants:

$$A = \frac{S_\infty}{1+S_\infty} \cdot \frac{\sqrt{D_M}}{2\gamma\sqrt{D_M}\cosh(1/\sqrt{D_M}) + (D_M+\gamma^2)\sinh(1/\sqrt{D_M})}, \tag{6.66}$$

$$B = \frac{\gamma A}{\sqrt{D_M}}. \tag{6.67}$$

Differentiating Eq. (6.65) then gives

$$M'(x) = -\frac{A}{\sqrt{D_M}}\sinh\left(\frac{1-x}{\sqrt{D_M}}\right) - \frac{B}{\sqrt{D_M}}\cosh\left(\frac{1-x}{\sqrt{D_M}}\right) < 0, \tag{6.68}$$

where the inequality follows from $A, B > 0$ and $1 - x \geq 0$. Hence, $M(x)$ is monotone decreasing and, consequently, our model with lipid-independent MDM kinetics $\psi_D = \psi_\beta = 0$ cannot qualitatively replicate the MDM densities found in the Nakashima images.

Since we use the results of our model with $\psi_D = \psi_\beta = 0$ for comparison in future sections, we continue to explore its steady state properties. Fig. 6.6 shows how various summary statistics depend on blood LDL content. Plots (a) and (b) respectively show the mean total lipid density, $\overline{L}_{\text{tot}}$ and HDL capacity, $\overline{H}$, as defined by Eqs (6.57). As expected, $\overline{L}_{\text{tot}}$ increases with $L^\star$. By contrast, $\overline{H}$ decreases with $L^\star$ due to increased rates of MDM efflux. Plots (c), (d) and (e) respectively show the mean MDM density, $\overline{M}$, lipid content, $\overline{L}_M$, and depth, $\overline{x}_M$, which are defined by

$$\overline{M} := \int_0^1 M dx, \qquad \overline{L}_M := \frac{1}{\kappa\overline{M}}\int_0^1 (L_M - M)dx, \qquad \overline{x}_M := \frac{1}{\overline{M}}\int_0^1 xM dx. \tag{6.69}$$

We note that $0 \leq \overline{L}_M \leq 1$ is normalised such that $\overline{L}_M = 0$ when all MDMs have no ingested lipid and $\overline{L}_M = 1$ when all MDMs are at maximal capacity. Both $\overline{M}$ and $\overline{L}_M$ increase with $L^\star$, whereas $\overline{x}_M$ appears to be independent of $L^\star$ and $H^\star$. Indeed, substituting the exact solution (6.65) into Eq. (6.69) shows that

$$\overline{x}_M = \frac{D_M^2 + \gamma - D_M\big(D_M\cosh(1/D_M) + \gamma\sinh(1/D_M)\big)}{\gamma - \gamma\cosh(1/D_M) - D_M\sinh(1/D_M)}. \tag{6.70}$$

Hence, when $\psi_D = \psi_\beta = 0$, the mean MDM depth only depends on the diffusivity, D_M, and egress rate, γ.

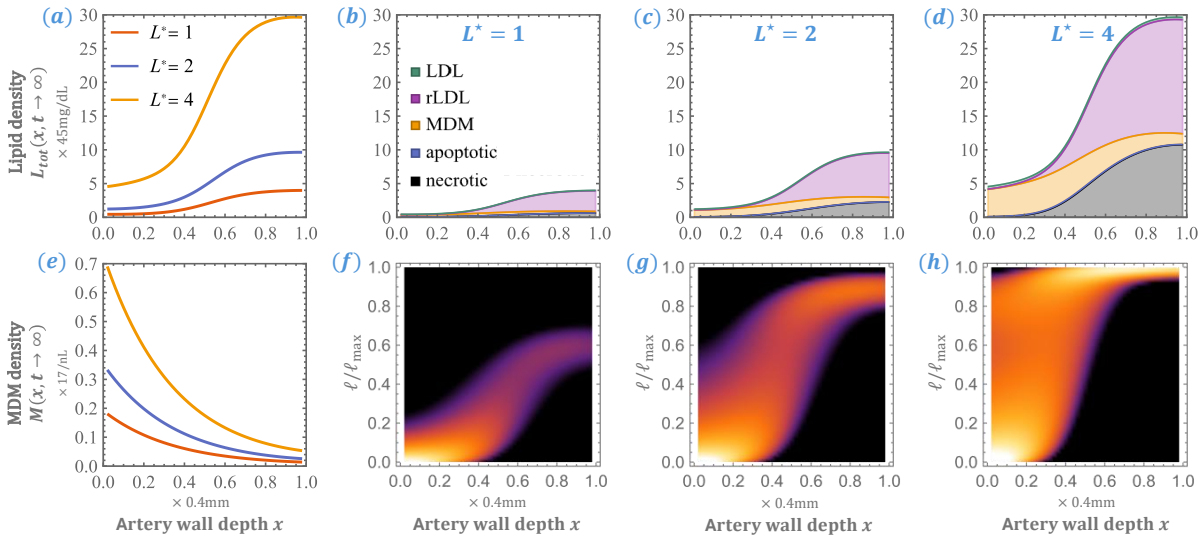


Figure 6.5: **Steady state lesion composition when MDM mobility and apoptosis are independent of lipid content:** $\psi_D = \psi_\beta = 0$. The plots depict solutions to the model equations at steady state for the blood LDL densities $L^\star = 1$, 2 and 4, and HDL capacity $H^\star = 1$. The top row depicts the lipid densities; plot (a) is the total lipid density, and plots (b)-(d) show the densities of the lipid components. The bottom row shows the MDM densities; plot (e) is the total MDM density, and plots (f)-(h) show the lipid-spatial MDM distribution, using the same colour scale as in Fig. 6.4. Note how the MDM density decreases monotonically with x, in contrast to the Nakashima images.

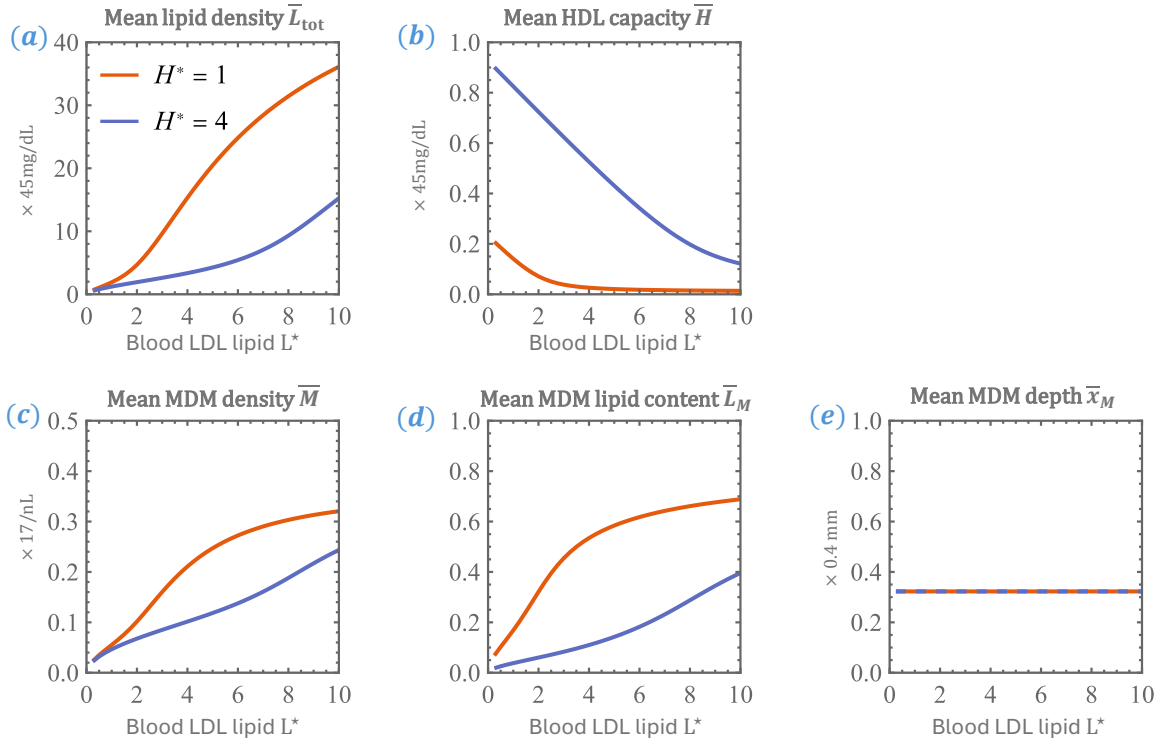


Figure 6.6: **Steady state summary statistics when MDM mobility and apoptosis are independent of lipid content:** $\psi_D = \psi_\beta = 0$. Plots (a) and (b) show the mean total lipid density and HDL capacity, defined in Eqs. (6.57). Plots (c)-(e) show the mean MDM density, (normalised) lipid content and depth, which are defined in Eqs. (6.69). Note how mean MDM depth is independent of both $L^\star$ and $H^\star$, by contrast to the other quantities.

6.3.2 Lipid-dependent apoptosis only: $\psi_D = 0$, $\psi_\beta > 0$

We next investigate whether lipid-dependent MDM apoptosis alone is sufficient to qualitatively replicate the Nakashima images. Hence, we set $\psi_\beta \geq 0$ and continue to fix $\psi_D = 0$ so that MDM mobility is independent of lipid content.

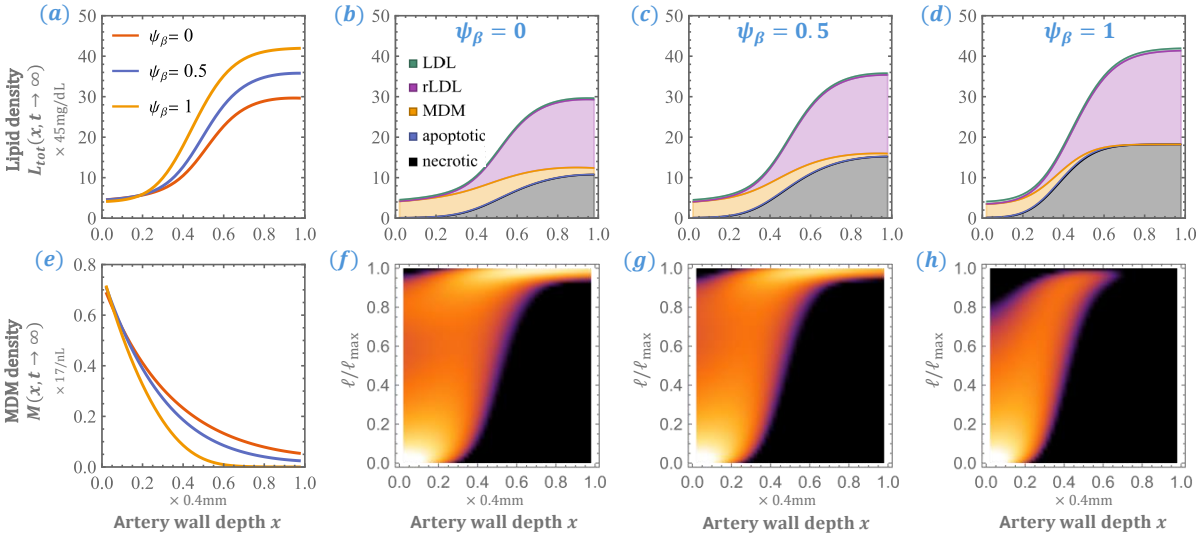


Figure 6.7: **Steady state lesion composition when MDM apoptosis increases with lipid content:** $\psi_\beta > \mathbf{0}, \psi_\mathbf{D} = \mathbf{0}$. We compute steady state solutions for $\psi_\beta = 0, 0.5, 1$, with $L^\star = 4$, $H^\star = 1$. Plot (a) shows the total lipid density and (b)-(d) the densities of the different lipid sub-types. Plot (e) depicts the density of MDMs and (f)-(h) the lipid-spatial MDM distribution, using the same colour scale as in Fig. 6.4. Note how increases in ψ_β yield a marked decline in MDM density deep in the lesion.

Fig. 6.7 shows typical steady state solutions for $\psi_\beta = 0$, 0.5 and 1. Plot (a) illustrates that increasing ψ_β increases the total lipid density, particularly deep in the lesion. By comparing plots (c) and (d) to (b), we note that the increase in lipid content reflects a rise in necrotic and rLDL lipid towards $x = 1$, despite smaller quantities of MDM lipid. Plot (e) shows that the decline in MDM lipid is not due to low lipid loads, but rather a reduction in MDM density towards $x = 1$. Indeed, plots (f)-(h) indicate that MDM lipid content increases with depth for $\psi_\beta = 0, 0.5, 1$. Together, these observations suggest that lipid-dependent MDM apoptosis drives increased rates of MDM death deep in the lesion, where lipid loads are greatest, causing buildup of necrotic and rLDL lipid. Since lipid-laden MDMs are more likely to die than nascent MDMs, there is less MDM lipid in the lesion and, hence, a lower rate of lipid efflux to HDL. The decreased efflux rate means that more of the lipid which enters the lesion via LDL remains in the lesion, increasing the total lipid burden.

We further highlight the impact of lipid-dependent apoptosis in Fig. 6.8 where we compare summary statistics for $\psi_\beta = 1$ to the lipid-independent case $\psi_\beta = 0$. Consistent with Fig. 6.7, plot (a) shows that $\psi_\beta = 1$ yields a greater mean lipid density, $\overline{L}_{\text{tot}}$, than $\psi_\beta = 0$ for all $L^\star \in (0, 10)$. Plot (b) shows that mean HDL capacity is also greater when $\psi_\beta = 1$, confirming a decline in HDL efflux when apoptosis depends on lipid content.

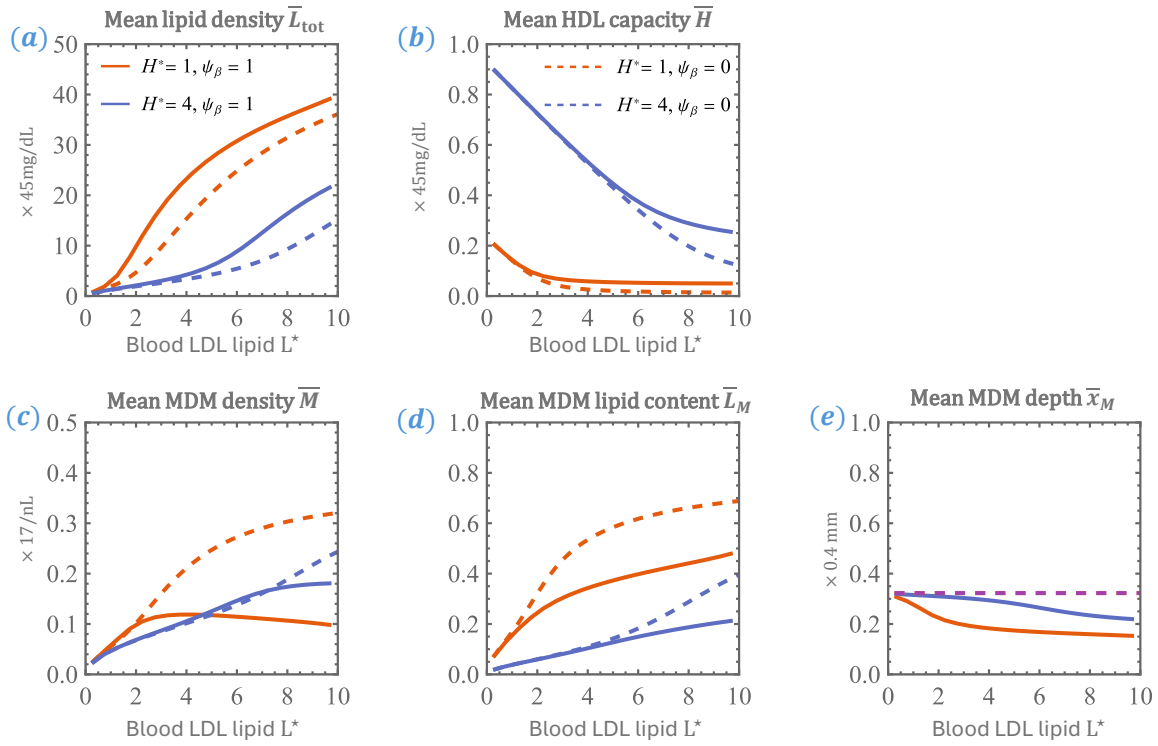


Figure 6.8: **Steady state summary statistics when MDM apoptosis increases with lipid content (solid) vs. lipid-independent apoptosis (dashed).** Plots (a) and (b) show how mean lipid density and HDL capacity, defined by Eqs. (6.57), are higher when $\psi_\beta = 1$. Plots (c), (d) and (e) respectively depict the reduction in mean MDM density, lipid content, and depth for $\psi_\beta = 1$. Note how the differences between the outputs for $\psi_\beta = 1$ and $\psi_\beta = 0$ are greater for higher values of blood LDL content, $L^\star$, and lower values of blood HDL capacity, $H^\star$.

Plots (c)-(e) show that mean MDM density, $\overline{M}$, lipid content, $\overline{L}_M$, and depth, $\overline{x}_M$, are all reduced relative to the case of lipid-independent death. The reduction is greater for high blood LDL densities, $L^\star$, where MDM lipid loads are greater and consequently rates of apoptosis.

Importantly, as suggested by Fig. 6.7(e), we note that the MDM densities for $\psi_\beta > 0 = \psi_D$ cannot exhibit a local maximum at steady state. Indeed, rearranging Eq. (6.34) at steady state gives

$$\frac{d^2M}{dx^2} = \frac{1}{D_M}\left[M + \psi_\beta \sum_{\ell=0}^{\ell_{\max}} \frac{\ell m_\ell}{\ell_{\max} - \psi_\beta \ell}\right] \geq 0, \tag{6.71}$$

where the inequality follows from $\psi_\beta < 1$ (the summand is non-negative). Hence, $M(x)$ is concave-up wherever it is nonzero and cannot attain an internal, local maximum. We conclude that introducing lipid-dependent apoptosis only to the model is not sufficient to qualitatively reproduce the Nakashima images.

6.3.3 Lipid-dependent mobility only: $\psi_D > 0$, $\psi_\beta = 0$

Here we examine whether introducing lipid-dependent MDM mobility only is sufficient to qualitatively replicate the Nakashima images. Accordingly, we set $\psi_D > 0$ and assume

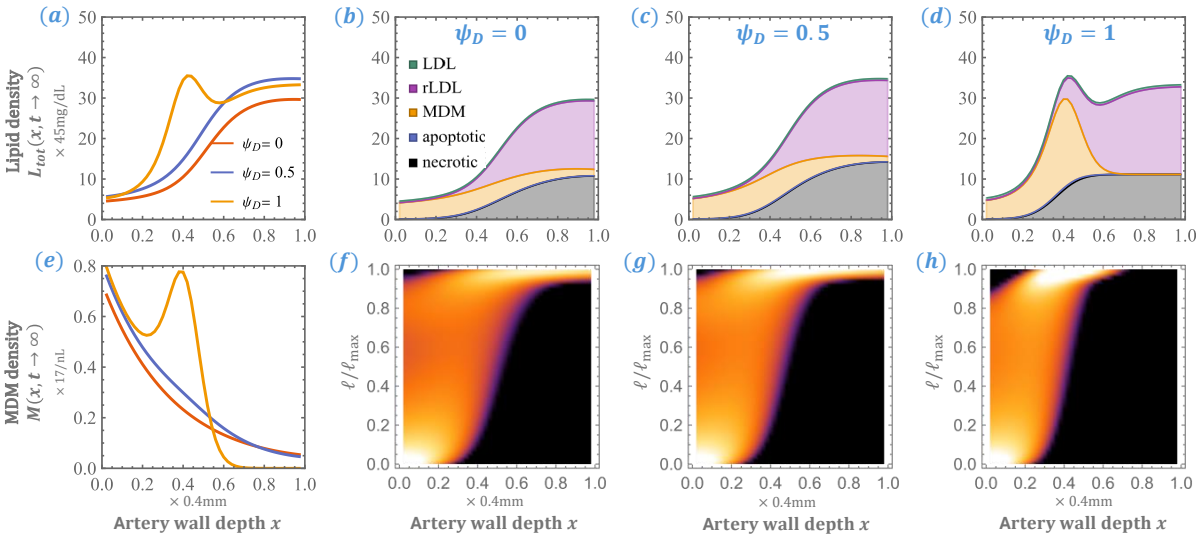


Figure 6.9: **Steady state lesion composition when MDM mobility decreases with lipid content: $\psi_D > 0, \psi_\beta = 0$.** We compute steady state solutions for $\psi_D = 0.0, 0.5, 1.0$, with $L^\star = 4$, $H^\star = 1$. Plot (a) shows the total lipid density and (b)-(d) the densities of the lipid sub-types. Plot (e) depicts the density of MDMs and (f)-(h) the lipid-spatial MDM distribution. Note how increases in ψ_D yield an accumulation of lipid and MDMs towards $x = 0$, with the formation of local maxima in the total lipid and MDM densities for $\psi_D = 1$.

$\psi_\beta = 0$ so that MDM apoptosis is independent of lipid content.

Fig. 6.9 shows typical steady state solutions for $\psi_D = 0.0$, 0.5 and 1.0. Plot (a) shows that increases in ψ_D yield greater total lipid densities, primarily closer to the endothelium. Moreover, the lipid density attains a local maximum at $x \approx 0.4$ for $\psi_D = 1$. Comparing plots (c) and (d) to (b) shows that this increase in lipid content and peak formation reflects an accumulation of MDM lipid for $x < \frac{1}{2}$, with minimal MDM lipid for $x > \frac{1}{2}$. Plot (e) shows that the MDM density also attains a local maximum at $x \approx 0.4$ for $\psi_D = 1$, with a rapid decrease in density with x to the right of the peak. Plots (f)-(h) show that MDM lipid loads are typically greater deeper in the lesion for all $\psi_D = 0.0, 0.5, 1.0$. Comparing Figs. 6.9(g, h) to Figs. 6.7(g, h) shows that there are considerably more lipid-laden MDMs deeper in the lesion when $\psi_D = 0.5, 1.0$ and $\psi_\beta = 0.0$ than when $\psi_\beta = 0.5, 1.0$ and $\psi_D = 0.0$. This is because introducing lipid-dependent mobility, $\psi_D > 0$, promotes the retention of lipid-laden MDMs, while introducing lipid-dependent apoptosis, $\psi_\beta > 0$, promotes their rapid death.

We compare summary statistics for the model with lipid-dependent mobility, $\psi_D = 1$, to the lipid-independent case, $\psi_D = 0$, in Fig. 6.10. Plot (a) shows that mean total lipid density is higher for $\psi_D = 1$. This reflects how MDMs are less able to emigrate from the lesion. Indeed, by contrast to Figs. 6.8(c,d) for ψ_β, Figs. 6.10(c,d) show that MDM density and mean lipid content are greater when $\psi_D = 1$ than when the MDM kinetics are independent of lipid. The greater amount of MDM lipid for $\psi_D = 1$ gives rise to a higher efflux rate to HDL, which yields the (marginally) lower HDL capacity levels seen in plot (b). Plot (e) indicates that mean MDM depth is also decreased for $\psi_D = 1$

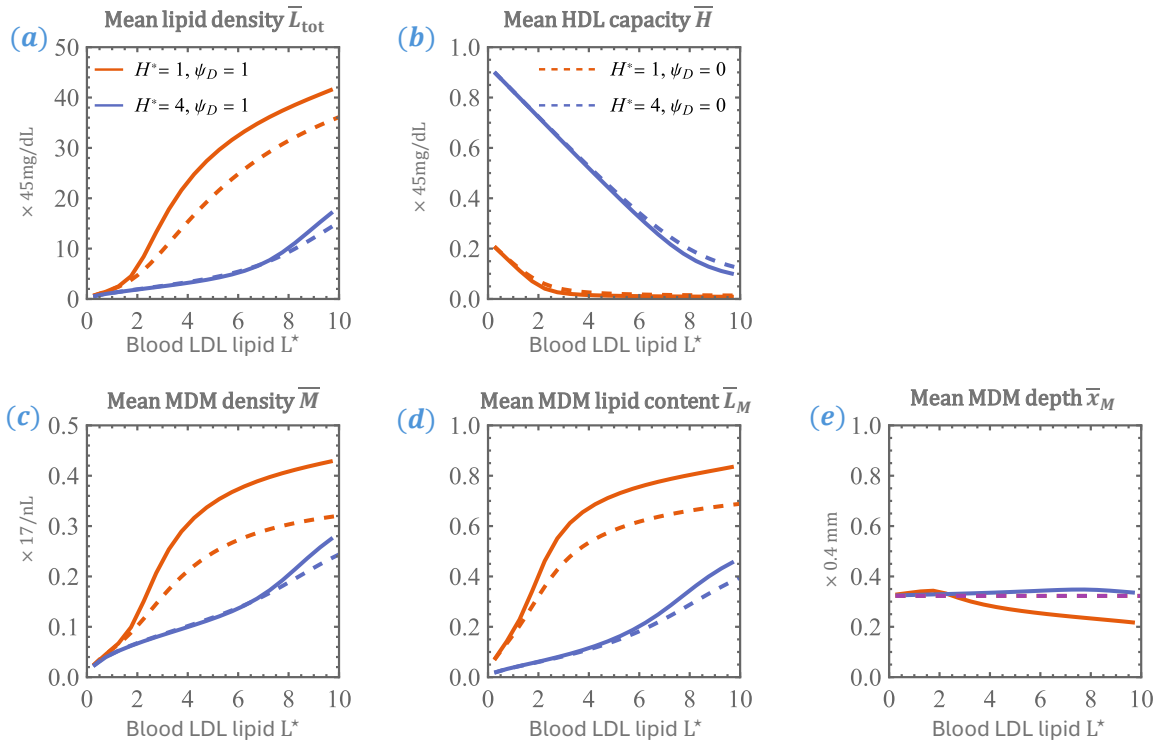


Figure 6.10: **Steady state summary statistics when MDM mobility decreases with lipid content (solid) vs. lipid-independent mobility (dashed).** Plots (a) and (b) show the mean lipid density and HDL capacity, defined by Eqs. (6.57). Plots (c), (d) and (e) respectively depict the increase in mean MDM density, lipid content, and reduction in depth for $\psi_D = 1$, particularly for $H^\star = 1$. We note again that the differences between the outputs for $\psi_D = 1$ and $\psi_D = 0$ are greater for higher values of blood LDL content, $L^\star$, and lower values of blood HDL capacity, $H^\star$.

when $H^\star = 1$, with only minimal difference compared to the $\psi_D = 0$ case when $H^\star = 4$. In general, the differences between the plots for $\psi_D = 1$ and $\psi_D = 0$ are greater when $H^\star = 1$ and HDL capacity is exhausted (see plot (b)). The lack of HDL capacity means that lipid-laden MDMs are retained deep in the lesion since they cannot recover their mobility by offloading lipid to HDL.

To briefly probe why $\psi_D > 0$ allows for the possibility of a local maximum in the MDM density (and hence, total lipid density), we rearrange Eq. (6.34) at steady state, assuming only $\psi_\beta = 0$, to obtain

$$\frac{d^2M}{dx^2} = \psi_D \sum_{\ell=0}^{\ell_{\max}} \left(\frac{\ell}{\ell_{\max}}\right) \frac{d^2 m_\ell}{dx^2} + \frac{M}{D_M} = \frac{\psi_D}{\kappa} \frac{d^2}{dx^2}(L_M - M) + \frac{M}{D_M}. \tag{6.72}$$

Hence M may become concave, $\frac{d^2M}{dx^2} < 0$, if the MDM ingested lipid density, $L_M - M$, is sufficiently concave:

$$\frac{d^2}{dx^2}(L_M - M) < -\frac{\kappa M}{\psi_D D_M}. \tag{6.73}$$

6.3.4 Lipid-dependent mobility and apoptosis: $\psi_D, \psi_\beta > 0$

We now suppose that both MDM mobility and apoptosis depend on lipid content: ψ_D, $\psi_\beta > 0$.

Fig. 6.11 shows an example solution for $\psi_D = 1.0$, $\psi_\beta = 0.1$. The model output provides an improved qualitative match to the Nakashima images (Fig. 6.1) than the case of lipid-independent MDM kinetics (c.f. Fig. 6.4). Specifically, column (a) shows that the model captures both the early accumulation of rLDL lipid deep in the lesion ($t \leq 1$), and subsequent formation of a lipid density peak towards the endothelium due to MDM lipid ($t \geq 5$). Column (b) indicates that the MDM density remains concentrated in the lesion interior for all times, with a negligible quantity of MDMs exiting the lesion at $x = 1$. Indeed, $M(x, t \geq 100) \approx 0$ for $x > 0.5$, with only a slightly larger spatial support at earlier times (e.g., $M(x, 5) \approx 0$ for $x > 0.8$). Column (c) shows that mean MDM lipid content increases with depth at all times, consistent with Fig. 6.4(c), albeit with a steeper rate of increase. Figs. 6.11(d,e) are similar to the case lipid-independent MDM kinetics; HDL capacity remains spatially uniform with unimodal time evolution, while mean lipid density increases monotonically with time.

To explore the range of model behaviours as ψ_D and ψ_β vary, we compute steady state solutions across $(\psi_D, \psi_\beta) \in [0, 1] \times [0, 1]$ using a grid resolution of 0.1 for $\psi_D < 0.9$ and 0.01 for $\psi_D \geq 0.9$. The results are summarised in Fig. 6.12. We colour the (ψ_D, ψ_β) subspace according to the qualitative behaviour of the MDM density in plot (a), and lipid density in plot (b). The results indicate that only a strikingly small region exhibits solutions with local maxima in $M(x)$ and $L_{\text{tot}}(x)$. In particular, peak formation in both requires large values of ψ_D ($\psi_D > 0.92$) and sufficiently small values of ψ_β ($\psi_\beta < 0.6$). Imposing the requirement that the local maxima in $M(x)$ and $L_{\text{tot}}(x)$ are also global maxima, as suggested by the Nakashima images, further restricts this region to a neighbourhood of $(\psi_D, \psi_\beta) = (1, 0)$. This region corresponds to MDM populations for which diffusivity decreases rapidly with lipid content, and mean lifespan decreases slowly with lipid content.

We further characterise model behaviour in terms of the blood densities of LDL lipid, $L^\star$, and HDL capacity, $H^\star$, in Fig. 6.13. Here we fix $\psi_D = 1$ and $\psi_\beta = 0.1$, to ensure that $M(x)$ and $L_{\text{tot}}(x)$ exhibit local maxima that coincide with their global maxima when $L^\star = 4.5$ and $H^\star = 0.5$ (see Fig. 6.12). The results represent steady state model output across the range of plausible values $(L^\star, H^\star) \in (0, 10] \times (0, 5]$. Plot (a) indicates that $M(x)$ exhibits a local maximum when $L^\star$ is large enough relative to $H^\star$. The local maximum coincides with the global maximum only when the difference is sufficiently large. Plot (b) shows that $L_{\text{tot}}(x)$ is also monotone unless $L^\star$ is sufficiently large relative to $H^\star$, although the separating curve is nonlinear. In contrast to the behaviour for $M(x)$, the region in which $L_{\text{tot}}(x)$ is monotonic is adjacent to the region in which it is unimodal and the local and global maxima coincide. In particular, fixing $H^\star < 2$ and increasing $L^\star$ leads to the formation of a local maximum in $L_{\text{tot}}(x)$ that coincides with the global maximum when it exists. By contrast, increasing $L^\star$ for fixed $H^\star > 2$ yields a local maximum whose

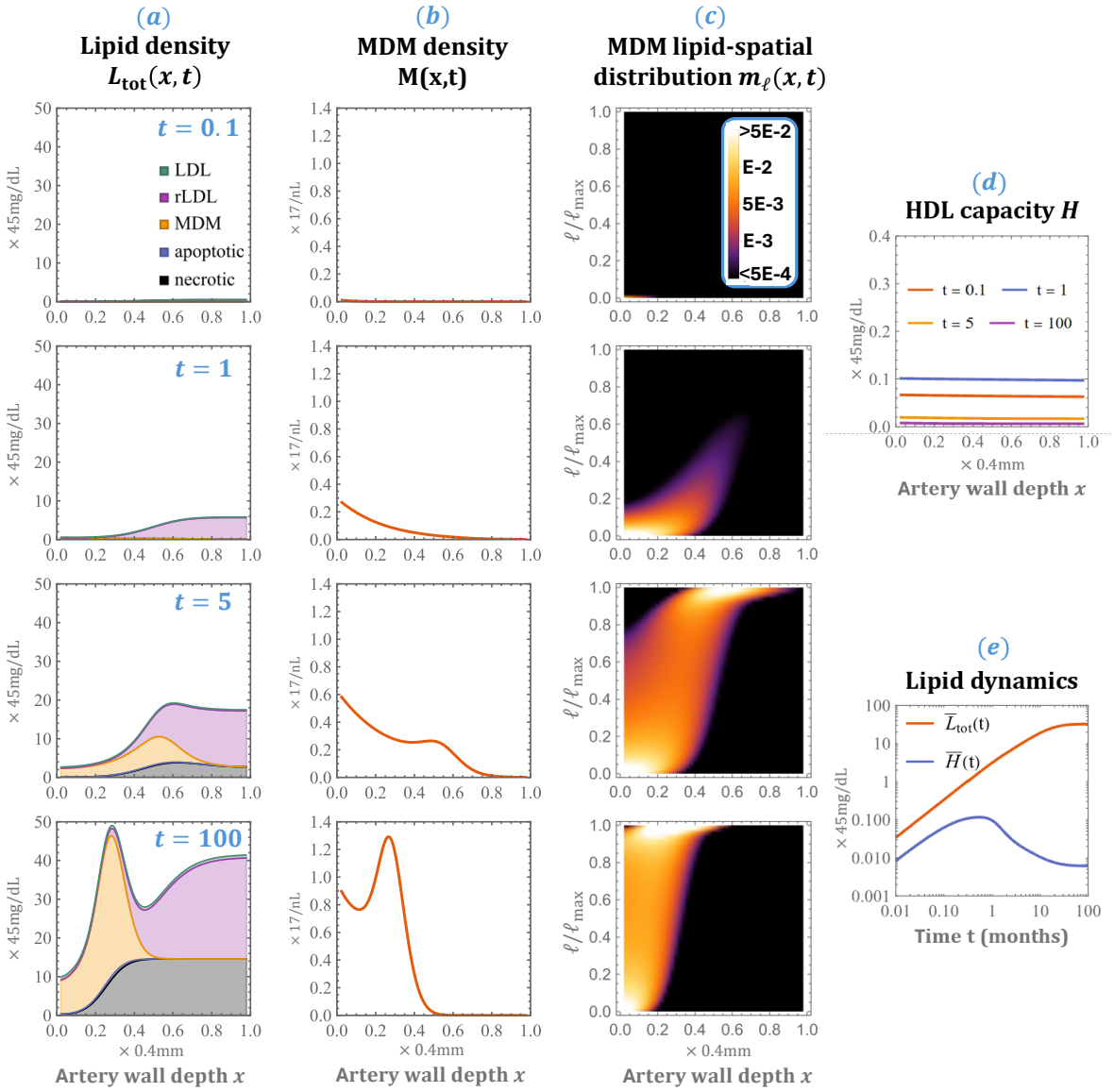


Figure 6.11: **Time evolution of the model lesion when MDM mobility and apoptosis depend on lipid content:** $\psi_D = 1, \psi_\beta = 0.1$**.** Columns (a), (b) and (c) show the lipid densities, MDM density, and MDM lipid-spatial distribution, respectively, at the times $t = 0.1$, 1, 5 and 100. Plot (d) highlights the spatial uniformity of HDL capacity, as indicated by result (6.62)-(6.63). Plot (e) shows the time evolution of mean total lipid density, $\overline{L}_{\text{tot}}$, and HDL capacity, $\overline{H}$, as defined in Eqs. (6.57). Note the peak formation at later times in columns (a) and (b), consistent with the Nakashima images. We use $L^\star = 4$, $H^\star = 0.5$.

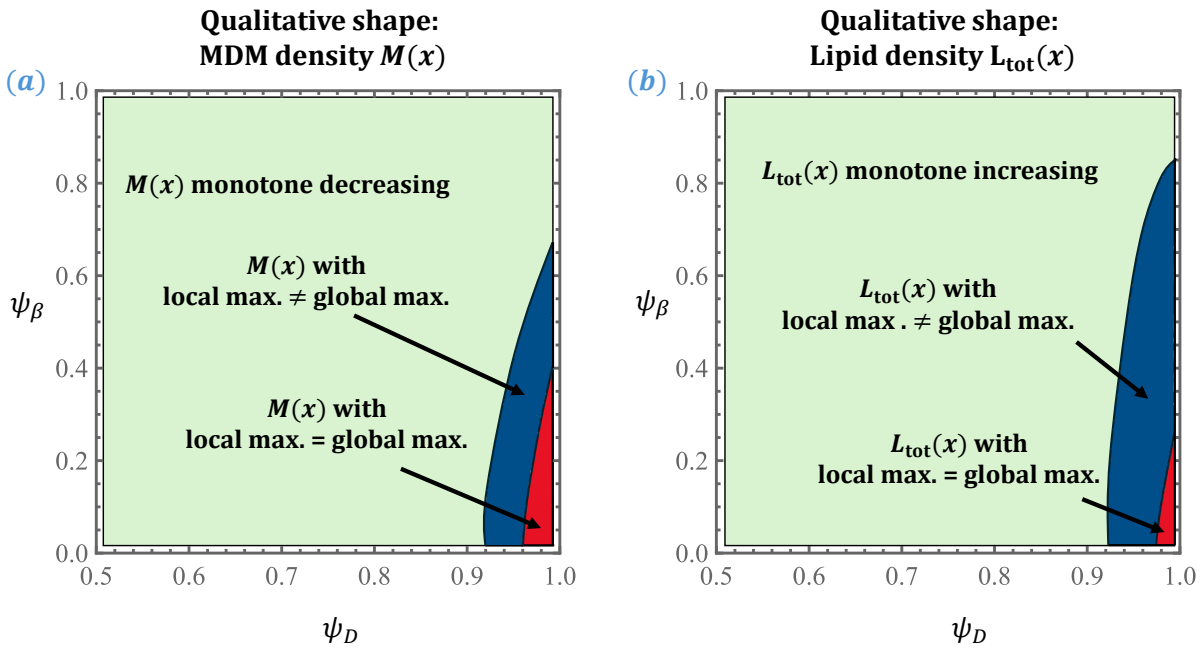


Figure 6.12: **The qualitative shape of the MDM (a) and lipid (b) densities as the sensitivities to lipid content of MDM diffusivity, ψ_D, and apoptosis, ψ_β, are varied.** The results represent steady state solutions across $(\psi_D, \psi_\beta) \in [0,1] \times [0,1]$ using a grid resolution of 0.1 for $\psi_D < 0.9$ and 0.01 for $\psi_D \geq 0.9$. We fix $L^\star = 4$ and $H^\star = 0.5$ and plot only $\psi_D > 0.5$ for visibility. Note how only a small neighbourhood of $(\psi_D, \psi_\beta) = (1, 0)$ admits solutions for which the MDM and lipid densities attain local maxima that coincide with their respective global maxima.

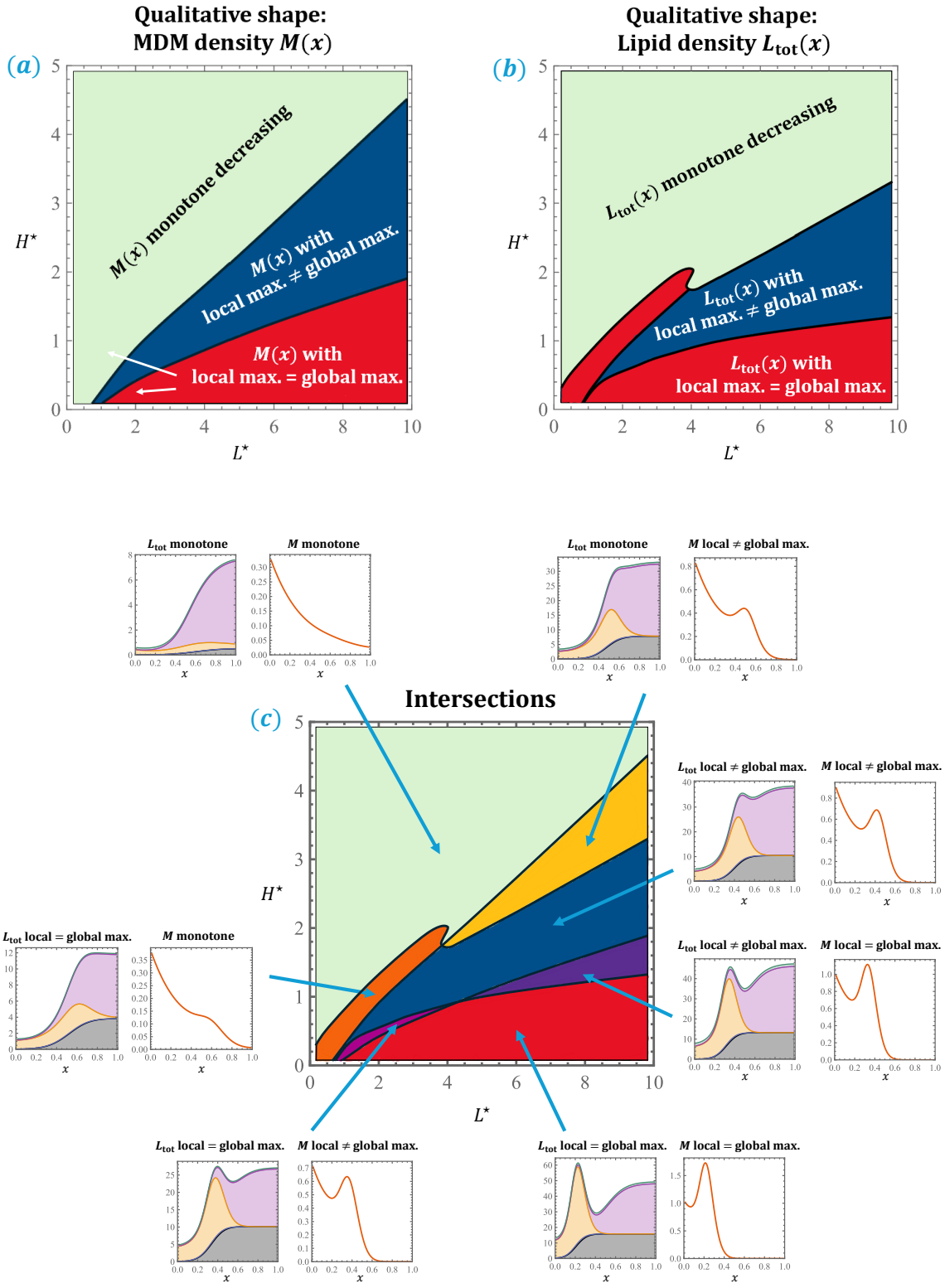


Figure 6.13: **The qualitative behaviour of the model with lipid content-dependent MDM mobility and apoptosis, ψ_D, $\psi_\beta > 0$, as blood LDL lipid, $L^\star$, and HDL capacity, $H^\star$, are varied.** We fix $\psi_D = 1$ and $\psi_\beta = 0.1$. The results represent steady state solutions across $(L^\star, H^\star) \in (0, 10] \times (0, 5]$ using a grid of resolution 0.2×0.1. Plots (a) and (b) show the qualitative behaviour of $M(x)$ and $L_{\text{tot}}(x)$ at steady state, respectively, and plot (c) illustrates their intersections. Note how the existence of maxima in $M(x)$ and $L_{\text{tot}}(x)$ requires $L^\star$ to be large relative to $H^\star$. The red region in (c) depicts the range of values for which the model steady state is qualitatively consistent with the Nakashima images.

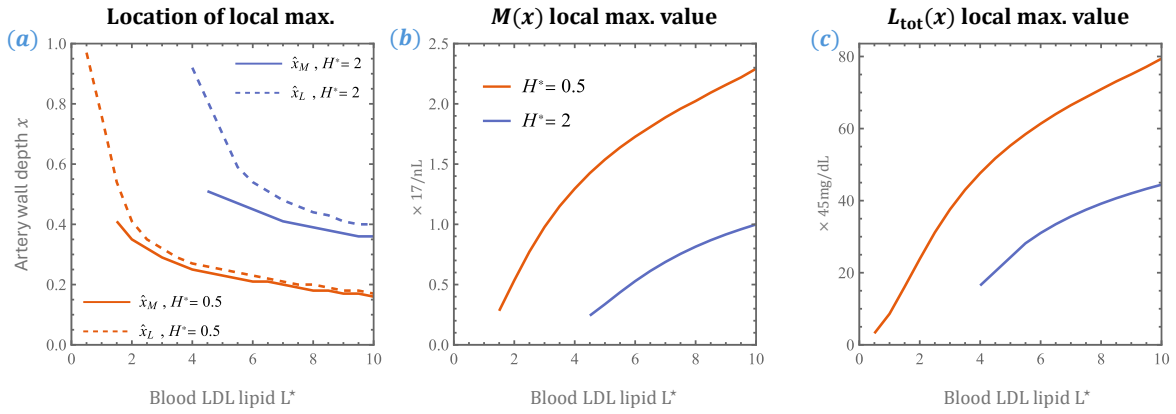


Figure 6.14: **Behaviour of the local maxima at steady state for the MDM and lipid densities, $M(x)$ and $L_{\text{tot}}(x)$, respectively.** Plot (a) shows how their peak location approximately coincides and decreases in depth for higher blood LDL levels, $L^\star$. Plots (b) and (c) show the value of the local maximum in $M(x)$ and $L_{\text{tot}}(x)$, respectively. Both maxima increase with $L^\star$. We fix $\psi_D = 1$, $\psi_\beta = 0.1$ and compute solutions for $H^\star = 0.5$ (blue) and $H^\star = 2$ (red).

peak value is less than $L_{\text{tot}}(1)$. Plot (c) shows the intersections between plots (a) and (b). We note that there is a large region for $H^\star < 1$ and $L^\star > 2$ where both $M(x)$ and $L_{\text{tot}}(x)$ attain local maxima that coincide with their global maxima, consistent with the Nakashima images.

Finally, we explore the behaviour of the local maxima in $M(x)$ and $L_{\text{tot}}(x)$ at steady state in Fig. 6.14. We compute solutions for $0 < L^\star \leq 10$ with $H^\star = 0.5$ (red) and $H^\star = 2$ (blue). Plot (a) shows that the location of the local maxima for M (solid) and L_{tot} (dashed) approximately coincide, with better agreement for larger $L^\star$. The location of both maxima decreases with $L^\star$, indicating that higher blood LDL levels push the local maxima towards the endothelium. Peak location is deeper for $H^\star = 2$ than for $H^\star = 0.5$, suggesting that increasing blood HDL capacity has the opposite effect, pushing the peak towards the tunica media. Plots (b) and (c) show the local maximum value of $M(x)$ and $L_{\text{tot}}(x)$, respectively. As expected, peak values are greater for higher blood LDL levels, $L^\star$, and lower values of HDL capacity, $H^\star$. Overall, the results presented in Figs. 6.13 and 6.14 show that blood levels of LDL lipid and HDL capacity strongly influence the qualitative behaviour of the lipid and MDM spatial density profiles.

6.4 Discussion

In this chapter we have developed a spatially-resolved and lipid-structured model for MDM populations in early human atherosclerosis. We consider a one-dimensional Cartesian geometry, where $0 \leq x \leq X$ represents depth into the artery wall. Lipid content is treated using a discrete index, $\ell = 0, 1, \ldots, \ell_{\max}$, to represent incremental changes to MDM lipid burden. The model couples the dynamics of the MDMs, $m_\ell(x,t)$, to the densities of free

LDL lipid, $L_{LDL}(x,t)$, retained LDL lipid, $L_{\mathrm{r}}(x,t)$, apoptotic lipid, $L_{\mathrm{ap}}(x,t)$, necrotic lipid, $L_{\mathrm{n}}(x,t)$, HDL lipid capacity, $H(x,t)$, and inflammatory mediators, $S(x,t)$.

Our model development and analysis were guided by the lipid and MDM densities presented in Nakashima *et al.* [9], reproduced in Fig. 6.1. Intima growth is minimal between the images, supporting our assumption of a fixed domain size: $X \approx 0.4$mm. The images exhibit two further features which we aimed to qualitatively replicate in our model:

1. Lipid first accumulates deep in the intima, towards the tunica media;

2. The lipid and MDM densities both eventually peak within the tunica media, rather than at the lumenal or medial boundaries.

We accounted for feature 1 by assuming a spatially non-uniform LDL retention capacity, $K_{\mathrm{r}}(x)$, which increases with x in a step-like manner. The steepness of the step is determined by a parameter, $\theta \approx 10$, which we approximate by comparison to Fig. 6.1(e, h). We note that it is insufficient to assume a spatially uniform LDL retention capacity, or to omit LDL retention entirely, since LDL enters the lesion from the bloodstream; the LDL spatial profile would skew towards the endothelium, contrary to Fig. 6.1(e, h). Feature 2 indicates behaviour that should fall within the scope of our model output. Since it pertains to lipid and MDM densities at the PIT stage, we interpret this feature as a property our model should be capable of exhibiting at steady state. This is reasonable since PIT is the most advanced pre-thrombotic stage prior to fibrous cap formation. Fibrous cap formation is driven by the later accumulation of smooth muscles cells towards the endothelium; capturing these dynamics is beyond the scope of our model.

Our model analysis in Sect. 6.3 focused on the impact of two key parameters, $\psi_\beta, \psi_D \in [0,1]$. The values of ψ_β and ψ_D respectively determine the sensitivity of MDM lifespan and MDM mobility to lipid content. These parameters alter how the dependent variables in our model are coupled to each other. In particular, the extracellular lipid and HDL densities form a closed subsystem when coupled to the total MDM density, $M(x,t)$, and lipid content, $L_M(x,t)$, when MDM lifespan and mobility are both independent of lipid content: $\psi_\beta = \psi_D = 0$. No such closed subsystem exists if either ψ_β or $\psi_D \neq 0$ since the PDE for $L_M(x,t)$ becomes coupled to higher order moments of the lipid distribution, $m_\ell(x,t)$, whose dynamics depend on successively higher order moments. We also explored the impact of the blood densities of LDL lipid and HDL capacity, $L^\star$ and $H^\star$, respectively. As both $L^\star$ and $H^\star$ depend on lifestyle choices, such as diet and exercise, it should be possible to change their values. We considered their impact across a range of plausible values: $L^\star \in (0,10)$ and $H^\star \in (0,5)$, with upper bounds corresponding to 450mg/dL and 225mg/dL, respectively. We fixed the remaining parameters to the values given in Table 4.1. Since these estimates are likely to carry high degrees of uncertainty, we focus our analysis on identifying qualitative trends rather than quantitative predictions. We discuss our findings below in relation to the key questions posed in Sect. 6.1.

Q1. **Under what circumstances does our model qualitatively reproduce the densities in the Nakashima images, shown in Fig. 6.1?**

The results presented in Sect. 6.3.1 suggest that our model cannot reproduce an internal peak in the lipid or MDM densities when MDM lifespan and mobility are independent of lipid content ($\psi_\beta = \psi_D = 0$). Despite successfully capturing the early lipid accumulation deep in the intima, the lipid and MDM densities maintain monotone increasing and decreasing profiles, respectively, as the model tends to steady state. A key issue is that the MDM density at steady state $M(x)$, decouples from the lipid densities. We used this to prove that $M(x)$ decreases monotonically for all parameter values, and that the mean MDM depth is independent of $L^\star$ and $H^\star$.

The steady state results in Sect. 6.3.2 indicate that if only the rate of apoptosis is lipid-dependent then the model is unable to replicate the Nakashima images. Although a closed-form analytical solution for $M(x)$ at steady state is not readily attainable when $\psi_\beta > 0 = \psi_D$, we proved that $M(x)$ is concave-up wherever it is nonzero and, hence, cannot attain an internal global maximum.

By contrast, the steady state results in Sect. 6.3.3 show that if only MDM mobility is lipid content-dependent then the MDM and lipid densities may attain internal global maxima. The steady state plots suggest that peak formation only occurs for ψ_D sufficiently large.

We confirm this hypothesis in Sect. 6.3.1, where we explore model behaviour in the case where both MDM lifespan and mobility depend on lipid content: $\psi_D, \psi_\beta > 0$. Our results indicate that the formation of internal global maxima in both the lipid and MDM densities only occurs when MDM mobility is highly sensitive to lipid content, $\psi_D > 0.98$, and MDM lifespan is comparably insensitive, $\psi_\beta < 0.2$. A further parameter sweep across plausible blood densities of LDL lipid, $L^\star$, and HDL capacity, $H^\star$, indicates that the formation of internal global maxima in both the lipid and MDM densities requires that $L^\star$ is sufficiently large relative to $H^\star$. This finding is unsurprising since higher blood LDL densities promote higher MDM lipid contents, and so they amplify the impact of lipid content-dependent MDM lifespan and mobility on the lipid and MDM densities. Low levels of blood LDL lipid relative to HDL capacity give rise to few lipid-laden MDMs in the lesion, promoting dynamics qualitatively similar to the case of lipid-independent MDM kinetics.

We note two apparent discrepancies between our model output and the Nakashima images in Fig. 6.1. First, comparing Fig. 6.1(i) to Fig. 6.11(b) at $t = 1$ suggests that our model overestimates MDM levels at early times. Since our model predicts lesion behaviour in noiseless conditions, this discrepancy may simply be due to noise in MDM numbers at early times. Indeed, Fig. 6.1(i) is not completely devoid of

MDMs. Moreover, the structure of our mathematical model ensures that MDMs can only enter the lesion after LDL retention, consistent with Fig. 6.1. Hence, this apparent difference is quantitative in nature and could be rectified by adjusting the recruitment parameter α. Nonetheless, it would be useful to run multiple simulations using the same parameter values in an equivalent stochastic model to explore the impact of noise in MDM numbers. Second, our model with lipid content-dependent MDM lifespan and mobility predicts that the MDM density infiltrates deeper into the lesion before retreating and forming a peak closer to the endothelium (see Fig. 6.11(b) at $t = 5, 100$). This behaviour contrasts with the monotone increase of MDM infiltration depth with time suggested by the Nakashima images (see Fig. 6.1(i, l, o, r)). A possible explanation is that our model shows a genuine intermediate stage of deep MDM infiltration, not captured in Fig. 6.1. This would mean that maximal MDM depth is a poor marker for disease progression, relative to total lipid density (which monotonically increases with time in our models). Since MDM levels are low deeper in the lesion, verifying this hypothesis would require analysis of many sample lesions to eliminate noise. Another possibility is that the retreat in maximal MDM depth is an artefact of our assumption of linearity in the decrease of MDM mobility with lipid content. This hypothesis could be explored via numerical simulations with nonlinear dependence of mobility on lipid content.

Q2. **What are the effects of introducing lipid content-dependence to MDM lifespan and mobility?**

The inclusion of lipid content-dependent MDM lifespan and mobility has minimal impact on model behaviour at early times, relative to the lipid-independent case (compare Fig. 6.4 and Fig. 6.11 for $t \leq 1$). This is because there are few lipid-laden MDMs early in lesion development. The impact of lipid-dependent MDM lifespan and mobility are most apparent at later times, as the model tends to steady state.

We explored the impact on the steady state solutions of allowing MDM lifespan to decrease with lipid content in Sect. 6.3.2. Relative to the constant lifespan case, we saw increases in the mean total lipid density and mean HDL capacity, and decreases in mean MDM density, MDM lipid content and depth. The decrease in mean MDM density and increase in mean lipid density are consistent with the analysis of lipid content-dependent apoptosis in the spatially-homogeneous model of Watson *et al.* [185]. However, their results suggest that mean MDM lipid load is higher in the case of lipid content-dependent lifespan. This discrepancy is likely due to differences in the treatment of MDM lipid content; the model in [185] allows for unrestricted lipid contents, while the present model imposes a maximal capacity for lipid content, $\ell_{\max}$. In our formulation, MDMs are less likely to consume lipid if they are already lipid-laden. Therefore, lipid-laden MDMs are more likely to die than to ingest the

excess apoptotic and necrotic lipid sourced by the death of nearby MDMs, reducing mean MDM lipid content overall.

We analysed the effect of lipid content-dependent MDM mobility on the steady state solutions in Sect. 6.3.3. Relative to the constant mobility case, we saw increases in mean total lipid density, MDM density and MDM lipid content, and decreases to mean HDL capacity and MDM depth. The increases in total lipid content, MDM density and MDM lipid content are consistent with the analysis of lipid content-dependent emigration in the spatially-homogeneous model of Watson *et al.* [185]. HDL capacity and spatial depth lack analogues in their model. These results are, nonetheless, intuitive on theoretical grounds. HDL capacity is lower since MDM lipid loads are greater and so MDMs offload greater amounts of lipid to HDL. MDM depth is decreased since MDMs are, on average, less mobile.

Q3. **How does MDM lipid content vary with spatial depth?**

Our results indicate that mean MDM lipid content increases with spatial depth at all times. This trend is robust to changes in the sensitivities of MDM lifespan and mobility to lipid content, ψ_β and ψ_D respectively, and to the blood densities of LDL lipid and HDL capacity, $L^\star$ and $H^\star$ respectively. These findings are unsurprising since LDL is initially retained deep in the lesion, forming a gradient of extracellular lipid that promotes higher MDM uptake rates deeper in the intima. Moreover, MDMs deeper in the intima are likely to be older (in terms of residence time) on average, than those near the endothelium; deeper MDMs have had more time to ingest lipid than nascent MDMs.

All generated plots of the MDM lipid-spatial distribution, $m_\ell(x,t)$, further suggest that the spread in MDM lipid content also decreases with depth at all times. This is also likely to be a consequence of the greater mean residence time of MDMs deeper in the intima; it is less likely to find nascent, lipid-poor MDMs deeper in the intima than MDMs which have neared an equilibrium between lipid uptake and efflux. This hypothesis could be explored more rigorously by computing an equivalent agent-based model.

Conclusions. In this chapter we have presented a new spatially-resolved and lipid-structured mathematical model for MDM populations in early human atherosclerotic lesions. Our model development and analysis are guided by the clinical observations of Nakashima *et al.* [9]. Consistent with their findings, the model predicts that lipid initially accumulates deep in the intima due to a spatially non-uniform LDL retention capacity. Our model is further capable of qualitatively reproducing their reported lipid and MDM densities provided that MDM mobility decreases sensitively with lipid content and MDM lifespan is sufficiently insensitive to lipid content. We further find that MDM lipid content increases with spatial depth, regardless of blood LDL and HDL content.

These results develop the current understanding of macrophage heterogeneity in lipid content and spatial position. In the following chapter, we build upon the current model to account for MDM phenotype.

Chapter 7

A spatially-resolved phenotype-lipid structured model

In this chapter, we combine the models developed in Chapters 5 and 6 so that the MDM population is spatially resolved and structured by both phenotype and lipid content. We use the principle of mass conservation to couple the MDM dynamics to the densities of free LDL lipid, rLDL lipid, apoptotic lipid, necrotic lipid, HDL capacity, inflammatory mediators and resolving mediators.

7.1 Introduction

Information on the spatial distribution of MDM phenotype in atherosclerotic lesions is limited. In particular, data on the spatial heterogeneity of MDM phenotype in early human lesions are not yet available, to the best of our knowledge. In late murine lesions, macrophages near the necrotic core are predominantly inflammatory M1-like while there is a balance between M1-like and resolving M2-like macrophages near the fibrous cap [111, 246]. These observations suggest that a spatially-resolved, phenotype gradient emerges during disease progression, with respect to distance from the endothelium. Whether this phenotype gradient is a late-stage feature, or is present during early atherosclerosis, is unknown. The impact of blood LDL and HDL levels on the spatial distribution of MDM phenotype is also unknown and a focus of this chapter.

A further focus of this chapter is to analyse whether certain results presented in Chapters 5 and 6 are robust to the addition of spatial and phenotype resolution, respectively. In summary, we use our model to investigate the following key questions:

Q1. **How does MDM phenotype vary with spatial depth?**

Q2. **How does the addition of spatial resolution impact the results concerning lesion composition from Chapter 5?**

Q3. **How does the addition of phenotype resolution impact the results concerning lipid-dependent MDM mobility and lifespan from Chapter 6?**

The remainder of the chapter is structured as follows. Sect. 7.2 introduces the full model and includes a derivation of the related, closed subsystems. Sect. 7.3 contains the results, which consist entirely of numerical solutions to these closed subsystems; we omit numerical solutions to the full model in this thesis since they require parallel decomposition of the phenotype-lipid-spatial domain for efficient computation. We first consider results when MDM mobility and mean lifespan are constant, and later introduce lipid content-dependence to these processes. Finally, in Sect. 7.4 we discuss the results in the context of the above questions.

7.2 Model development

In this section, we formulate a spatially-resolved PDE model for early atherosclerosis in which the MDM population is structured according to phenotype and lipid content.

7.2.1 Assumptions and definitions

We formulate the model as a system of partial differential equations, with associated boundary and initial conditions. The equations are defined in one Cartesian spatial dimension, $0 \leq x \leq X$, where x represents distance from the endothelium ($x = 0$) to the IEL ($x = X$). We assume for simplicity that the domain length, X, is fixed. This is reasonable for early lesions but is unlikely to hold for late-stage plaques.

We assume, for simplicity, that MDM phenotype and lipid content change by finite increments, $\Delta\phi = 1$ and $\Delta a > 0$, respectively, and structure the MDM population according to phenotype and lipid content. Specifically, we let $m_\ell^\phi(x,t)$ denote the density of MDMs with lipid content $a_0 + \ell\Delta a$ and phenotype ϕ at position x and time $t \geq 0$. The phenotype index runs over positive and negative integer values: $\phi = 0, \pm 1, \ldots, \pm\phi_{\max}$. MDMs with $\phi > 0$ have a pro-inflammatory, M1-like phenotype; those with $\phi < 0$ have a resolving, M2-like phenotype. The lipid index runs over non-negative values: $\ell = 0, 1, \ldots, \ell_{\max}$, so that MDM lipid content ranges from their endogenous content, $a_0 \geq 0$, to a maximum value, $a_0 + \kappa$, where $\kappa := \ell_{\max}\Delta a$ is the maximum capacity for ingested lipid.

We introduce additional variables to describe the extracellular environment. We denote by $L_{LDL}(x,t) \geq 0$, $L_{\mathrm{r}}(x,t) \geq 0$, $L_{\mathrm{ap}}(x,t) \geq 0$ and $L_{\mathrm{n}}(x,t) \geq 0$ the mass densities of free LDL lipid, retained LDL lipid, apoptotic lipid and necrotic lipid, respectively. We let $H(t)$ be the lipid capacity of HDL particles in the lesion. Finally, we denote by $S_+(x,t) \geq 0$ and $S_-(x,t) \geq 0$ the mass densities of inflammatory and resolving mediators, respectively.

7.2.2 Model equations

MDMs. We propose that the MDM population evolves according to the following PDEs:

$$\begin{aligned}\frac{\partial m_\ell^\phi}{\partial t} = &\underbrace{D_M\left[1-\psi_D\Big(\frac{\ell}{\ell_{\max}}\Big)\right]\frac{\partial^2 m_\ell^\phi}{\partial x^2}}_{\text{diffusion}} - \underbrace{\frac{\beta m_\ell^\phi}{1-\psi_\beta\big(\frac{\ell}{\ell_{\max}}\big)}}_{\text{apoptosis}}\\ &+\underbrace{\boldsymbol{k_L}\cdot\boldsymbol{L}\ \big[(\ell_{\max}-\ell+1)m_{\ell-1}^\phi-(\ell_{\max}-\ell)m_\ell^\phi\big]}_{\text{lipid uptake}}\\ &+\underbrace{k_H H\quad\big[(\ell+1)m_{\ell+1}^\phi-\ell m_\ell^\phi\big]}_{\text{lipid efflux to HDL}},\\ &+\underbrace{k_S\chi S_+\big[(\phi_{\max}-\phi+1)m_\ell^{\phi-1}-(\phi_{\max}-\phi)m_\ell^\phi\big]}_{\text{inflammatory phenotype modulation}}\\ &+\underbrace{k_S\chi S_-\big[(\phi_{\max}+\phi+1)m_\ell^{\phi+1}-(\phi_{\max}+\phi)m_\ell^\phi\big]}_{\text{resolving phenotype modulation}}\end{aligned} \tag{7.1}$$

for all $0\le x\le 1$ and $t\ge 0$. Eqs. (7.1) hold for all $\phi = 0,\pm1,\dots,\pm\phi_{\max}$ and $\ell = 0,1,\dots,\ell_{\max}$, and are subject to the closure conditions

$$m_{-1}^\phi = m_{\ell_{\max}+1}^\phi = m_\ell^{-\phi_{\max}-1} = m_\ell^{\phi_{\max}+1} = 0. \tag{7.2}$$

We define for notational brevity the vectors $\boldsymbol{k_L} := (k_{LDL}, k_{\mathrm{r}}, k_{\mathrm{ap}}, k_{\mathrm{n}})$ and $\boldsymbol{L} := (L_{LDL}, L_{\mathrm{r}}, L_{\mathrm{ap}}, L_{\mathrm{n}})$, so that $\boldsymbol{k_L}\cdot\boldsymbol{L} = k_{LDL}L_{LDL} + k_{\mathrm{r}}L_{\mathrm{r}} + k_{\mathrm{ap}}L_{\mathrm{ap}} + k_{\mathrm{n}}L_{\mathrm{n}}$.

The first line of the RHS of Eqs. (7.1) describes MDM random motion and apoptosis. As in Chapter 6, we assume that these processes occur at rates that depend on lipid content, ℓ. More specifically, we assume that MDM mobility and lifespan decrease linearly with ℓ with sensitivities $0\le\psi_D\le 1$ and $0\le\psi_\beta\le 1$, respectively. The remaining lines account for changes to lipid content and phenotype that are modelled using mass-action kinetics. Specifically, we describe lipid uptake with the reaction

$$\mathrm{M}_\ell^\phi + \Delta a \xrightarrow{k_i(\ell_{\max}-\ell)} \mathrm{M}_{\ell+1}^\phi, \tag{7.3}$$

for $i\in\{LDL, \mathrm{r}, \mathrm{ap}, \mathrm{n}\}$, lipid efflux to HDL with the reaction

$$\mathrm{M}_\ell^\phi \xrightarrow{k_H\ell} \mathrm{M}_{\ell-1}^\phi, \tag{7.4}$$

and phenotype modulation with the reaction

$$\mathrm{M}_{\phi,\ell} + \Delta s \to \begin{cases}\mathrm{M}_{\phi\pm1,\ell} & \text{with rate } p_\phi^\pm := k_S\chi(\phi_{\max}\mp\phi);\\ \mathrm{M}_{\phi,\ell} & \text{with rate } k_S(1-p_\phi^\pm),\end{cases} \tag{7.5}$$

for $\phi = 0,\pm1,\dots,\pm\phi_{\max}$ and $\ell = 0,1,\dots,\ell_{\max}$.

We close Eqs. (7.1) by imposing the following boundary conditions:

$$-D_M\frac{\partial m_\ell^\phi}{\partial x} = \begin{cases}R_\ell^\phi(t) - \gamma m_\ell^\phi & \text{at } x=0;\\ \gamma m_\ell^\phi & \text{at } x=X.\end{cases} \tag{7.6}$$

We assume that newly recruited MDMs enter the lesion at $x = 0$ carrying only endogenous lipid and with an uncommitted phenotype:

$$R_\ell^\phi(t) := \begin{cases} \sigma_M \left(\frac{S_+}{S_+ + S_+^{\mathrm{c50}} + \rho S_-} \right) \Big|_{x=0} & \text{if } (\phi, \ell) = (0,0); \\ 0 & \text{if } (\phi, \ell) \neq (0,0). \end{cases} \tag{7.7}$$

The recruitment rate is a first-order Hill function of the inflammatory mediator density, S_+, which saturates at the maximum value σ_M. Resolving mediators, S_-, inhibit recruitment by linearly increasing the threshold for half-maximal recruitment from the basal value S_+^{c50}; the parameter ρ governs the sensitivity of the recruitment rate to S_-. Eqs. (7.6) also account for MDM egress through either boundary. More specifically, we assume that MDMs at $x = 0, X$ exit the lesion at a rate proportional to their mobility: $\gamma\big[1 - \psi_D\big(\frac{\ell}{\ell_{\max}}\big)\big]$. We specify initial conditions later in this section.

Extracellular lipids. We assume the densities of free and retained LDL evolve according to the PDEs

$$\begin{aligned} \frac{\partial L_{\scriptscriptstyle LDL}}{\partial t} = \underbrace{D_{\scriptscriptstyle LDL} \frac{\partial^2 L_{\scriptscriptstyle LDL}}{\partial x^2}}_{\text{diffusion}} &- \underbrace{k_b L_{\scriptscriptstyle LDL}[K_{\mathrm{r}}(x) - L_{\mathrm{r}}]}_{\text{retention via ECM binding}} + \underbrace{k_{-b} L_{\mathrm{r}}}_{\text{unbinding}} \\ &\underbrace{- k_{\scriptscriptstyle LDL} \Delta a L_{\scriptscriptstyle LDL} \sum_{\phi,\ell} (\ell_{\max} - \ell) m_\ell^\phi}_{\text{uptake by MDMs}}, \end{aligned} \tag{7.8}$$

$$\frac{\partial L_{\mathrm{r}}}{\partial t} = k_b L_{\scriptscriptstyle LDL}[K_{\mathrm{r}}(x) - L_{\mathrm{r}}] - k_{-b} L_{\mathrm{r}} - k_{\mathrm{r}} \Delta a L_{\mathrm{r}} \sum_{\phi,\ell} (\ell_{\max} - \ell) m_\ell^\phi. \tag{7.9}$$

The first term in Eq. (7.8) accounts for random motion of free LDL, with diffusivity $D_{\scriptscriptstyle LDL}$. We also assume that free LDL binds to ECM proteoglycans with rate constant k_b in a capacity-limited manner, and unbinds at rate k_{-b}. Consistent with Chapter 6, we suppose that the capacity for LDL retention $K_r(x)$ is a sigmoidal function of position:

$$K_{\mathrm{r}}(x) := \bar{K}_r \cdot \left(\frac{2}{1 + e^{\theta(1/2 - x/X)}} \right), \quad \text{where } \bar{K}_r = \frac{1}{X} \int_0^X K_r(x) dx. \tag{7.10}$$

Here $\bar{K}_r$ is the mean rLDL capacity in the intima and $\theta > 0$ determines the steepness of $K_{\mathrm{r}}(x)$. The final terms in Eqs. (7.8)-(7.9) account for MDM uptake via reactions (7.3). We close Eq. (7.8) by imposing the following boundary conditions:

$$-D_{\scriptscriptstyle LDL} \frac{\partial L_{\scriptscriptstyle LDL}}{\partial x} = \begin{cases} P_L^{(0)}(L^\star - L_{\scriptscriptstyle LDL}) & \text{at } x = 0; \\ P_L^{(1)}(L_{\scriptscriptstyle LDL} - 0) & \text{at } x = X. \end{cases} \tag{7.11}$$

Here $P_L^{(0)}$ and $P_L^{(1)}$ denote the permeability to free LDL of the endothelium and IEL, respectively. We assume that the LDL lipid density is $L^\star > 0$ in the blood, and negligible in the media.

We propose that the apoptotic and necrotic lipid densities satisfy

$$\frac{\partial L_{\rm ap}}{\partial t} = \underbrace{D_{\rm ap}\frac{\partial^2 L_{\rm ap}}{\partial x^2}}_{\text{diffusion}} + \sum_{\phi,\ell}\Bigg[\underbrace{\frac{\beta(a_0+\ell\Delta a)}{1-\psi_\beta(\frac{\ell}{\ell_{\max}})}}_{\text{apoptosis}} - \underbrace{k_{\rm ap}\Delta a L_{\rm ap}(\ell_{\max}-\ell)}_{\text{uptake by MDMs}}\Bigg]m_\ell^\phi - \underbrace{\nu L_{\rm ap}}_{\text{necrosis}}, \tag{7.12}$$

$$\frac{\partial L_{\rm n}}{\partial t} = D_{\rm n}\frac{\partial^2 L_{\rm n}}{\partial x^2} + \nu L_{\rm ap} - k_{\rm n}\Delta a L_{\rm n}\sum_{\phi,\ell}(\ell_{\max}-\ell)m_\ell^\phi. \tag{7.13}$$

The terms on the first line of the RHS of Eq. (7.12) account for diffusion, lipid deposition due to MDM apoptosis and uptake by MDMs according to reaction (7.3). We further assume that apoptotic cells undergo secondary necrosis at rate ν, which provides linear sink and source terms in Eqs. (7.12) and (7.13), respectively. We close Eqs. (7.12)-(7.13) by imposing the following boundary conditions:

$$\frac{\partial L_{\rm ap}}{\partial x} = \frac{\partial L_{\rm n}}{\partial x} = 0 \quad \text{at } x = 0, X. \tag{7.14}$$

Eqs. (7.14) assume for simplicity that the endothelium and IEL are impermeable to both apoptotic and necrotic lipid.

HDL lipid capacity. We assume that the lipid capacity of the HDL particles is governed by the following PDE:

$$\frac{\partial H}{\partial t} = \underbrace{D_H\frac{\partial^2 H}{\partial x^2}}_{\text{diffusion}} \quad \underbrace{- k_H\Delta a H\sum_{\phi,\ell}\ell m_\ell^\phi}_{\text{lipid efflux by MDMs}}. \tag{7.15}$$

Eq. (7.15) accounts for HDL diffusion and MDM lipid efflux. We close Eq. (7.15) by imposing the following boundary conditions:

$$-D_H\frac{\partial H}{\partial x} = \begin{cases} P_H^{(0)}(H^\star - H) & \text{at } x = 0; \\ P_H^{(1)}(H-0) & \text{at } x = X. \end{cases} \tag{7.16}$$

The constants $P_H^{(0)}$ and $P_H^{(1)}$ denote the permeability to HDL of the endothelium and IEL, respectively. We assume that the density of HDL lipid capacity is $H^\star > 0$ in the blood, and negligible in the tunica media.

Inflammatory and resolving mediators. Finally, we propose that the densities of

inflammatory and resolving mediators evolve according to the following PDEs:

$$\begin{aligned}\frac{\partial S_+}{\partial t} &= \underbrace{D_S\frac{\partial^2 S_+}{\partial x^2}}_{\text{diffusion}} + \underbrace{\alpha L_{\mathrm{r}}}_{\substack{\text{resident}\\ \text{signals}}} + \mu\Big[\underbrace{(k_{LDL}L_{LDL} + k_{\mathrm{r}}L_{\mathrm{r}})\Delta a\sum_{\phi,\ell}(\ell_{\max}-\ell)m_\ell^\phi}_{\text{LDL-stimulated emission}} + \underbrace{\nu L_{\mathrm{ap}}}_{\text{DAMPs}}\Big] \\ &\quad + \underbrace{k_c\sum_{\phi,\ell}\Big(1+\frac{\phi}{\phi_{\max}}\Big)m_\ell^\phi}_{\text{MDM constitutive production}} - \underbrace{\Big[k_S\Delta s\sum_{\phi,\ell}m_\ell^\phi + \delta_S\Big]S_+}_{\text{MDM binding and decay}},\end{aligned} \tag{7.17}$$

$$\begin{aligned}\frac{dS_-}{dt} &= \underbrace{D_S\frac{\partial^2 S_-}{\partial x^2}}_{\text{diffusion}} + \mu\Big[\underbrace{k_{\mathrm{ap}}\Delta a L_{\mathrm{ap}}\sum_{\phi,\ell}(\ell_{\max}-\ell)m_\ell^\phi}_{\text{efferocytosis-stimulated emission}} + \underbrace{k_H\Delta a H\sum_{\phi,\ell}\ell m_\ell^\phi}_{\text{HDL-stimulated emission}}\Big] \\ &\quad + k_c\sum_{\phi,\ell}\Big(1-\frac{\phi}{\phi_{\max}}\Big)m_\ell^\phi - \Big[k_S\Delta s\sum_{\phi,\ell}m_\ell^\phi + \delta_S\Big]S_-.\end{aligned} \tag{7.18}$$

The first terms on the RHS of Eqs. (7.17) and (7.18) account for diffusion. We assume inflammatory and resolving mediators share a common diffusivity, D_S. Consistent with Chapter 5, we assume that inflammatory mediators are sourced by resident signals in response to rLDL, MDM uptake of LDL, secondary necrosis and phenotype-dependent constitutive expression by MDMs. Resolving mediators are sourced by MDM uptake of apoptotic lipid, lipid efflux to HDL and phenotype-dependent constitutive expression by MDMs. We assume both inflammatory and resolving mediators are lost to MDM binding via reactions (7.5) and natural decay at a common rate, δ_S.

We close Eqs. (7.17) and (7.18) with the boundary conditions

$$-D_S\frac{\partial S_\pm}{\partial x} = \begin{cases} P_S^{(0)}(0-S_\pm) & \text{at } x=0; \\ P_S^{(1)}(S_\pm - 0) & \text{at } x = X. \end{cases} \tag{7.19}$$

The constants $P_S^{(0)}$ and $P_S^{(1)}$ denote the endothelial and IEL mediator permeabilities, respectively. We assume for simplicity that mediator densities in the lumen and media are negligible.

Initial conditions. We impose the following conditions at $t = 0$:

$$m_\ell^\phi = 0 \quad \text{for every } (\phi,\ell), \qquad L_{LDL} = L_{\mathrm{r}} = L_{\mathrm{ap}} = L_{\mathrm{n}} = H = S_+ = S_- = 0. \tag{7.20}$$

Eqs. (7.20) assert that the model lesion is initially devoid of MDMs, extracellular lipid, HDL lipid capacity, and inflammatory and resolving mediators.

7.2.3 MDM population variables and PDE subsystems

We define the following population variables:

$$M(x,t) := \sum_{\phi,\ell} m_\ell^\phi(x,t), \tag{7.21}$$

$$L_M(x,t) := \sum_{\phi,\ell} (a_0 + \ell\Delta a) m_\ell^\phi(x,t), \tag{7.22}$$

$$\Phi_M(x,t) := \sum_{\phi,\ell} \left(\frac{\phi}{\phi_{\max}}\right) m_\ell^\phi(x,t). \tag{7.23}$$

Here $M(x,t) \geq 0$ and $L_M(x,t) \geq 0$ denote the total MDM density and lipid content, respectively. The variable $\Phi_M(x,t)$ is the aggregate MDM phenotype, and may take positive or negative values depending on whether the MDM population is net inflammatory or resolving, respectively. Using Eqs. (7.21)-(7.23), we may rewrite the PDEs for the extracellular variables:

$$\begin{aligned}
\frac{\partial L_{\text{LDL}}}{\partial t} &= D_{\text{LDL}} \frac{\partial^2 L_{\text{LDL}}}{\partial x^2} - k_b L_{\text{LDL}}[K_{\text{r}}(x) - L_{\text{r}}] + k_{-b} L_r - k_{\text{LDL}} L_{\text{LDL}}[(\kappa + a_0)M - L_M], \\
\frac{\partial L_{\text{r}}}{\partial t} &= k_b L_{\text{LDL}}[K_{\text{r}}(x) - L_{\text{r}}] - k_{-b} L_r - k_{\text{r}} L_{\text{r}}[(\kappa + a_0)M - L_M],
\end{aligned} \tag{7.24}$$

$$\begin{aligned}
\frac{\partial L_{\text{ap}}}{\partial t} &= D_{\text{ap}} \frac{\partial^2 L_{\text{ap}}}{\partial x^2} + \beta \left[L_M + \psi_\beta \sum_{\phi,\ell} \frac{(a_0 + \ell\Delta a)\ell m_\ell^\phi}{\ell_{\max} - \psi_\beta \ell} \right] - \nu L_{\text{ap}} \\
&\quad - k_{\text{ap}} L_{\text{ap}}[(\kappa + a_0)M - L_M],
\end{aligned} \tag{7.25}$$

$$\frac{\partial L_{\text{n}}}{\partial t} = D_{\text{n}} \frac{\partial^2 L_{\text{n}}}{\partial x^2} + \nu L_{\text{ap}} - k_{\text{n}} L_{\text{n}}[(\kappa + a_0)M - L_M], \tag{7.26}$$

$$\frac{\partial H}{\partial t} = D_H \frac{\partial^2 H}{\partial x^2} - k_H H(L_M - a_0 M), \tag{7.27}$$

$$\begin{aligned}
\frac{\partial S_+}{\partial t} &= D_S \frac{\partial^2 S_+}{\partial x^2} + \alpha L_{\text{r}} + \mu \Big[(k_{\text{LDL}} L_{\text{LDL}} + k_{\text{r}} L_{\text{r}}) \big((\kappa + a_0)M - L_M \big) + \nu L_{\text{ap}} \Big] \\
&\quad + k_c(M + \Phi_M) - (k_S \Delta s M + \delta_S) S_+,
\end{aligned} \tag{7.28}$$

$$\begin{aligned}
\frac{\partial S_-}{\partial t} &= D_S \frac{\partial^2 S_-}{\partial x^2} + \mu \Big[k_{\text{ap}} L_{\text{ap}} \big((\kappa + a_0)M - L_M \big) + k_H H(L_M - a_0 M) \Big] \\
&\quad + k_c(M - \Phi_M) - (k_S \Delta s M + \delta_S) S_-.
\end{aligned} \tag{7.29}$$

Eqs. (7.24)-(7.29) with their associated boundary conditions (7.11), (7.14), (7.16) and (7.19) form a closed system when appropriately coupled to the MDM dynamics. This can be done by directly coupling to the dual-structured Eqs. (7.1) and (7.6) for $m_\ell^\phi(x,t)$. The combined system is, however, computationally expensive to solve due to the large number of variables. We consider other options below.

- **Lipid-structured subsystem.** One possibility that is also valid for all values of ψ_β and ψ_D is to introduce the lipid content marginal variables:

$$m_\ell(x,t) := \sum_\phi m_\ell^\phi(x,t), \qquad \Phi_\ell(x,t) := \sum_\phi \left(\frac{\phi}{\phi_{\max}}\right) m_\ell^\phi, \tag{7.30}$$

for every $\ell = 0, 1, \ldots, \ell_{\max}$. Here $m_\ell(x,t)$ and $\Phi_\ell(x,t)$ denote the total density and aggregate phenotype, respectively, of the MDMs with lipid content ℓ. By summing Eqs. (7.1), (7.2) and (7.6) over $\phi = 0, \pm 1, \ldots, \pm\phi_{\max}$, we find that m_ℓ and Φ_ℓ satisfy the PDEs

$$\begin{aligned}\frac{\partial m_\ell}{\partial t} &= D_M\left[1 - \psi_D\Big(\frac{\ell}{\ell_{\max}}\Big)\right]\frac{\partial^2 m_\ell}{\partial x^2} - \frac{\beta m_\ell}{1 - \psi_\beta\big(\frac{\ell}{\ell_{\max}}\big)} \\ &\quad + \boldsymbol{k_L}\cdot\boldsymbol{L}\big[(\ell_{\max} - \ell + 1)m_{\ell-1} - (\ell_{\max} - \ell)m_\ell\big] + k_H H\big[(\ell+1)m_{\ell+1} - \ell m_\ell\big],\end{aligned} \tag{7.31}$$

$$\begin{aligned}\frac{\partial \Phi_\ell}{\partial t} &= D_M\left[1 - \psi_D\Big(\frac{\ell}{\ell_{\max}}\Big)\right]\frac{\partial^2 \Phi_\ell}{\partial x^2} - \frac{\beta \Phi_\ell}{1 - \psi_\beta\big(\frac{\ell}{\ell_{\max}}\big)} \\ &\quad + \boldsymbol{k_L}\cdot\boldsymbol{L}\big[(\ell_{\max} - \ell + 1)\Phi_{\ell-1} - (\ell_{\max} - \ell)\Phi_\ell\big] + k_H H\big[(\ell+1)\Phi_{\ell+1} - \ell\Phi_\ell\big] \\ &\quad + k_S\chi\Big[S_+(m_\ell - \Phi_\ell) - S_-(m_\ell + \Phi_\ell)\Big],\end{aligned} \tag{7.32}$$

the closure conditions

$$m_{-1} = m_{\ell_{\max}+1} = \Phi_{-1} = \Phi_{\ell_{\max}+1} = 0, \tag{7.33}$$

and the boundary conditions

$$-D_M\frac{\partial m_\ell}{\partial x} = \begin{cases} R_\ell^0 - \gamma m_\ell & \text{at } x = 0; \\ \gamma m_\ell & \text{at x=X,}\end{cases} \qquad -D_M\frac{\partial \Phi_\ell}{\partial x} = \begin{cases} -\gamma\Phi_\ell & \text{at } x = 0; \\ \gamma\Phi_\ell & \text{at x=X,}\end{cases} \tag{7.34}$$

for every $\ell = 0, 1, \ldots, \ell_{\max}$. Eqs. (7.31)-(7.34) form a closed PDE subsystem for m_ℓ, Φ_ℓ, $\boldsymbol{L}$, H and $S_\pm$ when coupled to Eqs. (7.24)-(7.29), (7.11), (7.14), (7.16) and (7.19). We use this lipid-structured subsystem for all simulations where ψ_D or $\psi_\beta \neq 0$.

- **Phenotype-structured subsystem for $\psi_D = \psi_\beta = 0$.** The case of lipid content-independent MDM mobility and death, $\psi_D = \psi_\beta = 0$, admits a subsystem in terms of the phenotype marginal variables:

$$m^\phi(x,t) := \sum_\ell m_\ell^\phi(x,t), \qquad L^\phi(x,t) := \sum_\ell (a_0 + \ell\Delta a)m_\ell^\phi(x,t). \tag{7.35}$$

Here $m^\phi(x,t)$ and $L^\phi(x,t)$ represent the density and lipid content of MDMs with phenotype $\phi = 0, \pm 1, \ldots, \pm\phi_{\max}$. Setting $\psi_\beta = \psi_D = 0$ and summing Eqs. (7.1), (7.2) and (7.6) over $\ell = 0, 1, \ldots, \ell_{\max}$, shows that $m^\phi(x,t)$ and $L^\phi(x,t)$ satisfy the PDEs

$$\begin{aligned}\frac{\partial m^\phi}{\partial t} &= D_M\frac{\partial^2 m^\phi}{\partial x^2} - \beta m^\phi + k_S\chi S_+\big[(\phi_{\max} - \phi + 1)m^{\phi-1} - (\phi_{\max} - \phi)m^\phi\big] \\ &\quad + k_S\chi S_-\big[(\phi_{\max} + \phi + 1)m^{\phi+1} - (\phi_{\max} + \phi)m^\phi\big],\end{aligned} \tag{7.36}$$

$$\begin{aligned}\frac{\partial L^\phi}{\partial t} &= D_M\frac{\partial^2 L^\phi}{\partial x^2} - \beta L^\phi + k_S\chi S_+\big[(\phi_{\max} - \phi + 1)L^{\phi-1} - (\phi_{\max} - \phi)L^\phi\big] \\ &\quad + k_S\chi S_-\big[(\phi_{\max} + \phi + 1)L^{\phi+1} - (\phi_{\max} + \phi)L^\phi\big], \\ &\quad + \boldsymbol{k_L}\cdot\boldsymbol{L}\big[(\kappa + a_0)m^\phi - L^\phi\big] + k_H H(L^\phi - a_0 m^\phi),\end{aligned} \tag{7.37}$$

the closure conditions

$$m^{-\phi_{\max}-1} = m^{\phi_{\max}+1} = L^{-\phi_{\max}-1} = L^{\phi_{\max}+1} = 0, \tag{7.38}$$

and the boundary conditions

$$-D_M \frac{\partial m^\phi}{\partial x} = \begin{cases} R_0^\phi - \gamma m^\phi & \text{at } x = 0; \\ \gamma m^\phi & \text{at } x = X, \end{cases} \quad -D_M \frac{\partial L^\phi}{\partial x} = \begin{cases} a_0 R_0^\phi - \gamma L^\phi & \text{at } x = 0; \\ \gamma L^\phi & \text{at } x = X, \end{cases} \tag{7.39}$$

for every $\phi = 0, \pm 1, \ldots, \pm\phi_{\max}$. Eqs. (7.36)-(7.39) form a closed subsystem for m^ϕ, L^ϕ, $\boldsymbol{L}$, H and $S_\pm$ when coupled to Eqs. (7.24)-(7.29), (7.11), (7.14), (7.16) and (7.19). We use this phenotype-structured subsystem to simulate the MDM phenotype-spatial distribution in the case of lipid content-independent MDM mobility and death.

- **Minimal subsystem for $\psi_D = \psi_\beta = 0$.** The case $\psi_D = \psi_\beta = 0$ also admits a subsystem in terms of $M(x,t)$, $L_M(x,t)$ and $\Phi_M(x,t)$. Differentiating Eqs. (7.21)-(7.23) with respect to t and substituting Eqs. (7.1) and (7.6) gives

$$\frac{\partial M}{\partial t} = D_M \frac{\partial^2 M}{\partial x^2} - \beta M, \tag{7.40}$$

$$\frac{\partial L_M}{\partial t} = D_M \frac{\partial^2 L_M}{\partial x^2} - \beta L_M + \boldsymbol{k_L} \cdot \boldsymbol{L}\big[(\kappa + a_0)M - L_M\big] + k_H H(L_M - a_0 M), \tag{7.41}$$

$$\frac{\partial \Phi_M}{\partial t} = D_M \frac{\partial^2 \Phi_M}{\partial x^2} - \beta \Phi_M + k_S \chi\big[S_+(M - \Phi_M) + S_-(M + \Phi_M)\big], \tag{7.42}$$

and the boundary conditions

$$-D_M \frac{\partial M}{\partial x} = \begin{cases} R_0^0 - \gamma M & \text{at } x = 0; \\ \gamma M & \text{at } x = X, \end{cases} \tag{7.43}$$

$$-D_M \frac{\partial L_M}{\partial x} = \begin{cases} a_0 R_0^0 - \gamma L_M & \text{at } x = 0; \\ \gamma L_M & \text{at } x = X, \end{cases} \tag{7.44}$$

$$-D_M \frac{\partial \Phi_M}{\partial x} = \begin{cases} -\gamma \Phi_M & \text{at } x = 0; \\ \gamma \Phi_M & \text{at } x = X. \end{cases} \tag{7.45}$$

Eqs. (7.40)-(7.45) form a closed subsystem for M, L_M, Φ_M, $\boldsymbol{L}$, H and $S_\pm$ when coupled to Eqs. (7.24)-(7.29), (7.11), (7.14) and (7.19). We use this minimal subsystem to efficiently sample the model output over over $(L^\star, H^\star)$ parameter space in the case of lipid content-independent MDM mobility and death.

7.2.4 Model parameters

The model depends on a large parameter set that is the union of the parameters in Chapters 5 and 6. We omit a detailed explanation here since we do not introduce any new parameters in this chapter. For completeness, we list the parameters and estimates of their values in Table 7.1.

Table 7.1: Model parameters

Parameter	Interpretation	Estimate	Source
$L^\star$	Lumen LDL lipid density	$0 - 440$ mg/dL	[32, 39]
$H^\star$	Lumen HDL lipid capacity	$0 - 230$ mg/dL	[202]
$P_L^{(0)}$	Endothelial permeability to LDL	0.37 mm month^{-1}	[203, 204]
$P_H^{(0)}$	Endothelial permeability to HDL	0.74 mm month^{-1}	[205]
$P_L^{(1)}$	IEL permeability to LDL	1.1 mm month^{-1}	[207]
$P_H^{(1)}$	IEL permeability to HDL	2.2 mm month^{-1}	[207]
$P_S^{(0)}$	Endothelial permeability to mediators	5.0 mm month^{-1}	[243]
$P_S^{(1)}$	IEL permeability to mediators	15 mm month^{-1}	[207]
$\overline{K}_r$	Mean LDL retention capacity	1900 mg/dL	[208, 210]
k_b	LDL retention rate	0.008 dL/mg month^{-1}	[206, 211]
k_{-b}	LDL unbinding rate	1.8 month^{-1}	[206, 211]
σ_M	Maximum MDM entry rate	6800 mm^{-2} month^{-1}	[212, 214]
β	Unladen MDM apoptosis rate	1.0 month^{-1}	[68, 215]
γ	Unladen MDM egress rate	0.08 mm month^{-1}	[214, 216]
ν	Secondary necrosis rate	37 month^{-1}	[217]
a_0	MDM endogenous lipid	27pg	[218, 219]
κ	MDM lipid capacity	800pg	[133]
k_{LDL}	LDL lipid uptake rate	0.00034 dL/mg month^{-1}	[90]
k_r	rLDL lipid uptake rate	0.023 dL/mg month^{-1}	[90]
k_ap	Apoptotic lipid uptake rate	0.060 dL/mg month^{-1}	[220, 221]
k_n	Necrotic lipid uptake rate	0.015 dL/mg month^{-1}	[222]
k_H	Lipid efflux rate	0.34 dL/mg month^{-1}	[223, 224]
S_+^{c50}	Half-max. MDM influx mediator density	5 ng/mL	[225, 226]
ρ	MDM influx sensitivity to res. mediators	0.40	[227]
δ_S	Mediator natural decay rate	1600 month^{-1}	[201]
Δs	Mediator mass	17 kDa	[228]
k_s	Mediator binding rate to MDMs	8800 mL/ng month^{-1}	[229, 230]
k_c	MDM constitutive mediator production	1.5 pg month^{-1}	[231]
μ	Mediator production per lipid stimulus	0.042	[231]
α	Resident inflammatory mediator production per rLDL lipid	3.5×10^{-3} month^{-1}	[68]
χ	MDM phenotypic plasticity	6.0×10^{-6}	[232]
Δa	MDM uptake/efflux increment of lipid	16 pg	[91, 233]
X	Tunica intima width	0.40 mm	[9]
θ	LDL retention profile shape	10	[9]
D_M	Diffusivity of unladen MDMs	0.02 mm^2 month^{-1}	[244]
D_ap	Diffusivity of apoptotic cells	0.005 mm^2 month^{-1}	est.
D_n	Diffusivity of necrotic cells	0.005 mm^2 month^{-1}	est.
D_{LDL}	Diffusivity of free LDL	9.2 mm^2 month^{-1}	[143]
D_H	Diffusivity of HDL	22 mm^2 month^{-1}	[143]
D_S	Diffusivity of mediators	500 mm^2 month^{-1}	[245]
ψ_D	MDM mobility sensitivity to lipid load	$\in [0, 1]$	-
ψ_β	MDM lifespan sensitivity to lipid load	$\in [0, 1]$	-
ℓ_max	MDM lipid capacity per Δa	100	$= \kappa/\Delta a$
ϕ_max	MDM phenotype resolution	50	-

7.2.5 Non-dimensionalisation

We define

$$\tilde{x} := \frac{x}{X}, \qquad \tilde{t} := \beta t, \tag{7.46}$$

so that spatial depth, $0 \leq \tilde{x} \leq 1$, is measured relative to the width of the tunica intima, $X \approx 0.40$mm, and time, $\tilde{t} \geq 0$, is measured in units of the mean lifespan of lipid-unladen MDMs, $\beta^{-1} \approx 1$ month. We scale the remaining variables as follows:

$$\begin{aligned}
&\tilde{m}_\ell^\phi(\tilde{x},\tilde{t}) := \frac{\beta X}{\sigma_M} m_\ell^\phi(x,t), && \tilde{m}^\phi(\tilde{x},\tilde{t}) := \frac{\beta X}{\sigma_M} m^\phi(x,t), && \tilde{m}_\ell(\tilde{x},\tilde{t}) := \frac{\beta X}{\sigma_M} m_\ell(x,t),\\
&\tilde{M}(\tilde{x},\tilde{t}) := \frac{\beta X}{\sigma_M} M(x,t), && \tilde{\Phi}_M(\tilde{x},\tilde{t}) := \frac{\beta X}{\sigma_M} M(x,t), && \tilde{\Phi}_\ell(\tilde{x},\tilde{t}) := \frac{\beta X}{\sigma_M} \Phi_\ell(x,t),\\
&\tilde{L}_M(\tilde{x},\tilde{t}) := \frac{\beta X}{a_0\sigma_M} L_M(x,t), && \tilde{L}^\phi(\tilde{x},\tilde{t}) := \frac{\beta X}{a_0\sigma_M} L^\phi(x,t), && \tilde{\mathbf{L}}(\tilde{x},\tilde{t}) := \frac{\beta X}{a_0\sigma_M} \mathbf{L}(x,t),\\
&\tilde{H}(\tilde{x},\tilde{t}) := \frac{\beta X}{a_0\sigma_M} H(x,t), && \tilde{S}_+(\tilde{x},\tilde{t}) := \frac{1}{S^{\mathrm{c50}}} S_+(x,t), && \tilde{S}_-(\tilde{x},\tilde{t}) := \frac{1}{S^{\mathrm{c50}}} S_-(x,t).
\end{aligned} \tag{7.47}$$

The scaling (7.47) measures the MDM densities relative to the maximum influx per MDM lifespan, $\sigma_M X^{-1}\beta^{-1} \approx 17000\text{mm}^{-3}$. The aggregate phenotype variables, Φ_M and Φ^ℓ, are also scaled by this factor; they carry dimensions of number density by definitions (7.23) and (7.30). The lipid densities and HDL capacity are measured relative to the maximum influx of MDM endogenous lipid per MDM lifespan, $a_0\sigma_M X^{-1}\beta^{-1} \approx 45$ mg/dL. The mediator densities are scaled relative to the density for half-maximal MDM recruitment, $S^{\mathrm{c50}} \approx 5$ ng/mL. We also introduce a number of dimensionless parameters in Table 7.2.

Applying the non-dimensionalisation (7.46)-(7.47) and definitions of Table 7.2, and dropping the tildes for notational convenience, we obtain the following dimensionless PDEs for the extracellular variables:

$$\begin{aligned}
\frac{\partial L_{\scriptscriptstyle LDL}}{\partial t} &= D_{\scriptscriptstyle LDL}\frac{\partial^2 L_{\scriptscriptstyle LDL}}{\partial x^2} - k_b L_{\scriptscriptstyle LDL}[K_{\mathrm{r}}(x) - L_{\mathrm{r}}] + k_{-b} L_r - k_{\scriptscriptstyle LDL} L_{\scriptscriptstyle LDL}[(\kappa+1)M - L_M],\\
\frac{\partial L_{\mathrm{r}}}{\partial t} &= k_b L_{\scriptscriptstyle LDL}[K_{\mathrm{r}}(x) - L_{\mathrm{r}}] - k_{-b} L_r - k_{\mathrm{r}} L_{\mathrm{r}}[(\kappa+1)M - L_M],
\end{aligned} \tag{7.48}$$

$$\frac{\partial L_{\mathrm{ap}}}{\partial t} = D_{\mathrm{ap}}\frac{\partial^2 L_{\mathrm{ap}}}{\partial x^2} + \beta\left[L_M + \psi_\beta \sum_{\phi,\ell} \frac{(1+\kappa\tilde{\ell})\tilde{\ell} m_\ell^\phi}{1-\psi_\beta\tilde{\ell}}\right] - \nu L_{\mathrm{ap}} - k_{\mathrm{ap}} L_{\mathrm{ap}}[(\kappa+1)M - L_M], \tag{7.49}$$

$$\frac{\partial L_{\mathrm{n}}}{\partial t} = D_{\mathrm{n}}\frac{\partial^2 L_{\mathrm{n}}}{\partial x^2} + \nu L_{\mathrm{ap}} - k_{\mathrm{n}} L_{\mathrm{n}}[(\kappa+1)M - L_M], \tag{7.50}$$

$$\frac{\partial H}{\partial t} = D_H\frac{\partial^2 H}{\partial x^2} - k_H H(L_M - M), \tag{7.51}$$

$$\begin{aligned}
\frac{\partial S_+}{\partial t} &= D_S\frac{\partial^2 S_+}{\partial x^2} + \alpha L_{\mathrm{r}} + \mu\Big[(k_{\scriptscriptstyle LDL} L_{\scriptscriptstyle LDL} + k_{\mathrm{r}} L_{\mathrm{r}})\big((\kappa+1)M - L_M\big) + \nu L_{\mathrm{ap}}\Big]\\
&\quad + k_c(M + \Phi_M) - (k_S M + \delta_S) S_+,
\end{aligned} \tag{7.52}$$

$$\begin{aligned}
\frac{\partial S_-}{\partial t} &= D_S\frac{\partial^2 S_-}{\partial x^2} + \mu\Big[k_{\mathrm{ap}} L_{\mathrm{ap}}\big((\kappa+1)M - L_M\big) + k_H H M(L_M - M)\Big]\\
&\quad + k_c(M - \Phi_M) - (k_S M + \delta_S) S_-,
\end{aligned} \tag{7.53}$$

Table 7.2: Dimensionless parameters in Eqs. (7.48)-(7.77)

Parameter	Definition	Interpretation	Estimate
$\tilde{L}^\star$	$\frac{\beta}{a_0\sigma_M}L^\star$	Lumen LDL lipid density	$0-10$
$\tilde{H}^\star$	$\frac{\beta}{a_0\sigma_M}H^\star$	Lumen HDL lipid capacity	$0-5$
$\tilde{K}_{\rm r}$	$\frac{\beta}{a_0\sigma_M}\overline{K}_r$	Mean LDL retention capacity	25
$\tilde{P}_L^{(0)}$	$\frac{1}{X\beta}P_L^{(0)}$	Endothelial LDL permeability	0.9
$\tilde{P}_H^{(0)}$	$\frac{1}{X\beta}P_H^{(0)}$	Endothelial HDL permeability	1.8
$\tilde{P}_S^{(0)}$	$\frac{1}{X\beta}P_S^{(0)}$	Endothelial mediator permeability	13
$\tilde{P}_L^{(1)}$	$\frac{1}{X\beta}P_L^{(1)}$	IEL LDL permeability	2.7
$\tilde{P}_H^{(1)}$	$\frac{1}{X\beta}P_H^{(1)}$	IEL HDL permeability	5.4
$\tilde{P}_S^{(1)}$	$\frac{1}{X\beta}P_S^{(1)}$	IEL mediator permeability	38
$\tilde{k}_b$	$\frac{a_0\sigma_M}{\beta^2}k_b$	LDL retention rate	2.7
$\tilde{k}_{-b}$	$\frac{1}{\beta}k_{-b}$	LDL unbinding rate	1.8
$\tilde{\gamma}$	$\frac{1}{\beta X}\gamma$	MDM egress rate	0.2
$\tilde{\nu}$	$\frac{1}{\beta}\nu$	Secondary necrosis rate	37
$\tilde{\kappa}$	$\frac{1}{a_0}\kappa$	MDM lipid capacity per endogenous lipid	29
$\tilde{k}_{LDL}$	$\frac{a_0\sigma_M}{\beta^2}k_{LDL}$	LDL uptake rate	0.016
$\tilde{k}_{\rm r}$	$\frac{a_0\sigma_M}{\beta^2}k_{\rm r}$	rLDL uptake rate	1.1
$\tilde{k}_{\rm ap}$	$\frac{a_0\sigma_M}{\beta^2}k_{\rm ap}$	Apoptotic lipid uptake rate	5.5
$\tilde{k}_{\rm n}$	$\frac{a_0\sigma_M}{\beta^2}k_{\rm n}$	Necrotic lipid uptake rate	1.4
$\tilde{k}_H$	$\frac{a_0\sigma_M}{\beta^2}k_H$	Lipid efflux rate	16
$\tilde{\rho}$	ρ	MDM influx sensitivity to resolving mediators	0.4
$\tilde{k}_S$	$\frac{\sigma_M\Delta_S}{\beta^2}k_S$	Mediator binding rate to MDM receptors	47
$\tilde{\delta}_S$	$\frac{1}{\beta}\delta_S$	Mediator natural decay rate	1600
$\tilde{k}_c$	$\frac{\sigma_M}{S_+^{\rm c50}\beta^2}k_c$	Constitutive MDM mediator production rate	5100
$\tilde{\mu}$	$\frac{a_0\sigma_M}{S_+^{\rm c50}\beta}\mu$	Lipid-stimulated mediator production	9200
$\tilde{\alpha}$	$\frac{a_0\sigma_M}{S_+^{\rm c50}\beta^2}\alpha$	Resident mediator production per rLDL lipid	850
$\tilde{\chi}$	$\frac{k_S S_+^{\rm c50}}{\sigma_M}\chi$	MDM phenotypic plasticity	0.28
$\tilde{\theta}$	θ	LDL retention profile shape	10
$\tilde{D}_M$	$\frac{1}{\beta X^2}D_M$	Diffusivity of unladen MDMs	0.12
$D_{\rm ap}$	$\frac{1}{\beta X^2}D_{\rm ap}$	Diffusivity of apoptotic cells	0.03
$D_{\rm n}$	$\frac{1}{\beta X^2}D_{\rm n}$	Diffusivity of necrotic cells	0.03
$\tilde{D}_{LDL}$	$\frac{1}{\beta X^2}D_{LDL}$	Diffusivity of free LDL	58
$\tilde{D}_H$	$\frac{1}{\beta X^2}D_H$	Diffusivity of HDL	140
$\tilde{D}_S$	$\frac{1}{\beta X^2}D_S$	Diffusivity of mediators	3600*
$\tilde{\psi}_D$	ψ_D	Sensitivity of MDM diffusivity to lipid load	$\in[0,1]$
$\tilde{\psi}_\beta$	ψ_D	Sensitivity of MDM lifespan to lipid load	$\in[0,1]$
$\phi_{\max}$	$\phi_{\max}$	MDM phenotype resolution	50
$\ell_{\max}$	$\ell_{\max}$	MDM maximum lipid capacity	100

where $\tilde{\ell} := \ell/\ell_{\max}$ and

$$K_{\mathrm{r}}(x) := \bar{K}_r \cdot \left(\frac{2}{1 + e^{\theta(1/2-x)}} \right). \tag{7.54}$$

We also obtain the corresponding boundary conditions:

$$-D_{LDL}\frac{\partial L_{LDL}}{\partial x} = \begin{cases} P_L^{(0)}(L^\star - L_{LDL}) & \text{at } x = 0; \\ P_L^{(1)}(L_{LDL} - 0) & \text{at } x = 1, \end{cases} \tag{7.55}$$

$$\frac{\partial L_{\mathrm{ap}}}{\partial x} = \frac{\partial L_{\mathrm{n}}}{\partial x} = 0 \quad \text{at } x = 0, 1, \tag{7.56}$$

$$-D_H\frac{\partial H}{\partial x} = \begin{cases} P_H^{(0)}(H^\star - H) & \text{at } x = 0; \\ P_H^{(1)}(H - 0) & \text{at } x = 1, \end{cases} \tag{7.57}$$

$$-D_S\frac{\partial S_\pm}{\partial x} = \begin{cases} P_S^{(0)}(0 - S_\pm) & \text{at } x = 0; \\ P_S^{(1)}(S_\pm - 0) & \text{at } x = 1. \end{cases} \tag{7.58}$$

Eqs. (7.48)-(7.58) form a closed system when coupled to the MDM dynamics in one of the following settings:

- **The full model** consists of the dual-structured PDEs

$$\begin{aligned} \frac{\partial m_\ell^\phi}{\partial t} = {} & D_M\left[1 - \psi_D\Big(\frac{\ell}{\ell_{\max}}\Big)\right]\frac{\partial^2 m_\ell^\phi}{\partial x^2} - \frac{\beta m_\ell^\phi}{1 - \psi_\beta\big(\frac{\ell}{\ell_{\max}}\big)} \\ & + \boldsymbol{k_L}\cdot\boldsymbol{L}\ \big[(\ell_{\max} - \ell + 1)m_{\ell-1}^\phi - (\ell_{\max} - \ell)m_\ell^\phi\big] \\ & + k_H H \quad \big[(\ell + 1)m_{\ell+1}^\phi - \ell m_\ell^\phi\big], \\ & + \chi S_+\big[(\phi_{\max} - \phi + 1)m_\ell^{\phi-1} - (\phi_{\max} - \phi)m_\ell^\phi\big] \\ & + \chi S_-\big[(\phi_{\max} + \phi + 1)m_\ell^{\phi+1} - (\phi_{\max} + \phi)m_\ell^\phi\big], \end{aligned} \tag{7.59}$$

  for $\ell = 0, 1 \ldots, \ell_{\max}$ and $\phi = 0, \pm 1, \ldots, \pm\phi_{\max}$, with closure conditions

$$m_{-1}^\phi = m_{\ell_{\max}+1}^\phi = m_\ell^{-\phi_{\max}-1} = m_\ell^{\phi_{\max}+1} = 0, \tag{7.60}$$

  and boundary conditions

$$-D_M\frac{\partial m_\ell^\phi}{\partial x} = \begin{cases} R_\ell^\phi(t) - \gamma m_\ell^\phi & \text{at } x = 0; \\ \gamma m_\ell^\phi & \text{at } x = 1, \end{cases} \tag{7.61}$$

  where

$$R_\ell^\phi(t) := \begin{cases} \Big(\frac{S_+}{S_+ + 1 + \rho S_-}\Big)\Big|_{x=0} & \text{if } (\phi, \ell) = (0, 0); \\ 0 & \text{if } (\phi, \ell) \neq (0, 0); \end{cases} \tag{7.62}$$

- **The lipid-structured subsystem** consists of the PDEs

$$\begin{aligned}\frac{\partial m_\ell}{\partial t} &= D_M\left[1-\psi_D\Big(\frac{\ell}{\ell_{\max}}\Big)\right]\frac{\partial^2 m_\ell}{\partial x^2} - \frac{m_\ell}{1-\psi_\beta\big(\frac{\ell}{\ell_{\max}}\big)} \\ &\quad + \boldsymbol{k_L}\cdot\boldsymbol{L}\big[(\ell_{\max}-\ell+1)m_{\ell-1} - (\ell_{\max}-\ell)m_\ell\big] + k_H H\big[(\ell+1)m_{\ell+1} - \ell m_\ell\big],\end{aligned} \tag{7.63}$$

$$\begin{aligned}\frac{\partial \Phi_\ell}{\partial t} &= D_M\left[1-\psi_D\Big(\frac{\ell}{\ell_{\max}}\Big)\right]\frac{\partial^2 \Phi_\ell}{\partial x^2} - \frac{\Phi_\ell}{1-\psi_\beta\big(\frac{\ell}{\ell_{\max}}\big)} \\ &\quad + \boldsymbol{k_L}\cdot\boldsymbol{L}\big[(\ell_{\max}-\ell+1)\Phi_{\ell-1} - (\ell_{\max}-\ell)\Phi_\ell\big] + k_H H\big[(\ell+1)\Phi_{\ell+1} - \ell\Phi_\ell\big] \\ &\quad + \chi\Big[S_+(m_\ell-\Phi_\ell) - S_-(m_\ell+\Phi_\ell)\Big],\end{aligned} \tag{7.64}$$

the closure conditions

$$m_{-1} = m_{\ell_{\max}+1} = \Phi_{-1} = \Phi_{\ell_{\max}+1} = 0, \tag{7.65}$$

and the boundary conditions

$$-D_M\frac{\partial m_\ell}{\partial x} = \begin{cases} R^0_\ell - \gamma m_\ell & \text{at } x=0; \\ \gamma m_\ell & \text{at x=1,}\end{cases} \qquad -D_M\frac{\partial \Phi_\ell}{\partial x} = \begin{cases} -\gamma\Phi_\ell & \text{at } x=0; \\ \gamma\Phi_\ell & \text{at x=1;}\end{cases} \tag{7.66}$$

- **The phenotype-structured subsystem** for $\psi_D = \psi_\beta = 0$ consists of the PDEs

$$\begin{aligned}\frac{\partial m^\phi}{\partial t} &= D_M\frac{\partial^2 m^\phi}{\partial x^2} - m^\phi + \chi S_+\big[(\phi_{\max}-\phi+1)m^{\phi-1} - (\phi_{\max}-\phi)m^\phi\big] \\ &\quad + \chi S_-\big[(\phi_{\max}+\phi+1)m^{\phi+1} - (\phi_{\max}+\phi)m^\phi\big],\end{aligned} \tag{7.67}$$

$$\begin{aligned}\frac{\partial L^\phi}{\partial t} &= D_M\frac{\partial^2 L^\phi}{\partial x^2} - L^\phi + \chi S_+\big[(\phi_{\max}-\phi+1)L^{\phi-1} - (\phi_{\max}-\phi)L^\phi\big] \\ &\quad + \chi S_-\big[(\phi_{\max}+\phi+1)L^{\phi+1} - (\phi_{\max}+\phi)L^\phi\big] \\ &\quad + \boldsymbol{k_L}\cdot\boldsymbol{L}\big[(\kappa+1)m^\phi - L^\phi\big] - k_H H(L^\phi - m^\phi),\end{aligned} \tag{7.68}$$

the closure conditions

$$m^{-\phi_{\max}-1} = m^{\phi_{\max}+1} = L^{-\phi_{\max}-1} = L^{\phi_{\max}+1} = 0, \tag{7.69}$$

and the boundary conditions

$$-D_M\frac{\partial m^\phi}{\partial x} = \begin{cases} R^\phi_0 - \gamma m^\phi & \text{at } x=0; \\ \gamma m^\phi & \text{at } x=1,\end{cases} \qquad -D_M\frac{\partial L^\phi}{\partial x} = \begin{cases} R^\phi_0 - \gamma L^\phi & \text{at } x=0; \\ \gamma L^\phi & \text{at } x=1;\end{cases} \tag{7.70}$$

- **The minimal subsystem** for $\psi_D = \psi_\beta = 0$ consists of the PDEs

$$\frac{\partial M}{\partial t} = D_M\frac{\partial^2 M}{\partial x^2} - M, \tag{7.71}$$

$$\frac{\partial L_M}{\partial t} = D_M\frac{\partial^2 L_M}{\partial x^2} - L_M + \boldsymbol{k_L}\cdot\boldsymbol{L}\big[(\kappa+1)M - L_M\big] + k_H H(L_M - M), \tag{7.72}$$

$$\frac{\partial \Phi_M}{\partial t} = D_M\frac{\partial^2 \Phi_M}{\partial x^2} - \Phi_M + \chi\big[S_+(M-\Phi_M) + S_-(M+\Phi_M)\big], \tag{7.73}$$

and the boundary conditions

$$-D_M\frac{\partial M}{\partial x} = \begin{cases} R_0^0 - \gamma M & \text{at } x = 0; \\ \gamma M & \text{at x=1,} \end{cases} \tag{7.74}$$

$$-D_M\frac{\partial L_M}{\partial x} = \begin{cases} R_0^0 - \gamma L_M & \text{at } x = 0; \\ \gamma L_M & \text{at x=1,} \end{cases} \tag{7.75}$$

$$-D_M\frac{\partial \Phi_M}{\partial x} = \begin{cases} -\gamma \Phi_M & \text{at } x = 0; \\ \gamma \Phi_M & \text{at x=1.} \end{cases} \tag{7.76}$$

We impose the following initial conditions:

$$m_\ell^\phi = m^\phi = m_\ell = L^\phi = \Phi_\ell = 0 \quad \forall(\phi,\ell), \quad L_{LDL} = L_{\rm r} = L_{\rm ap} = L_{\rm n} = H = S_\pm = 0. \tag{7.77}$$

7.2.6 Separation of timescales

As in Chapter 6, it is useful to separate the mediator and MDM timescales for numerical stability. We define

$$\epsilon := \delta_S^{-1} = 6.25\times 10^{-4} \ll 1, \quad \alpha = \epsilon^{-1}\hat{\alpha}, \quad D_S = \epsilon^{-1}\hat{D}_S, \quad k_c = \epsilon^{-1}\hat{k}_c, \quad \mu = \epsilon^{-1}\hat{\mu}, \tag{7.78}$$

and consider the limit $\epsilon \to 0$ where $\hat{\alpha}$, $\hat{D}_S$, $\hat{k}_c$, $\hat{\mu} = \mathcal{O}(1)$ as $\epsilon \to 0$. In this limit, Eqs. (7.52) and (7.53) become

$$\epsilon\frac{\partial S_\pm}{\partial t} = \hat{D}_S\frac{\partial^2 S_\pm}{\partial x^2} + F_\pm - (\epsilon k_S M + \hat{\delta}_S)S_\pm, \quad -\hat{D}_S\frac{\partial S_\pm}{\partial x} = \epsilon\begin{cases} P_S^{(0)}(0 - S_\pm) & \text{at } x = 0; \\ P_S^{(1)}(S_\pm - 0) & \text{at } x = 1, \end{cases} \tag{7.79}$$

where $F_\pm(x,t)$ are the source terms

$$F_+ := \hat{\alpha}L_{\rm r} + \hat{\mu}\Big[(k_{LDL}L_{LDL} + k_{\rm r}L_{\rm r})\big((\kappa+1)M - L_M\big) + \nu L_{\rm ap}\Big] + \hat{k}_c(M + \Phi_M), \tag{7.80}$$

$$F_- := \hat{\mu}\Big[k_{\rm ap}L_{\rm ap}\big((\kappa+1)M - L_M\big) + k_H H M(L_M - M)\Big] + \hat{k}_c(M - \Phi_M). \tag{7.81}$$

Substituting the expansions $S_\pm = S_\pm^{(0)} + \epsilon S_\pm^{(1)} + \dots$ into Eqs. (7.79) and balancing the leading order terms gives

$$0 = \hat{D}_S\frac{\partial^2 S_\pm^{(0)}}{\partial x^2} + F_\pm - \hat{\delta}_S S_\pm^{(0)}, \qquad \frac{\partial S_\pm^{(0)}}{\partial x} = 0 \quad \text{at } x = 0, 1. \tag{7.82}$$

Hence, $S_\pm$ satisfy quasi-steady approximations with no-flux boundary conditions at leading order. Eqs. (7.82) can be solved in terms of $F_\pm$ using variation of parameters. Doing so gives

$$\begin{aligned} S_\pm(x,t) \sim \frac{1}{\sqrt{\hat{D}_S}}\Bigg[&\int_x^1 F_\pm(\xi,t)\sinh\left(\frac{x-\xi}{\sqrt{\hat{D}_S}}\right)d\xi \\ &+ \operatorname{csch}\Big(\frac{1}{\sqrt{\hat{D}_S}}\Big)\cosh\left(\frac{1-x}{\sqrt{\hat{D}_S}}\right)\int_0^1 F_\pm(\xi,t)\cosh\left(\frac{\xi}{\sqrt{\hat{D}_S}}\right)d\xi\Bigg] \quad \text{as } \epsilon \to 0. \end{aligned} \tag{7.83}$$

7.2.7 Numerical scheme

We use the method of lines with spatial discretisation $\Delta x = 0.02$ to obtain numerical solutions of Eqs. (7.48)-(7.77) with expression (7.83) for $S_{\pm}(x,t)$. We approximate the second-order, spatial derivatives with a second-order central finite difference, and the integrals in Eqs. (7.83) with the Trapezoidal Rule. We solve the resulting ODE system with the *NDSolve* routine in Wolfram Mathematica. To ensure the validity of numerical solutions, we checked that the output of *NDSolve* was robust to decreases in Δx (i.e. the spatial discretisation), "MaxStepSize" (i.e. the temporal discretisation), and increases in "PrecisionGoal" and "AccuracyGoal".

7.3 Results

We present our results in two sections. In Sect. 7.3.1, we analyse numerical solutions when MDM mobility and lifespan are independent of lipid content: $\psi_D = \psi_\beta = 0$. We then present numerical solutions for $\psi_D, \psi_\beta > 0$ in Sect. 7.3.2.

7.3.1 Lipid-independent MDM kinetics: $\psi_D = \psi_\beta = 0$

Two typical spatial spatially-resolved numerical solutions are shown in Figs. 7.1 and 7.2. The solutions in Fig. 7.1 correspond to an unhealthy balance of LDL lipid to HDL capacity ($L^\star = 4$, $H^\star = 0.5$), while the solutions in Fig. 7.2 assume a healthy balance ($L^\star = 3$, $H^\star = 2$). We use numerical solutions to the lipid-structured subsystem (7.48)-(7.58), (7.63)-(7.66) to compute columns (a)-(c), and the phenotype-structured subsystem (7.48)-(7.58), (7.67)-(7.70) to compute column (d) in both figures. Column (a) shows the components of the total lipid density:

$$L_{\text{tot}}(x,t) := L_{LDL}(x,t) + L_{\text{r}}(x,t) + L_M(x,t) + L_{\text{ap}}(x,t) + L_{\text{n}}(x,t). \tag{7.84}$$

The solutions shown in Fig. 7.1 share many features with the equivalent phenotype-independent solutions in Chapter 6 (c.f. Fig. 6.4). In particular, the solutions of Fig. 7.1 exhibit early retention of LDL deep in the intima, monotone spatial profiles for $L_{\text{tot}}(x,t)$ and $M(x,t)$, and the same support for the MDM lipid-spatial distribution, $m_\ell(x,t)$, which excludes lipid-poor cells deep in the intima. A notable difference is that the MDM density is greater in the current model, especially at early times (Fig. 7.1(b,c)). This discrepancy arises because the early uptake of rLDL by MDMs drives inflammatory phenotype modulation and mediator production, which reinforce the MDM influx rate. We see this initial inflammatory phenotype modulation in Fig. 7.1(d). At early times ($t = 0.1$), the distribution $m^\phi(x,t)$ is localised at the origin $(\phi, x) = (0,0)$, since newly recruited MDMs enter the lesion at the endothelium with neutral phenotype. At slightly later times ($t = 1$), $m^\phi(x,t)$ skews towards $\phi > 0$ and $x = 1$. This reflects how MDMs become exposed to inflammatory mediators, produced by rLDL-induced resident signalling or rLDL uptake by other MDMs, as they diffuse into the lesion. The variation in ϕ for fixed x is smaller

towards $x = 1$, since fewer newly recruited MDMs with $\phi = 0$ are present deep in the lesion. This trend is prominent for $t = 1$, but is less notable at the later times $t = 5, 100$ when there is also substantial modulation towards resolving phenotypes.

The solutions in Fig. 7.2 for $(L^\star, H^\star) = (3, 2)$ differ from the unhealthy case in Fig. 7.1 in several aspects. First, we observe substantially smaller lipid densities, $L_{\text{tot}}(x, t)$ (Fig. 7.2(a)), smaller MDM densities, $M(x, t)$, (Fig. 7.2(b)), and lower MDM lipid loads (Fig. 7.2(c)). The MDM phenotype-spatial distribution $m^\phi(x, t)$, shown in Fig. 7.2(d), becomes skewed towards $\phi > 0$ at $t = 1$ before transitioning to a distribution centred about $\phi = 0$ at $t = 5, 100$. This reflects an early period of inflammatory phenotype modulation, followed by resolution towards a steady state with an even balance of inflammatory to resolving MDMs. Overall, there is limited spatial variation in MDM phenotype after early times $t > 1$.

We further investigate the model dynamics by plotting the spatial averages of the dependent variables in Fig. 7.3. More specifically, we define the integrals

$$\overline{f}(t) := \int_0^1 f(x, t)dx, \tag{7.85}$$

for $f \in \{M, \Phi_M, L_M, S_\pm, \mathbf{L}\}$. The quantities: $\overline{\hat{\Phi}}_M$ and $\overline{\hat{L}}_M$, that appear in plots (b) and (g) are the normalised mean phenotype and lipid content across the whole lesion, respectively:

$$\overline{\hat{\Phi}}_M := \frac{\overline{\Phi}_M}{\overline{M}}, \qquad\qquad \overline{\hat{L}}_M := \frac{\overline{L}_M - \overline{M}}{\kappa \overline{M}}. \tag{7.86}$$

These are related to the normalised mean phenotype and lipid content at x:

$$\hat{\Phi}_M(x, t) := \frac{\Phi_M(x, t)}{M(x, t)}, \qquad\qquad \hat{L}_M(x, t) := \frac{L_(x, t) - M(x, t)}{\kappa M(x, t)}, \tag{7.87}$$

via the relations

$$\overline{\hat{\Phi}}_M = \frac{1}{\overline{M}} \int_0^1 M(x, t)\hat{\Phi}_M(x, t)dx, \qquad \overline{\hat{\Phi}}_M = \frac{1}{\overline{M}} \int_0^1 M(x, t)\hat{L}_M(x, t)dx. \tag{7.88}$$

The quantity, $\overline{L} := \overline{L}_{\text{tot}} - \overline{L}_M$, in plots (d) and (i) is the extracellular lipid density. The solutions for $L^\star = 4$, $H^\star = 0.5$ are presented in the left column, and the solutions for $L^\star = 3$, $H^\star = 2$ in the right column. For $0 < t < 0.2$, we note from Figs. 7.3(e,f) that the model lesion undergoes an early phase of LDL infiltration and retention. The dynamics for $0.2 < t < 2$ are characterised by MDM influx (see Fig. 7.3(a,f)), lipid uptake and inflammatory phenotype modulation (see Fig. 7.3(b,g)). Inflammatory mediators dominate resolving mediators during this period (Fig. 7.3(c,h)). For $t > 2$, there is resolving phenotype modulation as the system tends to steady state, with resolving mediators dominating inflammatory mediators in the healthy case (see 7.3(c)).

There are several differences between Fig. 7.3 and the equivalent spatially homogeneous solutions of Fig. 5.3. First, we note from Figs. 7.3(d,e,i,j) that there is substantially more rLDL in the current model. This occurs because the LDL retention capacity

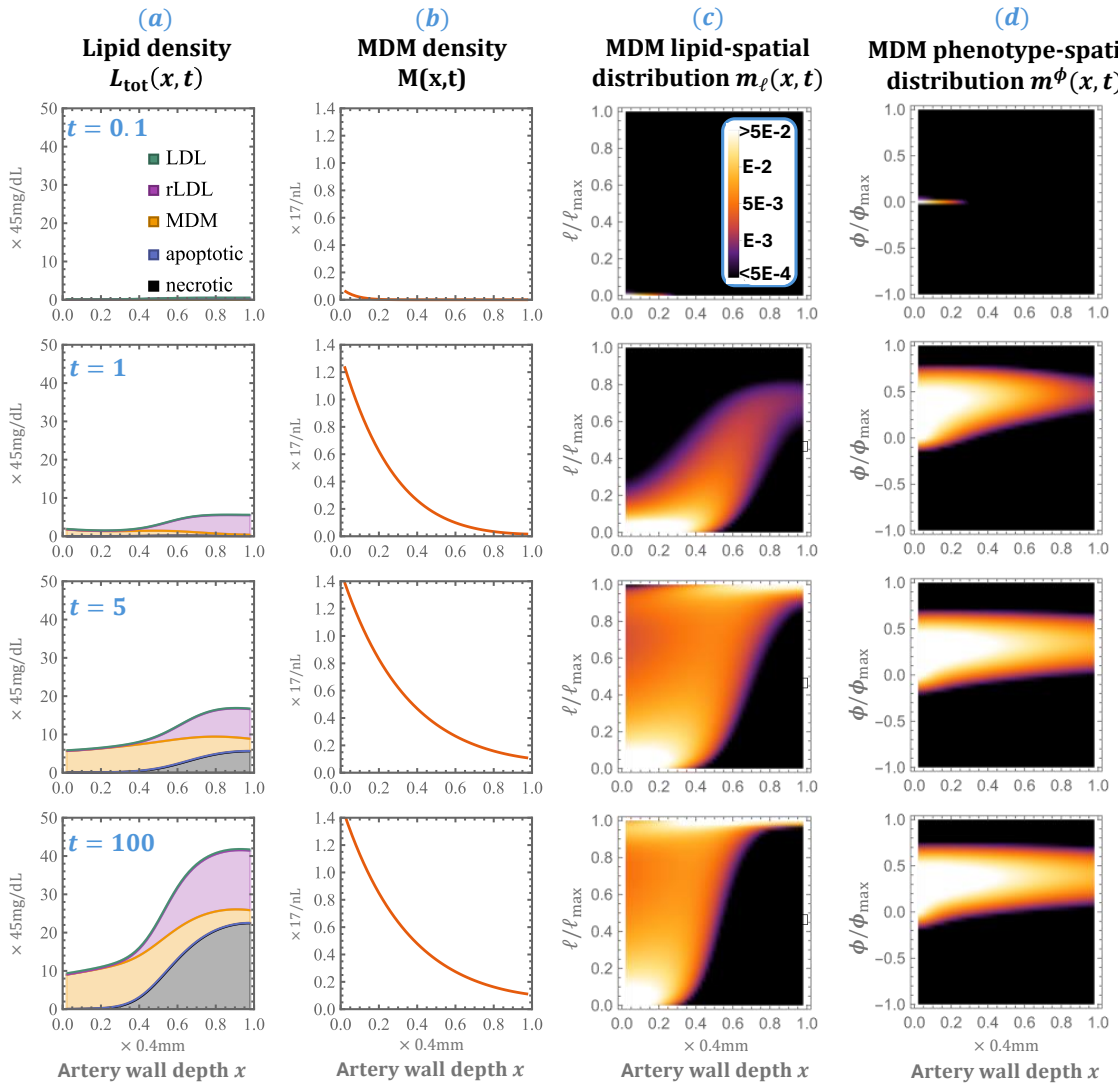


Figure 7.1: **Spatially-resolved dynamics for unhealthy blood levels of LDL lipid to HDL capacity: $L^\star = 4$, $H^\star = 0.5$.** We use numerical solutions to the lipid-structured subsystem (7.48)-(7.58), (7.63)-(7.66) to compute columns (a)-(c), and the phenotype-structured subsystem (7.48)-(7.58), (7.67)-(7.70) to compute column (d). Plot (a) shows the components of the total lipid density, $L_{\text{tot}}(x,t)$, defined in Eq. (7.84). Note how $m^\phi(x,t)$ skews to inflammatory phenotypes for $t \geq 1$ in column (d).

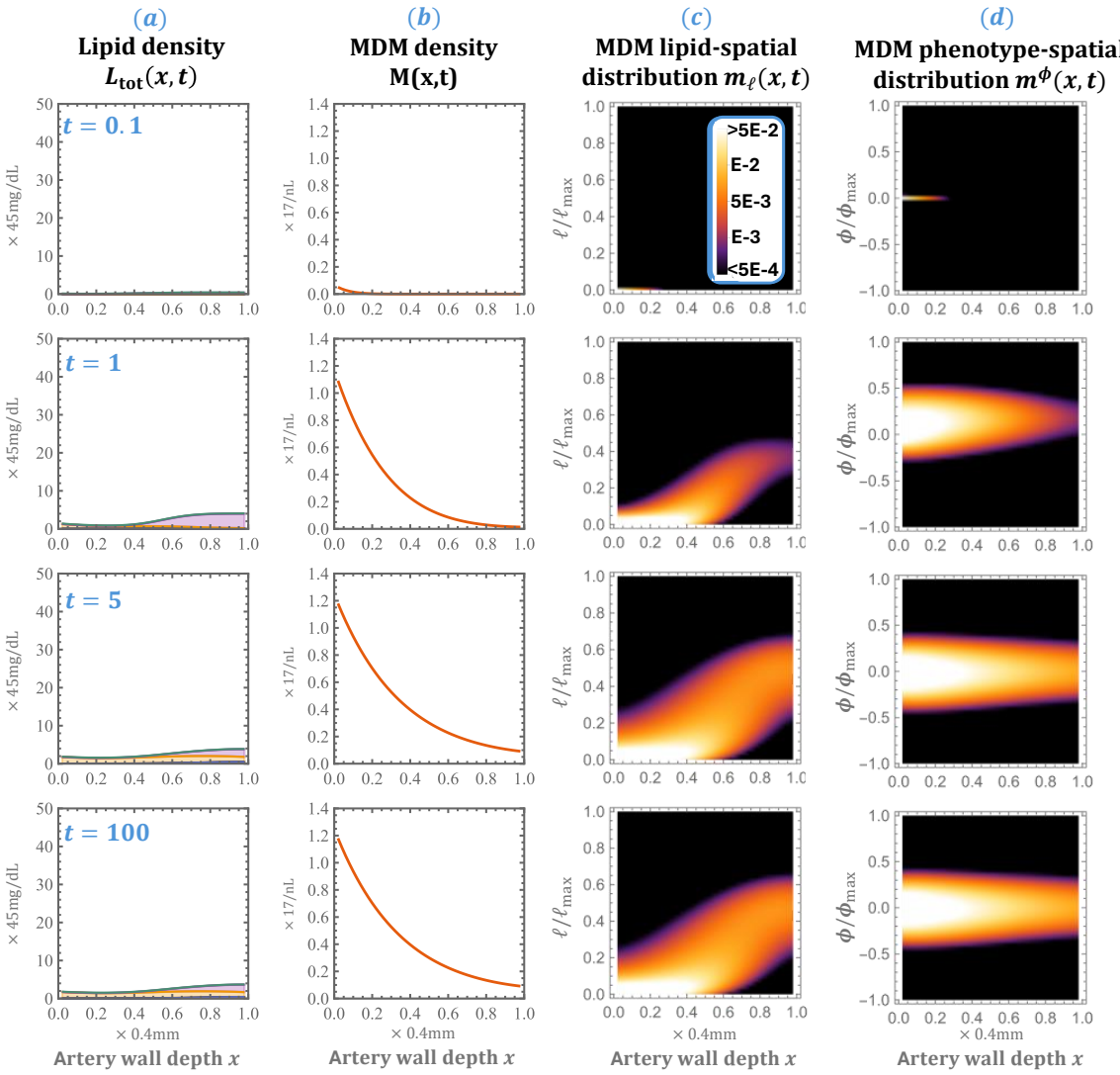


Figure 7.2: **Spatially-resolved dynamics for healthy blood levels of LDL lipid to HDL capacity:** $L^\star = 3$, $H^\star = 2$. We use numerical solutions to the lipid-structured subsystem (7.48)-(7.58), (7.63)-(7.66) to compute columns (a)-(c), and the phenotype-structured subsystem (7.48)-(7.58), (7.67)-(7.70) to compute column (d). Plot (a) shows the components of the total lipid density, $L_{\text{tot}}(x,t)$, defined in Eq. (7.84). Note how, in column(d), $m^\phi(x,t)$ skews to inflammatory phenotypes $\phi > 0$ at $t = 1$ before resolving towards an even balance of inflammatory and resolving MDMs at later times.

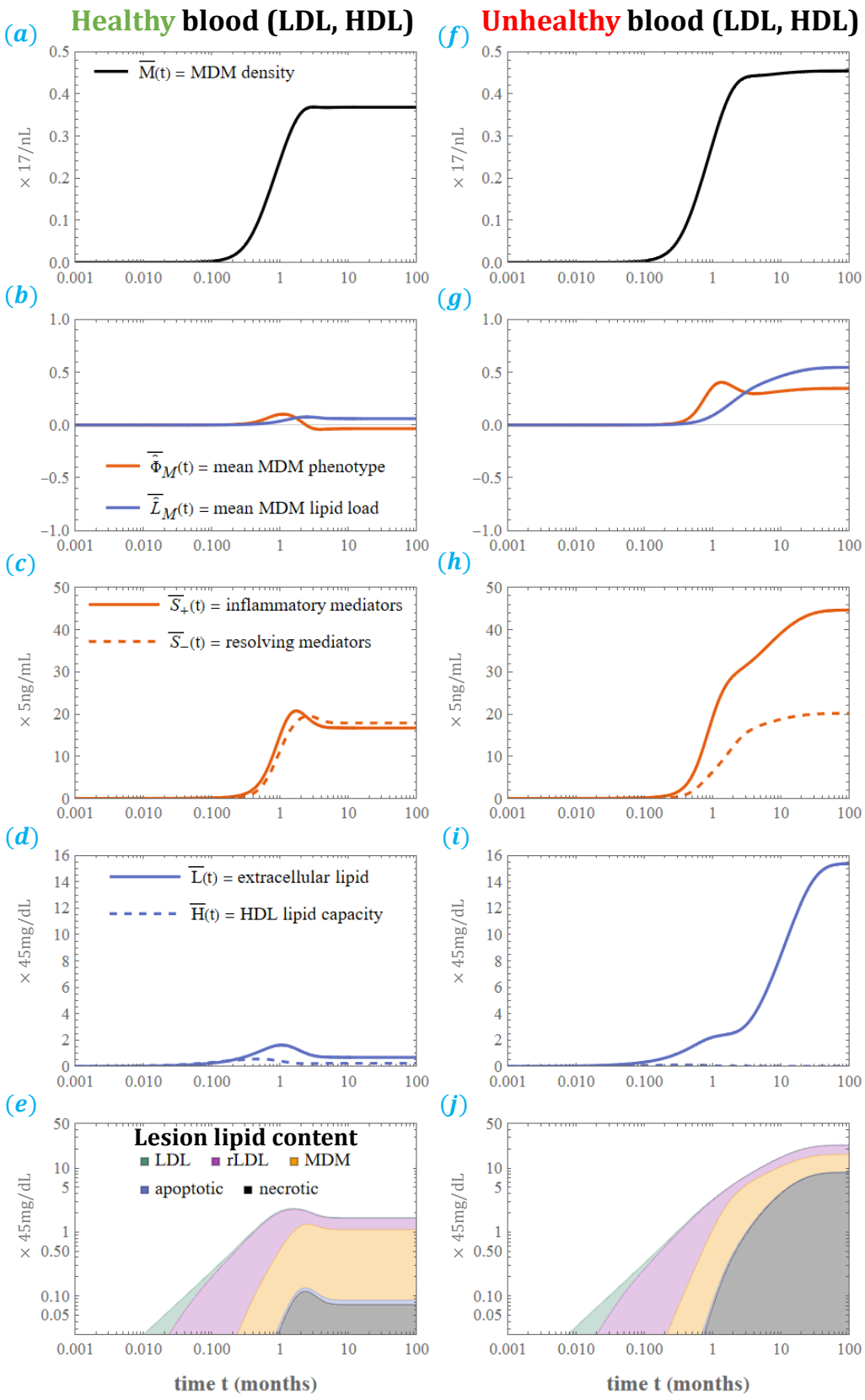


Figure 7.3: **Spatially averaged lesion composition dynamics.** The plotted quantities are spatial averages of the model dependent variables, defined in Eq. (7.85). Solutions for the case $(L^\star, H^\star) = (3, 2)$, representing the model response to healthy blood LDL and HDL levels, are shown in the left column. Solutions for $(L^\star, H^\star) = (4, 0.5)$, corresponding to unhealthy blood LDL and HDL levels, are shown in the right column.

is greater deeper in the lesion (recall Eq. (7.54) for $K_{\mathrm{r}}(x)$). Since the free LDL diffusivity exceeds that of MDMs (from Table 7.2: $D_{LDL} = 58 > D_M = 0.12$), fewer MDMs reach the deeper portions of the intima, where rLDL is most dense. Hence, in terms of spatial averages, less rLDL is accessible per MDM in the current model than in the spatially homogeneous model of Chapter 5. Second, the mean MDM density, $\overline{M}(t)$, is lower in the current model. This occurs because the density of inflammatory mediators attains its maximum value deep in the lesion (spatial profile not shown), where the rLDL density is greatest. A portion of these mediators decay as they diffuse towards the endothelium, $x = 0$. The rate of MDM influx is therefore lower than for the spatially homogeneous model of Chapter 5, where all inflammatory mediators contribute to MDM influx. Third, Fig. 7.3(e) shows that total lesion lipid content may decrease as the system tends to steady state. Although the reasons for this are not clear, Fig.7.3(b) shows that the decrease in $\overline{L}_{\mathrm{tot}}(t)$ is accompanied by a reduction in mean lipid load, $\overline{\hat{L}}_M(t)$. Hence, this effect may arise because most MDMs in the current model do not penetrate deep into the lesion where lipid levels are greatest, allowing the rate of efflux to eventually exceed that of uptake in the current model. Finally, Figs. 7.3(b,g) indicate that mean MDM phenotype is more inflammatory in the current model. This is likely due to the greater rLDL density in the current model, and, therefore, increased inflammatory mediator production by resident signalling. Nonetheless, Fig. 7.3(e) confirms that the phenotype distribution of Fig. 7.2(d) at $t = 100$ (near steady state) is resolving on average: $\overline{\hat{\Phi}}_M < 0$.

Steady state. The time-dependent solutions show that the model tends to a steady state as $t \to \infty$. We discuss below how this steady state changes as the blood densities of LDL lipid, $L^\star$, and HDL capacity, $H^\star$, are varied.

Fig. 7.4 shows how the steady state MDM phenotype-spatial distribution, $m^\phi(x)$, depends on $L^\star$ and $H^\star$. The plots show solutions to the phenotype-structured subsystem (7.48)-(7.58), (7.67)-(7.70) at steady state, computed using the *FindRoot* routine in Mathematica. We find that the mean phenotype at each position, $\hat{\Phi}_M(x)$, exhibits three distinct qualitative behaviours, summarised in Fig. 7.4(e). For sufficiently small $L^\star$ and large $H^\star$, $\hat{\Phi}_M(x)$ is monotone decreasing; when HDL capacity dominates LDL lipid in the blood, the MDMs deeper in the lesion are more resolving in phenotype than those near the endothelium. For intermediate values of $L^\star$, $0 < L^\star < 7$, and sufficiently large $H^\star$, $\hat{\Phi}_M(x)$ decreases from $x = 0$, attains a local minimum, and thereafter increases as $x \to 1$. We note that, in terms of spatial averages, these non-monotonic profiles are resolving: $\overline{\hat{\Phi}}_M < 0$. For $L^\star$ sufficiently large relative to $H^\star$, $\hat{\Phi}_M(x)$ is monotone increasing; when LDL lipid dominates HDL capacity in the blood, the MDMs deeper in the lesion are more inflammatory than those near the endothelium. An example of each case is shown in Fig. 7.4(a-c). The curve $\hat{\Phi}_M(x)$ is overlaid on each plot, and shown with smaller scale in Fig. 7.4(d).

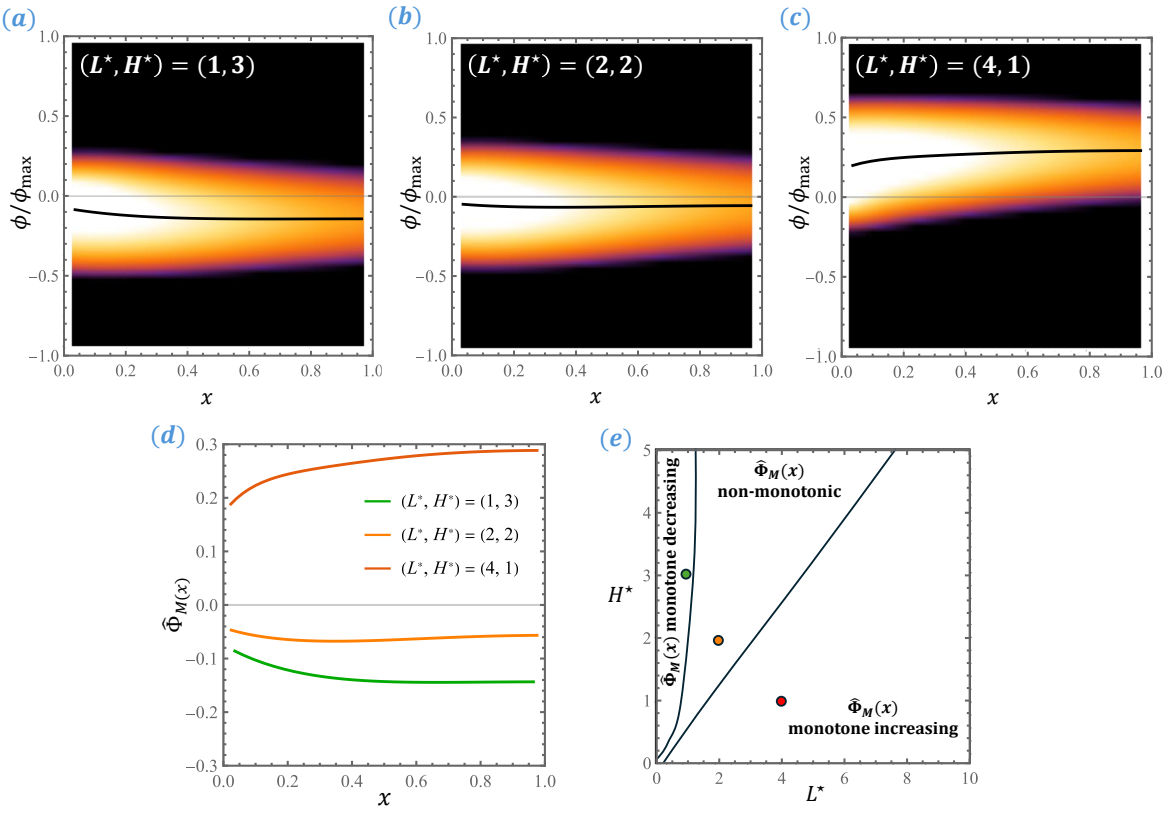


Figure 7.4: **MDM phenotype-spatial distribution at steady state.** Plots (a)-(c) show the steady state value of $m^\phi(x)$ for $(L^\star, H^\star) = (1, 3), (2, 4)$ and $(4, 1)$, computed by solving the phenotype-structured subsystem (7.48)-(7.58), (7.67)-(7.70) at steady state. The mean phenotype at each position, $\hat{\Phi}(x)$, is overlaid on plots (a)-(c) and plotted with smaller scale in (d). Plot (e) shows how the behaviour of $\hat{\Phi}(x)$ depends on the blood densities $L^\star$ and $H^\star$.

Fig. 7.5 shows how the spatial averages of the model outputs depend on $L^\star$ and $H^\star$. The plots show solutions to the minimal subsystem (7.48)-(7.58), (7.71)-(7.76) at steady state, using the *FindRoot* routine in Mathematica, across a grid of values $(L^\star, H^\star) \in (0, 10) \times (0, 5)$ with resolution 0.2×0.1. As expected, mean MDM density, $\overline{M}$, MDM phenotype, $\overline{\hat{\Phi}}_M$, MDM lipid content, $\overline{\hat{L}}_M$, and lesion lipid content, $\overline{L}_{\text{tot}}$, each increase with $L^\star$ and decrease with $H^\star$. By contrast, mean HDL capacity, $\overline{H}$, decreases with $L^\star$ and increases with $H^\star$. There are several differences between Fig. 7.5 and the equivalent steady state results of Fig. 6.13 for the spatially homogeneous model in Chapter 5. The current model exhibits lower MDM densities, $\overline{M}$, due to the decay of inflammatory mediators as they diffuse towards the endothelium. Total lesion lipid content is also lower due to the lesser influx of MDM endogenous lipid. A further discrepancy is that the mean MDM phenotype is greater (i.e., more inflammatory) in the current model. Indeed, the contour $\overline{\hat{\Phi}}_M = 0$ passes through the origin in Fig. 7.5, whereas in Fig. 5.5 the same contour passes through $(L^\star, H^\star) \approx (1, 0)$. To leading order, the dependence on $L^\star$ and $H^\star$ in the current model is approximately linear, of the form $0.66L^\star - H^\star = \text{constant}$; this dependence is steeper than that in Fig. 5.5, which approximately takes the form $0.4L^\star - H^\star = \text{constant}$.

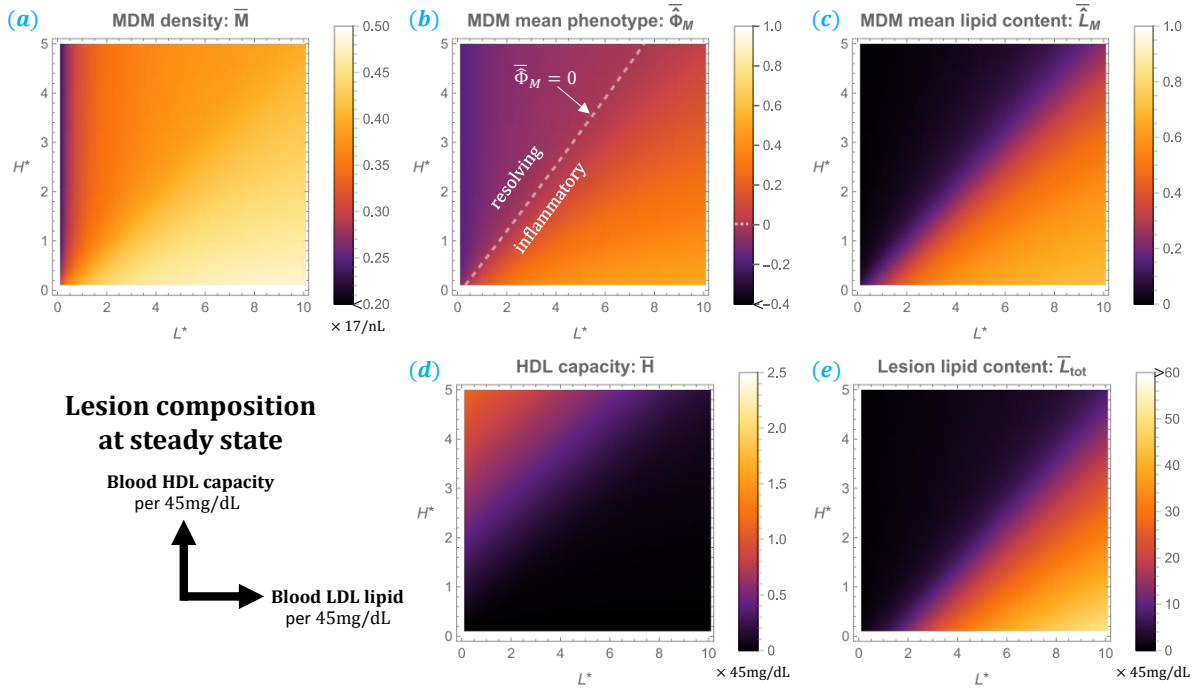


Figure 7.5: **Steady state lesion composition as blood LDL lipid ($L^\star$) and HDL capacity ($H^\star$) are varied.** The plots show solutions to the minimal subsystem (7.48)-(7.58), (7.71)-(7.76) at steady state across a grid of values $(L^\star, H^\star) \in (0, 10) \times (0, 5)$ with resolution 0.2×0.1. The plotted quantities are spatial averages, defined by Eq. (7.85). Note how lesion composition becomes more pathological as $L^\star$ increases and $H^\star$ decreases.

7.3.2 Lipid-dependent MDM mobility and lifespan: $\psi_D, \psi_\beta > 0$

In this section, we analyse the model behaviour when MDM mobility and lifespan depend on lipid content. As in Chapter 6, the values of $0 \leq \psi_D \leq 1$ and $0 \leq \psi_\beta \leq 1$, which determine the sensitivity to lipid content of MDM mobility and lifespan, respectively, are crucial in producing results that are in good qualitative agreement with the Nakashima images shown in Fig. 6.1. All simulations presented in this section are solutions of the lipid-structured subsystem (7.48)-(7.58), (7.63)-(7.66).

Fig. 7.6 shows a time-dependent solution for $\psi_D = 1$ and $\psi_\beta = 0.1$. We assume $L^\star = 4$ and $H^\star = 0.5$ so that LDL lipid dominates HDL capacity in the blood. Columns (a) and (b) show that, as the lesion develops, the lipid and MDM densities eventually attain internal global maxima. The plots in column (c) show that mean MDM phenotype, $\hat{\Phi}_M(x,t)$ and lipid content, $\hat{L}_M(x,t)$, increase with x for all times $t > 0$; MDMs deeper in the lesion are more lipid-laden and inflammatory. We note that $\hat{L}_M \approx 1$ for $x > 0.5$, indicating that MDMs in the deeper half of the intima are near their capacity for lipid content. Compared to the equivalent phenotype-independent simulation of Chapter 6, shown in Fig. 6.11, the current model exhibits greater lipid densities, $L_{\text{tot}}(x,t)$, and MDM densities, $M(x,t)$, near $x = 0$, but comparable values near $x = 1$.

In Fig. 7.7, we show how the qualitative behaviour of M and L_{tot} at steady state depends on ψ_D and ψ_β. Again, we set $L^\star = 4$ and $H^\star = 0.5$ so that LDL lipid dominates HDL capacity in the blood. Consistent with Fig. 6.12 for the spatial lipid-structured

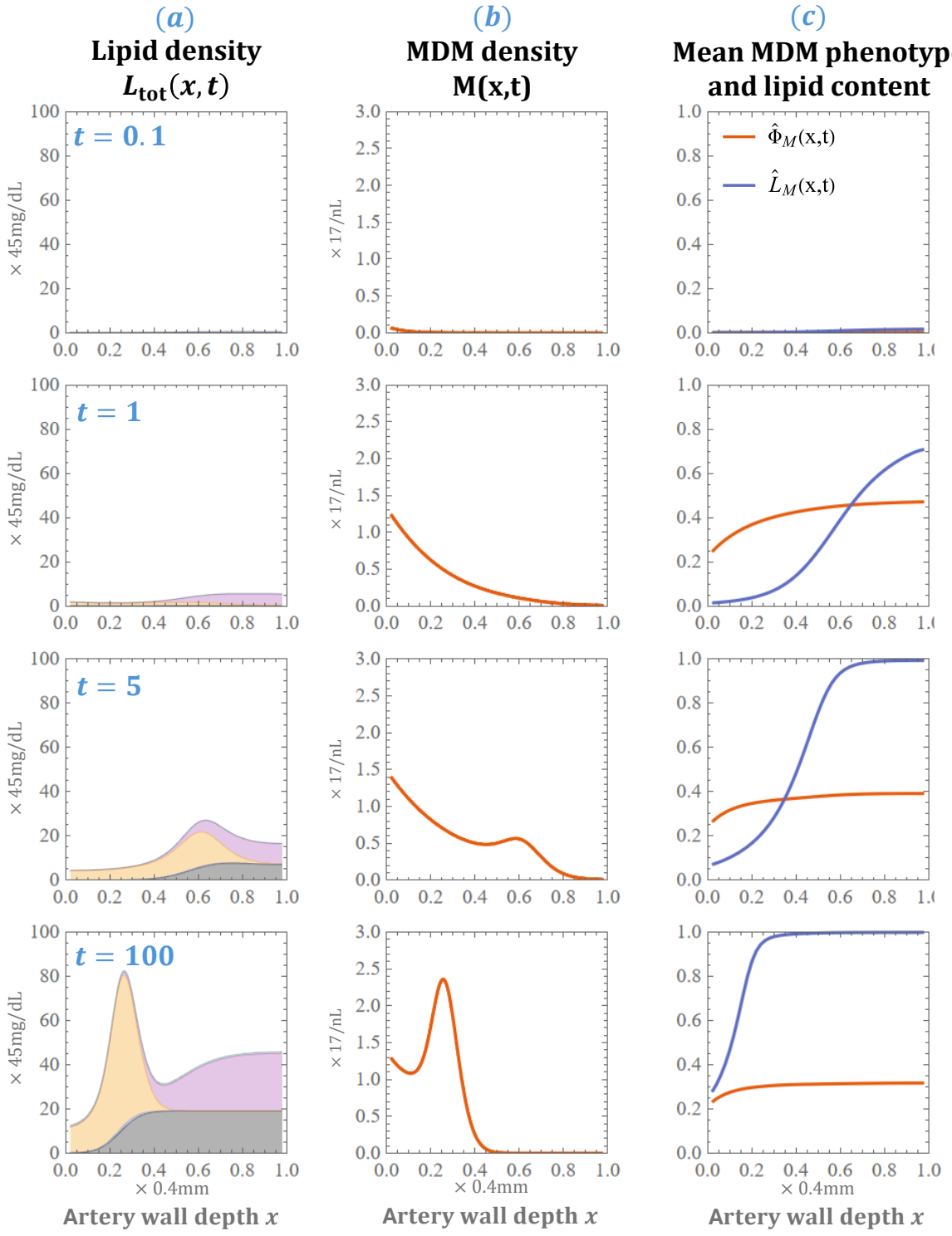


Figure 7.6: **Model dynamics when MDM mobility and lifespan depend on lipid content:** $\psi_D = 1$, $\psi_\beta = 0.1$. The plots show solutions for $L^\star = 4$ and $H^\star = 0.5$ of the lipid-structured subsystem (7.48)-(7.58), (7.63)-(7.66). Note the global internal maxima in the total lipid density, $L_{\text{tot}}(x,t)$, and MDM density, $M(x,t)$, at $t = 100$ (near steady state), consistent with the Nakashima images for PIT with foam cells in Fig. 6.1.

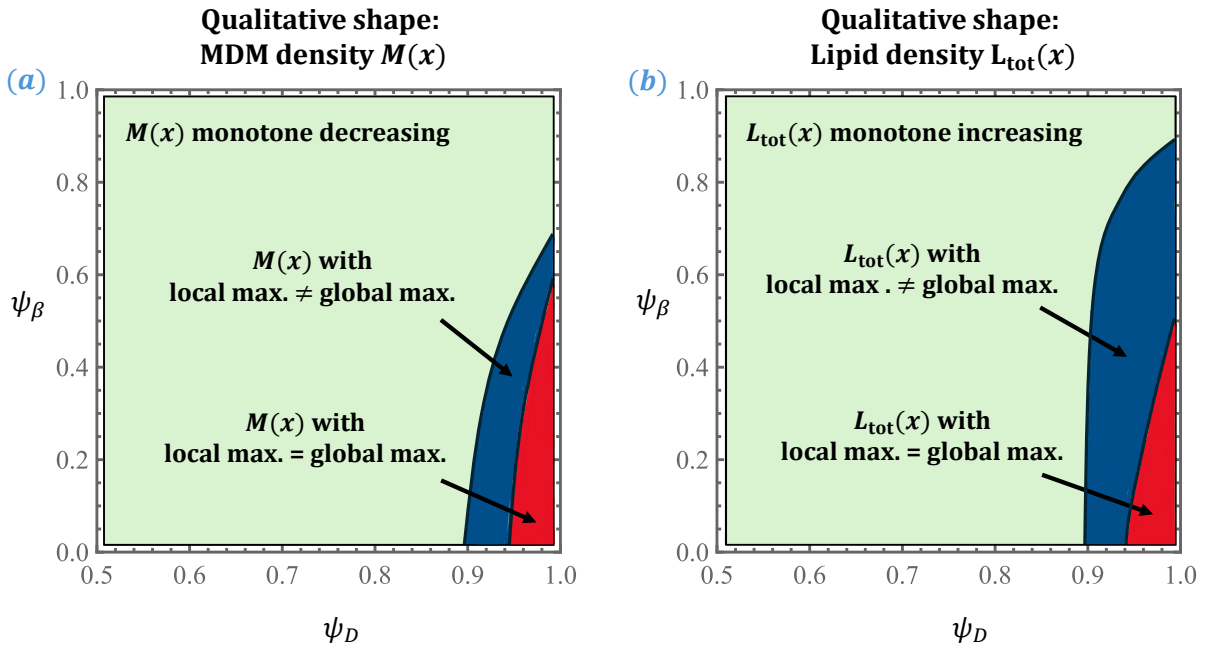


Figure 7.7: **Qualitative behaviour of the steady state MDM density, $M(x)$, and lesion lipid density, $L_{\text{tot}}(x)$, as the sensitivities ψ_D and ψ_β are varied.** The plots represent steady state solutions for $L^\star = 4$ and $H^\star = 0.5$ of the lipid-structured subsystem (7.48)-(7.58), (7.63)-(7.66). Note how the region for which global internal maxima exist in both $M(x)$ and $L_{\text{tot}}(x)$ is larger than the equivalent region for the model in Chapter 6 without phenotype resolution (c.f. Fig. 6.12).

model in Chapter 6, the current model requires large values of $\psi_D > 0.95$ and sufficiently small values of $\psi_\beta < 0.4$ to produce internal global maxima in $M(x)$ and $L_{\text{tot}}(x)$. The regions for which internal global maxima arise are larger in the current model than in Chapter 6, especially for $L_{\text{tot}}(x)$ (compare Figs. 7.7(b) and 6.12(b)). That is, the current model qualitatively reproduces the Nakashima images across a wider range of values for ψ_D and ψ_β.

We conclude this section by exploring how the steady state results in Sect. 7.3.1 for $\psi_D = \psi_\beta = 0$ differ relative to the case $\psi_D = 1$, $\psi_\beta = 0.1$. These values yield global internal maxima in the MDM and lipid densities at steady state. Fig. 7.8 shows how the decomposition of $(L^\star, H^\star)$ space according to the qualitative behaviour of mean MDM phenotype, $\hat{\Phi}(x)$, is minimally impacted by the introduction of lipid content-dependence. This is unsurprising since solutions with decreasing or non-monotonic $\hat{\Phi}(x)$ do not exhibit mean MDM lipid loads near capacity (compare Figs. 7.8(b) and 7.5(c)). Hence, the decrease in MDM mobility and lifespan, relative to the case $\psi_D = \psi_\beta = 0$, is expected to be small. Interestingly, Fig. 7.8(a) indicates that the solution $\hat{\Phi}_M(x)$ for $(L^\star, H^\star) = (4, 1)$ becomes smaller than the $\psi_D = \psi_\beta = 0$ case for large x. This likely occurs because, relative to the $\psi_D = \psi_\beta = 0$ case, there are fewer MDMs deeper in the lesion, and so lesser rLDL-stimulated inflammatory mediator production.

Fig. 7.9 summarises the steady state composition of the model lesion when $(\psi_D, \psi_\beta) = (1, 0.1)$. Compared to the case $\psi_D = \psi_\beta = 0$ (dashed), the solutions exhibit greater mean

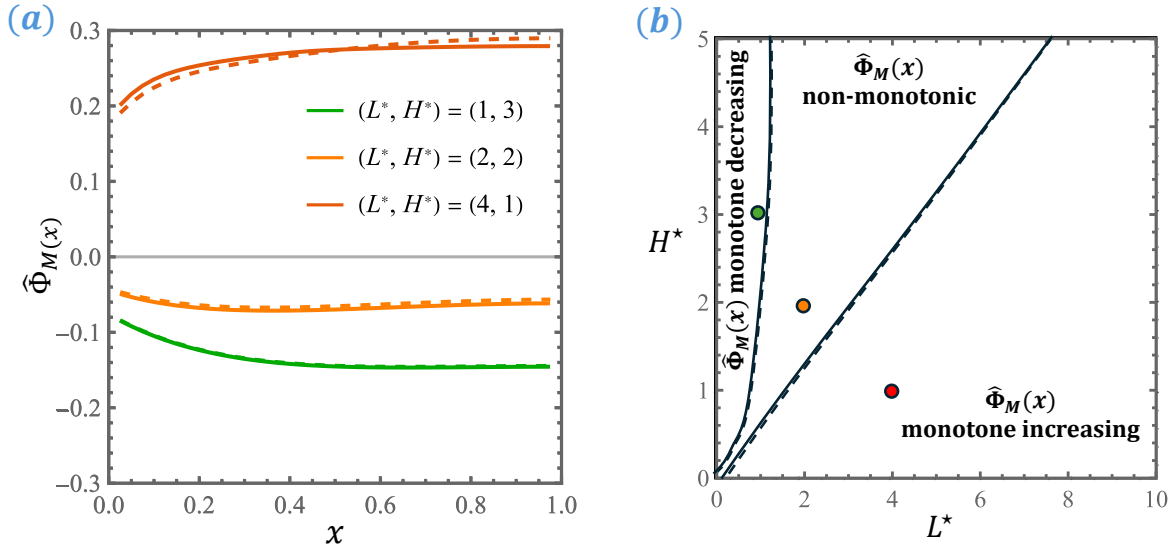


Figure 7.8: **MDM phenotype-spatial distribution at steady state when MDM mobility and lifespan depend on lipid content:** $\psi_D = 1$, $\psi_\beta = 0.1$. The plots show solutions to the lipid-structured subsystem (7.48)-(7.58), (7.63)-(7.66) at steady state. The results for $\psi_D = \psi_\beta = 0$ in Figs. 7.4(d) and (e) are overlaid with dashed curves in plots (a) and (b), respectively. These differ minimally from the solutions for $\psi_D = 1$, $\psi_\beta = 0.1$ (solid).

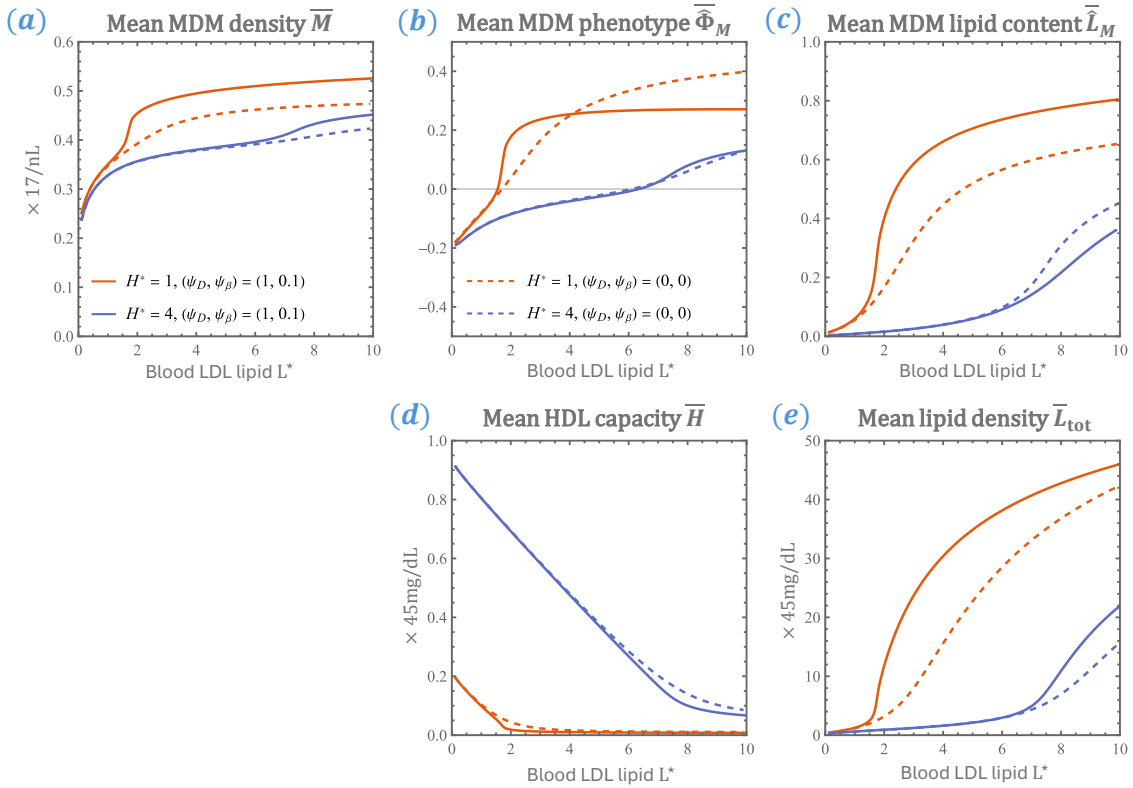


Figure 7.9: **Steady state lesion composition when MDM mobility and lifespan depend on lipid content:** $\psi_D = 1$, $\psi_\beta = 0.1$. The plots show solutions to the lipid-structured subsystem (7.48)-(7.58), (7.63)-(7.66) at steady state for $H^\star = 1$ (red) and $H^\star = 4$ (blue). Dashed curves represent solutions for $(\psi_D, \psi_\beta) = (0, 0)$. Note how introducing lipid content-dependence to MDM mobility and lifespan may decrease MDM phenotype for large $L^\star$ when $H^\star = 1$.

MDM densities, $\overline{M}$, mean MDM lipid contents, $\overline{\hat{L}}_M$, and lesion lipid densities, $\overline{L}_{\rm tot}$, and smaller mean HDL capacities, $\overline{H}$. The mean MDM phenotype, $\overline{\hat{\Phi}}_M$, is higher (i.e., more inflammatory) for $L^\star$ sufficiently small and is lower (i.e., more resolving) for $L^\star$ sufficiently large. The transition occurs at $L^\star \approx 9.5$ for $H^\star = 4$ and $L^\star \approx 4$ for $H^\star = 1$. This behaviour is also likely to be due to the reduction in MDM numbers deep in the lesion and the consequent lesser production of rLDL-stimulated inflammatory mediators.

7.4 Discussion

In this chapter, we have developed a spatially-resolved and phenotype-lipid structured model for MDM populations in early atherosclerosis. We consider a one-dimensional Cartesian domain, $0 \leq x \leq X$, which represents distance from the endothelium. MDM phenotype and lipid content are treated using discrete indices, $\phi = 0, \pm 1, \ldots, \pm\phi_{\max}$, and $\ell = 0, 1, \ldots, \ell_{\max}$, respectively, to allow for incremental changes in MDM internal state. The model couples the MDM dynamics, $m_\ell^\phi(x,t)$, to the densities of free LDL lipid, $L_{\scriptscriptstyle LDL}(x,t)$, retained LDL lipid, $L_{\rm r}(x,t)$, apoptotic lipid, $L_{\rm ap}(x,t)$, necrotic lipid, $L_{\rm n}(x,t)$, HDL capacity, $H(x,t)$, inflammatory mediators, $S_+(x,t)$, and resolving mediators, $S_-(x,t)$.

The full model is computationally expensive to solve due to the large number of dependent variables. Consequently, our analysis focused exclusively on solutions to closed subsystems that may be solved independently of the full model. This includes a lipid-structured subsystem where the extracellular variables above are coupled to the lipid-structured marginal MDM density, m_ℓ, and aggregate phenotype, Φ_ℓ. The lipid-structured subsystem is closed for all parameter values. Two further closed subsystems exist when MDM mobility and lifespan are independent of lipid content. This includes a phenotype-structured subsystem where the extracellular variables are coupled to the marginal phenotype-structured MDM density, m^ϕ, and aggregate lipid content, L^ϕ, and a minimal subsystem that casts the MDM population in terms of its aggregate density, M, phenotype, Φ_M, and lipid content, L_M. We note that the closure of the lipid-structured subsystem depends on the lack of phenotype dependence in the rates of lipid uptake, lipid efflux, MDM motion and apoptosis. If these processes are made to depend on ϕ, then the PDE for L^ϕ becomes coupled to higher order moments of m^ϕ, whose dynamics depend on consecutively higher order moments.

The model analysis in Sect. 7.3 focused on the impact of two key parameters, $L^\star$, and $H^\star$, which determine the blood densities of LDL lipid and HDL capacity, respectively. As these values depend on lifestyle choices, such as diet and exercise, we considered their impact across a range of plausible values: $L^\star \in (0, 10)$ and $H^\star \in (0, 5)$, with upper bounds corresponding to 450 mg/dL and 225 mg/dL, respectively. We also analysed the impact of the parameters $\psi_D \in [0,1]$ and $\psi_\beta \in [0,1]$ which determine the sensitivities of MDM mobility and mean lifespan to lipid content, respectively. We fixed the remaining

parameters to the values listed in Table 7.1. Since these estimates carry high degrees of uncertainty, our analysis focussed on qualitative trends rather than quantitative predictions. We discuss our findings below in relation to the key questions posed in Sect. 7.1.

Q1. **How does MDM phenotype vary with spatial depth?**

Time-dependent solutions in Sect. 7.3.1 indicate that the MDM phenotype-spatial distribution, $m^{\phi}(x,t)$, evolves in a manner sensitive to $L^{\star}$ and $H^{\star}$. At early times, most MDMs exhibit a neutral phenotype and are located near the endothelium. As the MDM population moves deeper into the intima, the MDMs furthest from the endothelium adopt a phenotype that is, on average, more inflammatory, than the MDM phenotype near the endothelium. This inflammatory phenotype modulation is likely due to exposure of MDMs to inflammatory mediators produced in response to rLDL, including rLDL-stimulated signalling by resident cells and mediator production by MDMs upon rLDL uptake. Since rLDL is retained in greater capacity deeper in the lesion, MDMs furthest from the endothelium are likely to undergo the highest levels of inflammatory phenotype modulation. At later times, the MDM population undergoes a period of resolving phenotype modulation as resolving mediators begin to accumulate in response to apoptotic lipid uptake and lipid efflux to HDL. During this time, the lesion develops a more spatially uniform distribution of phenotype, consisting of inflammatory to neutral cells if the blood LDL to HDL balance is unhealthy (i.e., $L^{\star} \gg H^{\star}$), and an even balance of inflammatory to resolving cells when the blood LDL to HDL balance is more healthy. Finally, as the model tends to steady state, lesions with unhealthy LDL to HDL balance undergo further inflammatory phenotype modulation due to DAMPs released from secondary necrosis. Although necrosis is more prevalent deep in the lesion, this effect does not cause a noticeable change to the spatial variation in phenotype.

Steady state analysis indicates that the spatial distribution of the mean MDM phenotype at equilibrium, $\hat{\Phi}_M(x)$, may adopt one of three qualitative behaviours depending on the values of $L^{\star}$ and $H^{\star}$. When HDL capacity dominates LDL lipid in the blood ($H^{\star} \gg L^{\star}$), $\hat{\Phi}_M(x)$ is monotone decreasing, which means that MDMs deeper in the lesion have a more resolving phenotype than those near the endothelium. When $L^{\star}$ and $H^{\star}$ are comparable there is an intermediate regime where $\hat{\Phi}_M(x)$ attains a local minimum. We note that spatial variation of phenotype is limited in these solutions; MDMs exhibit a similar and mildly resolving mean phenotype at all positions. Finally, when LDL lipid dominates HDL capacity in the blood ($L^{\star} \gg H^{\star}$), $\hat{\Phi}_M(x)$ is monotone increasing, and so MDMs deeper in the lesion have a more inflammatory phenotype than those near the endothelium. This result is consistent with reports that late lesions, which presumably develop in response to unhealthy blood LDL to HDL balances, contain predominantly inflammatory MDMs near the

necrotic core and a more even balance of inflammatory and resolving MDMs near the fibrous cap [111, 246].

The results in Sect. 7.3.2 indicate that the above characterisation of steady state mean MDM phenotype also holds when MDM mobility and lifespan depend on lipid content: $\psi_D, \psi_\beta > 0$. This is unsurprising since the transitions from monotone decreasing, non-monotonic and monotone increasing profiles for mean phenotype, $\hat{\Phi}_M(x)$, occur in regions of healthy blood LDL to HDL balance (approximately $H^\star > 0.66L^\star$) for which MDM lipid contents are low and, consequently, lipid content-dependent reductions in MDM mobility and lifespan are minimal.

Q2. **How does the addition of spatial resolution impact results concerning lesion composition in Chapter 5?**

We compared the time-dependent solutions for lesion composition of Chapter 5 to the time-evolution of the spatial averages of variables in the current model in Sect. 7.3.1. Our results indicate that the current model undergoes the same overall dynamical phases. Early times are characterised by the influx and retention of LDL. The subsequent influx of MDMs and wave of rLDL uptake drives increases to mean lipid content and modulation to inflammatory phenotypes. A period of resolving phenotype modulation follows due to resolving mediators produced via apoptotic lipid uptake and efflux to HDL. Finally, if the blood LDL to HDL balance is unhealthy, there is an additional phase of inflammatory phenotype modulation due to secondary necrosis as the lesion tends to steady state. There are, nonetheless, several differences between the current model output and the results of Chapter 5. The current model predicts greater amounts of rLDL and fewer MDMs, despite greater densities of inflammatory mediators relative to resolving mediators. These discrepancies arise because of the spatial dependence in rLDL retention capacity, which increases with depth in the lesion. The inflammatory mediators, produced primarily in the deep lesion due to rLDL stimulation, decay as they diffuse towards the endothelium and have lesser impact on MDM influx than in the well-mixed model of Chapter 5. In the healthy blood LDL to HDL case, the current model also predicts that lesion lipid content decreases towards steady state, in contrast to the monotone increasing trend found in Chapter 5. This behaviour may arise because most MDMs do not reach deep into the lesion where lipid levels are greatest. Hence, the rate of lipid efflux to HDL eventually exceed that of uptake, causing lipid levels to decrease with time.

The current model also exhibits the same overall qualitative dependence on $L^\star$ and $H^\star$ at steady state as the model of Chapter 5. Specifically, mean MDM density, MDM phenotype, MDM lipid content and lesion lipid content each increase with $L^\star$ and $H^\star$. By contrast, mean HDL capacity decreases with $L^\star$ and increases with $H^\star$. There are small discrepancies between the current model output and

equivalent results of Chapter 5. For instance, the current model predicts a more inflammatory mean MDM phenotype for the same values of $L^\star$ and $H^\star$. Further, the relative dependence on $L^\star$ and $H^\star$ in the current model is given by steeper contours approximately of the form $0.66L^\star - H^\star = \text{constant}$. Although it is not clear why these difference arise, it is unsurprising that changes to blood LDL lipid or HDL capacity would impact a spatially-resolved model differently than a spatially homogeneous model.

Q3. **How does the addition of phenotype resolution impact results concerning lipid-dependent MDM mobility and lifespan in Chapter 6?**

The results in Sect. 7.3.2 showed that the impact of introducing lipid content-dependence to MDM mobility and lifespan has a similar impact to the current model as to the model in Chapter 6. In particular, the current model can reproduce the global internal maxima in the MDM and total lipid densities seen in the Nakashima images (Fig. 6.1). However, the current model predicts greater MDM densities at early times compared to equivalent time-dependent solutions in Chapter 6. This is due to increased production of inflammatory mediators in the current model, which, in addition to resident signalling, accounts for rLDL uptake by MDMs and phenotype-dependent constitutive production. These inflammatory mediators promote MDM influx, which leads to further rLDL uptake and inflammatory mediator production in a positive feedback loop. The current model also exhibits a larger region in (ψ_D, ψ_β) space for which global internal maxima exist at steady state. That is, the phenotype-resolved model qualitatively reproduces the densities of the Nakashima images across a wider range of sensitivities for MDM mobility and lifespan than the model of Chapter 6. This is likely to be partially due to the increased MDM influx in the current model, which promotes accumulation of endogenous lipid near the endothelium. Finally, we note that introducing high sensitivities of MDM mobility to lipid content, which are necessary for global internal maxima formation, has a similar impact on steady state lesion composition in the current model as for the model in Chapter 6. Specifically, solutions for which MDM lipid content decreases rapidly with lipid content exhibit greater MDM densities, MDM mean lipid contents and total lipid densities, and lower HDL capacities relative to solutions for constant MDM mobility. Taken together, these results indicate that the qualitative observations concerning lipid content-dependent MDM lifespan and mobility are robust to the inclusion of phenotype resolution.

Conclusions. In this chapter, we have presented a new spatially-resolved and phenotype-lipid structured mathematical model for MDM populations in early human atherosclerotic lesions. The model indicates that mean MDM phenotype is more inflammatory deeper in the lesion at early times, but may adopt one of three qualitative spatial behaviours at

steady state. When HDL capacity dominates LDL lipid in the blood, mean MDM phenotype at steady state is more resolving deeper in the lesion than at the endothelium. When blood LDL lipid and HDL capacity are comparable, there is an intermediate regime where mean MDM phenotype depends non-monotonically with spatial depth. However, in these solutions spatial variation is minimal and the lesion exhibits an approximately uniform distribution of resolving phenotypes. When blood LDL lipid dominates HDL capacity, mean phenotype is more inflammatory deeper in the lesion than near the endothelium. Our results further indicate that trends concerning lesion composition in Chapter 5 and the impact of lipid content-dependent MDM mobility and mean lifespan in Chapter 6 are robust to the addition of spatial and phenotype resolution, respectively. Although we used the model primarily to explore spatial variation of MDM phenotype in this chapter, the model is readily adapted to explore additional effects, including cross-talk between MDMs and smooth muscle cells [247] and the impact of resolving mediator therapies [7, 248]. In the following and final chapter, we discuss these possibilities after summarising the findings of Chapters 4-7.

Chapter 8

Discussion and conclusions

In this thesis, we have developed a series of increasingly detailed structured population models to investigate how MDM heterogeneity may arise during early atherosclerosis. In this final chapter, we discuss how the analysis of these models has contributed to increasing understanding of lesion formation in early atherosclerosis. We summarise the key findings in Sect. 8.1, and discuss model limitations and future directions in Sect. 8.2.

8.1 Thesis summary

Atherosclerosis is a leading cause of death around the world [1]. A particular danger of this chronic inflammatory disease is the asymptomatic development of its early stages [2]. Our understanding of early atherosclerosis is hindered by the emergence of heterogeneity in lesion MDMs, which clouds their impact on disease development [7, 60]. MDM heterogeneity is driven by interactions between MDMs and the lesion microenvironment that promote cell-to-cell variation in lipid content, phenotype and spatial position. In this thesis, we have developed four structured population models to analyse the emergence and impact of MDM heterogeneity in early atherosclerotic lesions. We presented a new lipid-structured model in Chapter 4. We extended this model to account for phenotype resolution in Chapter 5, and spatial resolution in Chapter 6. Finally, we combined the models of Chapters 5 and 6 into a spatially-resolved phenotype-lipid structured model in Chapter 7. We summarise the contributions of these chapters below.

In **Chapter 4**, we considered a well-mixed lesion with an MDM population resolved by lipid content. We formulated the model as a system of ODEs that couples the MDM population to the densities of extracellular lipid and HDL lipid capacity. A key feature of the model that distinguishes it from other lipid-structured models in the literature [165, 166, 185], is the assumption that MDMs have a finite capacity for lipid and that their rate of lipid uptake depends on their available capacity. This property is consistent with observations of macrophage uptake *in vitro* [94]. Our analysis of time-dependent numerical solutions and asymptotic analysis of steady state solutions indicate that lesion composition is sensitive to the relative influx of LDL lipid and HDL capacity. The MDM lipid distribution evolves in a wave-like manner towards a steady state profile whose

qualitative form depends on the LDL lipid and HDL influxes. Lesions with unhealthy LDL to HDL balances give rise to distributions that attain a local maximum near the MDM lipid capacity, while distributions with healthy LDL to HDL balances may be monotone decreasing, quasi-uniform, or attain a local maximum at low lipid loads. Time-dependent solutions also show that the uptake rate of the MDM population diminishes substantially due to lipid ingestion as the lesion develops, even when the influx of LDL lipid is comparable to that of HDL capacity. We conclude that uptake feedback in MDMs due to high lipid loads is likely to contribute to defective efferocytosis in atherosclerotic lesions. Two aspects of our lipid-structured model warrant further comment.

First, the use of discrete structuring for lipid content is in contrast to the continuous structuring used in [165, 166, 185]. We use discrete structuring to avoid shock discontinuities that arise in the MDM lipid distribution in the equivalent continuous formulation. These discontinuities can be seen in the steady state outer solutions shown in Fig. 4.10 at the lipid content $a = a_c$ where the rate of lipid uptake equals that of efflux. Such discontinuities do not arise in earlier lipid-structured models since they assume that lipid uptake and efflux occur at rates independent of lipid content, but this is at odds with biological observations of finite MDM lipid capacity [94]. In the model of Chapter 4, discrete structuring contributes a regularising effect that manifests as a diffusion term in the continuum approximation of the MDM lipid distribution dynamics. The diffusion term smooths the discontinuity in a small neighbourhood of the critical lipid content $a = a_c$.

Second, the minimalist formulation of the extracellular environment may be overly simplistic, particularly the treatment of extracellular lipid as a single species. In real lesions, extracellular lipid is found within free-diffusing LDL, retained LDL, apoptotic MDMs, and necrotic debris, each with different rates of uptake and effects on MDM mediator production. The implicit treatment of blood LDL and HDL levels via influx rates is also noteworthy. As clinical readouts, these quantities are desirable as explicit model components. Moreover, in practice, LDL and HDL diffuse into the lesion from the blood and may diffuse back into the lumen depending on their concentrations on either side of the endothelium. We addressed these issues in Chapters 5-7, where we formulated mathematical models under a common framework that resolves the above extracellular lipid species and accounts for blood LDL lipid and HDL capacity as explicit parameters.

In **Chapter 5**, we considered a well-mixed lesion with an MDM population resolved by (inflammatory) phenotype and lipid content. We formulated the model as a system of ODEs that couples the MDM population to the densities of free LDL lipid, retained LDL lipid, apoptotic lipid, necrotic lipid, HDL capacity, inflammatory mediators and resolving mediators. MDM phenotype is incorporated via an additional structure index/variable, representing the spectrum of values between the (inflammatory) M1 and (resolving) M2 polarisation states. We used the model to investigate the distribution of MDM phenotype, its correlation with MDM lipid content, and relation to the densities of LDL lipid and HDL capacity in the blood. The model reduces to a simpler, closed subsystem whose

analysis shows how lesion composition becomes more pathological as blood LDL lipid increases and HDL capacity decreases. We found that the MDM phenotype distribution always attains a local maximum, while the lipid content distribution may be unimodal, quasi-uniform or decrease monotonically. Asymptotic analysis of the MDM phenotype-lipid distribution showed that MDM phenotype and lipid content are correlated via a power law at steady state. This power law predicts that the more lipid-laden MDMs have a more inflammatory phenotype at steady state in lesions where LDL lipid dominates HDL capacity in the blood, and a more resolving phenotype than lipid-poor MDMs when HDL capacity dominates LDL lipid in the blood.

In **Chapter 6**, we considered a spatially resolved lesion with an MDM population resolved by lipid content only. We formulated the model as a system of PDEs that couples the MDM population to the densities of free LDL lipid, retained LDL lipid, apoptotic lipid, necrotic lipid, HDL capacity and inflammatory mediators. We treated space using a one-dimensional Cartesian variable that ranges from the endothelium to the internal elastic lamina. Motivated by images of lipid and macrophage densities in early human coronary artery lesions (Fig. 6.1), we introduced a spatially non-uniform LDL retention capacity to capture the early retention of LDL deep in the intima. We assumed for simplicity that MDMs undergo unbiased random motion, but allowed MDM mobility and mean lifespan to depend on lipid content. We found that the model qualitatively reproduces the global internal maxima in the Nakashima images (Fig. 6.1) only when the MDM mobility is sufficiently sensitive to lipid content, and MDM lifespan sufficiently insensitive. Introducing lipid content-dependence to MDM mobility and mean lifespan produced minimal impact on model behaviour at early times, but strongly impacted lesion composition at steady state. Increases in the sensitivity of MDM lifespan to lipid content yield lesions with fewer MDMs, less total lesion lipid and reduced mean MDM infiltration depth. Increases in the sensitivity of MDM mobility also reduce the MDM infiltration depth, but increase the proportion of lipid-laden MDMs. Across all simulations, regardless of the treatment of MDM mobility and lifespan, we found that mean MDM lipid content increases with spatial depth.

Finally, in **Chapter 7**, we considered a spatially resolved lesion with an MDM population resolved by phenotype and lipid content. We formulated the model as a system of PDEs that couples the MDM population to the densities of free LDL lipid, retained LDL lipid, apoptotic lipid, necrotic lipid, HDL capacity, inflammatory mediators and resolving mediators. We exploited various closed subsystems of the model to investigate the relationship between MDM phenotype and spatial depth. Time-dependent numerical solutions showed that mean MDM phenotype is more inflammatory deeper in the lesion at early times, but may adopt one of three qualitative spatial behaviours at steady state. When HDL capacity dominates LDL lipid in the blood, mean MDM phenotype at steady state is more resolving deeper in the lesion than at the endothelium. When blood LDL lipid and HDL capacity are comparable, there is an intermediate regime where mean

MDM phenotype depends non-monotonically on spatial depth. However, in these solutions spatial variation is minimal and the lesion exhibits a near-uniform distribution of resolving phenotypes. When blood LDL lipid dominates HDL capacity, mean phenotype is more inflammatory deeper in the lesion than near the endothelium, consistent with observations in late lesions [111, 246]. We also used the model to investigate the robustness of trends observed in Chapters 5 and 6 to the addition of spatial and phenotype resolution, respectively. We found that lesion composition depends on blood LDL and HDL levels in a similar manner to the model of Chapter 5, albeit with more sensitive dependence on blood LDL lipid relative to HDL capacity. We also found that, consistent with the results of Chapter 6, sufficiently high sensitivities of MDM mobility and low sensitivities of MDM lifespan to lipid content are required to produce the global internal maxima observed in the Nakashima images.

The analyses presented in Chapters 5-7 suggest that MDM lipid content, phenotype and spatial depth are not independently distributed in early atherosclerotic lesions. Rather, these three aspects of MDM heterogeneity are correlated in a manner dependent on blood LDL and HDL levels. Our findings for lesions at steady state are summarised in Fig. 8.1. For healthy scenarios where HDL capacity dominates LDL lipid in the blood, MDMs deeper in the lesion exhibit higher lipid contents and more resolving phenotypes. For unhealthy scenarios where LDL lipid dominates HDL capacity in the blood, MDMs deeper in the lesion exhibit higher lipid loads and more inflammatory phenotypes. As noted in Chapter 5, the correlation between lipid content and phenotype changes depending on blood LDL and HDL levels; the more lipid laden cells may be more inflammatory or resolving depending on blood lipoprotein content. Hence, these two aspects of MDM heterogeneity cannot be used as proxies for each other in a model seeking to account for both healthy and unhealthy balances of LDL and HDL in the blood. By contrast, (mean) lipid content increases with spatial depth, regardless of blood LDL and HDL levels.

8.2 Model limitations and future work

Atherosclerosis is a complex process that involves the dynamic coordination of both cellular and mechanical activity. It was therefore necessary to make many simplifying assumptions in the development of the models of Chapters 4-7. We discuss below how several key assumptions may be relaxed in future work.

- **Single cell species.** In our models, we focused exclusively on the dynamics of MDMs and neglected the role of other cell species. There is considerable scope to include the dynamics of other cell types. In particular, the inclusion of smooth muscle cells (SMCs) would allow us to account for the time evolution of LDL retention capacity, which we assumed to be static (but spatially non-uniform). In practice, SMCs contribute to the LDL retention capacity by secreting LDL-binding proteoglycans [249]. The inclusion of SMC-mediated growth in LDL retention capacity may

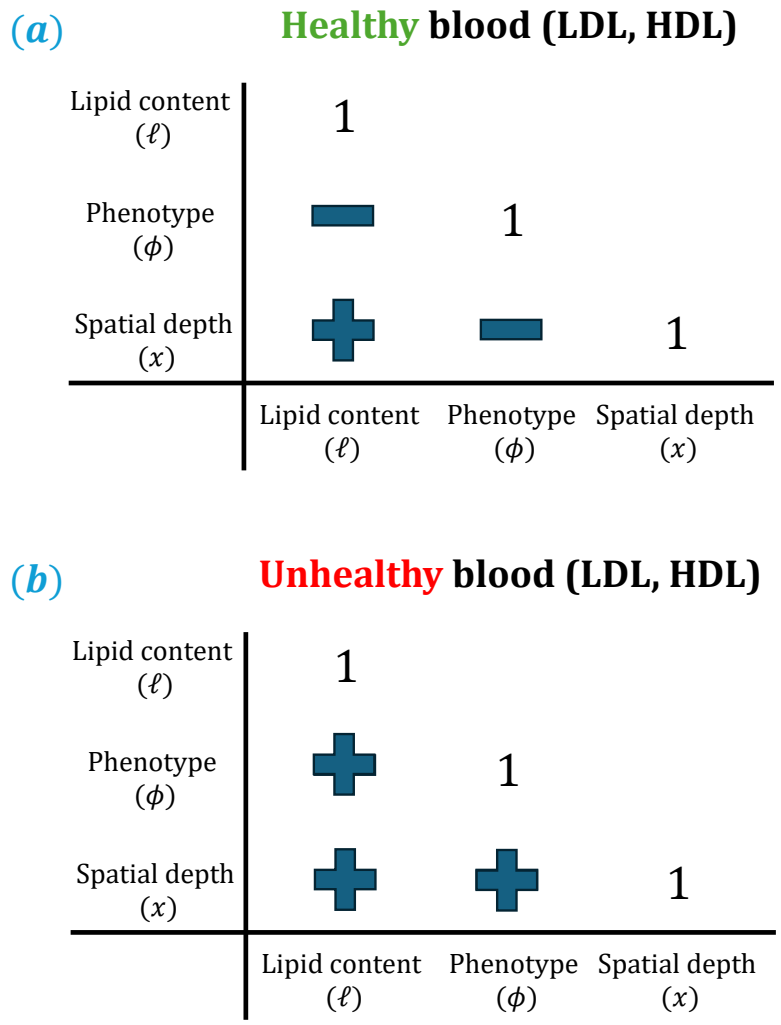


Figure 8.1: **Steady state correlations between the three aspects of MDM heterogeneity considered in this thesis.** Properties $a, b \in \{x, \phi, \ell\}$ are positively correlated (labelled '+') if MDMs with greater values of property a are more likely to exhibit greater values of property b (than other MDMs in the lesion) at steady state, and vice-versa. For instance, MDMs with greater spatial depth x are more likely to have higher lipid contents, ℓ. Conversely, MDMs with higher lipid loads are more likely to be deeper in the lesion. Properties $a, b \in \{x, \phi, \ell\}$ are negatively correlated (labelled '$-$') if MDMs with greater values of property a are more likely to exhibit lower values of property b, and vice-versa. For instance, in the healthy scenario where HDL capacity dominates LDL lipid in the blood, MDMs with greater lipid content, ℓ, or spatial depths, x, are likely to exhibit more resolving phenotypes, $\phi < 0$. Conversely, MDMs with a more inflammatory phenotype exhibit a lower lipid content and spatial depth. Trivial correlations are labelled '1'.

provide a slow timescale that increases the time to attain a steady state. In their current form, our models attain steady state solutions over timescales that range from months to years, which is consistent with mouse lesions, but fast compared to the decades-long development of human coronary atherosclerosis. Given that several *in vitro* studies suggest that SMCs take up excess lipids from macrophages and adopt a macrophage-like phenotype in response to lipid accumulation [250, 251], they may be most faithfully included within a lipid-structured setting. The role of SMCs in fibrous cap formation during mid-to-late stages has been explored using a multiphase framework by Watson *et al.* [149, 150]. Their results suggest that intimal SMC populations are primarily sustained by a balance between apoptosis and local proliferation, with infiltration from the media providing a smaller contribution.

- **Negligible local proliferation.** The inclusion of (local) proliferation in a lipid-structured population presents several difficulties. We neglected MDM proliferation in this thesis for simplicity, justified by observations that proliferation is limited in aortic macrophage populations [68], and may be more prominent in late rather than early lesions [252]. Proliferation induces a non-local effect on lipid content since the ingested lipid of the parent cell is split amongst two (or more) daughter cells upon division. An example of how proliferation may be incorporated in a lipid-structured framework is given in [166], where it is assumed that parent cell lipid content is divided evenly amongst two daughter cells at rate ρ, and that the additional endogenous lipid, a_0, required to produce two daughter cell membranes, is synthesised rapidly prior to division. In a discrete lipid-structured framework, the corresponding representation is based upon the reactions

$$m_\ell(x,t) \xrightarrow{\rho} \begin{cases} 2m_{\ell/2}(x,t) & \text{for } \ell = 0,2,4,\ldots; \\ m_{(\ell+1)/2}(x,t) + m_{(\ell-1)/2}(x,t) & \text{for } \ell = 1,3,5,\ldots, \end{cases} \tag{8.1}$$

which give rise to differential equations of the form

$$\frac{\partial m_\ell}{\partial t} = \rho\Big[\big(2m_{2\ell} + m_{2\ell-1} + m_{2\ell+1}\big) - m_\ell\Big] + \ldots, \qquad \ell = 0,1,\ldots. \tag{8.2}$$

In Eq. (8.2), the source terms account for the division of cells with lipid content $2\ell-1$, 2ℓ, $2\ell+1$ contributing daughter cells of lipid content ℓ, and the sink term accounts for loss of cells with lipid content ℓ due to division. Eqs. (8.1) and (8.2) are stated on an infinite lipid content domain: $\ell = 0,1,\ldots$. On a finite domain, $\ell = 0,1,\ldots,\ell_{\max}$, the source terms in Eq. (8.2) must be set to zero for all $2\ell+1 > \ell_{\max}$ for closure. Hence, a lipid-structured model that couples SMC and macrophage dynamics, according to the paragraph above, may be most simply represented in

the following form:

$$\frac{\partial s_\ell}{\partial t} = \rho\big[(2s_{2\ell} + s_{2\ell-1} + s_{2\ell+1}) - s_\ell\big] + k_{SL}\left(\sum_{\ell'=0}^{\ell_{\max}} \ell' m_{\ell'}\right)(s_{\ell-1} - s_\ell) \\ - k_{S\to M}\ell s_\ell + \ldots, \tag{8.3}$$

$$\frac{\partial m_\ell}{\partial t} = k_{SL}\left(\sum_{\ell'=0}^{\infty} s_{\ell'}\right)\big[(\ell+1)m_{\ell+1} - \ell m_\ell\big] + k_{S\to M}\ell s_\ell + \ldots. \tag{8.4}$$

In Eqs. (8.3) and (8.4), the SMC population is cast on an infinite domain, $s_0, s_1, \ldots$, and the macrophage population on a finite domain, $m_0, m_1, \ldots, m_{\ell_{\max}}$. The constant k_{SL} determines the rate at which macrophages transfer lipid to SMCs, and $k_{S\to M}\ell$ is the lipid content-dependent rate of (irreversible) transition to a macrophage phenotype. Eqs. (8.3) and (8.4) neglect macrophage proliferation, but assume that SMCs proliferate at rate ρ, independent of lipid content. We will pursue a model of the above form in a future study.

- **Homogeneity of nascent MDMs.** Our models also assumed for simplicity that newly recruited MDMs are homogeneous. Specifically, we assumed that all nascent MDMs carry only endogenous lipid and have an uncommitted phenotype. Although evidence in humans lacks consensus, some murine studies indicate that MDM heterogeneity may be partly attributable to diversity in monocyte progenitors [82, 83]. This effect could be included in our models by introducing biases to the entry lipid content or phenotype according to the distribution of monocyte subsets in the blood. The boundary conditions at the endothelium for the MDM population would take the form

$$-D_M \frac{\partial m_\ell^\phi}{\partial x}\bigg|_{x=0} = R_\ell^\phi(t) - \gamma m_\ell^\phi, \tag{8.5}$$

where $R_\ell^\phi(t)$, the entry rate of MDMs of phenotype ϕ and lipid content ℓ, is nonzero for $(\phi, \ell) \neq (0, 0)$ according to the blood monocyte distribution.

- **Fixed one-dimensional domain.** A further assumption in our models is that the spatial domain remains fixed as time progresses. As seen in the Nakashima images (Fig. 6.1), this is justified between the late diffuse intimal thickening and early pathological intimal thickening stages, during which fatty streak formation occurs. However, the inclusion of moving boundaries in our models would extend their temporal range of validity. To extend into earlier times (e.g., to account for diffuse intimal thickening) the position of the endothelium could be fixed and the position of internal elastic lamina allowed to move, to account for Glagov remodelling (i.e., preservation of lumen area with early lesion growth) [125]. To further extend the validity of our model (e.g., to account for late pathological intimal thickening or fibrous cap formation) the endothelium should also be allowed to move, to allow for lumenal narrowing. We may account for free boundaries by recasting our models

(or appropriately simplified versions) in a morphoelastic or multiphase framework, such as those developed by Fok [123] or Ahmed *et al.* [151, 152], respectively.

Following Fok [122], a basic morphoelastic model that accounts for MDM dynamics may assume that the artery wall is radially symmetric, consisting of concentric hyperelastic annuli, and that growth only occurs within the intima. The media and adventitia may be represented as a strain-stiffening material, and the intima as a neo-Hookean material. Intimal growth may be coupled to the MDM or SMC density in a lipid content-dependent manner by assuming a growth tensor of the form

$$\mathbf{F}_g := \mathrm{diag}(g, g, 1), \qquad \text{where } \frac{\partial g}{\partial t} = G\left[\left(\sum_{\ell=0}^{\infty}(w_\ell m_\ell + v_\ell s_\ell)\right) - c^\star\right]. \tag{8.6}$$

In Eq. (8.6), $G > 0$ is a constant that measures the sensitivity of growth to cellular densities and $c^\star$ is a critical cell density that produces local growth if exceeded, and contraction otherwise. The constants $w_\ell, v_\ell > 0$ are weights that allow cells of different lipid contents to influence growth differently (e.g., lipid-loading of SMCs impairs their ability to synthesise ECM components necessary for lesion growth [253]).

Following Ahmed *et al.* [151, 152], a basic lipid-structured multiphase model of early atherosclerosis may be cast on a domain: $x \in [0, R(t)]$, with $x = 0$ representing the endothelium and $x = R(t)$ the IEL. We may assume that the IEL boundary is free to allow for intimal expansion without obstructing the lumen, consistent with observations by Glagov [125]. The governing PDEs may take the form

$$\frac{\partial u}{\partial t} + \frac{\partial}{\partial x}\big(J_u + vu\big) = s_u, \tag{8.7}$$

where $u \in \{m_0, m_1, \ldots, m_{\ell_{\max}}, L, H\}$ denotes volume fractions for a lipid-structured MDM population, extracellular lipid and HDL phases, v is a common mixture velocity, J_u are phase-specific flux terms where we may account for lipid content-dependent MDM motion, and s_u are source and sink terms for uptake, efflux and apoptosis. The common mixture velocity, v, would be determined upon imposing boundary conditions and appropriate constitutive relations (e.g., a no-voids condition).

In the models of Chapters 6 and 7, we incorporated spatial variation perpendicular to the endothelium but neglected parallel variation. Observations in mice [24] and humans [9, 26, 110] show that various lesion features, in particular the LDL retention capacity, also vary along the axial and circumferential direction of the artery. We could account for these effects by introducing a second spatial coordinate (e.g., z for axial resolution) parallel to the endothelium, and setting $K_\mathrm{r} = K_\mathrm{r}(x, z)$. In this framework, we could study the spread of lesion MDMs and lipid parallel to the endothelium in response to arbitrary forms of K_r. To model an isolated, vulnerable region of artery wall, we may assume that K_r varies according to a Gaussian in z,

centred at the lesion centre. It would be interesting, for instance, to explore how closely the spread of lesion MDMs and lipid follows the spread in K_{r} along the z coordinate.

- **Phenotype coupling.** In the models of Chapters 5 and 7, phenotype influences the MDM dynamics via its impact on mediator production; macrophage phenotype is largely characterised by the profile of cytokines and effector molecules produced by the cell [254]. In practice, phenotype is also correlated with other behaviours, including: lipid uptake [255], lipid efflux to HDL [256] and mobility [257]. Whether these effects are fundamentally influenced by phenotype, or determined by the same processes that alter MDM lipid content is unknown. For instance, is the increased mobility of M2-like MDMs in progressing atherosclerotic lesions due to their phenotype, or because they typically have a lower lipid burden (recall Fig. 8.1) and lipid content-dependent mobility is fundamental? Nonetheless, assuming phenotype and lipid content influence these processes independently, we could incorporate these effects by allowing the rates of lipid uptake ($\mathbf{k_L}$), efflux (k_H), egress (γ) and diffusivity (D_M) to depend on ϕ.

- **Large parameter set.** Finally, we note that our models contain a large number of parameters. Although we calibrated the parameters to data from the biological literature, their point estimates are likely to carry high degrees of uncertainty. We have consequently focused our analysis on identifying trends rather than producing quantitative predictions. There is scope to derive more reliable estimates by fitting appropriately simplified versions of our models to *in vivo* data. For instance, the densities in the Nakashima images (Fig. 6.1) could be quantified and fitted to a simplified version of the lipid-spatial model of Chapter 6 using the method of least squares or Bayesian inference. A simplified version of the phenotype-lipid model of Chapter 5 could also be fitted to appropriately translated phenotype and lipid-resolved data from recent single cell RNA sequencing in humans [190].

  More fundamentally, the varying degrees of biological complexity in the models of Chapters 4-7 raise issues of parsimony. In particular, it may not be possible to uniquely resolve all parameter values for a given dataset (e.g., measurements of the MDM and lipid densities at fixed times); that is, the models may not be *practically identifiable* with respect to particular datasets. Non-identifiability may arise due to noise in the data, or because the underlying models are not *structurally identifiable* with respect to certain outputs. For instance, two different parameter sets of the well-mixed model in Chapter 5 may give rise to the same densities of MDMs and total lipid at steady state. This is plausible since a reduction in rLDL uptake may be compensated, for example, by a corresponding decrease in the rate of lipid efflux to HDL. However, since each extracellular lipid species is subject to distinct dynamics and spatial variation, we anticipate that the models of Chapters

5-7 would be structurally identifiable with respect to outputs consisting of lipid and MDM densities of sufficient temporal or spatial resolution. Regardless, it would be useful to formally investigate structural identifiability using available software packages (e.g., SIAN [258] or DAISY [259]). Our models may be simplified to counter non-identifiability. We note, for instance, that the free LDL and apoptotic lipid densities in Chapters 5-7 are consistently smaller than the densities of retained LDL and necrotic lipid. The small free LDL density is due to rapid LDL retention, while the small apoptotic density is due to rapid uptake and secondary necrosis. This suggests that, in future models, the free LDL and apoptotic lipid densities could be represented more simplistically via quasi-steady approximations.

The model of Chapter 7 may also be adapted to explore the impact of 'SPM therapies' that aim to treat the lesion via exogenous application of resolving mediators [7]. Resolving mediators cannot be efficiently delivered to the lesion in their natural form due to their rapid decay timescale. Rather, SPM therapies typically aim to deliver resolving mediators to lesions within stable nanoparticles that become retained in the lesion and release their resolving mediator cargo on a timescale of days [248]. To incorporate nanoparticle-delivered SPM therapy in our model, we could introduce additional variables, $N_f(x,t)$ and $N_b(x,t)$, for the density of resolving mediators contained within free and ECM-bound nanoparticles, respectively. The nanoparticle dynamics may be governed by PDEs and boundary conditions of the form

$$\frac{\partial N_f}{\partial t} = D_N \frac{\partial^2 N_f}{\partial x^2} - (k_N + r)N_f, \quad -D_N \frac{\partial N_f}{\partial x} = \begin{cases} P_N^{(0)}(N^\star(t) - N_f) & \text{at } x = 0; \\ P_N^{(1)}(N_f - 0) & \text{at } x = X, \end{cases} \tag{8.8}$$

$$\frac{\partial N_b}{\partial t} = k_N N_f - r N_b, \tag{8.9}$$

where D_N is the free nanoparticle diffusivity, k_N is the rate of free nanoparticle binding to ECM (assumed constant, for simplicity), r is the rate of mediator release from nanoparticles, $P_N^{(0)}$ and $P_N^{(1)}$ are the endothelial and IEL nanoparticle permeabilities, respectively, and $N^\star(t)$ is the nanoparticle density in the blood. Mediator release from nanoparticles contributes a source term in the lesion resolving mediator density dynamics, and may sustain a non-negligible resolving mediator density in the blood. Hence, the resolving mediator dynamics may take the form:

$$\frac{\partial S_-}{\partial t} = r(N_f + N_b) + \ldots, \qquad -D_S \frac{\partial S_-}{\partial x} = \begin{cases} P_S^{(0)}(S_-^\star(t) - S_-) & \text{at } x = 0 \\ P_S^{(1)}(S_- - 0) & \text{at } x = X. \end{cases} \tag{8.10}$$

Here $S_-^\star(t)$ is the density of resolving mediators in the blood. A complication is that endothelial cell activation is affected by resolving mediators, and so the MDM influx rate, R_0^0 may also depend on $S_-^\star$. A possible functional form is

$$R_0^0(t) = \sigma_M \left(\frac{S_+}{S_+^{c50} + S_+ + \rho_1 S_-^\star + \rho_2 S_-} \right) \Bigg|_{x=0}, \tag{8.11}$$

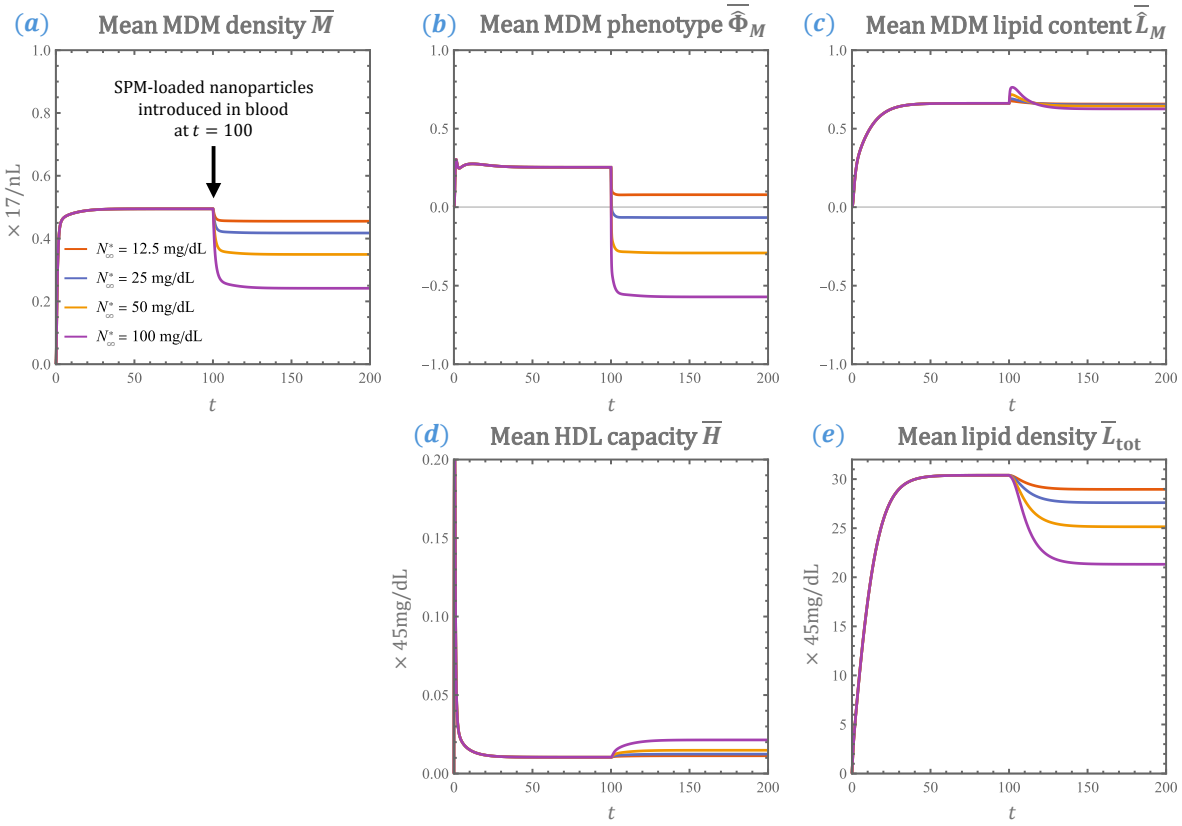


Figure 8.2: **Preliminary results for *in silico* SPM therapy.** The plots above are solutions to the lipid-structured subsystem (7.48)-(7.58), (7.63)-(7.66), augmented with Eqs. (8.10)-(8.11). We assume that $N^\star(t) = N^\star_\infty$ Heaviside$(t - 100)$ so that SPM-loaded nanoparticles are introduced in the blood at $t = 100$ MDM lifespans, and set $S^\star_- = 0$ for simplicity. The remaining parameters are set according to Table 7.1 with: $r = 8$ days^{-1}, $k_N = 4$ hours^{-1}, $D_N = D_S$, $\pi_N^{(i)} = \pi_S^{(i)}$ for $i = 0, 1$, $L^\star = 180$ mg/dL and $H^\star = 45$ mg/dL.

where ρ_1 and ρ_2 denote the sensitivities of MDM influx to resolving mediators in the blood and at $x = 0$ within the lesion, respectively. In the absence of data, we could take $\rho_1 = \rho_2 =: \frac{\rho}{2}$ so that MDM influx is influenced by the mean density of resolving mediators on either side of the endothelium. An alternative choice is to neglect the influence of resolving mediators in the blood, either by assuming $S^\star_- \equiv 0$, or $\rho_2 = 0$. We will explore these possibilities in a future study.

Preliminary results are shown in Fig. 8.2. We assume $N^\star(t) = N^\star_\infty$ Heaviside$(t - 100)$, so that SPM-loaded nanoparticles are introduced in the blood at $t = 100$. For simplicity, we neglect resolving mediators in the blood so that $S^\star_- = 0$. The results suggest that SPM therapies applied to early atherosclerotic lesions would lower the MDM and lipid densities (Fig. 8.2(a, e)), promote resolving MDM phenotypes (Fig. 8.2(b)) and increase HDL capacity (Fig. 8.2(d)) in a dose-dependent manner. Fig. 8.2(c) suggests that mean MDM lipid content is minimally impacted by SPM therapy, probably because the reduction in the MDM and lipid densities preserves their relative proportions. Nonetheless, since the absolute MDM density decreases, the lesion under continuous SPM therapy would contain fewer foam cells. The model response to more realistic (e.g., periodic) treatment protocols

requires further investigation.

Finally, we note that the models developed in this thesis may be translated to other areas of biology. One possibility is to adapt the lipid-structured models of Chapters 4 and 6 to model lipid content heterogeneity in hepatocytes, a major type of liver cell. Hepatocyte uptake of LDL has been studied by Wattis *et al.* using a detailed ODE model calibrated to *in vitro* data [260]. However, the model does not account for hepatocyte death or explicitly represent cell-to-cell heterogeneity. Given that intracellular lipid content is a key determinant for hepatocyte viability *in vivo* [261], it would be interesting to develop a lipid-structured model of hepatocytes *in vivo* with a lipid content-dependent rate of apoptosis. Another possibility is to adapt our models to the interactions between adipocytes and melanoma cells. Adipocytes transfer lipids to nearby melanoma cells, which causes melanoma cells to transition from proliferative to invasive phenotypes [262]. We could model this process using a lipid-structured melanoma cell population. Since lipid transfer is most prominent on the interface between melanoma cells and adipocytes, this process is best represented in a spatially resolved lipid-structured framework, as in Chapter 6, albeit adapted to account for lipid uptake at the boundary. If lipid content is insufficient as a proxy for melanoma cell phenotype, an additional phenotype index/variable could be included, as in Chapter 7, to model the switch from proliferative to invasive cell states.

In conclusion, the research presented in this thesis shows how mathematical modelling can increase our understanding of lesion formation during early atherosclerosis. We have developed a series of increasingly detailed structured population models to show how MDM heterogeneity arises during early atherosclerosis. Our results provide a framework for future model validation using data from single-cell RNA sequencing and images of MDM and lipid densities. The models are readily adapted to explore a range of scenarios including the interactions between MDMs and smooth muscle cells, and the impact of SPM therapies on human atherosclerotic lesions.

Bibliography

[1] A Lusis. Atherosclerosis. *Nature*, 407:233–241, 2000.

[2] E Murat Tuzcu, Samir R Kapadia, Eralp Tutar, Khaled M Ziada, Robert E Hobbs, Patrick M McCarthy, James B Young, and Steven E Nissen. High prevalence of coronary atherosclerosis in asymptomatic teenagers and young adults: evidence from intravascular ultrasound. *Circulation*, 103(22):2705–2710, 2001.

[3] John R Guyton and Keith F Klemp. Development of the lipid-rich core in human atherosclerosis. *Arteriosclerosis, Thrombosis, and Vascular Biology*, 16(1):4–11, 1996.

[4] Xiao-Hua Yu, Yu-Chang Fu, Da-Wei Zhang, Kai Yin, and Chao-Ke Tang. Foam cells in atherosclerosis. *Clinica Chimica Acta*, 424:245–252, 2013.

[5] Vasily N Sukhorukov, Victoria A Khotina, Yegor S Chegodaev, Ekaterina Ivanova, Igor A Sobenin, and Alexander N Orekhov. Lipid metabolism in macrophages: focus on atherosclerosis. *Biomedicines*, 8(8):262, 2020.

[6] Tessa J Barrett. Macrophages in atherosclerosis regression. *Arteriosclerosis, Thrombosis, and Vascular Biology*, 40(1):20–33, 2020.

[7] Magnus Bäck, Arif Yurdagul Jr, Ira Tabas, Katariina Öörni, and Petri T Kovanen. Inflammation and its resolution in atherosclerosis: mediators and therapeutic opportunities. *Nature Reviews Cardiology*, 16(7):389–406, 2019.

[8] Lisa Willemsen and Menno PJ de Winther. Macrophage subsets in atherosclerosis as defined by single-cell technologies. *The Journal of Pathology*, 250(5):705–714, 2020.

[9] Yutaka Nakashima, Hiroshi Fujii, Shinji Sumiyoshi, Thomas N Wight, and Katsuo Sueishi. Early human atherosclerosis: accumulation of lipid and proteoglycans in intimal thickenings followed by macrophage infiltration. *Arteriosclerosis, Thrombosis, and Vascular Biology*, 27(5):1159–1165, 2007.

[10] Keith L Chambers, Mary R Myerscough, and Helen M Byrne. A new lipid-structured model to investigate the opposing effects of LDL and HDL on atherosclerotic plaque macrophages. *Mathematical Biosciences*, 357:108971, 2023.

[11] Keith L Chambers, Mary R Myerscough, Michael G Watson, and Helen M Byrne. Blood lipoproteins shape the phenotype and lipid content of early atherosclerotic lesion macrophages: a dual-structured mathematical model. *Bulletin of Mathematical Biology*, 86(9):112, 2024.

[12] Victor Aboyans, Philippe Lacroix, and Michael H Criqui. Large and small vessels atherosclerosis: similarities and differences. *Progress in Cardiovascular Diseases*, 50(2):112–125, 2007.

[13] Shifa Jebari-Benslaiman, Unai Galicia-García, Asier Larrea-Sebal, Javier Rekondo

Olaetxea, Iraide Alloza, Koen Vandenbroeck, Asier Benito-Vicente, and César Martín. Pathophysiology of atherosclerosis. *International Journal of Molecular Sciences*, 23(6):3346, 2022.

[14] George D Giannoglou, Antonios P Antoniadis, Konstantinos C Koskinas, and Yiannis S Chatzizisis. Flow and atherosclerosis in coronary bifurcations. *EuroIntervention*, 6(Suppl J):J16–23, 2010.

[15] Godfrey S Getz and Catherine A Reardon. Animal models of atherosclerosis. *Arteriosclerosis, Thrombosis, and Vascular Biology*, 32(5):1104–1115, 2012.

[16] Anne M Robertson and Paul N Watton. Mechanobiology of the arterial wall. *Transport in Biological Media*, 2013:275–347, 2013.

[17] George Bou-Gharios, Markella Ponticos, Vineeth Rajkumar, and David Abraham. Extra-cellular matrix in vascular networks. *Cell Proliferation*, 37(3):207–220, 2004.

[18] Bethan A Brown, Helen Williams, and Sarah J George. Evidence for the involvement of matrix-degrading metalloproteinases (mmps) in atherosclerosis. *Progress in molecular biology and translational science*, 147:197–237, 2017.

[19] Medical gallery of Blausen Medical 2014, https://commons.wikimedia.org/wiki/file:blausen_0055_arterywallstructure.png, WikiJournal of Medicine, accessed: 27 Aug 2024.

[20] Lasse Bach Steffensen, Martin Bødtker Mortensen, Mads Kjolby, Mette Kallestrup Hagensen, Claus Oxvig, and Jacob Fog Bentzon. Disturbed laminar blood flow vastly augments lipoprotein retention in the artery wall: a key mechanism distinguishing susceptible from resistant sites. *Arteriosclerosis, Thrombosis, and Vascular Biology*, 35(9):1928–1935, 2015.

[21] Ira Tabas, Kevin Jon Williams, and Jan Borén. Subendothelial lipoprotein retention as the initiating process in atherosclerosis: update and therapeutic implications. *Circulation*, 116(16):1832–1844, 2007.

[22] Adel M Malek and Seigo Izumo. Mechanism of endothelial cell shape change and cytoskeletal remodeling in response to fluid shear stress. *Journal of cell science*, 109(4):713–726, 1996.

[23] Michael A Gimbrone Jr and Guillermo García-Cardeña. Vascular endothelium, hemodynamics, and the pathobiology of atherosclerosis. *Cardiovascular Pathology*, 22(1):9–15, 2013.

[24] Esmeralda A Lewis, Rocío Muñiz-Anquela, Ibon Redondo-Angulo, Leticia González-Cintado, Verónica Labrador-Cantarero, and Jacob F Bentzon. Capacity for LDL (low-density lipoprotein) retention predicts the course of atherogenesis in the murine aortic arch. *Arteriosclerosis, Thrombosis, and Vascular Biology*, 43(5):637–649, 2023.

[25] Yutaka Nakashima, Yong-Xiang Chen, Naoko Kinukawa, and Katsuo Sueishi. Distributions of diffuse intimal thickening in human arteries: preferential expression in atherosclerosis-prone arteries from an early age. *Virchows Archiv*, 441:279–288, 2002.

[26] Yutaka Nakashima, Thomas N Wight, and Katsuo Sueishi. Early atherosclerosis in humans: role of diffuse intimal thickening and extracellular matrix proteoglycans. *Cardiovascular research*, 79(1):14–23, 2008.

[27] Hiroyuki Jinnouchi, Frank D Kolodgie, Maria Romero, Renu Virmani, and Aloke V Finn. Pathophysiology of coronary artery disease. *Vessel Based Imaging Techniques: Diagnosis, Treatment, and Prevention*, pages 211–227, 2020.

[28] Anna van Veelen, Niels MR van der Sangen, José PS Henriques, and Bimmer EPM Claessen. Identification and treatment of the vulnerable coronary plaque. *Reviews in cardiovascular medicine*, 23(1):39, 2022.

[29] Vasanthy Narayanaswami, Robert S Kiss, and Paul MM Weers. The helix bundle: a reversible lipid binding motif. *Comparative Biochemistry and Physiology Part A: Molecular & Integrative Physiology*, 155(2):123–133, 2010.

[30] Kenneth R Feingold. Introduction to lipids and lipoproteins. *Endotext [Internet] https://www.ncbi.nlm.nih.gov/books/NBK305896/*, 2024.

[31] Graham R Bayly. Lipids and disorders of lipoprotein metabolism. *Clinical Biochemistry: Metabolic and Clinical Aspects. Elsevier*, 1:702–36, 2014.

[32] Jae-Geun Lee, Sung Joo Koh, So Yeon Yoo, Jung Re Yu, Sang Ah Lee, Gwanpyo Koh, and Daeho Lee. Characteristics of subjects with very low serum low-density lipoprotein cholesterol and the risk for intracerebral hemorrhage. *The Korean journal of internal medicine*, 27(3):317, 2012.

[33] Leticia Fernández-Friera, Valentín Fuster, Beatriz López-Melgar, Belén Oliva, José M García-Ruiz, José Mendiguren, Héctor Bueno, Stuart Pocock, Borja Ibáñez, Antonio Fernández-Ortiz, et al. Normal LDL-cholesterol levels are associated with subclinical atherosclerosis in the absence of risk factors. *Journal of the American College of Cardiology*, 70(24):2979–2991, 2017.

[34] Brian A Ference, Henry N Ginsberg, Ian Graham, Kausik K Ray, Chris J Packard, Eric Bruckert, Robert A Hegele, Ronald M Krauss, Frederick J Raal, Heribert Schunkert, et al. Low-density lipoproteins cause atherosclerotic cardiovascular disease. 1. evidence from genetic, epidemiologic, and clinical studies. a consensus statement from the european atherosclerosis society consensus panel. *European heart journal*, 38(32):2459–2472, 2017.

[35] Jan Boren, M John Chapman, Ronald M Krauss, Chris J Packard, Jacob F Bentzon, Christoph J Binder, Mat J Daemen, Linda L Demer, Robert A Hegele, Stephen J Nicholls, et al. Low-density lipoproteins cause atherosclerotic cardiovascular disease: pathophysiological, genetic, and therapeutic insights: a consensus statement from the european atherosclerosis society consensus panel. *European heart journal*, 41(24):2313–2330, 2020.

[36] Frank LJ Visseren, François Mach, Yvo M Smulders, David Carballo, Konstantinos C Koskinas, Maria Bäck, Athanase Benetos, Alessandro Biffi, José-Manuel Boavida, Davide Capodanno, et al. 2021 esc guidelines on cardiovascular disease prevention in clinical practice: Developed by the task force for cardiovascular disease prevention in clinical practice with representatives of the european society of cardiology and 12 medical societies with the special contribution of the european association of preventive cardiology (eapc). *European heart journal*, 42(34):3227–3337, 2021.

[37] Scott M Grundy, Neil J Stone, Alison L Bailey, Craig Beam, Kim K Birtcher, Roger S Blumenthal, Lynne T Braun, Sarah De Ferranti, Joseph Faiella-Tommasino, Daniel E Forman, et al. 2018 AHA/ACC/AACVPR/AAPA/ABC /ACPM/ADA/AGS/APhA/ASPC/NLA/PCNA guideline on the management of

blood cholesterol: executive summary: a report of the american college of cardiology/american heart association task force on clinical practice guidelines. *Circulation*, 139(25):e1046–e1081, 2018.

[38] Kim M Huffman, Victoria H Hawk, Sarah T Henes, Christine I Ocampo, Melissa C Orenduff, Cris A Slentz, Johanna L Johnson, Joseph A Houmard, Gregory P Samsa, William E Kraus, et al. Exercise effects on lipids in persons with varying dietary patterns—does diet matter if they exercise? responses in studies of a targeted risk reduction intervention through defined exercise i. *American heart journal*, 164(1):117–124, 2012.

[39] Elena V Orlova, Michael B Sherman, Wah Chiu, Hiro Mowri, Louis C Smith, and Antonio M Gotto Jr. Three-dimensional structure of low density lipoproteins by electron cryomicroscopy. *Proceedings of the National Academy of Sciences*, 96(15):8420–8425, 1999.

[40] Anand Rohatgi, Amit Khera, Jarett D Berry, Edward G Givens, Colby R Ayers, Kyle E Wedin, Ian J Neeland, Ivan S Yuhanna, Daniel R Rader, James A de Lemos, et al. HDL cholesterol efflux capacity and incident cardiovascular events. *New England Journal of Medicine*, 371(25):2383–2393, 2014.

[41] Gerd Assmann and Antonio M Gotto Jr. HDL cholesterol and protective factors in atherosclerosis. *Circulation*, 109(23_suppl_1):III–8, 2004.

[42] Peter W Wilson, Robert J Garrison, William P Castelli, Manning Feinleib, Patricia M McNamara, and William B Kannel. Prevalence of coronary heart disease in the framingham offspring study: role of lipoprotein cholesterols. *The American journal of cardiology*, 46(4):649–654, 1980.

[43] David J Gordon and Basil M Rifkind. High-density lipoprotein—the clinical implications of recent studies. *New England Journal of Medicine*, 321(19):1311–1316, 1989.

[44] Boden WE, Probstfield JL, Anderson T, Chaitman BR, Desvignes-Nickens P, Koprowicz K, McBride R, Teo K, and Weintraub W. Niacin in patients with low HDL cholesterol levels receiving intensive statin therapy. *New England Journal of Medicine*, 365(24):2255–67, 2011.

[45] Daniel Keene, Clare Price, Matthew J Shun-Shin, and Darrel P Francis. Effect on cardiovascular risk of high density lipoprotein targeted drug treatments niacin, fibrates, and CETP inhibitors: meta-analysis of randomised controlled trials including 117 411 patients. *British Medical Journal*, 349, 2014.

[46] Mireille Ouimet, Tessa J Barrett, and Edward A Fisher. HDL and reverse cholesterol transport: Basic mechanisms and their roles in vascular health and disease. *Circulation research*, 124(10):1505–1518, 2019.

[47] Maria T Soria-Florido, Helmut Schröder, Maria Grau, Montserrat Fito, and Camille Lassale. High density lipoprotein functionality and cardiovascular events and mortality: a systematic review and meta-analysis. *Atherosclerosis*, 302:36–42, 2020.

[48] Maria Pia Adorni, Nicoletta Ronda, Franco Bernini, and Francesca Zimetti. High density lipoprotein cholesterol efflux capacity and atherosclerosis in cardiovascular disease: pathophysiological aspects and pharmacological perspectives. *Cells*, 10(3):574, 2021.

[49] Jane J Lee, Gerald Chi, Clara Fitzgerald, Syed Hassan A Kazmi, Arzu Kalayci,

Serge Korjian, Danielle Duffy, Alka Shaunik, Bronwyn Kingwell, Robert W Yeh, et al. Cholesterol efflux capacity and its association with adverse cardiovascular events: a systematic review and meta-analysis. *Frontiers in cardiovascular medicine*, 8:774418, 2021.

[50] Aleksandra Milutinović, Dušan Šuput, and Ruda Zorc-Pleskovič. Pathogenesis of atherosclerosis in the tunica intima, media, and adventitia of coronary arteries: An updated review. *Bosnian journal of basic medical sciences*, 20(1):21, 2020.

[51] Matilde Alique, Carlos Luna, Julia Carracedo, and Rafael Ramírez. LDL biochemical modifications: a link between atherosclerosis and aging. *Food & nutrition research*, 59(1):29240, 2015.

[52] Anastasia V Poznyak, Nikita G Nikiforov, Alexander M Markin, Dmitry A Kashirskikh, Veronika A Myasoedova, Elena V Gerasimova, and Alexander N Orekhov. Overview of oxLDL and its impact on cardiovascular health: focus on atherosclerosis. *Frontiers in Pharmacology*, page 2248, 2021.

[53] Katariina Öörni and Petri T Kovanen. Aggregation susceptibility of low-density lipoproteins—a novel modifiable biomarker of cardiovascular risk. *Journal of clinical medicine*, 10(8):1769, 2021.

[54] Katherine L Olin, Susan Potter-Perigo, P Hugh R Barrett, Thomas N Wight, and Alan Chait. Biglycan, a vascular proteoglycan, binds differently to HDL2 and HDL3: role of apoe. *Arteriosclerosis, Thrombosis, and Vascular Biology*, 21(1):129–135, 2001.

[55] Santa Mundi, Marika Massaro, Egeria Scoditti, Maria Annunziata Carluccio, Victor WM Van Hinsbergh, Marial Luisa Iruela-Arispe, and Raffaele De Caterina. Endothelial permeability, LDL deposition, and cardiovascular risk factors—a review. *Cardiovascular research*, 114(1):35–52, 2018.

[56] Katariina Öörni, Markku O Pentikäinen, Mika Ala-Korpela, and Petri T Kovanen. Aggregation, fusion, and vesicle formation of modified low density lipoprotein particles: molecular mechanisms and effects on matrix interactions. *Journal of lipid research*, 41(11):1703–1714, 2000.

[57] John C Khoo, Elizabeth Miller, Patricia McLoughlin, and Daniel Steinberg. Enhanced macrophage uptake of low density lipoprotein after self-aggregation. *Arteriosclerosis: An Official Journal of the American Heart Association, Inc.*, 8(4):348–358, 1988.

[58] Kevin Jon Williams and Ira Tabas. The response-to-retention hypothesis of early atherogenesis. *Arteriosclerosis, Thrombosis, and Vascular Biology*, 15(5):551–561, 1995.

[59] Kevin Jon Williams and Ira Tabas. Lipoprotein retention—and clues for atheroma regression, 2005.

[60] Kathryn J Moore and Ira Tabas. Macrophages in the pathogenesis of atherosclerosis. *Cell*, 145(3):341–355, 2011.

[61] Valerie E Espinoza and Prabhu D Emmady. Histology, monocytes. In *StatPearls [Internet] https://www.ncbi.nlm.nih.gov/books/NBK557618/*. StatPearls Publishing, 2023.

[62] Sébastien Trzebanski and Steffen Jung. Plasticity of monocyte development and monocyte fates. *Immunology Letters*, 227:66–78, 2020.

[63] Charikleia Papadopoulou, Valerie Corrigall, Peter R Taylor, and Robin N Poston. The role of the chemokines mcp-1, gro-α, il-8 and their receptors in the adhesion of monocytic cells to human atherosclerotic plaques. *Cytokine*, 43(2):181–186, 2008.

[64] Javier Mestas and Klaus Ley. Monocyte-endothelial cell interactions in the development of atherosclerosis. *Trends in cardiovascular medicine*, 18(6):228–232, 2008.

[65] Yuri V Bobryshev. Dendritic cells and their role in atherogenesis. *Laboratory investigation*, 90(7):970–984, 2010.

[66] Malgorzata Kloc, Jacek Z Kubiak, and Rafik M Ghobrial. Macrophage-, dendritic-, smooth muscle-, endothelium-, and stem cells-derived foam cells in atherosclerosis. *International Journal of Molecular Sciences*, 23(22):14154, 2022.

[67] Gwendalyn J Randolph, Sylvie Beaulieu, Serge Lebecque, Ralph M Steinman, and William A Muller. Differentiation of monocytes into dendritic cells in a model of transendothelial trafficking. *Science*, 282(5388):480–483, 1998.

[68] Jesse W Williams, Konstantin Zaitsev, Ki-Wook Kim, Stoyan Ivanov, Brian T Saunders, Patricia R Schrank, Kyeongdae Kim, Andrew Elvington, Seung Hyeon Kim, Christopher G Tucker, et al. Limited proliferation capacity of aortic intima resident macrophages requires monocyte recruitment for atherosclerotic plaque progression. *Nature immunology*, 21(10):1194–1204, 2020.

[69] Eileen Uribe-Querol and Carlos Rosales. Phagocytosis: our current understanding of a universal biological process. *Frontiers in immunology*, 11:1066, 2020.

[70] Kiyoshi Takahashi, Motohiro Takeya, and Naomi Sakashita. Multifunctional roles of macrophages in the development and progression of atherosclerosis in humans and experimental animals. *Medical electron microscopy*, 35:179–203, 2002.

[71] Malgorzata Kloc, Ahmed Uosef, Jacek Z Kubiak, and Rafik Mark Ghobrial. Role of macrophages and rhoa pathway in atherosclerosis. *International Journal of Molecular Sciences*, 22(1):216, 2020.

[72] Patrick M Hutchins and Jay W Heinecke. Cholesterol efflux capacity, macrophage reverse cholesterol transport and cardioprotective HDL. *Current opinion in lipidology*, 26(5):388–393, 2015.

[73] Kathryn J Moore, Simon Koplev, Edward A Fisher, Ira Tabas, Johan LM Björkegren, Amanda C Doran, and Jason C Kovacic. Macrophage trafficking, inflammatory resolution, and genomics in atherosclerosis: Jacc macrophage in cvd series (part 2). *Journal of the American College of Cardiology*, 72(18):2181–2197, 2018.

[74] Kathryn J Moore, Frederick J Sheedy, and Edward A Fisher. Macrophages in atherosclerosis: a dynamic balance. *Nature Reviews Immunology*, 13(10):709–721, 2013.

[75] RG Gerrity and HK Naito. Lipid clearance from fatty streak lesions by foam cell migration. *Artery*, 8(3):215–219, 1980.

[76] Guido RY De Meyer, Michelle Zurek, Pauline Puylaert, and Wim Martinet. Programmed death of macrophages in atherosclerosis: mechanisms and therapeutic targets. *Nature Reviews Cardiology*, 21(5):312–325, 2024.

[77] Susan Elmore. Apoptosis: a review of programmed cell death. *Toxicologic pathology*, 35(4):495–516, 2007.

[78] Pin Mei Yao and Ira Tabas. Free cholesterol loading of macrophages is associated with widespread mitochondrial dysfunction and activation of the mitochondrial apoptosis pathway. *Journal of Biological Chemistry*, 276(45):42468–42476, 2001.

[79] Monika Sachet, Ying Yu Liang, and Rudolf Oehler. The immune response to secondary necrotic cells. *Apoptosis*, 22(10):1189–1204, 2017.

[80] Megan L Brophy, Yunzhou Dong, Hao Wu, HN Ashiqur Rahman, Kai Song, and Hong Chen. Eating the dead to keep atherosclerosis at bay. *Frontiers in Cardiovascular Medicine*, 4:2, 2017.

[81] Pengbo Hou, Jiankai Fang, Zhanhong Liu, Yufang Shi, Massimiliano Agostini, Francesca Bernassola, Pierluigi Bove, Eleonora Candi, Valentina Rovella, Giuseppe Sica, et al. Macrophage polarization and metabolism in atherosclerosis. *Cell Death & Disease*, 14(10):691, 2023.

[82] Filip K Swirski, Ralph Weissleder, and Mikael J Pittet. Heterogeneous in vivo behavior of monocyte subsets in atherosclerosis. *Arteriosclerosis, Thrombosis, and Vascular Biology*, 29(10):1424–1432, 2009.

[83] Adele V Ruder, Suzan MW Wetzels, Lieve Temmerman, Erik AL Biessen, and Pieter Goossens. Monocyte heterogeneity in cardiovascular disease. *Cardiovascular research*, 119(11):2033–2045, 2023.

[84] Hiroyuki Jinnouchi, Liang Guo, Atsushi Sakamoto, Sho Torii, Yu Sato, Anne Cornelissen, Salome Kuntz, Ka Hyun Paek, Raquel Fernandez, Daniela Fuller, et al. Diversity of macrophage phenotypes and responses in atherosclerosis. *Cellular and Molecular Life Sciences*, 77:1919–1932, 2020.

[85] John F Sheehan. Foam cell plaques in intima of myometrial arteries: A presumptive sign of previous irradiation. *American Journal of Clinical Pathology*, 19(1):30–34, 1949.

[86] Justin M Donegan. The eye in experimental arteriosclerosis. *Transactions of the American Ophthalmological Society*, 51:475, 1953.

[87] Howar S Kruth. Fluid-phase pinocytosis of LDL by macrophages: a novel target to reduce macrophage cholesterol accumulation in atherosclerotic lesions. *Current pharmaceutical design*, 19(33):5865–5872, 2013.

[88] Manoj K Barthwal, Joshua J Anzinger, Qing Xu, Thomas Bohnacker, Matthias P Wymann, and Howard S Kruth. Fluid-phase pinocytosis of native low density lipoprotein promotes murine m-csf differentiated macrophage foam cell formation. *PLOS One*, 8(3):e58054, 2013.

[89] Howard S Kruth. Sequestration of aggregated low-density lipoproteins by macrophages. *Current opinion in lipidology*, 13(5):483–488, 2002.

[90] Gabriela M Sanda, Camelia S Stancu, Mariana Deleanu, Laura Toma, Loredan S Niculescu, and Anca V Sima. Aggregated LDL turn human macrophages into foam cells and induce mitochondrial dysfunction without triggering oxidative or endoplasmic reticulum stress. *PLOS One*, 16(1):e0245797, 2021.

[91] Nima Taefehshokr, Charles Yin, and Bryan Heit. Rab gtpases in the differential processing of phagocytosed pathogens versus efferocytosed apoptotic cells. *Histol. Histopathol*, 36:123–135, 2021.

[92] Arif Yurdagul Jr, Amanda C Doran, Bishuang Cai, Gabrielle Fredman, and Ira A

Tabas. Mechanisms and consequences of defective efferocytosis in atherosclerosis. *Frontiers in cardiovascular medicine*, 4:86, 2018.

[93] Georgia K Atkin-Smith. Phagocytic clearance of apoptotic, necrotic, necroptotic and pyroptotic cells. *Biochemical Society Transactions*, 49(2):793–804, 2021.

[94] Clive S Zent and Michael R Elliott. Maxed out macs: physiologic cell clearance as a function of macrophage phagocytic capacity. *The FEBS journal*, 284(7):1021–1039, 2017.

[95] Anouk G Groenen, Benedek Halmos, Alan R Tall, and Marit Westerterp. Cholesterol efflux pathways, inflammation, and atherosclerosis. *Critical reviews in biochemistry and molecular biology*, 56(4):426–439, 2021.

[96] Marit Westerterp, Andrea E Bochem, Laurent Yvan-Charvet, Andrew J Murphy, Nan Wang, and Alan R Tall. ATP-binding cassette transporters, atherosclerosis, and inflammation. *Circulation research*, 114(1):157–170, 2014.

[97] John F Oram. HDL apolipoproteins and abca1: partners in the removal of excess cellular cholesterol. *Arteriosclerosis, Thrombosis, and Vascular Biology*, 23(5):720–727, 2003.

[98] Anneleen Remmerie and Charlotte L Scott. Macrophages and lipid metabolism. *Cellular Immunology*, 330:27–42, 2018.

[99] Zuzana Strizova, Iva Benesova, Robin Bartolini, Rene Novysedlak, Eva Cecrdlova, Lily Koumbas Foley, and Ilja Striz. M1/m2 macrophages and their overlaps–myth or reality? *Clinical Science*, 137(15):1067–1093, 2023.

[100] SeoYeon Kim, Wonkyoung Cho, Inyeong Kim, Sang-Hak Lee, Goo Taeg Oh, and Young Mi Park. Oxidized LDL induces vimentin secretion by macrophages and contributes to atherosclerotic inflammation. *Journal of Molecular Medicine*, 98:973–983, 2020.

[101] Weiwei Liu, Yanlin Yin, Zihui Zhou, Min He, and Yalei Dai. OxLDL-induced IL-1beta secretion promoting foam cells formation was mainly via CD36 mediated ROS production leading to NLRP3 inflammasome activation. *Inflammation Research*, 63:33–43, 2014.

[102] Ryan M Allen, Danielle L Michell, Ashley B Cavnar, Wanying Zhu, Neil Makhijani, Danielle M Contreras, Chase A Raby, Elizabeth M Semler, Carlisle DeJulius, Mark Castleberry, et al. LDL delivery of microbial small rnas drives atherosclerosis through macrophage tlr8. *Nature cell biology*, 24(12):1701–1713, 2022.

[103] Jong Seong Roh and Dong Hyun Sohn. Damage-associated molecular patterns in inflammatory diseases. *Immune network*, 18(4), 2018.

[104] Chong Chen and Damir B Khismatullin. Oxidized low-density lipoprotein contributes to atherogenesis via co-activation of macrophages and mast cells. *PLOS One*, 10(3):e0123088, 2015.

[105] Suguru Kadomoto, Kouji Izumi, and Atsushi Mizokami. Macrophage polarity and disease control. *International Journal of Molecular Sciences*, 23(1):144, 2021.

[106] Christa Decker, Sudeshna Sadhu, and Gabrielle Fredman. Pro-resolving ligands orchestrate phagocytosis. *Frontiers in immunology*, 12:660865, 2021.

[107] Michael R Elliott, Kyle M Koster, and Patrick S Murphy. Efferocytosis signaling in

the regulation of macrophage inflammatory responses. *The Journal of Immunology*, 198(4):1387–1394, 2017.

[108] Charles N Serhan, Bruce D Levy, et al. Resolvins in inflammation: emergence of the pro-resolving superfamily of mediators. *The Journal of clinical investigation*, 128(7):2657–2669, 2018.

[109] Panagiotis Fotakis, Vishal Kothari, David G Thomas, Marit Westerterp, Matthew M Molusky, Elissa Altin, Sandra Abramowicz, Nan Wang, Yi He, Jay W Heinecke, et al. Anti-inflammatory effects of HDL (high-density lipoprotein) in macrophages predominate over proinflammatory effects in atherosclerotic plaques. *Arteriosclerosis, Thrombosis, and Vascular Biology*, 39(12):e253–e272, 2019.

[110] Kazunori Nakagawa, Mitsuru Tanaka, Tae-Hun Hahm, Huu-Nghi Nguyen, Toshiro Matsui, Yong-Xiang Chen, and Yutaka Nakashima. Accumulation of plasma-derived lipids in the lipid core and necrotic core of human atheroma: imaging mass spectrometry and histopathological analyses. *Arteriosclerosis, Thrombosis, and Vascular Biology*, 41(11):e498–e511, 2021.

[111] Jiayong Wu, Shengping He, Zhengkun Song, Sikai Chen, Xuefeng Lin, Huimei Sun, Pengyu Zhou, Qinbao Peng, Songlin Du, Shaoyi Zheng, et al. Macrophage polarization states in atherosclerosis. *Frontiers in Immunology*, 14:1185587, 2023.

[112] Karl Perktold, Reinfried Odo Peter, Michael Resch, and Georg Langs. Pulsatile non-newtonian blood flow in three-dimensional carotid bifurcation models: a numerical study of flow phenomena under different bifurcation angles. *Journal of biomedical engineering*, 13(6):507–515, 1991.

[113] JC Misra, MK Patra, and SC Misra. A non-newtonian fluid model for blood flow through arteries under stenotic conditions. *Journal of biomechanics*, 26(9):1129–1141, 1993.

[114] Cheng Tu and Michel Deville. Pulsatile flow of non-newtonian fluids through arterial stenoses. *Journal of biomechanics*, 29(7):899–908, 1996.

[115] Samuel A Kock, Jens V Nygaard, Nikolaj Eldrup, Ernst-Torben Frund, Anette Klærke, William P Paaske, Erling Falk, and W Yong Kim. Mechanical stresses in carotid plaques using mri-based fluid–structure interaction models. *Journal of biomechanics*, 41(8):1651–1658, 2008.

[116] Dalin Tang, Zhongzhao Teng, Gador Canton, Chun Yang, Marina Ferguson, Xueying Huang, Jie Zheng, Pamela K Woodard, and Chun Yuan. Sites of rupture in human atherosclerotic carotid plaques are associated with high structural stresses. *Stroke*, 2009.

[117] Shigeo Wada and Takeshi Karino. Theoretical prediction of low-density lipoproteins concentration at the luminal surface of an artery with a multiple bend. *Annals of biomedical engineering*, 30:778–791, 2002.

[118] Martin Prosi, Paolo Zunino, Karl Perktold, and Alfio Quarteroni. Mathematical and numerical models for transfer of low-density lipoproteins through the arterial walls: a new methodology for the model set up with applications to the study of disturbed lumenal flow. *Journal of biomechanics*, 38(4):903–917, 2005.

[119] Ning Yang and Kambiz Vafai. Modeling of low-density lipoprotein (LDL) transport in the artery—effects of hypertension. *International Journal of Heat and Mass Transfer*, 49(5-6):850–867, 2006.

[120] Ning Yang and Kambiz Vafai. Low-density lipoprotein (LDL) transport in an artery–a simplified analytical solution. *International Journal of Heat and Mass Transfer*, 51(3-4):497–505, 2008.

[121] Mahsa Dabagh, Payman Jalali, and John M Tarbell. The transport of LDL across the deformable arterial wall: the effect of endothelial cell turnover and intimal deformation under hypertension. *American Journal of Physiology-Heart and Circulatory Physiology*, 297(3):H983–H996, 2009.

[122] Pak-Wing Fok. Multi-layer mechanical model of glagov remodeling in coronary arteries: differences between in-vivo and ex-vivo measurements. *PLOS One*, 11(7):e0159304, 2016.

[123] Pak-Wing Fok and Kun Gou. Finite element simulation of intimal thickening in 2d multi-layered arterial cross sections by morphoelasticity. *Computer Methods in Applied Mechanics and Engineering*, 363:112860, 2020.

[124] Moritz P Thon, André Hemmler, Almut Glinzer, Matthias Mayr, Moritz Wildgruber, Alma Zernecke-Madsen, and Michael W Gee. A multiphysics approach for modeling early atherosclerosis. *Biomechanics and modeling in mechanobiology*, 17:617–644, 2018.

[125] Seymour Glagov, Elliot Weisenberg, Christopher K Zarins, Regina Stankunavicius, and George J Kolettis. Compensatory enlargement of human atherosclerotic coronary arteries. *New England Journal of Medicine*, 316(22):1371–1375, 1987.

[126] Anna Ougrinovskaia, Rosemary S Thompson, and Mary R Myerscough. An ode model of early stages of atherosclerosis: mechanisms of the inflammatory response. *Bulletin of mathematical biology*, 72:1534–1561, 2010.

[127] Muhammad AK Bulelzai and Johan LA Dubbeldam. Long time evolution of atherosclerotic plaques. *Journal of theoretical biology*, 297:1–10, 2012.

[128] Anna Cohen, Mary R Myerscough, and Rosemary S Thompson. Athero-protective effects of high density lipoproteins (HDL): an ode model of the early stages of atherosclerosis. *Bulletin of mathematical biology*, 76:1117–1142, 2014.

[129] Gigi Lui and Mary R Myerscough. Modelling preferential phagocytosis in atherosclerosis: delineating timescales in plaque development. *Bulletin of Mathematical Biology*, 83(9):96, 2021.

[130] Vladimir Bezyaev, Nail Sadekov, and Vitaly Volpert. A model of chronic inflammation in atherosclerosis. In *ITM Web of Conferences*, volume 31, page 04002. EDP Sciences, 2020.

[131] Moritz P Thon, Hugh Z Ford, Michael W Gee, and Mary R Myerscough. A quantitative model of early atherosclerotic plaques parameterized using in vitro experiments. *Bulletin of Mathematical Biology*, 80(1):175–214, 2018.

[132] CA Cobbold, JA Sherratt, and SRJ Maxwell. Lipoprotein oxidation and its significance for atherosclerosis: a mathematical approach. *Bulletin of mathematical biology*, 64(1):65–95, 2002.

[133] Hugh Z Ford, Lynda Zeboudj, Gareth SD Purvis, Annemieke Ten Bokum, Alexander E Zarebski, Joshua A Bull, Helen M Byrne, Mary R Myerscough, and David R Greaves. Efferocytosis perpetuates substance accumulation inside macrophage populations. *Proceedings of the Royal Society B*, 286(1904):20190730, 2019.

[134] Cameron McKay, Sean McKee, Nigel Mottram, Tony Mulholland, Stephen Wilson, Simon Kennedy, and Roger Wadsworth. Towards a model of atherosclerosis. *University of Strathclyde*, pages 1–29, 2005.

[135] N El Khatib, Stéphane Génieys, and Vitaly Volpert. Atherosclerosis initiation modeled as an inflammatory process. *Mathematical Modelling of Natural Phenomena*, 2(2):126–141, 2007.

[136] Vincent Calvez, Abderrhaman Ebde, Nicolas Meunier, and Annie Raoult. Mathematical modelling of the atherosclerotic plaque formation. In *ESAIM: proceedings*, volume 28, pages 1–12. EDP Sciences, 2009.

[137] Mark P Little, Anna Gola, and Ioanna Tzoulaki. A model of cardiovascular disease giving a plausible mechanism for the effect of fractionated low-dose ionizing radiation exposure. *PLoS computational biology*, 5(10):e1000539, 2009.

[138] Nader El Khatib, Stéphane Génieys, Bogdan Kazmierczak, and Vitaly Volpert. Reaction–diffusion model of atherosclerosis development. *Journal of mathematical biology*, 65:349–374, 2012.

[139] Wenrui Hao and Avner Friedman. The LDL-HDL profile determines the risk of atherosclerosis: a mathematical model. *PLOS One*, 9(3):e90497, 2014.

[140] Avner Friedman and Wenrui Hao. A mathematical model of atherosclerosis with reverse cholesterol transport and associated risk factors. *Bulletin of mathematical biology*, 77:758–781, 2015.

[141] Alexander D Chalmers, Anna Cohen, Christina A Bursill, and Mary R Myerscough. Bifurcation and dynamics in a mathematical model of early atherosclerosis: How acute inflammation drives lesion development. *Journal of mathematical biology*, 71:1451–1480, 2015.

[142] Alexander D Chalmers, Christina A Bursill, and Mary R Myerscough. Nonlinear dynamics of early atherosclerotic plaque formation may determine the efficacy of high density lipoproteins (HDL) in plaque regression. *PLOS One*, 12(11):e0187674, 2017.

[143] Moritz P Thon, Mary R Myerscough, and Michael W Gee. A spatially resolved and quantitative model of early atherosclerosis. *Bulletin of mathematical biology*, 81(10):4022–4068, 2019.

[144] Pak-Wing Fok. Growth of necrotic cores in atherosclerotic plaque. *Mathematical medicine and biology: a journal of the IMA*, 29(4):301–327, 2012.

[145] Ougrinovskaia A. *Mathematical models of atherosclerosis*. PhD thesis, University of Sydney, 2010.

[146] Debasmita Mukherjee, Lakshmi Narayan Guin, and Santabrata Chakravarty. A reaction–diffusion mathematical model on mild atherosclerosis. *Modeling Earth Systems and Environment*, 5:1853–1865, 2019.

[147] Ghazal Rashidi and Elizabeth A Ostrowski. Phagocyte chase behaviours: discrimination between gram-negative and gram-positive bacteria by amoebae. *Biology Letters*, 15(1):20180607, 2019.

[148] Mengchen Liu, Yan Cai, Jichao Pan, Karlheinz Peter, and Zhiyong Li. Macrophage polarization as a potential therapeutic target for atherosclerosis: a dynamic stochastic modelling study. *Royal Society open science*, 9(8):220239, 2022.

[149] Michael G Watson, Helen M Byrne, Charlie Macaskill, and Mary R Myerscough. A two-phase model of early fibrous cap formation in atherosclerosis. *Journal of Theoretical Biology*, 456:123–136, 2018.

[150] Michael G Watson, Helen M Byrne, Charlie Macaskill, and Mary R Myerscough. A multiphase model of growth factor-regulated atherosclerotic cap formation. *Journal of Mathematical Biology*, 81(2):725–767, 2020.

[151] Ishraq U Ahmed, Helen M Byrne, and Mary R Myerscough. Macrophage anti-inflammatory behaviour in a multiphase model of atherosclerotic plaque development. *Bulletin of Mathematical Biology*, 85(5):37, 2023.

[152] Ishraq U Ahmed and Mary R Myerscough. HDL and plaque regression in a multiphase model of early atherosclerosis. *Mathematical Biosciences*, 373:109208, 2024.

[153] Francesco Pappalardo, Alessandro Cincotti, Alfredo Motta, and Marzio Pennisi. Agent based modeling of atherosclerosis: a concrete help in personalized treatments. In *Emerging Intelligent Computing Technology and Applications. With Aspects of Artificial Intelligence: 5th International Conference on Intelligent Computing, ICIC 2009 Ulsan, South Korea, September 16-19, 2009 Proceedings 5*, pages 386–396. Springer, 2009.

[154] Anna Corti, Claudio Chiastra, Monika Colombo, Marc Garbey, Francesco Migliavacca, and Stefano Casarin. A fully coupled computational fluid dynamics–agent-based model of atherosclerotic plaque development: multiscale modeling framework and parameter sensitivity analysis. *Computers in biology and medicine*, 118:103623, 2020.

[155] Jichao Pan, Yan Cai, Mengchen Liu, and Zhiyong Li. Role of vascular smooth muscle cell phenotypic switching in plaque progression: A hybrid modeling study. *Journal of Theoretical Biology*, 526:110794, 2021.

[156] Jichao Pan, Yan Cai, Hongliang He, Ning Gu, and Zhiyong Li. A multiscale modeling study of nanoparticle-based targeting therapy against atherosclerosis. *Journal of Biomechanics*, 166:112067, 2024.

[157] Jan van Groenendael, Hans de Kroon, and Hal Caswell. Projection matrices in population biology. *Trends in ecology & evolution*, 3(10):264–269, 1988.

[158] Daniel F Doak, Ellen Waddle, Ryan E Langendorf, Allison M Louthan, Nathalie Isabelle Chardon, Reilly R Dibner, Douglas A Keinath, Elizabeth Lombardi, Christopher Steenbock, Robert K Shriver, et al. A critical comparison of integral projection and matrix projection models for demographic analysis. *Ecological Monographs*, 91(2):e01447, 2021.

[159] Patrick H Leslie. On the use of matrices in certain population mathematics. *Biometrika*, 33(3):183–212, 1945.

[160] JM Cushing. Nonlinear matrix models and population dynamics. *Natural Resource Modeling*, 2(4):539–580, 1988.

[161] Arild Wikan. Dynamic consequences of reproductive delay in leslie matrix models with nonlinear survival probabilities. *Mathematical biosciences*, 146(1):37–62, 1997.

[162] Suzanne L Robertson, Shandelle M Henson, Timothy Robertson, and JM Cushing. A matter of maturity: To delay or not to delay? continuous-time compartmental models of structured populations in the literature 2000–2016. *Natural Resource Modeling*, 31(1):e12160, 2018.

[163] Francis R Sharpe and Alfred J Lotka. L. a problem in age-distribution. *The London, Edinburgh, and Dublin Philosophical Magazine and Journal of Science*, 21(124):435–438, 1911.

[164] Luis M Abia, Oscar Angulo, Juan C López-Marcos, and MA López-Marcos. Numerical schemes for a size-structured cell population model with equal fission. *Mathematical and Computer Modelling*, 50(5-6):653–664, 2009.

[165] Hugh Z Ford, Helen M Byrne, and Mary R Myerscough. A lipid-structured model for macrophage populations in atherosclerotic plaques. *Journal of Theoretical Biology*, 479:48–63, 2019.

[166] Keith L Chambers, Michael G Watson, and Mary R Myerscough. A lipid-structured model of atherosclerosis with macrophage proliferation. *Bulletin of Mathematical Biology*, 86(8):104, 2024.

[167] AG McKendrick. Applications of mathematics to medical problems. edimburgh mathematical society, 1926.

[168] LM Abia, O Angulo, and JC López-Marcos. Age-structured population models and their numerical solution. *Ecological modelling*, 188(1):112–136, 2005.

[169] Rebecca H Chisholm, Tommaso Lorenzi, Laurent Desvillettes, and Barry D Hughes. Evolutionary dynamics of phenotype-structured populations: from individual-level mechanisms to population-level consequences. *Zeitschrift für angewandte Mathematik und Physik*, 67:1–34, 2016.

[170] Jesús J Bosque, Gabriel F Calvo, David Molina-García, Julián Pérez-Beteta, Ana M García Vicente, and Víctor M Pérez-García. Metabolic activity grows in human cancers pushed by phenotypic variability. *Iscience*, 26(3), 2023.

[171] Jonathan AD Wattis, Qi Qi, and Helen M Byrne. Mathematical modelling of telomere length dynamics. *Journal of Mathematical Biology*, 80:1039–1076, 2020.

[172] Hao Kang, Xi Huo, and Shigui Ruan. Nonlinear physiologically structured population models with two internal variables. *Journal of Nonlinear Science*, 30:2847–2884, 2020.

[173] Arran Hodgkinson, Laurent Le Cam, Dumitru Trucu, and Ovidiu Radulescu. Spatio-genetic and phenotypic modelling elucidates resistance and re-sensitisation to treatment in heterogeneous melanoma. *Journal of theoretical biology*, 466:84–105, 2019.

[174] Béatrice Laroche and Antoine Perasso. Threshold behaviour of a si epidemiological model with two structuring variables. *Journal of Evolution Equations*, 16(2):293–315, 2016.

[175] Marie Doumic. Analysis of a population model structured by the cells molecular content. *Mathematical Modelling of Natural Phenomena*, 2(3):121–152, 2007.

[176] Samuel Bernard, Laurent Pujo-Menjouet, and Michael C Mackey. Analysis of cell kinetics using a cell division marker: mathematical modeling of experimental data. *Biophysical journal*, 84(5):3414–3424, 2003.

[177] Olivier Restif, Yun S Goh, Matthieu Palayret, Andrew J Grant, Trevelyan J McKinley, Michael R Clark, and Pietro Mastroeni. Quantification of the effects of antibodies on the extra-and intracellular dynamics of salmonella enterica. *Journal of The Royal Society Interface*, 10(79):20120866, 2013.

[178] Giulia L Celora, Helen M Byrne, and PG Kevrekidis. Spatio-temporal modelling of phenotypic heterogeneity in tumour tissues and its impact on radiotherapy treatment. *Journal of Theoretical Biology*, 556:111248, 2023.

[179] Giada Fiandaca, Sara Bernardi, Marco Scianna, and Marcello Edoardo Delitala. A phenotype-structured model to reproduce the avascular growth of a tumor and its interaction with the surrounding environment. *Journal of Theoretical Biology*, 535:110980, 2022.

[180] Yingli Pan. Propagation dynamics for an age-structured population model in time-space periodic habitat. *Journal of Mathematical Biology*, 84(3):19, 2022.

[181] Abed Boulouz. A spatially and size-structured population model with unbounded birth process. *Discrete & Continuous Dynamical Systems-Series B*, 27(12), 2022.

[182] Wenjie Hu. Spatial–temporal patterns of a two age structured population model with spatial non-locality. *Computers & Mathematics with Applications*, 78(1):123–135, 2019.

[183] Zhihua Liu, Hui Tang, and Pierre Magal. Hopf bifurcation for a spatially and age structured population dynamics model. *Discr. Cont. Dyn. Syst. B*, 20:1735–1757, 2015.

[184] Nicolas Meunier and Nicolas Muller. Mathematical study of an inflammatory model for atherosclerosis: a nonlinear renewal equation. *Acta Applicandae Mathematicae*, 161:107–126, 2019.

[185] Michael G Watson, Keith L Chambers, and Mary R Myerscough. A lipid-structured model of atherosclerotic plaque macrophages with lipid-dependent kinetics. *Bulletin of Mathematical Biology*, 85(9):85, 2023.

[186] Adriana Valeria Jäger, Paula Arias, Maria Virginia Tribulatti, Marcela Adriana Brocco, Maria Victoria Pepe, and Arlinet Kierbel. The inflammatory response induced by pseudomonas aeruginosa in macrophages enhances apoptotic cell removal. *Scientific Reports*, 11(1):1–13, 2021.

[187] Ivan KH Poon, Christopher D Lucas, Adriano G Rossi, and Kodi S Ravichandran. Apoptotic cell clearance: basic biology and therapeutic potential. *Nature Reviews Immunology*, 14(3):166–180, 2014.

[188] Jae A Collins, Cynthia A Schandl, Kristy K Young, Josef Vesely, and Mark C Willingham. Major dna fragmentation is a late event in apoptosis. *Journal of Histochemistry & Cytochemistry*, 45(7):923–934, 1997.

[189] Kyeongdae Kim, Dahee Shim, Jun Seong Lee, Konstantin Zaitsev, Jesse W Williams, Ki-Wook Kim, Man-Young Jang, Hyung Seok Jang, Tae Jin Yun, Seung Hyun Lee, et al. Transcriptome analysis reveals nonfoamy rather than foamy plaque macrophages are proinflammatory in atherosclerotic murine models. *Circulation research*, 123(10):1127–1142, 2018.

[190] Lea Dib, Lada A Koneva, Andreas Edsfeldt, Yasemin-Xiomara Zurke, Jiangming Sun, Mihaela Nitulescu, Moustafa Attar, Esther Lutgens, Steffen Schmidt, Marie W Lindholm, et al. Lipid-associated macrophages transition to an inflammatory state in human atherosclerosis, increasing the risk of cerebrovascular complications. *Nature cardiovascular research*, 2(7):656–672, 2023.

[191] Yoko Kojima, Irving L Weissman, and Nicholas J Leeper. The role of efferocytosis in atherosclerosis. *Circulation*, 135(5):476–489, 2017.

[192] Telma Silva, Willi Jäger, Maria Neuss-Radu, and Adélia Sequeira. Modeling of the early stage of atherosclerosis with emphasis on the regulation of the endothelial permeability. *Journal of Theoretical Biology*, 496:110229, 2020.

[193] Johannes Westman, Sergio Grinstein, and Pedro Elias Marques. Phagocytosis of necrotic debris at sites of injury and inflammation. *Frontiers in immunology*, 10:3030, 2020.

[194] Thomas A Angelovich, Anna C Hearps, Anna Maisa, Theodoros Kelesidis, and Anthony Jaworowski. Quantification of monocyte transmigration and foam cell formation from individuals with chronic inflammatory conditions. *Journal of Visualized Experiments*, page e56293, 2017.

[195] Angie Ghattas, Helen R Griffiths, Andrew Devitt, Gregory YH Lip, and Eduard Shantsila. Monocytes in coronary artery disease and atherosclerosis: where are we now? *Journal of the American College of Cardiology*, 62(17):1541–1551, 2013.

[196] Norms in ndsolve—wolfram language documentation. https://reference.wolfram.com/language/tutorial/NDSolveVectorNorm.html.

[197] Kummer confluent hypergeometric function. https://functions.wolfram.com/HypergeometricFunctions/Hypergeometric1F1/.

[198] Hermite hypergeometric function. https://functions.wolfram.com/HypergeometricFunctions/HermiteHGeneral/.

[199] Ira Tabas and Karin E Bornfeldt. Macrophage phenotype and function in different stages of atherosclerosis. *Circulation research*, 118(4):653–667, 2016.

[200] Anette Christ, Siroon Bekkering, Eicke Latz, and Niels P Riksen. Long-term activation of the innate immune system in atherosclerosis. In *Seminars in Immunology*, volume 28, pages 384–393. Elsevier, 2016.

[201] Chao Liu, Dewei Chu, Kourosh Kalantar-Zadeh, Jacob George, Howard A Young, and Guozhen Liu. Cytokines: From clinical significance to quantification. *Advanced Science*, 8(15):2004433, 2021.

[202] Christian M Madsen, Anette Varbo, and Børge G Nordestgaard. Extreme high high-density lipoprotein cholesterol is paradoxically associated with high mortality in men and women: two prospective cohort studies. *European heart journal*, 38(32):2478–2486, 2017.

[203] Lars Bo Nielsen. Transfer of low density lipoprotein into the arterial wall and risk of atherosclerosis. *Atherosclerosis*, 123(1-2):1–15, 1996.

[204] Gerhard A Holzapfel, Gerhard Sommer, Christian T Gasser, and Peter Regitnig. Determination of layer-specific mechanical properties of human coronary arteries with nonatherosclerotic intimal thickening and related constitutive modeling. *American Journal of Physiology-Heart and Circulatory Physiology*, 289(5):H2048–H2058, 2005.

[205] S Stender and DB Zilversmit. Transfer of plasma lipoprotein components and of plasma proteins into aortas of cholesterol-fed rabbits. molecular size as a determinant of plasma lipoprotein influx. *Arteriosclerosis: An Official Journal of the American Heart Association, Inc.*, 1(1):38–49, 1981.

[206] Elspeth B Smith and Eileen M Staples. Plasma protein concentrations in interstitial

fluid from human aortas. *Proceedings of the Royal Society of London. Series B. Biological Sciences*, 217(1206):59–75, 1982.

[207] Marc S Penn, Gerald M Saidel, and Guy M Chisolm. Relative significance of endothelium and internal elastic lamina in regulating the entry of macromolecules into arteries in vivo. *Circulation research*, 74(1):74–82, 1994.

[208] Thomas N Wight. A role for proteoglycans in vascular disease. *Matrix Biology*, 71:396–420, 2018.

[209] John R Guyton and Keith F Klemp. The lipid-rich core region of human atherosclerotic fibrous plaques. prevalence of small lipid droplets and vesicles by electron microscopy. *The American journal of pathology*, 134(3):705, 1989.

[210] Martin Liu, Saurabhi Samant, Charu Hasini Vasa, Ryan M Pedrigi, Usama M Oguz, Sangjin Ryu, Timothy Wei, Daniel R Anderson, Devendra K Agrawal, and Yiannis S Chatzizisis. Co-culture models of endothelial cells, macrophages, and vascular smooth muscle cells for the study of the natural history of atherosclerosis. *PLOS One*, 18(1):e0280385, 2023.

[211] Cristina Bancells, Sònia Benítez, Matti Jauhiainen, Jordi Ordóñez-Llanos, Petri T Kovanen, Sandra Villegas, José Luis Sánchez-Quesada, O Katariina, et al. High binding affinity of electronegative ldl to human aortic proteoglycans depends on its aggregation level. *Journal of lipid research*, 50(3):446–455, 2009.

[212] Marcie R Williams, Yumiko Sakurai, Susu M Zughaier, Suzanne G Eskin, and Larry V McIntire. Transmigration across activated endothelium induces transcriptional changes, inhibits apoptosis, and decreases antimicrobial protein expression in human monocytes. *Journal of leukocyte biology*, 86(6):1331–1343, 2009.

[213] David S Nelson. *Immunobiology of the Macrophage*. Academic Press, 2014.

[214] Seung Jin Lee, Seung Eun Baek, Min A Jang, and Chi Dae Kim. SIRT1 inhibits monocyte adhesion to the vascular endothelium by suppressing Mac-1 expression on monocytes. *Experimental & Molecular Medicine*, 51(4):1–12, 2019.

[215] Simon Yona, Ki-Wook Kim, Yochai Wolf, Alexander Mildner, Diana Varol, Michal Breker, Dalit Strauss-Ayali, Sergey Viukov, Martin Guilliams, Alexander Misharin, et al. Fate mapping reveals origins and dynamics of monocytes and tissue macrophages under homeostasis. *Immunity*, 38(1):79–91, 2013.

[216] Jesse W Williams, Catherine Martel, Stephane Potteaux, Ekaterina Esaulova, Molly A Ingersoll, Andrew Elvington, Brian T Saunders, Li-Hao Huang, Andreas J Habenicht, Bernd H Zinselmeyer, et al. Limited macrophage positional dynamics in progressing or regressing murine atherosclerotic plaques—brief report. *Arteriosclerosis, Thrombosis, and Vascular Biology*, 38(8):1702–1710, 2018.

[217] Antti Saraste and Kari Pulkki. Morphologic and biochemical hallmarks of apoptosis. *Cardiovascular research*, 45(3):528–537, 2000.

[218] RJ Sokol, J Wales, G Hudson, DJ Goldstein, and NT James. Changes in cellular dry mass during macrophage development. *Cells Tissues Organs*, 142(3):246–248, 1991.

[219] Geoffrey Cooper and Kenneth Adams. *The cell: a molecular approach*. Oxford University Press, 2022.

[220] Kyle Taruc, Charles Yin, Daniel G Wootton, and Bryan Heit. Quantification of effe-

rocytosis by single-cell fluorescence microscopy. *Journal of Visualized Experiments*, (138):e58149, 2018.

[221] Dorien M Schrijvers, Guido RY De Meyer, Mark M Kockx, Arnold G Herman, and Wim Martinet. Phagocytosis of apoptotic cells by macrophages is impaired in atherosclerosis. *Arteriosclerosis, Thrombosis, and Vascular Biology*, 25(6):1256–1261, 2005.

[222] Greet Brouckaert, Michael Kalai, Dmitri V Krysko, Xavier Saelens, Dominique Vercammen, Matladi Ndlovu, Guy Haegeman, Katharina D'Herde, and Peter Vandenabeele. Phagocytosis of necrotic cells by macrophages is phosphatidylserine dependent and does not induce inflammatory cytokine production. *Molecular biology of the cell*, 15(3):1089–1100, 2004.

[223] Leonard Kritharides, Aimee Christian, Genevieve Stoudt, Dianne Morel, and George H Rothblat. Cholesterol metabolism and efflux in human thp-1 macrophages. *Arteriosclerosis, Thrombosis, and Vascular Biology*, 18(10):1589–1599, 1998.

[224] Nicholas J Woudberg, Sarah Pedretti, Sandrine Lecour, Rainer Schulz, Nicolas Vuilleumier, Richard W James, and Miguel A Frias. Pharmacological intervention to modulate hdl: what do we target? *Frontiers in pharmacology*, 8:989, 2018.

[225] Simon J O'Carroll, Dan Ting Kho, Rachael Wiltshire, Vicky Nelson, Odunayo Rotimi, Rebecca Johnson, Catherine E Angel, and E Scott Graham. Pro-inflammatory tnfα and il-1β differentially regulate the inflammatory phenotype of brain microvascular endothelial cells. *Journal of neuroinflammation*, 12:1–18, 2015.

[226] JMR6ME Pugin, CC Schürer-Maly, Didier Leturcq, Ann Moriarty, Richard J Ulevitch, and Peter S Tobias. Lipopolysaccharide activation of human endothelial and epithelial cells is mediated by lipopolysaccharide-binding protein and soluble cd14. *Proceedings of the National Academy of Sciences*, 90(7):2744–2748, 1993.

[227] Xiaojin Sha, Shu Meng, Xinyuan Li, Hang Xi, Massimo Maddaloni, David W Pascual, Huimin Shan, Xiaohua Jiang, Hong Wang, and Xiao-feng Yang. Interleukin-35 inhibits endothelial cell activation by suppressing mapk-ap-1 pathway. *Journal of Biological Chemistry*, 290(31):19307–19318, 2015.

[228] F Atzeni and P Sarzi-Puttini. Tumor necrosis factor. *Brenner's Encyclopedia of Genetics*, pages 229–231, 2013.

[229] Naoki Watanabe, Hiroshi Kuriyama, Hisao Sone, Hiroshi Neda, Naofumi Yamauchi, Masahiro Maeda, and Yoshiro Niitsu. Continuous internalization of tumor necrosis factor receptors in a human myosarcoma cell line. *Journal of Biological Chemistry*, 263(21):10262–10266, 1988.

[230] Yoshiro Niitsu, Naoki Watanabe, Hisao Sone, Hiroshi Neda, Naofumi Yamauchi, Masahiro Maeda, and Ichiro Urushizaki. Analysis of the tnf receptor on kym cells by binding assay and affinity cross-linking. *Journal of Immunotherapy*, 7(3):276–282, 1988.

[231] Robert J Schutte, Andreina Parisi-Amon, and W Monty Reichert. Cytokine profiling using monocytes/macrophages cultured on common biomaterials with a range of surface chemistries. *Journal of Biomedical Materials Research Part A: An Official Journal of The Society for Biomaterials, The Japanese Society for Biomaterials, and The Australian Society for Biomaterials and the Korean Society for Biomaterials*, 88(1):128–139, 2009.

[232] Abdullah A Tarique, Jayden Logan, Emma Thomas, Patrick G Holt, Peter D Sly, and Emmanuelle Fantino. Phenotypic, functional, and plasticity features of classical and alternatively activated human macrophages. *American journal of respiratory cell and molecular biology*, 53(5):676–688, 2015.

[233] Anatol Kontush, Patrice Therond, Amal Zerrad, Martine Couturier, Anne Négre-Salvayre, Juliana A de Souza, Sandrine Chantepie, and M John Chapman. Preferential sphingosine-1-phosphate enrichment and sphingomyelin depletion are key features of small dense hdl3 particles: relevance to antiapoptotic and antioxidative activities. *Arteriosclerosis, Thrombosis, and Vascular Biology*, 27(8):1843–1849, 2007.

[234] S Yoneda, S Shibata, Y Yamashita, and M Yanagishita. Biosynthesis of versican by rat dental pulp cells in culture. *Archives of oral biology*, 47(6):435–442, 2002.

[235] Erine A Kupetsky-Rincon, Qiaoli Li, and Jouni Uitto. Magnesium reduces carotid intima-media thickness in a mouse model of pseudoxanthoma elasticum: a novel treatment biomarker. *Clinical and translational science*, 5(3):259–264, 2012.

[236] Ilka Ott, Cornelia Michaelis, Maren Schuermann, Birgit Steppich, Isabell Seitz, Mieke Dewerchin, Dietlind Zohlnhofer, Rainer Wessely, Martina Rudelius, Albert Schömig, et al. Vascular remodeling in mice lacking the cytoplasmic domain of tissue factor. *Circulation research*, 97(3):293–298, 2005.

[237] Salvador Pérez and Sergio Rius-Pérez. Macrophage polarization and reprogramming in acute inflammation: a redox perspective. *Antioxidants*, 11(7):1394, 2022.

[238] William Insull Jr. The pathology of atherosclerosis: plaque development and plaque responses to medical treatment. *The American journal of medicine*, 122(1):S3–S14, 2009.

[239] Brian E Sansbury and Matthew Spite. Resolution of acute inflammation and the role of resolvins in immunity, thrombosis, and vascular biology. *Circulation research*, 119(1):113–130, 2016.

[240] Maria Pataki, Gabor Lusztig, and Horst Robenek. Endocytosis of oxidized LDL and reversibility of migration inhibition in macrophage-derived foam cells in vitro. a mechanism for atherosclerosis regression? *Arteriosclerosis and Thrombosis: A Journal of Vascular Biology*, 12(8):936–944, 1992.

[241] Linmu Chen, Jun Zhang, Xi Yang, Yan Liu, Xiao Deng, and Chao Yu. Lysophosphatidic acid decreased macrophage foam cell migration correlated with downregulation of fucosyltransferase 8 via hnf1α. *Atherosclerosis*, 290:19–30, 2019.

[242] Navid Mohammad Mirzaei, William S Weintraub, and Pak-Wing Fok. An integrated approach to simulating the vulnerable atherosclerotic plaque. *American Journal of Physiology-Heart and Circulatory Physiology*, 319(4):H835–H846, 2020.

[243] Wei Yuan, Guanglei Li, and Bingmei M Fu. Effect of surface charge of immortalized mouse cerebral endothelial cell monolayer on transport of charged solutes. *Annals of biomedical engineering*, 38:1463–1472, 2010.

[244] Katrina M Adlerz, Helim Aranda-Espinoza, and Heather N Hayenga. Substrate elasticity regulates the behavior of human monocyte-derived macrophages. *European Biophysics Journal*, 45:301–309, 2016.

[245] AE Ross and RR Pompano. Diffusion of cytokines in live lymph node tissue using microfluidic integrated optical imaging. *Analytica chimica acta*, 1000:205–213, 2018.

[246] Sonia Eligini, Erica Gianazza, Alice Mallia, Stefania Ghilardi, and Cristina Banfi. Macrophage phenotyping in atherosclerosis by proteomics. *International Journal of Molecular Sciences*, 24(3):2613, 2023.

[247] Arif Yurdagul Jr. Crosstalk between macrophages and vascular smooth muscle cells in atherosclerotic plaque stability. *Arteriosclerosis, Thrombosis, and Vascular Biology*, 42(4):372–380, 2022.

[248] Gabrielle Fredman, Nazila Kamaly, Stefano Spolitu, Jaclyn Milton, Devram Ghorpade, Raymond Chiasson, George Kuriakose, Mauro Perretti, Omid Farokhzad, and Ira Tabas. Targeted nanoparticles containing the proresolving peptide ac2-26 protect against advanced atherosclerosis in hypercholesterolemic mice. *Science translational medicine*, 7(275):275ra20–275ra20, 2015.

[249] Sima Allahverdian, Carleena Ortega, and Gordon A Francis. Smooth muscle cell-proteoglycan-lipoprotein interactions as drivers of atherosclerosis. *Prevention and Treatment of Atherosclerosis*, 270:335–358, 2020.

[250] Sönke Weinert, David M Poitz, Susanne Auffermann-Gretzinger, Lars Eger, Joerg Herold, Senad Medunjanin, Alexander Schmeisser, Ruth H Strasser, and Ruediger C Braun-Dullaeus. The lysosomal transfer of ldl/cholesterol from macrophages into vascular smooth muscle cells induces their phenotypic alteration. *Cardiovascular research*, 97(3):544–552, 2013.

[251] Cuiwen He, Haibo Jiang, Wenxin Song, Howard Riezman, Peter Tontonoz, Thomas A Weston, Paul Guagliardo, Paul H Kim, Rachel Jung, Patrick Heizer, et al. Cultured macrophages transfer surplus cholesterol into adjacent cells in the absence of serum or high-density lipoproteins. *Proceedings of the National Academy of Sciences*, 117(19):10476–10483, 2020.

[252] Clinton S Robbins, Ingo Hilgendorf, Georg F Weber, Igor Theurl, Yoshiko Iwamoto, Jose-Luiz Figueiredo, Rostic Gorbatov, Galina K Sukhova, Louisa Gerhardt, David Smyth, et al. Local proliferation dominates lesional macrophage accumulation in atherosclerosis. *Nature medicine*, 19(9):1166–1172, 2013.

[253] Matthew J Frontini, Caroline O'Neil, Cynthia Sawyez, Bosco MC Chan, Murray W Huff, and J Geoffrey Pickering. Lipid incorporation inhibits src-dependent assembly of fibronectin and type i collagen by vascular smooth muscle cells. *Circulation research*, 104(7):832–841, 2009.

[254] Bryan N Brown, Jolene E Valentin, Ann M Stewart-Akers, George P McCabe, and Stephen F Badylak. Macrophage phenotype and remodeling outcomes in response to biologic scaffolds with and without a cellular component. *Biomaterials*, 30(8):1482–1491, 2009.

[255] Daniel Schulz, Yannik Severin, Vito Riccardo Tomaso Zanotelli, and Bernd Bodenmiller. In-depth characterization of monocyte-derived macrophages using a mass cytometry-based phagocytosis assay. *Scientific reports*, 9(1):1925, 2019.

[256] Ping Lin, Hong-Hai Ji, Yan-Jie Li, and Shou-Dong Guo. Macrophage plasticity and atherosclerosis therapy. *Frontiers in molecular biosciences*, 8:679797, 2021.

[257] Kui Cui, Christopher L Ardell, Nataly P Podolnikova, and Valentin P Yakubenko. Distinct migratory properties of m1, m2, and resident macrophages are regulated by αdβ2 and αmβ2 integrin-mediated adhesion. *Frontiers in immunology*, 9:2650, 2018.

[258] Hoon Hong, Alexey Ovchinnikov, Gleb Pogudin, and Chee Yap. Sian: software for structural identifiability analysis of ode models. *Bioinformatics*, 35(16):2873–2874, 2019.

[259] Giuseppina Bellu, Maria Pia Saccomani, Stefania Audoly, and Leontina D'Angiò. Daisy: A new software tool to test global identifiability of biological and physiological systems. *Computer Methods and Programs in Biomedicine*, 88(1):52–61, 2007.

[260] JAD Wattis, B O'Malley, H Blackburn, L Pickersgill, J Panovska, HM Byrne, and KG Jackson. Mathematical model for low density lipoprotein (LDL) endocytosis by hepatocytes. *Bulletin of Mathematical Biology*, 70:2303–2333, 2008.

[261] Liang Sheng, Bijie Jiang, and Liangyou Rui. Intracellular lipid content is a key intrinsic determinant for hepatocyte viability and metabolic and inflammatory states in mice. *American Journal of Physiology-Endocrinology and Metabolism*, 305(9):E1115–E1123, 2013.

[262] Maomao Zhang, Julie S Di Martino, Robert L Bowman, Nathaniel R Campbell, Sanjeethan C Baksh, Theresa Simon-Vermot, Isabella S Kim, Pearce Haldeman, Chandrani Mondal, Vladimir Yong-Gonzales, et al. Adipocyte-derived lipids mediate melanoma progression via fatp proteins. *Cancer Discovery*, 8(8):1006–1025, 2018.